UNIVERSITY OF CALIFORNIA SAN DIEGO

Beyond Stretchability: The Mechanical Properties of Semiconducting Polymers

A dissertation submitted in partial satisfaction of the
requirements for the degree Doctor of Philosophy

in

Chemical Engineering

by

Alexander Chen

Committee in charge:

Professor Darren Lipomi, Chair
Professor Shengqiang Cai
Professor Zheng Chen
Professor David Fenning
Professor Nathan Romero

2023

The dissertation of Alexander Chen is approved, and it is acceptable in quality and form for publication on microfilm and electronically.

University of California San Diego

2023

DEDICATION

To Mom, Dad, and 辉辉 for their love and support.

EPIGRAPH

And now here is my secret, a very simple secret: It is only with the heart that one can see rightly; what is essential is invisible to the eye.

Antoine de Saint-Exupéry

TABLE OF CONTENTS

LIST OF FIGURES

LIST OF TABLES

ACKNOWLEDGEMENTS

I would like to first and foremost thank my family. Mom (Yili Xu) and Dad (Xiaoyi Chen), this PhD would not have been possible without all your love, sacrifice, and support. You have given me everything, and there is no way I can ever repay that or fully express the extent of my gratitude. To my cat, 辉辉, thank you for being my best friend for 18 years. I love you and miss you so much; thank you for all you have given me. To Christina Cui and William Luo, thank you for always being there for me no matter what. I miss the two of you dearly, and would give anything for us to end up in the same place again.

To my advisor, Prof. Darren Lipomi, I would like to express my gratitude for your unwavering support. Thank you for taking the chance on me, and for never giving up on me. Thank you for all that you have taught me, all the opportunities you have given me, and all the wonderful discussions about science that inspired me. I could not have asked for a better advisor, colleague, or friend. To Prof. David Fenning, thank you for your mentorship and guidance, as well as your constant motivation. Working with you has undoubtedly made me a better scientist, researcher, and manager. I appreciate that you had the same high expectations and demand for scientific rigor for me as you did for your own students, and for dedicating time to me as if you were my advisor. I am truly grateful for all that you have taught me. Darren and David, thank you both for helping me realize what a privilege it is to be completely immersed in research during this time of my life, and how fortunate I am to be able to spend my days thinking about science. To Prof. Zheng Chen, Prof. Shengqiang Cai, and Prof. Nathan Romero: thank you all for serving on my committee, and for the many helpful discussions over these last few years.

I'm so grateful to my wonderful colleagues in the Lipomi Lab. How lucky I am to have something that makes saying goodbye so hard! Prof. Laure Kayser, Prof. Charles Dhong, Prof. Moon Sung Kang, Dr. Rachel Blau, Dr. Rory Runser, Dr. Julian Ramirez, Dr. Andrew Kleinschmidt, Dr. Allison Lim, Dr. Beril Polat, Dr. Mickey Finn, Guillermo Esparza, Samuel Edmunds, Laura Becerra, Tarek Rafeedi, Robert Ramji, Abdulhameed Abdal, Kartik Choudhary, Jordan Bunch, Sarah Brew, Ignasi Simon, Finn Oneill, Yi Qie, and Jaden Cramlet have been instrumental to my growth as a scientist and researcher, as well as the work

presented in this dissertation. Laure and Charles, thank you for being excellent role models to look up to. Julian, thank you for your wisdom and humor, although often not in that particular order. Beril, your determination and self-assuredness constantly inspired me. Andrew, your encouragement and mentorship motivated me to go on with my PhD, particularly when I was a new graduate student. Rory, thank you for extending your friendship to me and for reminding me to keep a healthy work-life balance. Allison, thank you for your thoughtfulness and compassion. Robert, thank you for constantly reminding me to stay young at heart ("to be cringe is to be free," as you might say). Guillermo, your creativity has always pushed me to think clearly, critically, and creatively about science. Rachel, your tireless scientific curiosity and work ethic has driven me to improve my own. Abdul, in addition to your ambition, creativity, and work ethic, I admire how you are always the first to volunteer to help, regardless of what the task may be. Rory, Andrew, Guillermo, Laura, Allison, and Robert, sharing an office with you was a wonderful and welcome detriment to my productivity, and your company made me look forward to going to work every day. Kartik, thank you for trusting me as your mentor, even when I had no idea what I was doing at first. Your boundless curiosity, resilience, and passion are truly a gift. Jordan, Ignasi, Sarah, and Finn: I could not have asked for a better undergraduate team, and I look forward to seeing all the wonderful things you all accomplish in the future. Dana Jimenez and Ji Song (who were both invaluable de facto members of the Lipomi Lab), thank you both for working so hard to make my job so much easier. Nothing in the department would have ever gotten done without the two of you. I will miss your positive attitudes and cheerful optimism. I have also been fortunate to have the chance to work closely with many members of the Fenning Research Group: Dr. Moses Kodur, Dr. Sean Dunfield, Dr. Rishi Kumar, Deniz Cakan, Jack Palmer, Connor Dolan, and Apoorva Gupta. To all my mentors, colleagues, and collaborators, I will miss talking and joking around with you in lab while trying to do good science. Thank you for being so welcoming and helpful, and for teaching me so much. I could not have asked for better teammates.

Darren, thank you for your constant support and encouragement during the first 4 years of GradAMP, first in your capacity as my advisor and later as Associate Dean for Students. Dr. David Artis and Dr. Tom Brown, thank you for your helpful discussions and encouragement that facilitated the

development and growth of GradAMP at UC San Diego. Dr. Betty Ramirez and Dr. Angeline Yang, thank you for supporting the institutionalization of GradAMP, and for finding a home for the program within GEPA. Finally, thank you to all the PhD student mentors who have volunteered their time to serve as mentors for GradAMP. GradAMP could not have existed without your time and labor.

To all my friends, old and new, who have supported me from near and far, thank you for constantly believing in me. Jonathan Wang and Patrick Lin, thank you for being my friends, no matter how long we go without talking or how far away you live. Rory Runser, Yixuan Li, Darren Tan, I will miss our hot pot dinners. Thomas Chan, thank you for always being willing to go out of your way to get food with me.

I suppose lastly, I will thank myself. These were the longest days and shortest years of my life. There were many times when I thought that I should give up. I am proud of myself for my perseverance, my resilience, and my growth both as a person and as a scientist. Thank you for learning to have the courage to truly try your best. Thank you for learning to step outside of your comfort zone and try new things. Thank you for learning to get over the embarrassment of being bad at things, and for choosing to work hard towards learning to be better instead of giving up. Thank you for learning the value of your own time, and for learning when and why to quit. Thank you for learning to stop being afraid of failure. Thank you for learning that you are still a work in progress, and making peace with that realization.

I have always been afraid to put myself out there. I think when you're a kid, it's very easy to pretend like it's cool to not try and to not care about things. I think a part of this is because caring and trying means that you have to open yourself up to criticism (particularly in regard to work ethic) and confront your own flaws, when it's far easier to tell yourself that others are simply "better" at something. I was not a stellar student at all, and to be honest, I ended up in a PhD almost by chance. During my last two years of undergraduate studies, I saw all the senior students get manufacturing and engineering jobs in petroleum, food, and consumer goods, which seemed so dull to me. I ended up applying to graduate school even though I had no idea what that meant; all I knew was that it was probably better than staring at a reactor or at Aspen all day. Graduate school was where I truly learned to try my best. I can honestly say that after some growing pains, I tried my hardest during these last couple of years, that I put everything I had into this. This PhD,

into which I have invested my blood, sweat, and tears, has been a whirlwind of emotions. It has been fun, amazing, joyful, enlightening, fascinating, interesting, painful, lonely, frustrating, agonizing, and miserable. But it has never been boring.

Chapter 1 and Appendix A, in full, is a reprint of the material "Beyond Stretchability: Strength, Toughness, and Elastic Range in Semiconducting Polymers" as it appears in Chemistry of Materials in 2020, by **A.X. Chen**, A.T. Kleinschmidt, K. Choudhary, and D.J. Lipomi. The dissertation author was the first author of this paper, and all authors contributed to this work.

Chapter 2 and Appendix B, in full, is a reprint of the material "Comparison of the Mechanical Properties of a Conjugated Polymer Deposited Using Spin Coating, Interfacial Spreading, Solution Shearing, and Spray Coating" as it appears in ACS Applied Materials and Interfaces in 2021, by **A.X. Chen***, K. Choudhary*, G.M. Pitch, R. Runser, A. Urbina, T.J. Dunn, M. Kodur, A.T. Kleinschmidt, B.G. Wang, J.A. Bunch, D.P. Fenning, and D.J. Lipomi. The dissertation author was co-first author of this paper (as indicated by *), and all authors contributed to this work.

Chapter 3 and Appendix C, in full, is a reprint of the material "Increasing the Strength, Hardness, and Survivability of Semiconducting Polymers by Crosslinking" as it appears in Advanced Materials Interfaces in 2022, by **A.X. Chen**, J.D. Hilgar, A.A. Samoylov, S.S. Pazhankave, J.A. Bunch, K. Choudhary, G.L. Esparza, A. Lim, X. Luo, H. Chen, R. Runser, I. McCulloch, J. Mei, C.G. Hoover, A.D. Printz, N.A. Romero, and D.J. Lipomi. The dissertation author was the first author of this paper, and all authors contributed to this work.

Chapter 4 and Appendix D, in full, is a reprint of the material "Adhesive Properties of Semiconducting Polymers: Poly(3-alkylthiophene) as an Ersatz Glue" as it appears in Chemistry of Materials in 2023, by **A.X. Chen**, S.S. Pazhankave, J.A. Bunch, A. Lim, K. Choudhary, G.L. Esparza, R. Runser, C.G. Hoover, and D.J. Lipomi. The dissertation author was the first author of this paper, and all authors contributed to this work.

VITA

2018	Bachelor of Science, Chemical Engineering, University of California Davis
2018	Minor, English, University of California Davis
2020	Master of Science, Chemical Engineering, University of California San Diego
2023	Doctor of Philosophy, Chemical Engineering, University of California San Diego

PUBLICATIONS

† = authors contributed equally to the work
* = corresponding authors contributed equally to the work

1. R. Runser†, S.E. Root†, D.E. Ober, K. Choudhary, **A.X. Chen**, C. Dhong, A.D. Urbina, and D.J. Lipomi. "*Interfacial Drawing: Roll-to-Roll Coating of Semiconducting Polymer and Barrier Films onto Plastic Foils and Textiles*." Chemistry of Materials, 31, 9078-9086, **2019**, https://doi.org/10.1021/acs.chemmater.9b03343.

2. **A.X. Chen**, A.T. Kleinschmidt, K. Choudhary, and D.J. Lipomi. "*Beyond Stretchability: Strength, Toughness, and Elastic Range in Semiconducting Polymers*." Chemistry of Materials, 32, 7582-7601, **2020**, https://doi.org/10.1021/acs.chemmater.0c03019.

3. **A.X. Chen**†, K. Choudhary†, G.M. Pitch, R. Runser, A.D. Urbina, T.J. Dunn, M. Kodur, A.T. Kleinschmidt, B.G. Wang, J.A. Bunch, D.P. Fenning, A.L. Ayzner, and D.J. Lipomi. "*Comparison of the Mechanical Properties of a Conjugated Polymer Deposited Using Spin Coating, Interfacial Spreading, Solution Shearing, and Spray Coating*." ACS Applied Materials & Interfaces, 13, 51436-51446, **2021**, https://doi.org/10.1021/acsami.1c13043.

4. R. Blau, **A.X. Chen**, B. Polat, L.L. Becerra, R. Runser, B. Zamanimeymian, K. Choudhary, and D.J. Lipomi. "*Intrinsically Stretchable Block Copolymer Based on PEDOT:PSS for Improved Performance in Bioelectronic Applications*." ACS Applied Materials & Interfaces, 14, 4823-4835, **2022**, https://doi.org/10.1021/acsami.1c18495.

5. A.T. Kleinschmidt, **A.X. Chen**, T.A. Pascal*, and D.J. Lipomi*. "*Computational Modeling of Molecular Mechanics for the Experimentally Inclined*." Chemistry of Materials, 34, 7620-7634, **2022**, https://doi.org/10.1021/acs.chemmater.2c00292.

6. **A.X. Chen**, J.D. Hilgar, A.A. Samoylov, S.S. Pazhankave, J.A. Bunch, K. Choudhary, G.L. Esparza, A. Lim, X. Luo, H. Chen, R. Runser, I. McCulloch, J. Mei, C.G. Hoover, A.D. Printz, N.A. Romero, and D.J. Lipomi. "*Increasing the Strength, Hardness, and Survivability of Semiconducting Polymers by Crosslinking*." Advanced Material Interfaces, 10, 2202053, **2022**, https://doi.org/10.1002/admi.202202053.

7. G.L. Esparza†, M. Kodur†, **A.X. Chen**, B.G. Wang, R. Runser, D.P. Fenning, and D.J. Lipomi. "*Solvent-Free Transfer of Freestanding Large-Area Conjugated Polymer Films for Optoelectronic Applications*." Advanced Materials, **2023**, https://doi.org/10.1002/adma.202207798. In Press.

8. B. Polat, T. Rafeedi, L.L. Becerra, **A.X. Chen**, K. Chiang, V. Kaipu, R. Blau, P.P. Mercier, C.-K. Cheng, and D.J. Lipomi "*External Measurement of Swallowed Volume during Exercise Enabled by Stretchable Derivatives of PEDOT:PSS, Graphene, Metallic Nanoparticles, and Machine Learning*." Advanced Sensor Research, 2, 2200060, **2023**, https://doi.org/10.1002/adsr.202200060.

9. W. Yao, M. Chouchane, W. Li, S. Bai, Z. Liu, L. Li, **A.X. Chen**, B. Sayahpour, R. Shimizu, G. Raghavendran, M.A. Schroeder, Y. Chen, D.H.S. Tan, B. Sreenarayanan, C.K. Waters, A. Sichler, B. Gould, D.J. Kountz, D.J. Lipomi, M. Zhang, Y.S. Meng. "*A 5V-class Cobalt-free Battery Cathode with High Loading Enabled by Dry Coating*." Energy & Environmental Sciences, 16, 1620-1630, **2023**, https://doi.org/10.1039/D2EE03840D.

10. A.T. Kleinschmidt, **A.X. Chen**, R.S. Ramji, T.A. Pascal*, and D.J. Lipomi*. "*Decoupling Planarizing and Steric Energetics to Accurately Model the Rigidity of π-Conjugated Polymers*." Journal of Physical Chemistry B, 127, 2092-2102, **2023**, https://doi.org/10.1021/acs.jpcb.2c08843.

11. J. Sun†, K. Ma†, Z.-Y. Lin, Y. Tang, D. Varadharajan, **A.X. Chen**, H.R. Atapattu, Y. Lee, K. Chen, B.W. Boudouris, K.R. Graham, D.J. Lipomi, J. Mei*, B.M. Savoie*, and L. Dou*. "*Tailoring Molecular-Scale Contact at Perovskite/Polymeric Hole Transporting Material Interface for Efficient Solar Cells*." Advanced Materials, **2023**, https://doi.org/10.1002/adma.202300647. In Press.

12. **A.X. Chen**, S.S. Pazhankave, J.A. Bunch, A. Lim, K. Choudhary, G.L. Esparza, R. Runser, C.G. Hoover, and D.J. Lipomi. "*Adhesive Properties of Semiconducting Polymers: Poly(3-alkylthiophene) as an Ersatz Glue*." Chemistry of Materials, 35, 3329-3342, **2023,** https://doi.org/10.1021/acs.chemmater.3c00485.

13. **A.X. Chen** and D.J. Lipomi. "*Navigating the Graduate Application Process through Mentorship*." Trends in Chemistry, **2023,** https://doi.org/10.1016/j.trechm.2023.04.009. In Press.

14. **A.X. Chen**, G.L. Esparza, I. Simon, S.P. Dunfield, Y. Qie, J.A. Bunch, R. Blau, A. Lim, H. Zhang, S.E. Brew, F.M. O'Neill, D.P. Fenning*, and D.J. Lipomi*. "*Effect of Additives on the Surface Morphology, Energetics, and Contact Resistance of PEDOT:PSS*." **Submitted**.

15. L.L. Becerra, T. Rafeedi, S. Ramanarayanan, I.T. Frankel, J. Miller, **A.X. Chen**, Y. Qie, D.J. Lipomi, H. Garudadri, and T.N. Ng. "*Bi-directional Venturi Flowmeter Based on Capacitive Sensors for Spirometry*." **Submitted**.

16. **A.X. Chen**, A. Valdez, R. Blau, S. Brew, N. Azpiroz, G.L. Esparza, Y. Qie, F.M. O'Neill, J.A. Bunch, I. Simon, D. Harwood, D.J. Lipomi*, and D.P. Fenning*. "*Silver-free conductive adhesives based on a semiconducting polymer matrix for shingled solar cells*." **In Preparation**.

ABSTRACT OF THE DISSERTATION

Beyond Stretchability: The Mechanical Properties of Semiconducting Polymers

by

Alexander Chen

Doctor of Philosophy in Chemical Engineering

University of California San Diego, 2023

Professor Darren Lipomi, Chair

The promise of π-conjugated (semiconducting) polymers is to combine the electronic functionality of semiconductors with the processability and mechanical robustness of plastics. However, most research done on the mechanical properties of polymeric semiconductors (e.g., for organic photovoltaics, thin-film transistors, wearable sensors) has had the underlying goal of increasing the "stretchability": the deformability and softness. Yet, softness is the wrong characteristic for many applications envisioned for organic semiconductors, including electronic interconnects, conductive paints and coatings, conductive adhesives, touch screens and displays, electronic textiles and fabrics, chemical sensors, and distributed

sources of solar energy at risk of damage by indentation, scratching, and abrasion. For example, for organic photovoltaics, solar cells that can be integrated into surfaces already modified by human artifacts (e.g., rooftops, roads, and painted outdoor surfaces) comprise a greater potential source of renewable energy than the niche uses envisioned for portable and wearable solar cells. As such, a focus on modulus and ultimate extensibility—properties characteristic of "stretchability"—at the expense of mechanical robustness (e.g., strength, toughness, elasticity, and adhesion)—leaves many potentially lucrative applications on the table. Thus, the mechanical performance of a semiconducting polymer film must be tailored to the mechanical requirements for the device in which it is incorporated. Likewise, a semiconducting polymer film must also serve a structural role, as a glue that holds the device stack together; it must have sufficient cohesive and adhesive energy to retain electronic function of the device even when deformed. As such, the polymeric semiconductor also must function as an adhesive, despite this not being the primary function. This dissertation discusses two methods for controlling the mechanical properties of semiconducting polymer films that are common to conventional polymers, yet rarely applied to conjugated polymers. The first is the processing of the polymer film using continuous deposition methods common for industrial manufacturing of plastic materials. The second is the use of a crosslinker to introduce covalent bonds between polymer chains (common for commercial rubbers and elastomers). Finally, this dissertation discusses how changes to the side chain length of a model conjugated polymer affect the adhesive function of the polymer film.

Chapter 1. Introduction to the Mechanical Properties of Semiconducting Polymers

1.1.1 Introduction

Modern life is replete with objects coated with polymeric films exhibiting exceptional resistance to indentation, scratch, and abrasion. These properties are exemplified by everyday products such as car paint, flooring, scratch-resistant eyeglasses, and the surfaces of roads and parking lots. The functionality of many of these objects could be profitably augmented by the incorporation of electronic polymers for applications in sensing, optics, or energy harvesting, but such polymers would require the ability to sustain mechanical insults of the real world—i.e., hardness. However, the current zeitgeist in the chemistry of electronic polymers favors flexibility and stretchability—i.e., softness.[1] In the field of soft electronics, it is common to contrast the mechanical properties of metals and inorganic semiconductors with those of polymers and biological structures. In this conception, "hard electronics" are associated with inflexibility and also possibly brittleness. However, this association is not accurate, as flexibility is an extensive property determined as much by thinness as by intrinsic mechanical properties.[2] Moreover, it is routine to engineer a polymer with high strength, toughness, and abrasion resistance but without brittleness (e.g. thermosetting polyurethane).

π-Conjugated (semiconducting) polymers have the potential to combine electronic functionality with mechanical robustness. However, the goal of nearly all work in this area has been focused on increasing the stretchability and flexibility (the notable exception being a subset of literature – primarily by Dauskardt and coworkers – measuring the physical stability and failure mechanisms of semiconducting materials[2–9]).[10–17] Achieving these properties stands to enable potential applications of conjugated polymers in in wearable health monitors,[18,19] neurological recording,[20,21] and solar tarps for disaster relief.[22] However, the exclusive focus on facile deformability comes with at least three costs. First, the most common organic semiconductors can often be rubbed off a substrate with tissue paper or a gloved finger. While most envisioned applications will involve encapsulation, the weakness of the active material will cause the device stack to decohere under shear and torsion.[2,3,7,8] Second, the "stretchability" of most organic semiconductors

beyond 10% is plastic and irreversible. (One questions whether an object can be considered "stretchable" at all if it does not return to equilibrium.[23]) Third, the properties required for good charge transport are often (but not always)[24–27] antithetical to those required for stretchability. For example, highly extensible conjugated polymers have long, flexible alkyl side chains. However, because charge is conducted primarily among the polymer backbone,[28] the large volume fraction occupied by the insulating side chains is likely to reduce the maximum achievable charge-carrier mobility of the solid film. On the other hand, the characteristics associated with high mobility (e.g., high molecular weight, high degrees of polymerization, strong intermolecular interactions, and low free volume) naturally favor mechanical properties associated with strength and toughness.

This Perspective argues that the range of potential applications for organic semiconductors that are merely stretchable is far surpassed by those envisioned for ones that are strong, tough, and rebound elastically, especially for polymer solar cells. It is true that interest in (and funding for) organic photovoltaics has waned in recent years (at least in the U.S.) due to better power conversion efficiencies of devices based on perovskite absorbers; perovskite absorbers, however, are mechanically weak.[29–31] Thus, enthusiasm for polymer solar cells may increase if they can be shown to exhibit high mechanical robustness, which is a necessary characteristic for integrating solar cells with human-transformed surfaces already subject to mechanical insult. Moreover, the highest-efficiency perovskite solar cells generally contain organic semiconductors as either the hole- or electron-transporting layers,[32–35] and thus any effort to increase the robustness of semiconducting polymers will be automatically transferred to the benefit of perovskites. Beyond solar cells, strong, tough, and resilient organic semiconductors will also be to the benefit of flexible, interactive displays based on OLEDs, and wearable biosensors, whose active components are by necessity exposed to prodding by human users.

Measurements of strength, toughness, and elastic range in thin films of conjugated polymers were hampered until recently by a lack of testing protocols. While thick samples of inexpensive, easy-to-

synthesize polymers are amenable to conventional pull testing, the fragility of films with thicknesses less than approximately 100 nm precludes this method. Thus, in the first several years of the rebirth of interest in the mechanical properties of conjugated polymers, quantities such as elastic modulus, crack-onset strain, and yield point were measured using the surface wrinkling technique.[36–39] This technique takes advantage of the buckling instability that manifests when stiff films (e.g., conjugated polymers) are subjected to small (<5%) compressive strains on elastomeric substrates (e.g., polydimethylsiloxane, PDMS).[40] However, since the mechanical response is dominated by the thick substrate (and cannot be decoupled from the mechanical response of the film itself), forces and energies accommodated by film cannot be obtained directly. Thus, other approaches are needed to measure ultimate tensile strength (N m^{-2}) and modulus of toughness (J m^{-3}).

In 2013, Kim and coworkers introduced a technique that made it possible to obtain a pull test from an ultrathin film by suspending it on water.[41] The high surface tension of water prevents the film from collapsing on itself. A force gauge with a sensitive load cell is positioned horizontally, and grips made from PDMS adhere to the ends of the film by van der Waals forces. Film-on-water (FOW), however, is not without its own weaknesses. The fragility of these polymer films can result in wrinkles, bends, and tears – particularly along defect sites – that result in a high localization of stress. For example, bends in the stress-strain curve that seem to indicate plastic deformation can instead occur due to physical tears in the film. Likewise, water can slowly diffuse into the film and affect the measurement, although it is not clear to what degree this impacts the mechanical data, and the ways in which water influences the measurement are likely to be dependent on the chemical structure of the polymer.

Since the initial report, stress-strain behavior has been reported for a variety of semiconducting polymers. In most of these studies, quantities related to stretchability—e.g., modulus and strain at fracture—were the key figures of merit, and quantities related to hardness such as strength and toughness were not always calculated, even though these quantities were embedded in the data. In this Perspective, we compiled

and re-analyzed the stress-strain data from papers which have performed pull tests on conjugated polymers. The goal of performing this analysis was to serve as a starting point for understanding the molecular and microstructural parameters that influence these important but overlooked mechanical properties.

1.1.2 Mechanical Properties of Organic Semiconductors

In a solid film of a semiconducting polymer, mechanical energy is stored or dissipated by a variety of mechanisms.[5,6,42] The dominant mechanisms depend on the molecular structure (e.g., atomic arrangement and degree of polymerization) and its properties in the condensed phase at a particular operating temperature. Important aspects include the microstructure, rubbery or glassy state, density, cohesive energy, entanglements, and other properties which may be mutually dependent.[43] For an amorphous polymer below its glass transition temperature (T_g), energy is stored elastically in the bending and stretching of covalent bonds and also by mechanical modulation of the van der Waals forces between chains. Energy can be dissipated by sub-T_g relaxation mechanisms, such as bond rotations.[44] Catastrophic failure ultimately results from the breakage of covalent bonds. In ordered domains within semicrystalline samples, energy is stored by the reversible displacement of monomer residues and whole chains about their equilibrium positions within crystallites. Energy is dissipated by slip and ultimately disruption of crystallites.[45] In amorphous domains of crosslinked or semicrystalline samples above their T_g, energy is stored as an entropic spring, and dissipated by breaking van der Waals interactions between chains and ultimately by chain pullout.[44] The T_g is dependent on a number of factors, including the flexibility of the backbone (more flexibility corresponds to a lower T_g), the steric effects of side chains (bulkier side chains reduce the packing density and intermolecular forces between main chains and thus decrease the T_g), and the free volume (more free volume lowers the T_g). In general, the free volume increases due to inefficient packing (e.g. high polydispersity, low molecular weight, the presence of plasticizers, and configural isomerism).

A large body of knowledge and literature is devoted to the task of increasing the durability of commodity polymers and engineering plastics. Transferring this knowledge to the field of semiconducting

polymers, however, is not straightforward. A semiconducting polymer has characteristics not found in conventional plastics. First, it has a rigid π-conjugated backbone which gives rise to efficient charge transport but also makes the material insoluble at even moderate degrees of polymerization. In order to process this material from solution, alkyl side chains must be added. These flexible side chains increase the entropy of the polymer in solution relative to the unsubstituted structure and thus promote solubility. The side chains are also anathema to strength.[46] On the other hand, unsubstituted conjugated polymers tend to have the solubility and mechanical properties of "brick dust" (a term used pejoratively in organic synthesis but which reflects the properties of strength and hardness that we are seeking).

In the initial days of conjugated polymers, researchers treated mechanical strength as a desirable characteristic. For example, the high tensile strength of polyacetylene was attractive for applications requiring high durability and light weight, such as for overhead transmission lines.[47] In fact, Akagi et al. noted that bulk samples of trans polyacetylene had elastic moduli and tensile strengths of 100 GPa and 0.9 GPa, respectively.[48] These values are comparable to those of engineering plastics such as Kevlar.[48] Such values are rarely achieved in modern, low-bandgap, solution-processible conjugated polymers, mainly because of the plasticizing effects of the side chains.

Another characteristic which runs counter to high strength in low-bandgap conjugated polymers is low degree of polymerization. The degree of polymerization is largely a consequence of the low solubility and also of the synthetic methodology, which usually proceeds by step-growth polycondensation of AA and BB monomers. The degree of polymerization of the resulting polymers is therefore limited first by the difficulty of obtaining absolutely pure monomers and thus by small, stoichiometric imbalances (as predicted by Carothers).[44] Additionally, the degree of polymerization is limited by the already low solubility of conjugated polymers, which decreases with increasing degree of polymerization. We emphasize that this argument refers to the degree of polymerization, as opposed to the molecular weight. The exceptionally

large monomer residues of semiconducting polymers guarantee a relatively high molecular weight even with a relatively low degree of polymerization.

Despite these differences in structure, many synthetic approaches that improve the strength and toughness apply to both conjugated and non-conjugated polymers (e.g., commodity polymers and engineering plastics).[49] For example, blending of polymers and modifications to the side chain. The molecular weight and degree of polymerization are especially important in determining the mechanical properties of a solid structure. Plasticizers can be used in polymers of all types to tune both the processability and mechanical properties. Chemical crosslinking[50–52] is a ubiquitous approach to producing thermosets (e.g., epoxy resin) and elastomers (e.g., silicone rubber). However, chemical crosslinking has not yet been explored extensively as a means of increasing the robustness of conjugated polymers. Approaches in which the polymer chains are crosslinked physically—e.g., hydrogen bonding,[53–56] increased van der Waals interactions,[57] and double networks involving topologies that intertwine (common in advanced hydrogels)[58–61]—all potentially offer strategies for tuning the strength, toughness, and elastic range in conjugated polymers.

1.1.3 Testing of Mechanical Properties and their Definitions

The conventional way in which mechanical properties of solid materials are measured is a tensile test. In a tensile test, grips are applied to the ends of a slab of material. The load (force) is plotted as a function of the elongation (engineering strain, $\frac{\Delta L}{L_0}$, where L_0 is the length of the dimension at equilibrium and ΔL is the amount of deformation). The force is converted to engineering stress by dividing by the initial cross-sectional dimensions of the sample ($\frac{F}{w*t}$). The sample is elongated until breakage. A generic, idealized stress-strain curve is shown in **Figure 1.1**. In the elastic region, the stress of the film increases linearly with respect to the strain applied as described by Hooke's law, where the slope is the tensile (Young's) modulus. The elastic regime terminates at the elastic limit, followed immediately by the yield point, beyond which further deformation is permanent. Materials undergoing plastic deformation fracture in a ductile manner,

while those that break prior to the onset of plastic flow fracture in a brittle manner. The area under the curve in the elastic regime is the maximum energy storable, termed the resilience. The area under the entire curve is the maximum energy absorbed prior to fracture, termed the toughness. The ultimate tensile strength (UTS, or just strength) is the maximum stress achieved during the test.

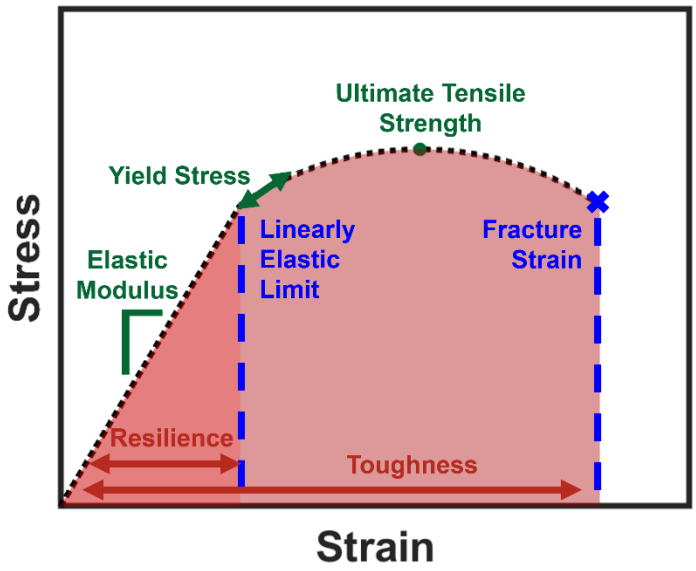

Figure 1.1 A generic stress-strain curve. Labeled are mechanical properties of interest associated with strain (blue), stress (green), and energy (red). The units associated with each, respectively, are generally given in % strain, MPa, and MJ/m^3.

1.2 Scope and Methodology

This Perspective uses published data to investigate the effects of molecular structure on strength, toughness, and linear elasticity (a proxy for elastic range) in semiconducting polymers. We adopted two principal criteria for inclusion in our analysis. The first criterion is that the data were obtained using the film-on-water test. While there are other methods of good standardization—e.g., the buckling based metrology and the four-point-bend/double-cantilever-beam tests—the simplicity of the analysis and measurement of the mechanical properties without adhesion to any other substrate allows for the most straightforward comparison of experiments carried out by different groups. Our second criterion for a study

to be included is that some aspect of molecular structure is varied systematically (i.e., the approach characteristic of physical organic chemistry).[62] In particular, we examined the effects of seven systematic modifications: degree of polymerization, regioregularity, inclusion of electron-donating units, inclusion of nonconjugated monomer units, inclusion of conjugation-break spacers, side chain length, and composition of the active layer in two-component blends. There are other parameters that influence the mechanical properties that are independent of chemical structure—e.g., strain rate, thickness, and solvent. In general, we find that increasing the strain rate and thickness increased the measured tensile strength (**Figure A1, A2**),[63] while increasing the dielectric constant of the solvent resulted in weaker but more deformable films (**Figure A3**).[64] Detailed discussions of these parameters are included in **Appendix A**. As we discuss in **A.1.1**, the mechanical properties of polymer films can exhibit dependence on thickness, typically for films <100 nm, along with strain rate. In the papers covered by this Perspective, each set of polymer thin films were approximately 100 nm in thickness and tested at similar strain rates unless otherwise stated.

Methodology. Data from stress-strain curves were extracted from literature using WebPlotDigitizer before being reproduced and analyzed in Matlab R2017b. Toughness was calculated as the area under the reproduced stress-strain curve. The ultimate tensile strength was calculated as the maximum stress applied to the material. The linear elasticity was calculated using a moving linear regression such that the elastic range ends at the strain where the coefficient of determination dropped below $R^2 = 0.95$. In doing so, we use the range of linear elasticity as a proxy for elastic range. While this approximation may fail for polymers with extremely viscoelastic behavior (e.g. a T_g far below the operating temperature), where it is possible for elasticity to become nonlinear, we expect this assumption to hold for most polymers at moderate strain rates.

In general, we favor comparisons between polymers using the degree of polymerization as opposed to the molecular weight, because molecular weight is influenced by the relatively large mass fraction embodied in the side chains. For example, if the length of the side chain is increased while the structure and

length of the backbone remains constant, then the molecular weight will increase while the contour length will remain the same. Thus, differences in mechanical properties known to be affected by the topological length of the chain—e.g., any quantity influenced by entanglements—plotted against molecular weight might be falsely ascribed. The degree of polymerization is also more intuitive than molecular weight because it does not require mental normalization by the molecular weight of the monomer.

1.3 Discussion

1.3.1 Effect of Degree of Polymerization

The minimum criterion for mechanical robustness of any kind is high number-average degree of polymerization (X_n).[65,66] Having a high degree of polymerization increases the durability of a polymeric material by increasing the density of entanglements (locations where two chains can slide past each other, but not through each other). Shown in **Figure 1.2** is a comparison of the mechanical properties of poly(3-hexylthiophene) (P3HT), as tested using film-on-water by Rodriquez et al.,[66] and bulk samples, as tested using traditional tensile tests by Koch et al.,[67] relative to degree of polymerization. The molecular weight corresponding to the onset of entanglement is referred to as the critical entanglement molecular weight, M_C. By measuring the viscosity of polymer solutions, Stingelin and coworkers found a sharp increase at X_n = 179 and thus determined that P3HT chains become entangled between M_C = 25 – 35 kDa (X_n = 127 – 179).[67] The effect of entanglement, relative to degree of polymerization, is reflected in the tensile strength and toughness of both types of samples (**Fig 1.2d-e**). Thus, samples below M_C, i.e. X_n = 127, showed brittle behavior. Additionally, since P3HT undergoes strain alignment and associated strengthening in both the bulk and thin-film format (**Fig 1.2b-c**),[68] the tensile strength scales with increasing density of entanglements (i.e., degree of polymerization). Although the toughness increases significantly with increasing degree of polymerization, the range of linear elasticity was between 4% to 12% strain with opposite trends between thin films and bulk samples (**Fig 1.2f**).

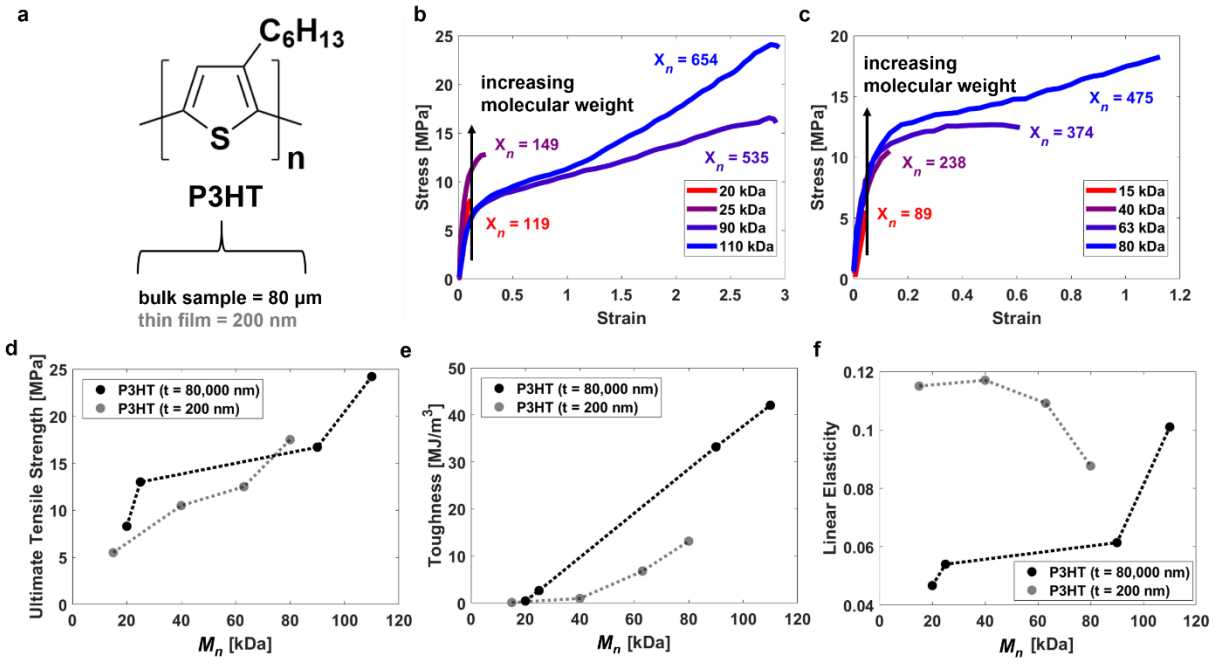

Figure 1.2. Mechanical properties of poly(3-hexylthiophene) samples as a function of degree of polymerization (and thus molecular weight). (**a**) Chemical structure of poly(3-hexylthiophene). (**b**) Stress-strain curves of 80 μm bulk P3HT samples and their respective degrees of polymerization, replotted from Koch et al. 2013.[67] (**c**) Stress-strain curves of 200 nm thin film P3HT samples and their respective degrees of polymerization, replotted from Rodriquez et al. 2017.[66] (**d**) Ultimate tensile strength and (**e**) toughness of P3HT samples increase as the molecular weight and degree of polymerization increase. (**f**) The linear elasticity of these samples was between 4% and 12% strain.

The effects of Increasing the density of entanglements on strain at failure has been well-documented for both engineering polymers and π-conjugated polymers. For example, a high density of entanglements increases the energetic barriers for both cavitation (void formation in the amorphous matrix) and crazing (crack formation from local stretching).[1,69–72] Additionally, increased degree of polymerization results in greater connectivity between crystallites in P3HT and self-aggregation of polymer chains, which increases resistance to failure by chain-pullout.[65,73,74] It is also worth mentioning that greater connectivity between crystallites and increased self-aggregation promote good charge transport in semiconducting polymers,[75–77] again showing a synergistic relationship between electronic and mechanical properties. The effect of the degree of polymerization on the mechanical properties is applicable to both homopolymer and donor–acceptor (D–A) polymer systems.[78,79] Galuska et al. validated these findings by measuring the

mechanical properties of a poly(naphthalene diimide) (PNDI)-based polymer at varying molecular weights (which we have converted to degree of polymerization) as shown in **Figure 1.3** below.[79]

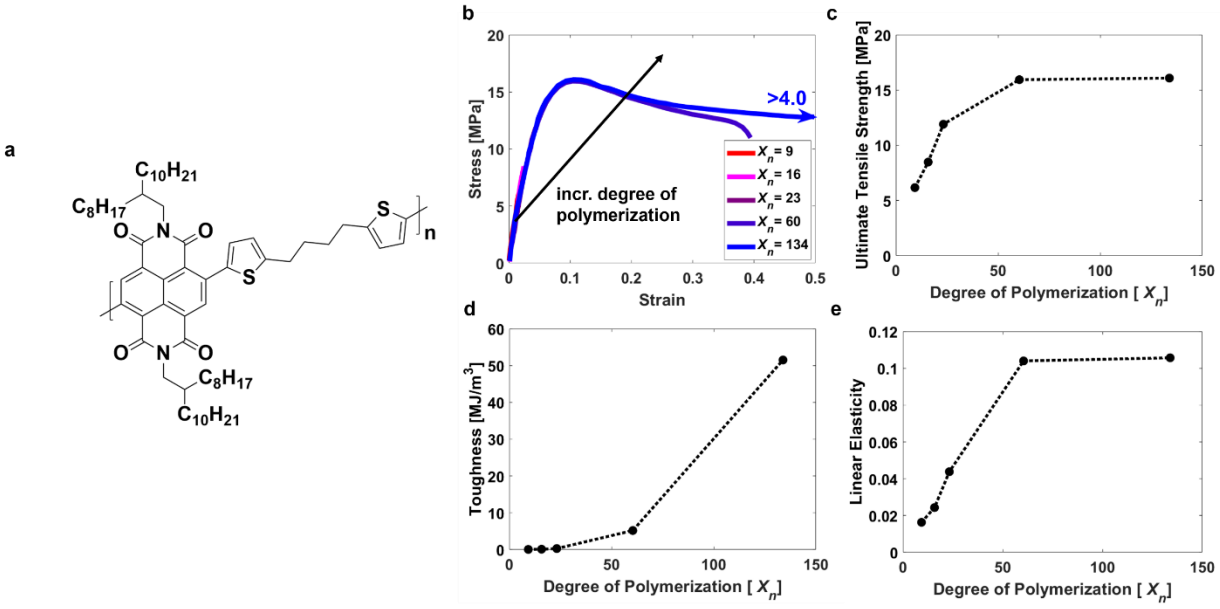

Figure 1.3. Mechanical properties of a poly(naphthalene diimide) (PNDI)-based polymer relative to degree of polymerization (and thus molecular weight). PNDI differs from P3HT in that it is a donor–acceptor (D–A) polymer. (**a**) Chemical structure of PNDI-C4. (**b**) Stress-strain curves of PNDI-C4 at different degrees of polymerization, replotted from Galuska et al. 2020.[79] (**c**) Ultimate tensile strength, (**d**) toughness, and (**e**) linear elasticity all increase as the degree of polymerization increases.

The most striking observation from the stress-strain curves (**Fig 1.3b**) is how significantly the fracture strain increases as the degree of polymerization increases. PNDI-C4 with a X_n = 9 has a fracture strain of <5%, but increasing the X_n to 134 results in a fracture strain of >400% (**Fig 1.3d**) (along with a tensile strength that is twice as high, **Fig 1.3c**). This drastic increase in fracture strain results in a toughness that is three magnitudes larger (0.056 MJ m^{-3} compared to 51.5 MJ m^{-3}). The increase in linear elasticity (<2% to >10%, **Fig 1.3e**) validates the same trend from Koch et al. (**Fig 1.2f**), suggesting that the range of linear elasticity is also expected to scale with increasing number of entangled chains. As such, Galuska and coworkers offer two guidelines for increasing the number of entanglements in a system: (1) reducing the M_C while maintaining the M_n, or (2) increasing the M_n while maintaining the M_C.[79] From this analysis, we

see that sufficient degree of polymerization is crucial for ensuring good mechanical properties of semiconducting polymer films.

1.3.2 Effect of Regioregularity

Another criterion that affects the mechanical properties of conjugated polymers is the bonding orientation of monomer residues with asymmetric structures, or the regioregularity.[80,81] This effect is especially apparent in poly(3-alkylthiophenes) (P3ATs), of which poly(3-hexylthiophene) (P3HT) has been widely studied as a model for conjugated polymers.[82] As shown in **Figure 1.4a**, P3ATs allow for three possible orientations when two thiophene rings are coupled. The first is 2-5' coupling, or head-to-tail (HT) coupling, and polymer samples with a majority of HT orientations are referred to as regioregular P3ATs. Regiorandom P3ATs are composed mainly of head-to-head (5-5', HH) coupling and tail-to-tail coupling (2-2', TT). P3ATs are semicrystalline polymers, with crystalline domains embedded within an amorphous matrix.[83] The ratio of polymer in crystalline domains is controlled by the regioregularity, and thus the regioregularity affects the mechanical properties. Shown below in **Figure 1.4** is a comparison of the mechanical properties relative to the regioregularity of P3HT samples as determined by Kim and coworkers in 2015.[80]

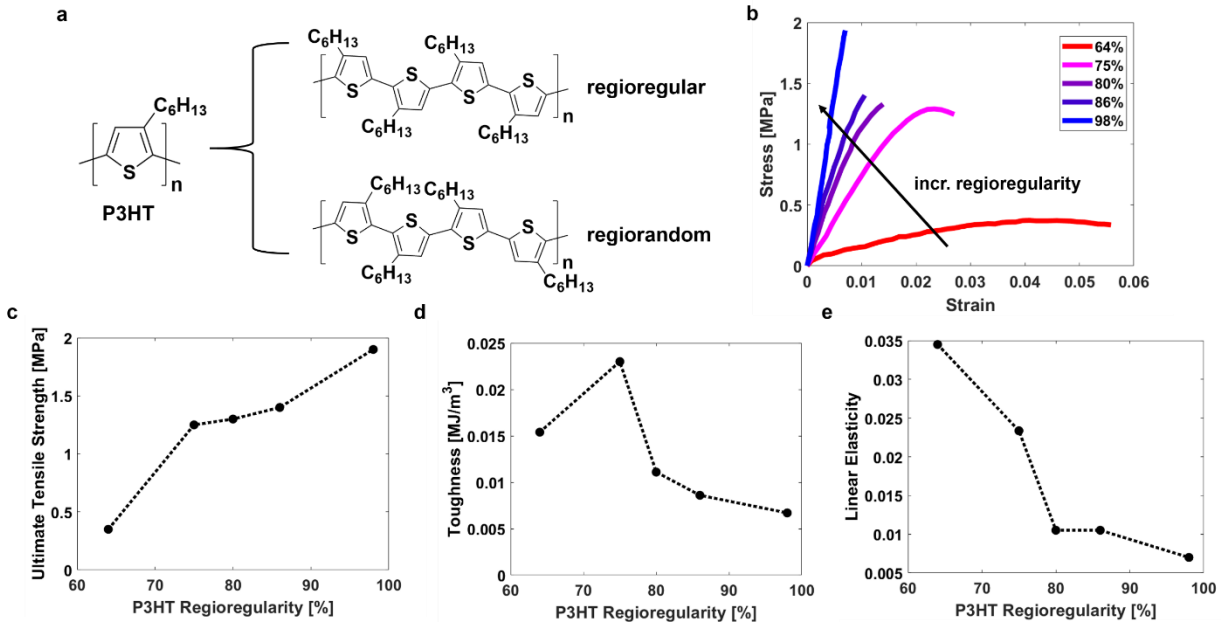

Figure 1.4. Mechanical properties of poly(3-hexylthiophene) films measured by FOW as a function of regioregularity. (**a**) Chemical structure of P3HT and the three possible coupling orientations of the thiophene backbone. (**b**) Stress-strain curves of P3HT thin films of increasing regioregularity replotted from Kim et al. 2015.[80] (**c**) Ultimate tensile strength has a direct relationship with increasing regioregularity. (**d**) Toughness is maximized for P3HT films that are 75% regioregular. (**e**) Linear elasticity has an inverse relationship with increasing regioregularity.

The most salient trends visible in the mechanical response of P3HT with increasing regioregularity are increasing strength, and decreasing toughness (overall) and linear elasticity. These trends can be attributed to an increase in the fraction of polymer in ordered (aggregated or crystalline) domains versus amorphous domains. The amorphous domains are in a rubbery state, with the T_g of regioregular P3HT just below room temperature.[84] In contrast, the melting temperature of crystalline P3HT is >200 C, with high cohesive energy. Thus, P3HT can be treated as a composite of rubbery domains held together by domains of relatively high order, whose rigidity is brought about by a greater density of van der Waals interactions between the closely packed conjugated rings.[80,85] The elasticity of highly regioregular P3HT is limited by the decreased ability of the relatively low fraction of rubbery amorphous domains to accommodate strain the lower fraction of chains present in rubbery domains. Such an effect is also observed in annealed films

of PBTTT, which is possibly the most crystalline conjugated polymer known. It undergoes brittle fracture when annealed and ductile fracture untreated, i.e., "as-cast."[38]

The samples measured by Kim et al. also give us the opportunity to compare the effects of regioregularity with the effects of degree of polymerization. Notably, the brittle behavior of the P3HT sample with 98% regioregularity can in part be explained by a relatively low degree of polymerization (X_n = 103), or similar to the most brittle films measured in **Figure 1.2c**. Nevertheless, the highly regioregular samples exhibited brittle behavior despite having over double the X_n of that with the lowest regioregularity. Given the fact that these observable properties arise from the collective responses of large ensembles of domains and polymer chains, it is important not to overinterpret individual data points. For example, the maximum in toughness occurring in the 75% regioregular sample is a consequence of its lying at a transition between principally rubbery and principally brittle behavior. That is, the energy dissipated by plastic flow at a relatively high stress leads to a somewhat higher energy density at the point of fracture even though it has neither the highest tensile strength nor fracture strain (**Fig 1.4d**).

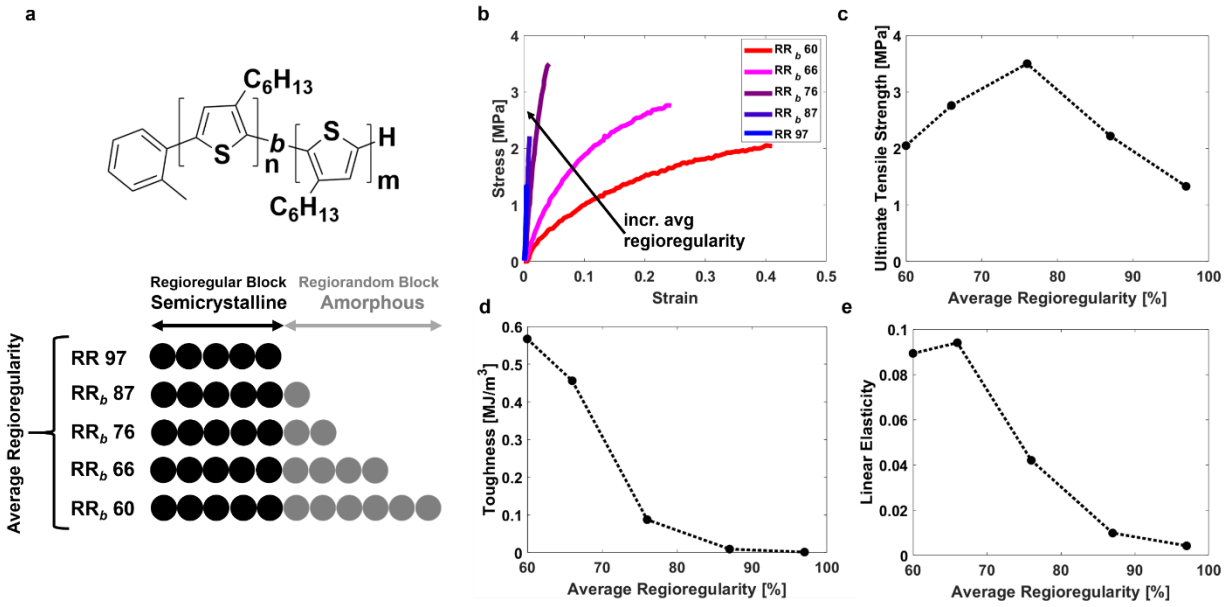

Figure 1.5. Mechanical properties of regioregular-*block*-regiorandom poly(3-hexylthiophene) films measured by FOW relative to increasing length of the regiorandom block. (**a**) Chemical structure of regioregular-*block*-regiorandom P3HT (rre-*b*-rra P3HT) and the increasing lengths of regiorandom blocks added. The average regioregularity is shown for each sample. Regioregular blocks had an average X_n of 56 – 61, while regiorandom blocks ranged from 15 – 168. (**b**) Stress-strain curves of rre-*b*-rra P3HT thin films of increasing average regioregularity replotted from Park et al. 2019.[81] (**c**) Ultimate tensile strength, (**d**) toughness, and (**e**) linear elasticity are shown relative to the average regioregularity.

One of the disadvantages of using a homopolymer with randomly incorporated head-to-head defects is the way in which it limits the extent of the ordered domains. Park et al. reasoned that greater control could be achieved using a block copolymerization strategy (**Figure 1.5**).[81] The authors synthesized a series of P3HT block copolymers consisting of a highly regioregular block of constant length (M_n = 11 – 12 kDa, X_n = 56 – 65) and a regiorandom block of increasing length (M_n = 3 – 33 kDa, X_n = 15 – 168) (**Fig 1.5a**).[81] The most significant conclusion of this study was that block copolymerization can be used to tune the regioregularity in order to maximize the toughness and linear elasticity while maintaining a relatively high tensile strength due to the retention of ordered domains even in samples with a high degree of overall regiorandomness. Block copolymers thus present a promising route to imbue toughness through optimizing both strain at failure and tensile strength, allowing for the "best of both worlds." We see a similar trend for

low regioregularity P3HT samples that are dispersed with P3HT nanowires (NWs) of higher regioregularity, thus increasing the average regioregularity of the sample (**Figure A4**).

1.3.3 Effect of Isolated Thiophene Units and Fused Thiophene Rings

In recent years, efforts have been dedicated to synthesizing conjugated polymers with better electronic properties while maintaining their favorable mechanical properties.[57,86] These low bandgap donor–acceptor polymers (D–A polymers) differ from earlier generations of conjugated polymers (e.g. polyphenylenevinylene and polythiophenes) in that they use alternating donor and acceptor units along the backbone to decrease the band gap through the "push-pull effect".[87] The push-pull effect additionally results in more rigid backbones, which in turn results in D–A polymers having higher glass transition temperatures than homopolymers (e.g. P3ATs) with side chains of comparable length.[43,84,88] D–A polymers additionally tend to have a higher number of fused rings in their structures, further increasing backbone rigidity and T_g.[89,90] Conjugated polymers exemplifying these characteristics are those that contain the acceptor unit diketopyrrolopyrrole (DPP). These polymers are among the most well studied, with high carrier mobilities demonstrated for many structures within this class.[91–96] The nucleophilic nitrogen atom permits straightforward attachment of functional side chains,[52,97] or those with a variety of length, branching, and flexibility.[98–100] Additionally, the modular synthetic pathway based on metal-mediated polycondensation makes it a relatively simple matter to build libraries with different donor units.[91,101–103] Thus, DPP-based polymers have been used for a variety of investigations into the ways in which systematic changes to structure affect the electronic (and increasingly mechanical) properties.

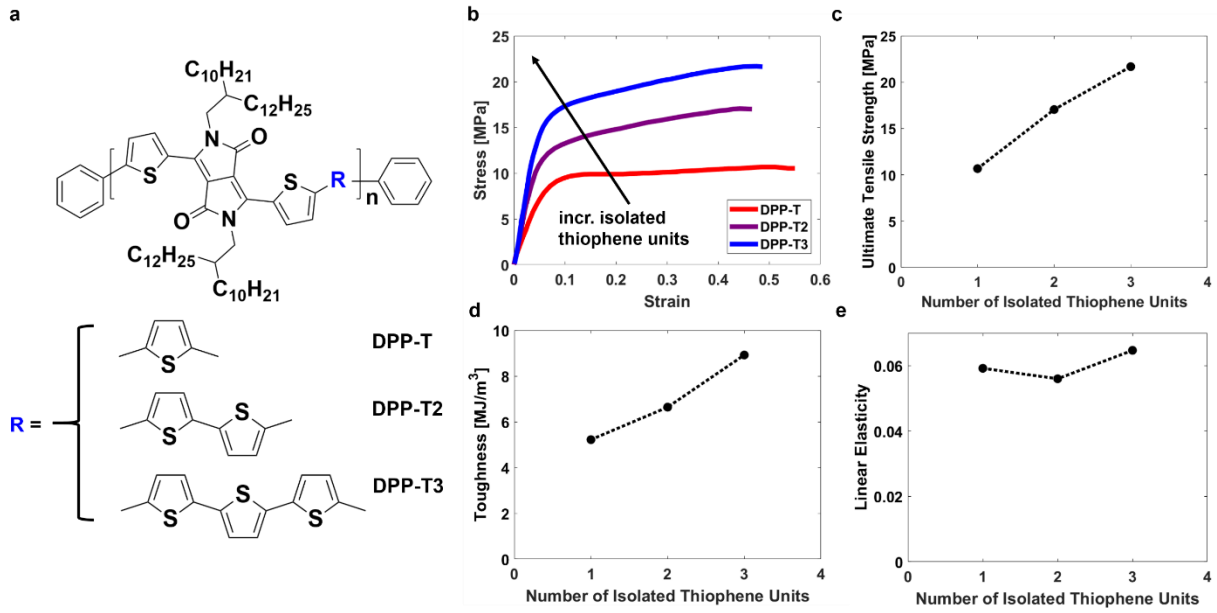

Figure 1.6. Mechanical properties of diketopyrrolopyrrole (DPP)-based conjugated polymer films measured by FOW relative to number of intervening thiophene units. (**a**) Chemical structure of the DPP-based polymer and the increasing thiophene units added to the R position shown in blue. (**b**) Stress-strain curves of DPP thin films replotted from Zhang et al. 2019.[91] (**c**) Ultimate tensile strength, (**d**) toughness, and (**e**) linear elasticity are shown relative to the number of isolated thiophene units added to the polymer.

In this vein, Zhang and coworkers studied the effect of electron-donating thiophene (donor) units on the mechanical properties of a DPP-based polymer, as shown in **Figure 1.6** and **Figure 1.7**.[91] Increasing the number of isolated thiophene units at the R position of the DPP-based polymer in **Fig 1.6a** produced potentially competing effects on the mechanical properties. First, one would expect that increasing the number of isolated thiophene units would decrease the rigidity of the backbone due to the dilution of the stiffening effect of the fused DPP unit. However, increasing the distance between DPP units—which contain the side chains—with unsubstituted rings also has the effect of decreasing the overall attachment density of the side chains. Indeed, we find over and over that the side chains determine the solubility, glass transition, and modulus. In fact, the authors measured an increase in T_g from –4-11 °C for DPP-T to 19 °C for DPP-T3.[91] Thus, DPP-T3 is glassier and stronger, despite probably having a more flexible backbone. (Similar effects have been observed in polymers in which the spacer units along the backbone were aliphatic—i.e., even greater expected flexibility based on the main chain.)[104] Remarkably, we see that this

dramatic increase in strength (**Fig 1.6c**) and toughness (**Fig 1.6d**) occurs despite the "T3" sample (X_n = 20) having a degree of polymerization half that of "T2" (X_n = 34) and "T1" (X_n = 39). The fact that the T_g is still below room temperature for the "T3" sample might account for sufficient mobility of chains to permit plastic flow and thus a relatively high toughness.

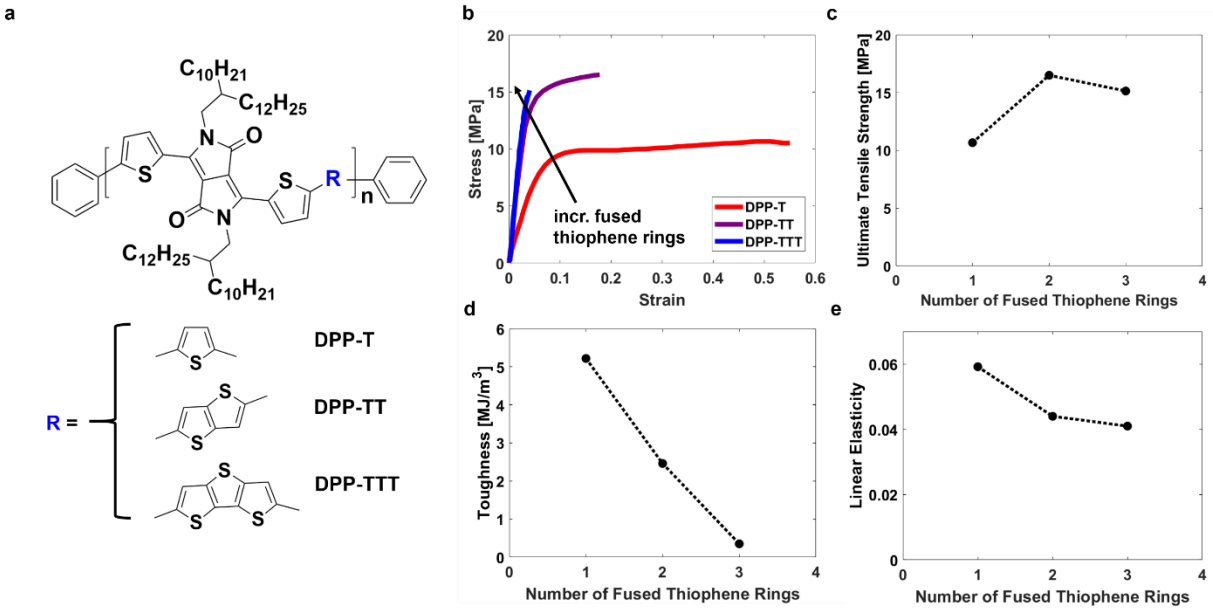

Figure 1.7. Mechanical properties of diketopyrrolopyrrole (DPP)-based conjugated polymer films measured by FOW relative to increasing fused ring size. (**a**) Chemical structure of the DPP-based polymer and the fused thiophene rings added to the R position. (**b**) Stress-strain curves of DPP thin films replotted from Zhang et al. 2019.[91] (**c**) Ultimate tensile strength, (**d**) toughness, and (**e**) linear elasticity are shown relative to the number of fused thiophene rings added to the polymer.

Superficially similar to the approach of increasing the number of isolated thiophene rings is one which systematically increases the number of fused thiophene rings. In particular, Zhang et al. reported a system in which the size of the donor unit was increased from thiophene (T) to thienothiophene (TT) to dithienothiophene (TTT). This systematic modification had a smaller overall effect on the attachment density of the side chain but had a profound effect on the stiffness—"ladder-like character"—of the main chain. Interestingly, its effects on the T_g were similar. For example, increasing the size of the fused thiophene donor from T to TTT increased the T_g from –4-11 °C (T) to 3 °C (TT) to 4-22 °C (TTT).[91]

However, fused thiophene rings have less rotational and conformational freedom than an equivalent number of isolated thiophene units. A conjugated polymer with large fused ring structures is thus unable to dissipate energy as effectively though sub-T_g relaxation mechanisms and experiences catastrophic failure at smaller strains. This embrittlement is reflected in the dramatic decrease in fracture strain and toughness for the fused ring systems (**Fig 1.7d**).

1.3.4 Effect of Nonconjugated Monomer Units in Block Copolymers

Block copolymers offer the opportunity to tune the mechanical properties of the system by connecting a block engineered for its mechanical properties to a block engineered for its semiconducting properties. Following the resurgence of interest in the mechanical properties of semiconducting polymers, one of the earliest mechanical studies characterized the behavior of P3HT-*b*-PE block copolymers using traditional tensile tests (by Müller and coworkers in 2007), as shown in **Figure 1.8** below.[26] Since then, similar synthetic techniques have been applied toward D–A block copolymers. **Figure 1.9** is a comparison of the mechanical properties of interest relative to the composition of a diketopyrrolopyrole and polycaprolactone (PDPP-*b*-PCL) block copolymer by our laboratory.[25] In both systems, the nonconjugated unit has a much lower glass transition temperature than its conjugated counterpart (PCL T_g ~ 60 °C,[25] PE T_g ~ –80 °C).[105]

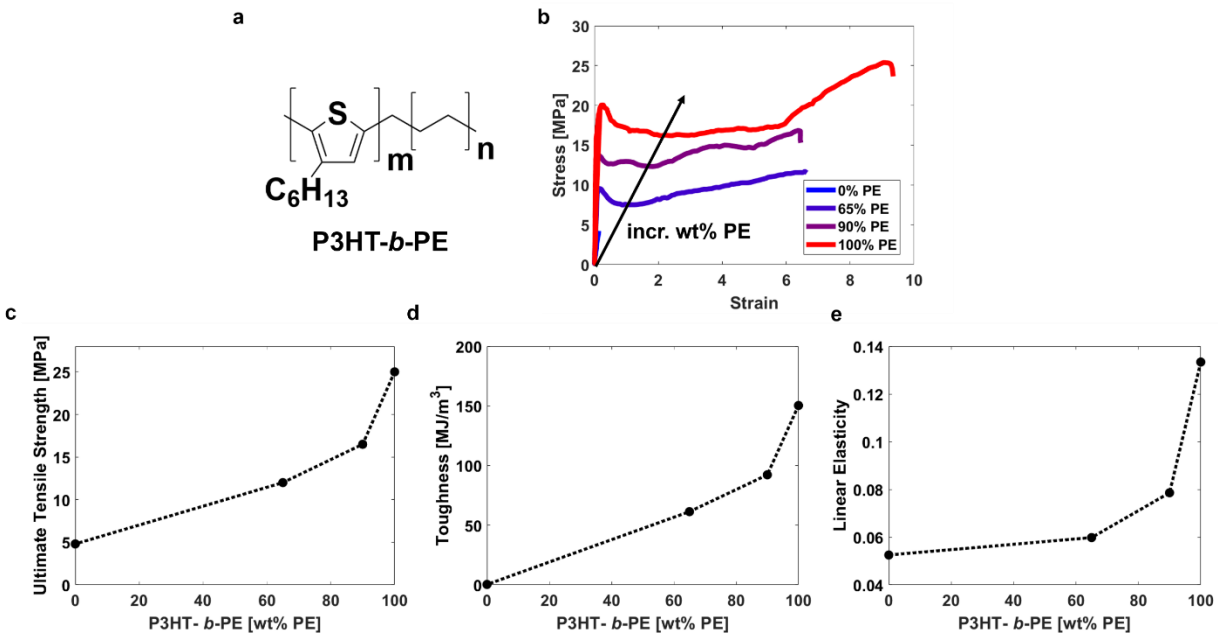

Figure 1.8. Mechanical properties of bulk P3HT-*b*-PE copolymer samples measured using a pull test. (**a**) Chemical structure of the poly(3-hexylthiophene) (P3HT) and polyethylene (PE) block copolymer. (**b**) Stress-strain curves of P3HT-*b*-PE samples relative to increasing wt% of PE replotted from Muller et al. 2007. (**c**) Toughness, (**d**) tensile strength, and (**e**) linear elasticity tended to decrease relative to increased weight fraction of PE.

Figure 1.8 shows the effect of increasing the weight percentage of polyethylene (PE) in a P3HT:PE block copolymer. In each sample, the size of the P3HT block was kept approximately the same (X_n of ~77–112), while an increasing block length of polyethylene was added. Increasing the size of the polyethylene block results in an increase in tensile strength (**Fig 1.8c**), toughness (**Fig 1.8d**), and linear elasticity (**Fig 1.8e**). Despite the significant increase in insulator fraction, the block copolymers with the most favorable mechanical properties retained or improved their electronic performance. This transformation in mechanical properties of the block copolymer can be attributed to the well-known deformability of PE, which can be either waxy or tough depending on its molecular weight and extent of branching (i.e., high- and low-density PE). If one considers (admittedly simplistically) simply the degree of polymerization with increase in the length of the PE block, one finds that the X_n of the pure P3HT sample was 83, whereas the X_n of the pure PE sample was 3600. So, the effect of this strategy was not only to introduce a block with

favorable mechanical properties per se, but also to increase the length of the chains dramatically (and also the density of entanglements). Such an increase in length permitted these P3HT-b-PE copolymers to achieve fracture strains that are >200% those of pure P3HT samples while also increasing the strength (~20 MPa).

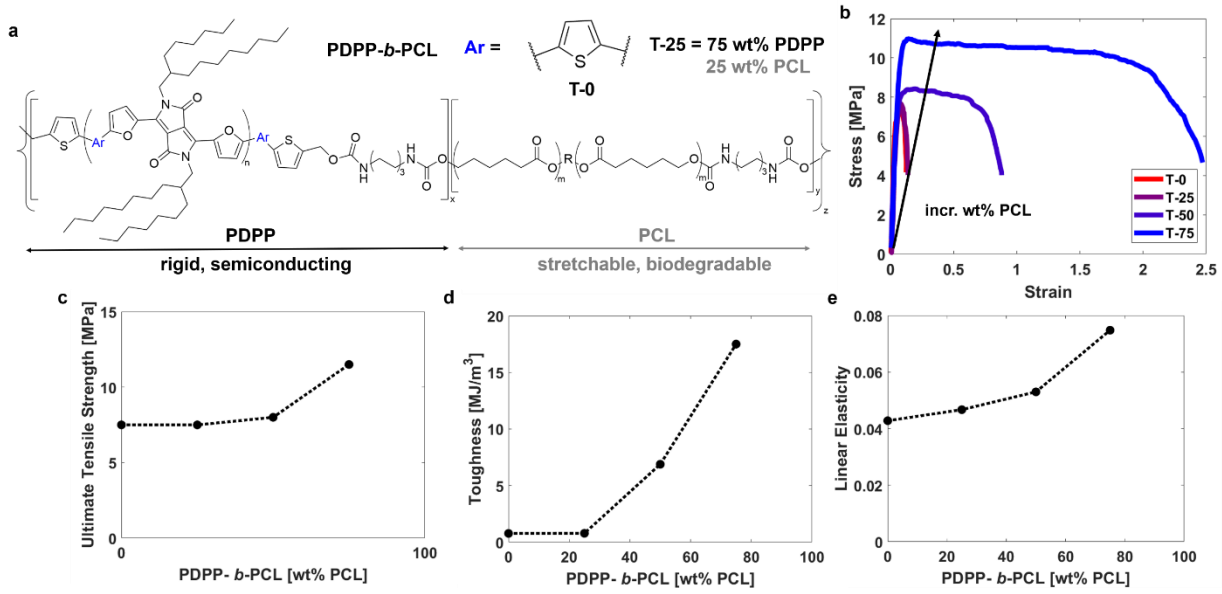

Figure 1.9. Mechanical properties of PDPP-*b*-PCL copolymer films measured using a FOW tensile test. (**a**) Chemical structure of PDPP-*b*-PCL, which is composed of a rigid semiconducting diketopyrrolopyrrole (DPP) segment attached to a stretchable, insulating polycaprolactone (PCL) segment. The PDPP-*b*-PCL samples had relatively similar molecular weights (M_n = 19 – 22 kDa), and thus similar degrees of polymerization. (**b**) Stress-strain curves of block copolymer films containing increasing wt% of PCL replotted from Sugiyama et al. 2018.[25] (**c**) Tensile strength, (**d**) toughness, and (**e**) linear elasticity all increase relative to increasing weight % of PCL.

Figure 1.9a shows the structure of a block copolymer composed of a rigid conjugated polymer, PDPP2F-T (PDPP), and an engineering polymer, poly(□ □caprolactone) (PCL). As the weight percentage of PCL in the block copolymer increased, the fracture strain increased significantly while maintaining a similar elastic modulus and tensile strength (**Fig 1.9c**), resulting in a significant increase in the toughness (**Fig 1.9d**) and the linear elasticity (**Fig 1.9e**). The authors also showed that increasing the mass fraction of PCL lowered the T_g of the entire block copolymer from 133 °C for T-0 to 58 °C for T-50.[98,106] Therefore the increase in fracture strain, toughness, and linear elasticity is primarily explained by (1) an increase in operating temperature relative to the T_g and (2) more characteristics of the PCL block being imparted as the

PCL fraction increases. In contrast to the P3HT-*b*-PE study, the increase in PCL fraction resulted in a proportional decrease in hole mobility. Yet remarkably, when the thiophene highlighted in **Fig 1.9a** was replaced with a thienothiophene, the charge-carrier mobility of the block copolymer retained the electronic performance of the pure PDPP block up to a fraction of 90 wt% PCL due to the more favorable ordering of the PDPP segments.[106]

1.3.5 Effect of Conjugation-Break Spacers

As the results of Müller showed for P3HT-*b*-PE, it is possible for a polymer to retain favorable charge-transport properties despite a large fraction of insulator. However, in those cases, the conjugated units were uninterrupted. Mei and coworkers showed that some donor–acceptor polymers could retain much of their electronic performance while interrupting the rigid conjugated backbones with flexible aliphatic linkers.[107] In a collaboration between our group and the Thompson group at USC, we have found that the effects of these nonconjugated segments (conjugation-break spacers, CBS) in a conjugated backbone can be quite subtle.[104,108] Shown below in **Figure 1.10** is a comparison of mechanical properties of modified P3HT-DPP polymers relative to increasing CBS length and mass fraction.

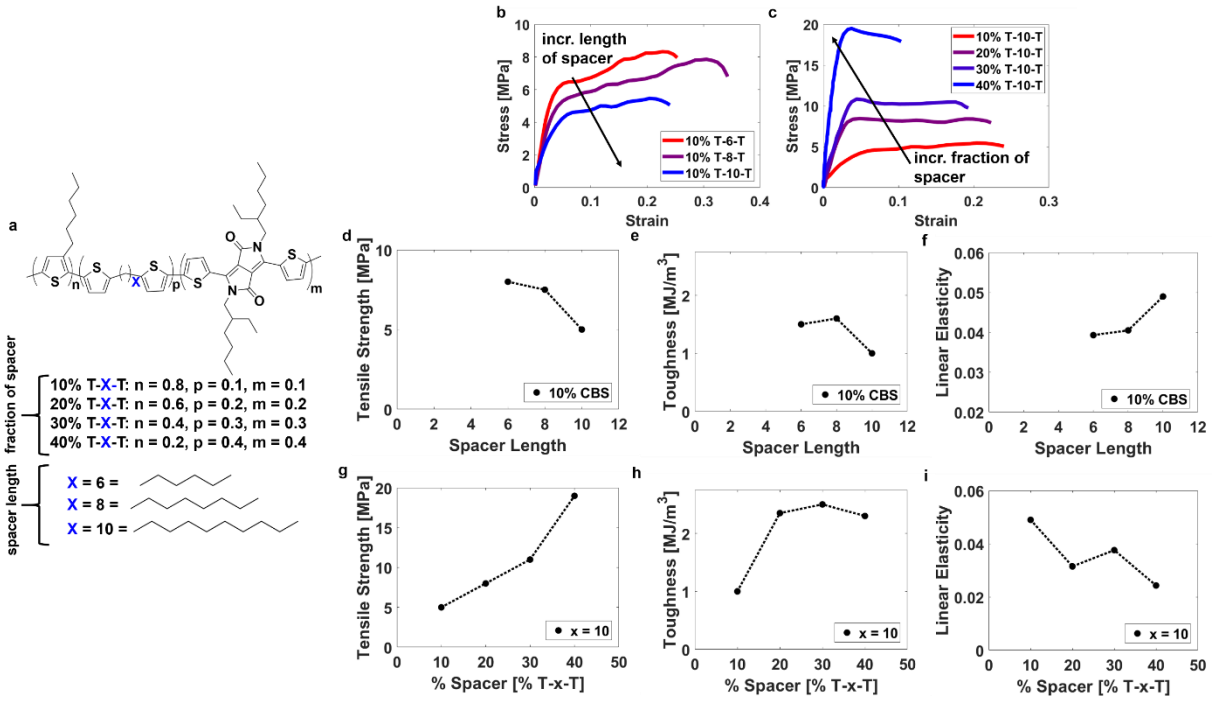

Figure 1.10. Mechanical properties of modified P3HT-DPP polymers relative to conjugation-break spacer length and concentration. (**a**) Chemical structure of the P3HT-DPP library used. Spacer fractions ranged from 10% to 40% with an equivalent fraction of DPP, while the spacer length varied between hexane and decane. The molecular weights were relatively similar (M_n = 10–15 kDa). (**b**) Stress-strain curves of P3HT-DPP polymers relative to spacer length and (**c**) spacer concentration replotted from Melenbrink et al. 2018.[108] (**d**) Tensile strength and (**e**) toughness decreased relative to increasing spacer length while the (**f**) linear elasticity increased. In contrast, the (**g**) tensile strength and (**h**) toughness increased relative to increasing spacer fraction while the (**i**) linear elasticity decreased.

This data examines two effects of conjugation-break spacers that are incorporated into the design of the semiconducting polymer backbone. The first is the effect of increasing the length of the alkyl chain used as the CBS (**Fig 1.10b**), and the second is the effect of increasing the mass fraction of the CBS unit (**Fig 1.10c**). The most interesting result of this study is that these substitutions have opposite effects on the mechanical properties. In general, increasing the length of the CBS decreases the ultimate tensile strength and toughness, and increases the linear elasticity (**Fig 1.10d-f**). In contrast, increasing the fraction of CBS increases the tensile strength and toughness while decreasing the linear elasticity (**Fig 1.10g-i**). The increase in tensile strength and toughness relative to CBS fraction is attributed to the DPP monomer fraction increasing proportionally, as noted in **Fig 1.10a**. The flexibility of the CBS regions imparts a moderately

high strain at failure, allowing for a tough film. However, despite the addition of flexible break spacers, this entire library of polymers is less tough than the library of DPP-T–T3 polymers (**Fig 1.6d**).

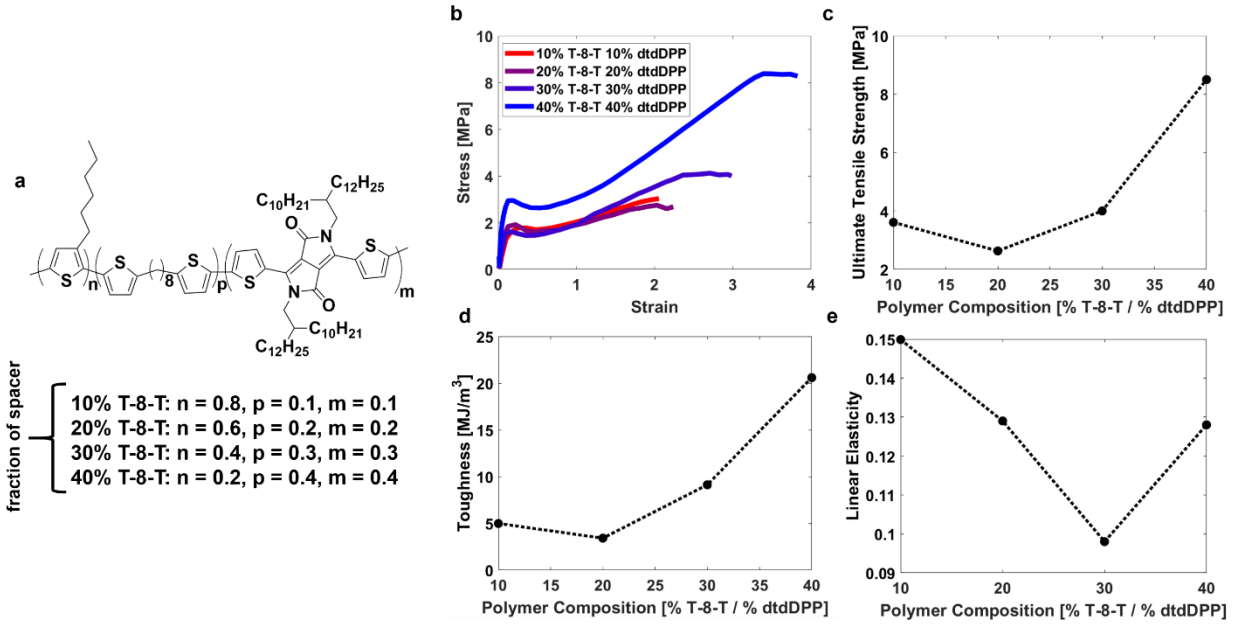

Figure 1.11. Mechanical properties of modified P3HT-dtdDPP polymers relative to conjugation-break spacer length and concentration. (**a**) Chemical structure of the P3HT-dtdDPP library used. Spacer fractions ranged from 10% to 40% with an equivalent fraction of dtdDPP, while the spacer length remained constant (n = 8, octane). (**b**) Stress-strain curves of P3HT-dtdDPP polymers relative to CBS and dtdDPP fraction replotted from Melenbrink et al. 2019.[109] (**c**) Tensile strength and (**d**) toughness increased relative to increasing CBS and dtdDPP fractions, whereas (**e**) linear elasticity increased relative to spacer length and decreased relative to spacer fraction.

Two new libraries of polymers were synthesized by the Thompson group to further explore the mechanical effects of CBS monomers. **Fig 1.11a** shows the chemical structure of the DPP-based conjugated polymer with a 2-decyltetradecyl-DPP (dtdDPP) monomer unit (the only difference being the side chain length). This library of P3HT-dtdDPP polymers resembles those in **Fig 1.10a** in that the fraction of DPP is equivalent to the fraction of CBS, and the trends shown (**Fig 1.11c-e)** are consistent with those found with the original P3HT-DPP library. The second library of polymers (from which no clear trends can be drawn) is discussed in detail in Appendix A (**Figure A5**). More interestingly, polymers with longer spacer lengths demonstrated improved electronic performance and no change in average conjugation length.[108] 10% T-6-

T, T-8-T, and T-10-T polymers were measured to have hole mobilities of 2.90×10^{-6}, 2.08×10^{-5}, and 2.53×10^{-4} $cm^2 V^{-1} s^{-1}$ respectively, with each two-carbon increase in the spacer length corresponding to a one magnitude increase in mobility. This improved electronic performance can be attributed to the increased conformational freedom (i.e. increasing the number of sp^3 bonds in the backbone) allowing polymer chains to pack more favorably for charge transport.[108] This suggests that strategies exist to increase both mechanical and electronic performance (thus, they are not necessarily antitheses of one another) by optimizing the packing structure.

Additional work to (1) isolate how conjugation-break spacers affect the rigidity of the backbone and (2) investigate the effect of CBS units on an n-type polymer has also been performed. This work is significant because active layers in organic solar cells require both a p-type and n-type material for charge generation and transport; thus, the optimization of electronic and mechanical properties for both materials is necessary. An active layer blended with semiconducting materials of varying efficiencies of charge transport will be limited by the least efficient material. Likewise, the mechanical properties of the p- and n-type polymers must be complimentary to prevent device failure (e.g. elastic mismatch[110] or adhesive failure[3,4,9] between two layers). A collaboration between the Gu and Mei groups in 2020 investigated the mechanical properties of a poly(naphthalene diimide) (PNDI)-based system incorporated with varying lengths of alkyl chain break spacers (**Figure 1.12**).[79]

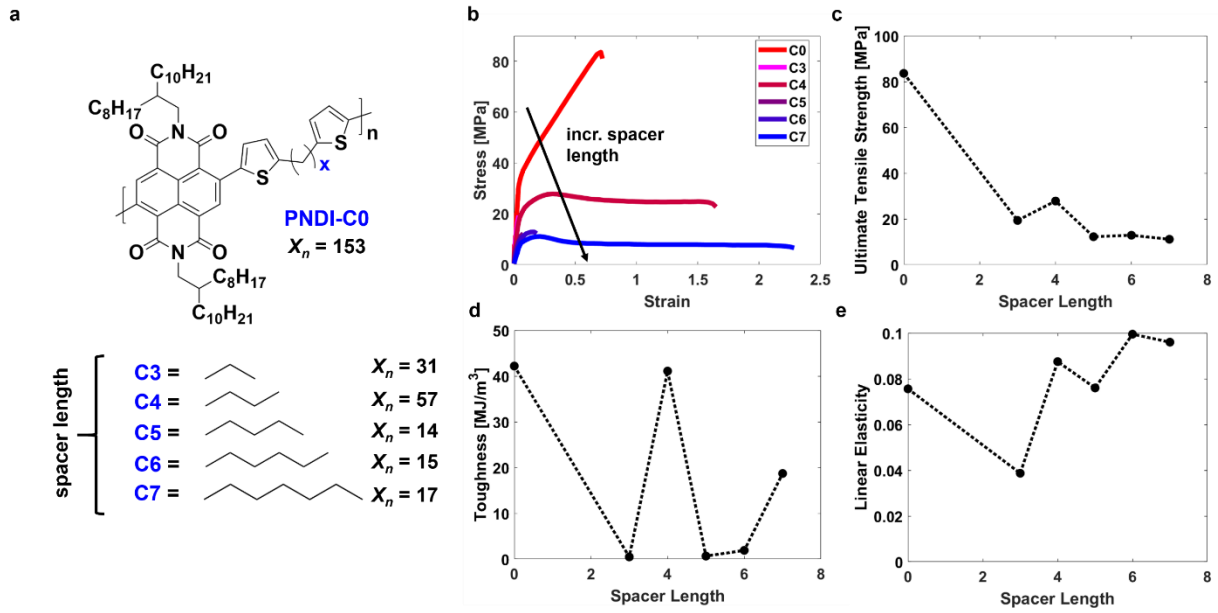

Figure 1.12. Mechanical properties of modified poly(naphthalene diimide) (PNDI)-based polymers (PNDI-Cx) relative to conjugation-break spacer length. (**a**) Chemical structure of the PNDI-Cx library used. Alkyl chain spacers ranged from a spacer length of zero (PNDI-C0) to a spacer length of seven (PNDI-C7). (**b**) Stress-strain curves of the PNDI-Cx polymers relative to break spacer length replotted from Galuska et al. 2020.[79] The (**c**) tensile strength, (**d**) toughness, and (**e**) linear elasticity for each system are shown.

Longer conjugation-break spacers have additionally been shown to increase fracture strain (**Fig 1.12b**) and decrease tensile strength (**Fig 1.12c**) in PNDI polymers. The fracture strains (and thus toughness) of the PNDI-Cx samples vary greatly. We can attribute this deviation in mechanical behavior primarily to differences in degree of polymerization (which varies from X_n = 153 for PNDI-C0 to X_n = 14 for PNDI-C5, **Fig 1.12a**). From the data discussed in this Perspective, we are able to make rudimentary comparisons between n-type and p-type CBS polymers. In particular, we see that PNDI-C7 seems to have very similar mechanical properties to the polymers in the P3HT-dtdDPP library (**Fig 1.11a**). However, for the purposes of optimizing strength, PNDI-C0 has by far the highest strength (and degree of polymerization) of all CBS samples. In conjunction with the stress-strain analysis of PNDI-C4 relative to molecular weight (**Figure 1.3**), the authors were able to offer two insights to how backbone rigidity affects mechanical properties. First, CBS can be used to substantially lower the T_g of a polymer, allowing for mobile, viscoelastic chains that are able to reorganize to accommodate more stress (and thus reduces crack propagation near defect

sites).[79] Second, decreasing the rigidity of the backbone lowers the critical entanglement molecular weight, M_C, which allows for a greater number of entanglements.[79]

1.3.6 Effect of Side Chain Structure

Much of this Perspective has discussed chemical modifications to the backbone structure of conjugated polymers, from which the unique semiconducting properties arise. However, the aliphatic side chains also play a crucial role in determining the mechanical properties of semiconducting polymers. For example, it is well understood that bulky side chains lower the T_g of both a conventional and conjugated polymer.[111,112] While early studies of the mechanical effects of alkyl side chains focused on polythiophenes as a model polymer,[111] the recent emergence of D–A polymers has generated interest in understanding how side chain engineering can be used to improve their thermomechanical and electronic properties.[53,55,113] For example, a paper published earlier by the Gu group investigates how the mechanical properties of a polydiketopyrrolopyrrole (PDPP)-based polymer changes relative to side chain length (**Figure 1.13**).[113]

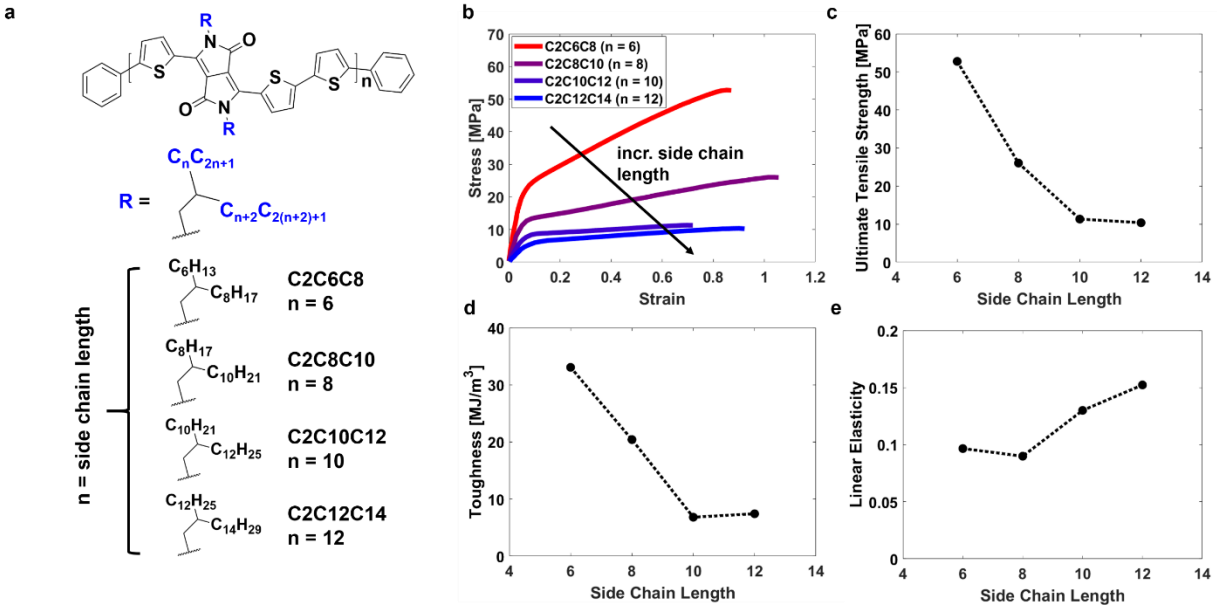

Figure 1.13. Mechanical properties of modified polydiketopyrrolopyrrole (PDPP)-based polymers relative to side chain length. (**a**) Chemical structure of the PDPP library used. (**b**) Stress-strain curves of the PDPP polymers relative to side chain length replotted from Zhang et al 2020.[113] The (**c**) tensile strength, (**d**) toughness, and (**e**) linear elasticity for each system are shown.

Increasing the alkyl side chain length (and steric bulk) were shown to result in a lowered elastic modulus (**Fig 1.13b**) and tensile strength (**Fig 1.13c**) in PDPP polymers. Although the fracture strain of the PDPP library remains approximately the same (~70% for C2C10C12 to ~85% for C2C8C10), the tensile strength decreases from ~50 MPa to ~10 MPa, resulting in a >300% decrease in toughness. This is only the second dataset discussed in which we see changes in the toughness primarily as a result of the tensile strength (the first being a DPP-based library by Zhang et al 2019 in **Figure 1.6**). In addition, C2C12C14 shows the largest range of linear elasticity of all polymer films studied in this Perspective, reaching >15% (**Fig 1.13e**). In fact, this entire PDPP library achieves a better fracture strain, strength, toughness, and linear elasticity than their DPP-T–T3 relatives (**Figure 1.6**) as well as the P3HT-DPP CBS polymers (**Figure 1.10**). The P3HT-dtdDPP polymers (**Figure 1.11**) have a very similar side chain structure on the DPP monomer and achieve greater fracture strains, but because the tensile strength of the PDPP library (**Fig 1.13c**) is so much greater, the toughness are similar (**Fig 1.11d**, **Fig 1.13d**). What is striking is that this same trend appears due to opposite effects (i.e. increasing fracture strain compared to increasing tensile strength). The toughest P3HT-dtdDPP polymer is the one with the highest fraction of CBS and DPP monomers (hence the greatest fracture strain), while the toughest PDPP polymer is C2C6C8 (due to the extremely high tensile strength), which has the shortest side chain.

From this analysis, we see that side chains are not just a necessity for increasing solubility, but rather also an avenue for tuning the thermomechanical properties. In the last couple of years, published literature exploring side chain engineering beyond simple alkyl chains has already started to emerge. For example, Yao et al. has shown that side chains with hydrogen bonding interactions have been shown to improve the electronic properties of DPP polymers.[55] Likewise, a collaboration by the Gu and Rondeau-Gagné groups has started to explore how hydrogen bonding in amide-containing side chains can modulate the mechanical properties (e.g. through energy dissipation).[53] Such side chain engineering strategies are (1)

complimentary to backbone engineering for rational polymer design and (2) synergistic in that they benefit both the development of stronger polymers as well as polymers with higher fracture strains.

1.3.7 Effect of Bulk Heterojunction Composition

We now return to our interest in organic solar cells for envisioned applications requiring substantial resistance to mechanical insult (e.g., car paint). The active layers of an organic solar cell typically require blending two materials together, one which donates the electrons and transports the holes, and one which transports the electrons. The most common type of this "bulk heterojunction" (BHJ) has been a polymeric donor and fullerene-based acceptor (e.g., [6,6]-phenyl-C61-butyric acid methyl ester, PCBM).[88] Kim and coworkers at KAIST used FOW to measure the evolution in mechanical properties as a function of loading fraction of PCBM, and also with or without the presence of 1,8-diiodooctane (an additive used to control film morphology) (**Figure 1.14**).

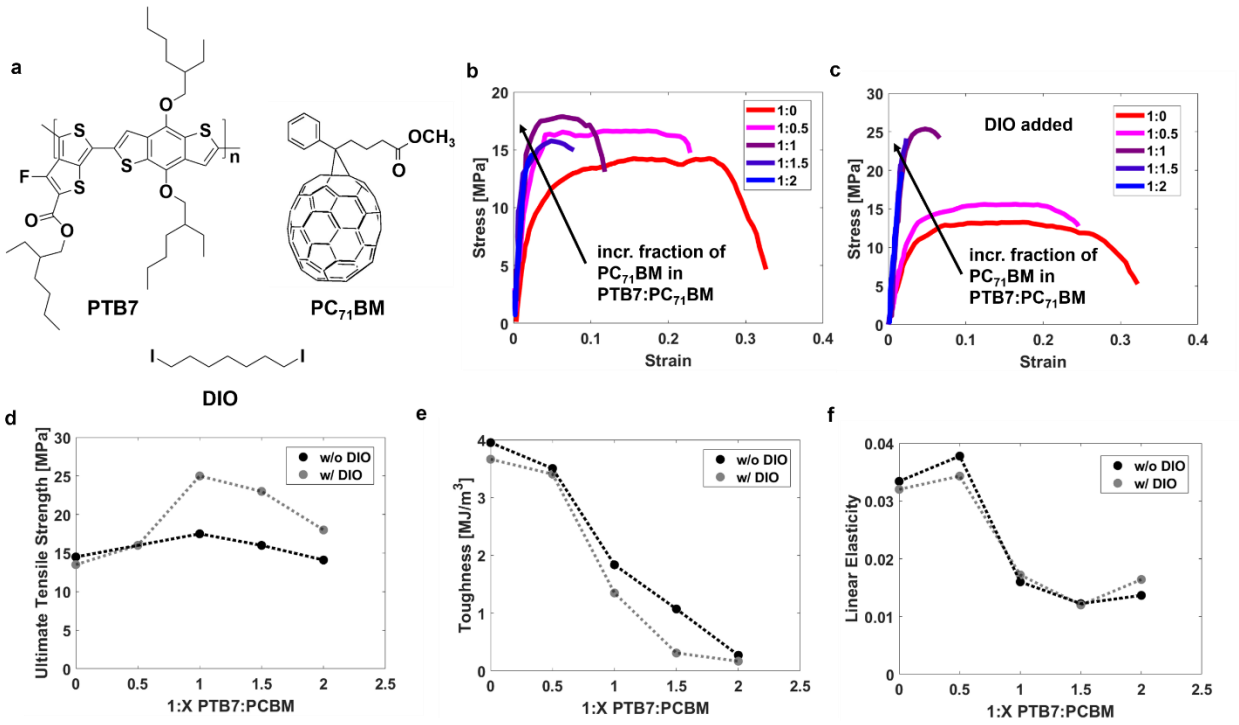

Figure 1.14. Mechanical properties of polymer-fullerene thin films with varying fractions of fullerene. Likewise, the mechanical properties are examined when 1,8-diiodooctane is added as a plasticizer used to induce finer morphology. (**a**) Chemical structures of PTB7 (the polymer electron donor), $PC_{71}BM$ (the fullerene electron acceptor), and 1,8-diiodooctane (DIO). (**b**) Stress strain curves of PTB7:$PC_{71}BM$ with increasing concentrations of $PC_{71}BM$ and (**c**) with DIO added replotted from Kim et al. 2017.[114] (**d**) Tensile strength remains relatively similar for increasing concentrations of $PC_{71}BM$, but films with DIO added tend to have greater tensile strengths than their counterparts. (**e**) Toughness decreases relative to increasing $PC_{71}BM$ concentration for both films with and without DIO added. (**f**) Linear elasticity, in general, decreases relative to increasing $PC_{71}BM$ concentration for films with and without DIO added.

PCBM (as a neat film) is a van der Waals solid with a high cohesive energy and a very high modulus relative to other small molecules commonly used in organic electronics.[115] It functions as an antiplasticizer when added to polymer active layers and embrittles them (**Fig 1.14b-c**).[116] This increased brittleness occurs due to the fullerenes acting as defects within the polymer matrix, which creates sites for cavitation formation.[6,117] Bulk heterojunctions treated with DIO follow the same trends, generally making the effects of PCBM more pronounced. Although the embrittling effects of PCBM reduce the fracture strain and the toughness under all conditions tested, in the presence of DIO, it possibly increases the strength by a non-negligible amount for ratios of PCBM ≥1. The toughness of the samples with DIO added were lower than

their counterparts with no additives. The toughness was driven primarily by the fracture strain. AFM images of DIO and non-DIO samples suggest that the addition of DIO results in a more even distribution of PCBM throughout the active layer (due to its selective solubility for PCBM).[118–120] Finer domains of PCBM in a matrix of PTB7 possibly results in a greater propensity for fracture (fractures are easily formed at interfacial regions in the bulk heterojunction).[114] So, for applications requiring strength and toughness, the dispersion of the fullerene in the donor needed for efficient charge generation must be balanced with its considerable effects on the mechanical properties.

In contrast to polymer-fullerene blends, all-polymer active layers offer several advantages. For example, conjugated polymers generally (1) have higher absorption coefficients for visible wavelengths and (2) can be tuned more efficiently in order to achieve an optimized bandgap for a given device.[121] Polymers can also be optimized more easily for mechanical properties.[122] However, few mechanical studies have been conducted on all-polymer solar cells in which some molecular structure has been varied systematically. Nevertheless, stark differences in deformability between polymer-polymer and polymer-fullerene systems have been highlighted in recent work. **Figure 1.15** compares the mechanical properties of two similar D–A polymer-polymer blends from two different studies[123,124] to results obtained for a polymer-fullerene blend.

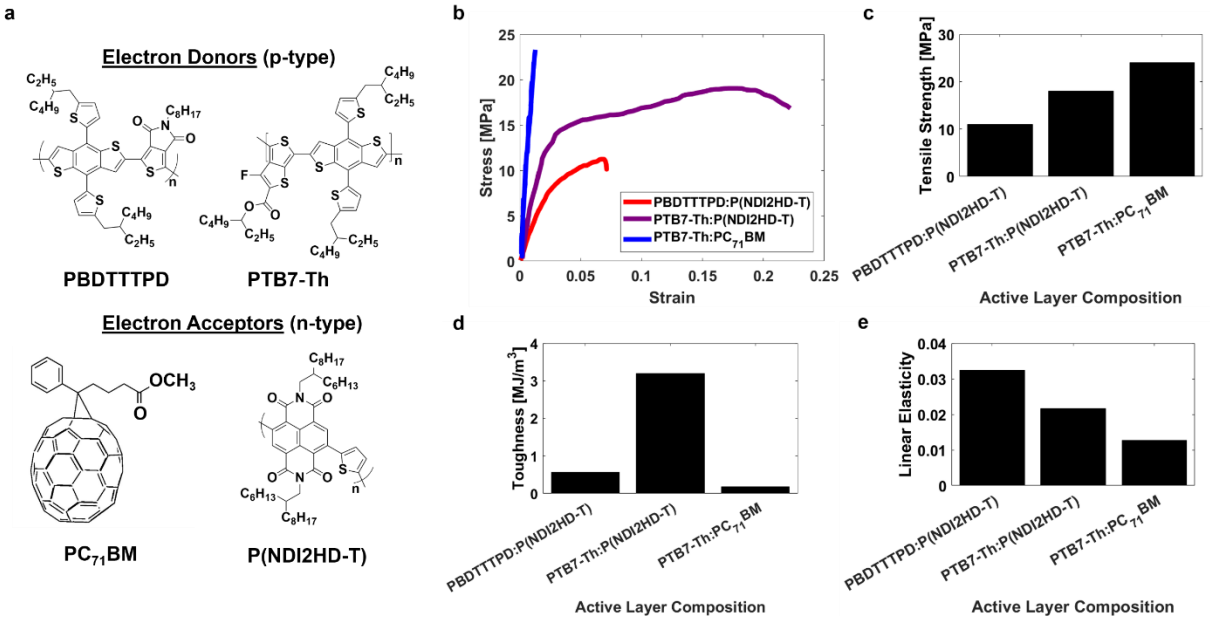

Figure 1.15. Mechanical properties of donor–acceptor thin film bulk heterojunctions. (**a**) Chemical structures of PBDTTTPD and PTB7-Th (electron donors), as well as $PC_{71}BM$ and P(NDI2HD-T) (electron acceptors). (**b**) Stress strain curves of bulk heterojunction thin films replotted from Taek-Soo Kim, Bumjoon J. Kim, and coworkers in 2015 and 2018.[123,124] The (**c**) tensile strength, (**d**) toughness, and (**e**) linear elasticity for each system is shown.

Although it is difficult to compare mechanical data across different studies, both PBDTTTPD and PTB7-Th share a common bis(thienyl)benzodithiophene backbone and were synthesized to be of similar molecular weight (M_n ~ 22 – 23 kDa). Their monomer structures are slightly different, but their degrees of polymerization are very similar (X_n ~ 25). The PTB7-Th:$PC_{71}BM$ blend showed the highest tensile strength (**Fig 1.15c**); this is likely due to the mechanical properties of the $PC_{71}BM$ being imparted onto the polymer blend as discussed above. However, this brittleness resulted in an extremely low toughness (**Fig 1.15d**) and linear elasticity (**Fig 1.15e**). Although the two all-polymer films have lower tensile strengths, both exhibited a higher toughness and linear elasticity. Of the two all-polymer samples, the PTB7-Th blend had a higher tensile strength and toughness, while the PBDTTTPD blend had a slightly higher linear elasticity. This comparison of the two all-polymer blends is simplified by the similarities between the donor polymers, particularly in chemical structure, degree of polymerization, and glass transition temperature (PBDTTTPD

T_g ~135 °C,[125] PTB7-Th T_g ~130 °C).[126] It is worth noting that the degrees of polymerization for the acceptor polymer differed slightly, with the P(NDI2HD-T) X_n ~ 58 for the PBDTTTPD blend and the X_n ~ 46 for the PTB7-Th blend.[123,124] However, this rudimentary comparison of the two polymers suggests that PTB7-Th clearly has better mechanical properties in a bulk heterojunction. Likewise, this again highlights the importance of conducting systematic studies of blended polymer systems as opposed to just single-polymer systems.

1.4 Conclusions

This Perspective takes the position that quantities such as strength, toughness, and elastic range are more important than quantities reflective of the ease of deformation: e.g., low modulus and high "stretchability." Our analysis reinforces the importance of side chains and main-chain rigidity in determining the mechanical robustness. Copolymerization strategies have shown ways in which favorable mechanical properties can coexist with retention of charge-carrier mobility and, in some cases—and perhaps inadvertently—lead to an increase in strength. For solar cells, our analysis highlights the importance of dispersion of fullerene units in polymer-fullerene blends in determining the mechanical properties. It also highlights the promise of all-polymer blends for applications requiring strength and resistance to abrasion. However, in none of the cases we examined were the structures of the polymers designed with the optimization of strength or elastic range as the primary goal. The most significant molecular effects on tensile strength and fracture strain are summarized in **Figure 1.16** below.

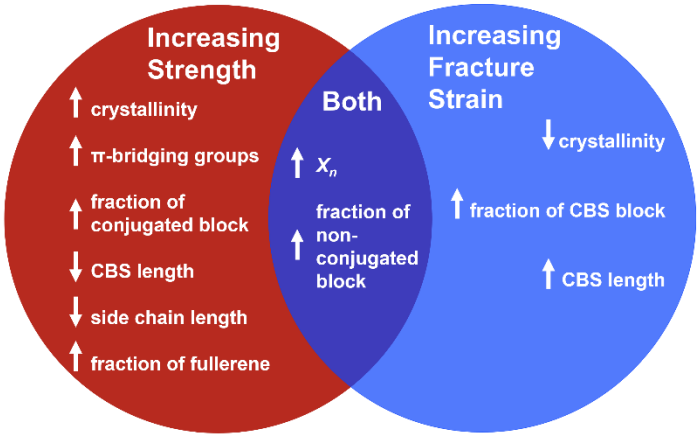

Figure 1.16. A summary of the most significant molecular effects on tensile strength (red), fracture strain (blue), and toughness (purple) discussed in this Perspective. Degree of polymerization and conjugation-break spacer are respectively abbreviated as X_n and CBS.

Thus, the strength and resilience of the state of the art in conjugated polymers is really quite poor (green oval, **Figure 1.17**). In order to enable a greater range of applications and capture more value—perhaps in the form of sunlight that strikes surfaces already transformed by humans—the development of conjugated polymers needs to proceed in a different direction. Research activities currently concerned with "stretchability" should shift their focus to robustness. In other words, be somewhat less concerned about the *x*-axis of the stress-strain curve and more concerned about the *y*-axis. Such a shift would be aided by the fact that seeming misalignment between the properties needed for stretchability and those needed for charge transport no longer applies. In fact, high density, strong intermolecular forces, crystalline and glassy microstructures—anathema to softness and stretchability—are precisely the qualities needed for strength and abrasion resistance, i.e., hardness. Synthetic approaches that include crosslinking,[50–52,99] removable side chains,[127–129] interdigitation of side chains,[130–132], the optimization of intermolecular forces within polymer blends (e.g. hydrogen bonding),[53–55,133,134] and—of course—molecular weights that are as high as possible without sacrificing solubility, are likely to produce new insights.

The toughness in particular will benefit greatly from Improvements to the stress axis while maintaining the progress our community has made in the strain axis. We envision many strategies for increasing the toughness involving material composites. For example, the incorporation of engineering polymers or elastomers in conjugated systems,[135–139] doping conjugated polymers with additives to maintain good charge transport in insulating matrices,[27,140] or the embedding of semicrystalline polymers in disordered matrices to create low crystalline systems with favorable electronic properties.[24] A deeper understanding of how molecular structure affects the elastic behavior of semiconducting polymers will also give insight into improving the elastic range, as right now calculations of the elastic limit must assume purely Hookean behavior. Such knowledge is gathered by expanding the analysis done by our community to other mechanical tests (e.g. compressive nanoindentation[56,141]) more familiar to the conventional polymer industry. Currently, we are ~1 magnitude away from achieving mechanical properties necessary for applications that require high strengths and elastic deformability. However, what can be achieved now in terms of softness and stretchability in conjugated polymers seemed unimaginable a decade ago, and thus there is little doubt that the community is up to the challenge.

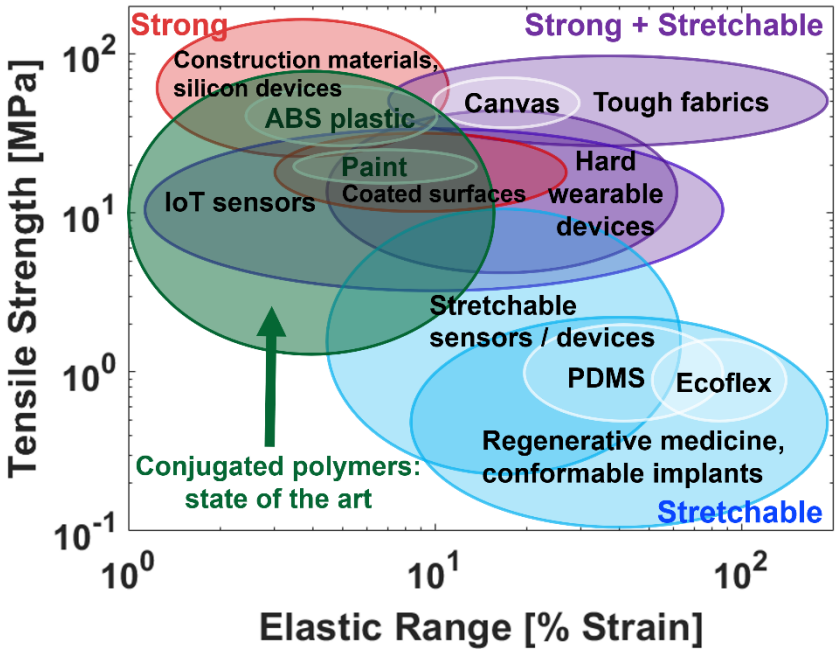

Figure 1.17. Shown in green is a general categorization of the data discussed in this Perspective relative to the desired mechanical properties for envisioned applications of semiconducting polymers.

1.5 Acknowledgments

This work was supported by the Air Force Office of Scientific Research (AFOSR) grant no. FA9550-19-1-0278 and a gift from the B Quest Giving Fund made to D.J.L. through Benefunder.

1.6 References

(1) Root, S. E.; Savagatrup, S.; Printz, A. D.; Rodriquez, D.; Lipomi, D. J. Mechanical Properties of Organic Semiconductors for Stretchable, Highly Flexible, and Mechanically Robust Electronics. *Chem. Rev.* **2017**, *117*, 6467–6499.

(2) Finn, M.; Martens, C. J.; Zaretski, A. V.; Roth, B.; Søndergaard, R. R.; Krebs, F. C.; Lipomi, D. J. Mechanical Stability of Roll-to-Roll Printed Solar Cells under Cyclic Bending and Torsion. *Sol. Energy Mater. Sol. Cells* **2018**, *174*, 7–15.

(3) Brand, V.; Bruner, C.; Dauskardt, R. H. Cohesion and Device Reliability in Organic Bulk Heterojunction Photovoltaic Cells. *Sol. Energy Mater. Sol. Cells* **2012**, *99*, 182–189.

(4) Dupont, S. R.; Voroshazi, E.; Heremans, P.; Dauskardt, R. H. Adhesion Properties of Inverted Polymer Solarcells: Processing and Film Structure Parameters. *Org. Electron. physics, Mater. Appl.* **2013**, *14*, 1262–1270.

(5) Bruner, C.; Miller, N. C.; McGehee, M. D.; Dauskardt, R. H. Molecular Intercalation and Cohesion of Organic Bulk Heterojunction Photovoltaic Devices. *Adv. Funct. Mater.* **2013**, *23*, 2863–2871.

(6) Tummala, N. R.; Bruner, C.; Risko, C.; Brédas, J. L.; Dauskardt, R. H. Molecular-Scale Understanding of Cohesion and Fracture in P3HT: Fullerene Blends. *ACS Appl. Mater. Interfaces* **2015**, *7*, 9957–9964.

(7) Bruner, C.; Novoa, F.; Dupont, S.; Dauskardt, R. Decohesion Kinetics in Polymer Organic Solar Cells. *ACS Appl. Mater. Interfaces* **2014**, *6*, 21474–21483.

(8) Dupont, S. R.; Oliver, M.; Krebs, F. C.; Dauskardt, R. H. Interlayer Adhesion in Roll-to-Roll Processed Flexible Inverted Polymer Solar Cells. *Sol. Energy Mater. Sol. Cells* **2012**, *97*, 171–175.

(9) Rodriquez, D.; Kohl, J. G.; Morel, P.; Burrows, K.; Favaro, G.; Root, S. E.; Ramírez, J.; Alkhadra,

M. A.; Carpenter, C. W.; Fei, Z.; Boufflet, P.; Heeney, M.; Lipomi, D. J. Measurement of Cohesion and Adhesion of Semiconducting Polymers by Scratch Testing: Effect of Side-Chain Length and Degree of Polymerization. *ACS Macro Lett.* **2018**, *7*, 1003–1009.

(10) Root, S. E.; Savagatrup, S.; Printz, A. D.; Rodriquez, D.; Lipomi, D. J. Mechanical Properties of Organic Semiconductors for Stretchable, Highly Flexible, and Mechanically Robust Electronics. *Chem. Rev.* **2017**, *117*, 6467–6499.

(11) Lipomi, D. J. Organic Photovoltaics: Focus on Its Strengths. *Joule* **2018**, *2*, 195–198.

(12) Onorato, J.; Pakhnyuk, V.; Luscombe, C. K. Structure and Design of Polymers for Durable, Stretchable Organic Electronics. *Polym. J.* **2017**, *49*, 41–60.

(13) Rogers, J. A.; Someya, T.; Huang, Y. Materials and Mechanics for Stretchable Electronics. *Science.* **2010**, *327*, 1603–1607.

(14) Ocheje, M. U.; Charron, B. P.; Nyayachavadi, A.; Rondeau-Gagné, S. Stretchable Electronics: Recent Progress in the Preparation of Stretchable and Self-Healing Semiconducting Conjugated Polymers. *Flex. Print. Electron.* **2017**, *2*.

(15) Qian, Y.; Zhang, X.; Xie, L.; Qi, D.; Chandran, B. K.; Chen, X.; Huang, W. Stretchable Organic Semiconductor Devices. *Adv. Mater.* **2016**, *28*, 9243–9265.

(16) Wang, M.; Baek, P.; Akbarinejad, A.; Barker, D.; Travas-Sejdic, J. Conjugated Polymers and Composites for Stretchable Organic Electronics. *J. Mater. Chem. C* **2019**, *7*, 5534–5552.

(17) Wang, G. J. N.; Gasperini, A.; Bao, Z. Stretchable Polymer Semiconductors for Plastic Electronics. *Adv. Electron. Mater.* **2018**, *4*, 1–21.

(18) Ramírez, J.; Rodriquez, D.; Urbina, A. D.; Cardenas, A. M.; Lipomi, D. J. Combining High Sensitivity and Dynamic Range: Wearable Thin-Film Composite Strain Sensors of Graphene,

Ultrathin Palladium, and PEDOT:PSS. *ACS Appl. Nano Mater.* **2019**, *2*, 2222–2229.

(19) Ramírez, J.; Rodriquez, D.; Qiao, F.; Warchall, J.; Rye, J.; Aklile, E.; Chiang, A. S. C.; Marin, B. C.; Mercier, P. P.; Cheng, C. K.; Hutcheson, K. A.; Shinn, E. H.; Lipomi, D. J. Metallic Nanoislands on Graphene for Monitoring Swallowing Activity in Head and Neck Cancer Patients. *ACS Nano* **2018**, *12*, 5913–5922.

(20) Kayser, L. V.; Lipomi, D. J. Stretchable Conductive Polymers and Composites Based on PEDOT and PEDOT:PSS. *Adv. Mater.* **2019**, *31*, 1–13.

(21) Inal, S.; Rivnay, J.; Suiu, A. O.; Malliaras, G. G.; McCulloch, I. Conjugated Polymers in Bioelectronics. *Acc. Chem. Res.* **2018**, *51*, 1368–1376.

(22) Runser, R.; Root, S. E.; Ober, D. E.; Choudhary, K.; Chen, A. X.; Dhong, C.; Urbina, A. D.; Lipomi, D. J. Interfacial Drawing: Roll-to-Roll Coating of Semiconducting Polymer and Barrier Films onto Plastic Foils and Textiles. *Chem. Mater.* **2019**, *31*, 9078–9086.

(23) Lipomi, D. J. Stretchable Figures of Merit in Deformable Electronics. *Adv. Mater.* **2016**, *28*, 4180–4183.

(24) Zheng, Y.; Wang, G. J. N.; Kang, J.; Nikolka, M.; Wu, H. C.; Tran, H.; Zhang, S.; Yan, H.; Chen, H.; Yuen, P. Y.; Mun, J.; Dauskardt, R. H.; McCulloch, I.; Tok, J. B. H.; Gu, X.; Bao, Z. An Intrinsically Stretchable High-Performance Polymer Semiconductor with Low Crystallinity. *Adv. Funct. Mater.* **2019**, *29*, 1–12.

(25) Sugiyama, F.; Kleinschmidt, A. T.; Kayser, L. V.; Alkhadra, M. A.; Wan, J. M. H.; Chiang, A. S. C.; Rodriquez, D.; Root, S. E.; Savagatrup, S.; Lipomi, D. J. Stretchable and Degradable Semiconducting Block Copolymers. *Macromolecules* **2018**, *51*, 5944–5949.

(26) Müller, C.; Goffri, S.; Breiby, D. W.; Andreasen, J. W.; Chanzy, H. D.; Janssen, R. A. J.; Nielsen, M. M.; Radano, C. P.; Sirringhaus, H.; Smith, P.; Stingelin-Stutzmann, N. Tough, Semiconducting

Polyethylene-Poly(3-Hexylthiophene) Diblock Copolymers. *Adv. Funct. Mater.* **2007**, *17*, 2674–2679.

(27) Mun, J.; Kang, J.; Zheng, Y.; Luo, S.; Wu, Y.; Gong, H.; Lai, J. C.; Wu, H. C.; Xue, G.; Tok, J. B. H.; Bao, Z. F4-TCNQ as an Additive to Impart Stretchable Semiconductors with High Mobility and Stability. *Adv. Electron. Mater.* **2020**, *6*, 1–9.

(28) Printz, A. D.; Lipomi, D. J. Competition between Deformability and Charge Transport in Semiconducting Polymers for Flexible and Stretchable Electronics. *Appl. Phys. Rev.* **2016**, *3*, 1–17.

(29) Rolston, N.; Bush, K. A.; Printz, A. D.; Gold-Parker, A.; Ding, Y.; Toney, M. F.; McGehee, M. D.; Dauskardt, R. H. Engineering Stress in Perovskite Solar Cells to Improve Stability. *Adv. Energy Mater.* **2018**, *8*, 1–7.

(30) Watson, B. L.; Rolston, N.; Printz, A. D.; Dauskardt, R. H. Scaffold-Reinforced Perovskite Compound Solar Cells. *Energy Environ. Sci.* **2017**, *10*, 2500–2508.

(31) Rolston, N.; Printz, A. D.; Tracy, J. M.; Dauskardt, R. H. Effect of Composition and Microstructure on the Mechanical Stability of Perovskite Solar Cells. *2018 IEEE 7th World Conf. Photovolt. Energy Conversion, WCPEC 2018 - A Jt. Conf. 45th IEEE PVSC, 28th PVSEC 34th EU PVSEC* **2018**, 3509–3513.

(32) Liu, Y.; Renna, L. A.; Bag, M.; Page, Z. A.; Kim, P.; Choi, J.; Emrick, T.; Venkataraman, D.; Russell, T. P. High Efficiency Tandem Thin-Perovskite/Polymer Solar Cells with a Graded Recombination Layer. *ACS Appl. Mater. Interfaces* **2016**, *8*, 7070–7076.

(33) Sun, C.; Wu, Z.; Yip, H. L.; Zhang, H.; Jiang, X. F.; Xue, Q.; Hu, Z.; Hu, Z.; Shen, Y.; Wang, M.; Huang, F.; Cao, Y. Amino-Functionalized Conjugated Polymer as an Efficient Electron Transport Layer for High-Performance Planar-Heterojunction Perovskite Solar Cells. *Adv. Energy Mater.*

2016, *6*, 1–10.

(34) Kwon, Y. S.; Lim, J.; Yun, H. J.; Kim, Y. H.; Park, T. A Diketopyrrolopyrrole-Containing Hole Transporting Conjugated Polymer for Use in Efficient Stable Organic-Inorganic Hybrid Solar Cells Based on a Perovskite. *Energy Environ. Sci.* **2014**, *7*, 1454–1460.

(35) Chen, W.; Bao, X.; Zhu, Q.; Zhu, D.; Qiu, M.; Sun, M.; Yang, R. Simple Planar Perovskite Solar Cells with a Dopant-Free Benzodithiophene Conjugated Polymer as Hole Transporting Material. *J. Mater. Chem. C* **2015**, *3*, 10070–10073.

(36) Printz, A. D.; Zaretski, A. V.; Savagatrup, S.; Chiang, A. S. C.; Lipomi, D. J. Yield Point of Semiconducting Polymer Films on Stretchable Substrates Determined by Onset of Buckling. *ACS Appl. Mater. Interfaces* **2015**, *7*, 23257–23264.

(37) Sun, T.; Song, R.; Balar, N.; Sen, P.; Kline, R. J.; O'Connor, B. T. Impact of Substrate Characteristics on Stretchable Polymer Semiconductor Behavior. *ACS Appl. Mater. Interfaces* **2019**, *11*, 3280–3289.

(38) O'Connor, B.; Chan, E. P.; Chan, C.; Conrad, B. R.; Richter, L. J.; Kline, R. J.; Heeney, M.; McCulloch, I.; Soles, C. L.; DeLongchamp, D. M. Correlations between Mechanical and Electrical Properties of Polythiophenes. *ACS Nano* **2010**, *4*, 7538–7544.

(39) Tahk, D.; Lee, H. H.; Khang, D.-Y. Elastic Moduli of Organic Electronic Materials by the Buckling Method. *Macromolecules* **2009**, *42*, 7079–7083.

(40) Stafford, C. M.; Harrison, C.; Beers, K. L.; Karim, A.; Amis, E. J.; Vanlandingham, M. R.; Kim, H. C.; Volksen, W.; Miller, R. D.; Simonyi, E. E. A Buckling-Based Metrology for Measuring the Elastic Moduli of Polymeric Thin Films. *Nat. Mater.* **2004**, *3*, 545–550.

(41) Kim, J.; Nizami, A.; Hwangbo, Y.; Jang, B.; Lee, H.; Woo, C.; Hyun, S.; Kim, T. Tensile Testing of Ultra-Thin Films on Water Surface. *Nat. Commun.* **2013**, *4*, 1–6.

(42) Sawyer, E. J.; Zaretski, A. V; Printz, A. D.; de los Santos, N. V; Bautista-Gutierrez, A.; Lipomi, D. J. Large Increase in Stretchability of Organic Electronic Materials by Encapsulation. *Extrem. Mech. Lett.* **2016**, *8*, 78–87.

(43) Root, S. E.; Jackson, N. E.; Savagatrup, S.; Arya, G.; Lipomi, D. J. Modelling the Morphology and Thermomechanical Behaviour of Low-Bandgap Conjugated Polymers and Bulk Heterojunction Films. *Energy Environ. Sci.* **2017**, *10*, 558–569.

(44) Hiemenz, P. C.; Lodge, T. P. *Polymer Chemistry*, 2nd ed.; CRC Press, 2007.

(45) Awartani, O.; Zhao, B. X.; Currie, T.; Kline, R. J.; Zikry, M. A.; O'Connor, B. T. Anisotropic Elastic Modulus of Oriented Regioregular Poly(3-Hexylthiophene) Films. *Macromolecules* **2016**, *49*, 327–333.

(46) Postema, A. R.; Liou, K.; Wudl, F.; Smith, P. Highly Oriented, Low-Modulus Materials from Liquid Crystalline Polymers: The Ultimate Penalty for Solubilizing Alkyl Side Chains. *Macromolecules* **1990**, *23*, 1842–1845.

(47) Chiang, C. K.; Fincher, Jr., C. R.; Park, Y. W.; Heeger, A. J.; Shirakawa, H.; Louis, E. J.; Gau, S. C.; MacDiarmid, A. G. Electrical Conductivity of I2-Doped Polyacetylene. *Phys. Rev. Lett.* **1977**, *39*, 1098–1101.

(48) Akagi, K.; Suezaki, M.; Shirakawa, H.; Kyotani, H.; Shimomura, M.; Tanabe, Y. Synthesis of Polyacetylene Films with High Density and High Mechanical Strength. *Synth. Met.* **1989**, *28*, D1–D10.

(49) Nielsen, L. E.; Landel, R. F. *Mechanical Properties of Polymers and Composites*, 2nd editio.; 1993.

(50) Rumer, J. W.; McCulloch, I. Organic Photovoltaics: Crosslinking for Optimal Morphology and Stability. *Mater. Today* **2015**, *18*, 425–435.

(51) Yang, Y.; Chen, S.; Xu, L. Enhanced Conductivity of Polyaniline by Conjugated Crosslinking. *Macromol. Rapid Commun.* **2011**, *32*, 593–597.

(52) Wang, G. J. N.; Shaw, L.; Xu, J.; Kurosawa, T.; Schroeder, B. C.; Oh, J. Y.; Benight, S. J.; Bao, Z. Inducing Elasticity through Oligo-Siloxane Crosslinks for Intrinsically Stretchable Semiconducting Polymers. *Adv. Funct. Mater.* **2016**, *26*, 7254–7262.

(53) Ocheje, M. U.; Selivanova, M.; Zhang, S.; Van Nguyen, T. H.; Charron, B. P.; Chuang, C. H.; Cheng, Y. H.; Billet, B.; Noori, S.; Chiu, Y. C.; Gu, X.; Rondeau-Gagné, S. Influence of Amide-Containing Side Chains on the Mechanical Properties of Diketopyrrolopyrrole-Based Polymers. *Polym. Chem.* **2018**, *9*, 5531–5542.

(54) Zheng, Y.; Ashizawa, M.; Zhang, S.; Kang, J.; Nikzad, S.; Yu, Z.; Ochiai, Y.; Wu, H.-C.; Tran, H.; Mun, J.; Zheng, Y.-Q.; Tok, J. B.-H.; Gu, X.; Bao, Z. Tuning the Mechanical Properties of a Polymer Semiconductor by Modulating Hydrogen Bonding Interactions. *Chem. Mater.* **2020**, 32, 5700–5714.

(55) Yao, J.; Yu, C.; Liu, Z.; Luo, H.; Yang, Y.; Zhang, G.; Zhang, D. Significant Improvement of Semiconducting Performance of the Diketopyrrolopyrrole-Quaterthiophene Conjugated Polymer through Side-Chain Engineering via Hydrogen-Bonding. *J. Am. Chem. Soc.* **2016**, *138*, 173–185.

(56) Worfolk, B. J.; Rider, D. A.; Elias, A. L.; Thomas, M.; Harris, K. D.; Buriak, J. M. Bulk Heterojunction Organic Photovoltaics Based on Carboxylated Polythiophenes and PCBM on Glass and Plastic Substrates. *Adv. Funct. Mater.* **2011**, *21*, 1816–1826.

(57) Zhai, L.; Khondaker, S. I.; Thomas, J.; Shen, C.; McInnis, M. Ordered Conjugated Polymer Nano- and Microstructures: Structure Control for Improved Performance of Organic Electronics. *Nano Today* **2014**, *9*, 705–721.

(58) Nakajima, T.; Sato, H.; Zhao, Y.; Kawahara, S.; Kurokawa, T.; Sugahara, K.; Gong, J. P. A

Universal Molecular Stent Method to Toughen Any Hydrogels Based on Double Network Concept. *Adv. Funct. Mater.* **2012**, *22*, 4426–4432.

(59) Gong, J. P.; Katsuyama, Y.; Kurokawa, T.; Osada, Y. Double-Network Hydrogels with Extremely High Mechanical Strength. *Adv. Mater.* **2003**, *15*, 1155–1158.

(60) Sun, J. Y.; Zhao, X.; Illeperuma, W. R. K.; Chaudhuri, O.; Oh, K. H.; Mooney, D. J.; Vlassak, J. J.; Suo, Z. Highly Stretchable and Tough Hydrogels. *Nature* **2012**, *489*, 133–136.

(61) Peak, C. W.; Wilker, J. J.; Schmidt, G. A Review on Tough and Sticky Hydrogels. *Colloid Polym. Sci.* **2013**, *291*, 2031–2047.

(62) Whitesides, G. M. Physical-Organic Chemistry: A Swiss Army Knife. *Isr. J. Chem.* **2016**, *56*, 66–82.

(63) Zhang, S.; Ocheje, M. U.; Luo, S.; Ehlenberg, D.; Appleby, B.; Weller, D.; Zhou, D.; Rondeau-Gagné, S.; Gu, X. Probing the Viscoelastic Property of Pseudo Free-Standing Conjugated Polymeric Thin Films. *Macromol. Rapid Commun.* **2018**, *39*, 1–8.

(64) Lin, B.; Zhang, L.; Zhao, H.; Xu, X.; Zhou, K.; Zhang, S.; Gou, L.; Fan, B.; Zhang, L.; Yan, H.; Gu, X. D.; Ying, L.; Huang, F.; Cao, Y.; Ma, W. Molecular Packing Control Enables Excellent Performance and Mechanical Property of Blade-Cast All-Polymer Solar Cells. *Nano Energy* **2019**, *59*, 277–284.

(65) Bruner, C.; Dauskardt, R. H. Role of Molecular Weight on the Mechanical Device Properties of Organic Polymer Solar Cells. *Macromolecules* **2013**, *47*, 1117–1121.

(66) Rodriquez, D.; Kim, J.-H.; Root, S. E.; Fei, Z. P.; Boufflet, P.; Heeney, M.; Kim, T.-S.; Lipomi, D. J. Comparison of Methods for Determining the Mechanical Properties of Semiconducting Polymer Films for Stretchable Electronics. *ACS Appl. Mater. Interfaces* **2017**, *9*, 8855–8862.

(67) Koch, F. P. V.; Rivnay, J.; Foster, S.; Müller, C.; Downing, J. M.; Buchaca-Domingo, E.; Westacott, P.; Yu, L.; Yuan, M.; Baklar, M.; Fei, Z.; Luscombe, C.; McLachlan, M. A.; Heeney, M.; Rumbles, G.; Silva, C.; Salleo, A.; Nelson, J.; Smith, P.; Stingelin, N. The Impact of Molecular Weight on Microstructure and Charge Transport in Semicrystalline Polymer Semiconductors-Poly(3-Hexylthiophene), a Model Study. *Prog. Polym. Sci.* **2013**, *38*, 1978–1989.

(68) O'Connor, T. F.; Rajan, K. M.; Printz, A. D.; Lipomi, D. J. Toward Organic Electronics with Properties Inspired by Biological Tissue. *J. Mater. Chem. B* **2015**, *3*, 4947–4952.

(69) Bruner, C.; Dauskardt, R. Role of Molecular Weight on the Mechanical Device Properties of Organic Polymer Solar Cells. *Macromolecules* **2014**, *47*, 1117–1121.

(70) Wu, S. Chain Structure, Phase Morphology, and Toughness Relationships in Polymers and Blends. *Polym. Eng. Sci.* **1990**, *30*, 753–761.

(71) Tummala, N. R.; Risko, C.; Bruner, C.; Dauskardt, R. H.; Brédas, J. L. Entanglements in P3HT and Their Influence on Thin-Film Mechanical Properties: Insights from Molecular Dynamics Simulations. *J. Polym. Sci. Part B Polym. Phys.* **2015**, *53*, 934–942.

(72) Balar, N.; Rech, J. J.; Henry, R.; Ye, L.; Ade, H.; You, W.; O'Connor, B. T. The Importance of Entanglements in Optimizing the Mechanical and Electrical Performance of All-Polymer Solar Cells. *Chem. Mater.* **2019**, *31*, 5124–5132.

(73) Vijayakumar, V.; Zaborova, E.; Biniek, L.; Zeng, H.; Herrmann, L.; Carvalho, A.; Boyron, O.; Leclerc, N.; Brinkmann, M. Effect of Alkyl Side Chain Length on Doping Kinetics, Thermopower, and Charge Transport Properties in Highly Oriented F 4 TCNQ-Doped PBTTT Films. *ACS Appl. Mater. Interfaces* **2019**, *11*, 4942–4953.

(74) Noriega, R.; Rivnay, J.; Vandewal, K.; Koch, F. P. V.; Stingelin, N.; Smith, P.; Toney, M. F.; Salleo, A. A General Relationship between Disorder, Aggregation and Charge Transport in

Conjugated Polymers. *Nat. Mater.* **2013**, *12*, 1038–1044.

(75) Wang, S.; Fabiano, S.; Himmelberger, S.; Puzinas, S.; Crispin, X.; Salleo, A.; Berggren, M. Experimental Evidence That Short-Range Intermolecular Aggregation Is Sufficient for Efficient Charge Transport in Conjugated Polymers. *Proc. Natl. Acad. Sci. U. S. A.* **2015**, *112*, 10599–10604.

(76) Fratini, S.; Nikolka, M.; Salleo, A.; Schweicher, G.; Sirringhaus, H. Charge Transport in High-Mobility Conjugated Polymers and Molecular Semiconductors. *Nat. Mater.* **2020**, *19*, 491–502.

(77) Noriega, R.; Rivnay, J.; Vandewal, K.; Koch, F. P. V; Stingelin, N.; Smith, P.; Toney, M. F.; Salleo, A. A General Relationship between Disorder, Aggregation and Charge Transport in Conjugated Polymers. *Nat. Mater.* **2013**, *12*, 1038–1044.

(78) Pei, D.; Wang, Z.; Peng, Z.; Zhang, J.; Deng, Y.; Han, Y.; Ye, L.; Geng, Y. Impact of Molecular Weight on the Mechanical and Electrical Properties of a High-Mobility Diketopyrrolopyrrole-Based Conjugated Polymer. *Macromolecules* **2020**, *53*, 4490–4500.

(79) Galuska, L.; McNutt, W.; Qian, Z.; Zhang, S.; Weller, D.; Dhakal, S.; King, E.; Morgan, S.; Azoulay, J.; Mei, J.; Gu, X. Impact of Backbone Rigidity on the Thermomechanical Properties of Semiconducting Polymers with Conjugation Break Spacers. *Macromolecules* **2020**.

(80) Kim, J.; Kim, J.; Lee, W.; Yu, H.; Kim, H. J.; Song, I.; Shin, M.; Oh, J. H.; Jeong, U.; Kim, T.; Kim, B. J. Tuning Mechanical and Optoelectrical Properties of Poly(3- Hexylthiophene) through Systematic Regioregularity Control. *Macromolecules* **2015**, *48*, 4339–4346.

(81) Park, H.; Ma, B. S.; Kim, J.; Kim, Y.; Kim, H. J.; Kim, D.; Yun, H.; Han, J.; Kim, F. S.; Kim, T.; Kim, B. J. Regioregular- Block -Regiorandom Poly(3-Hexylthiophene) Copolymers for Mechanically Robust and High-Performance Thin- Film Transistors. *Macromolecules* **2019**, *52*, 7721–7730.

(82) Kleinschmidt, A. T.; Root, S. E.; Lipomi, D. J. Poly(3-Hexylthiophene) (P3HT): Fruit Fly or Outlier in Organic Solar Cell Research? *J. Mater. Chem. A* **2017**, *5*, 11396–11400.

(83) Brinkmann, M. Structure and Morphology Control in Thin Films of Regioregular Poly(3-Hexylthiophene). *J. Polym. Sci. Part B Polym. Phys.* **2011**, *49*, 1218–1233.

(84) Savagatrup, S.; Printz, A. D.; Wu, H.; Rajan, K. M.; Sawyer, E. J.; Zaretski, A. V.; Bettinger, C. J.; Lipomi, D. J. Viability of Stretchable Poly(3-Heptylthiophene) (P3HpT) for Organic Solar Cells and Field-Effect Transistors. *Synth. Met.* **2015**, *203*, 208–214.

(85) Botiz, I.; Stingelin, N. Influence of Molecular Conformations and Microstructure on the Optoelectronic Properties of Conjugated Polymers. *Materials (Basel).* **2014**, *7*, 2273–2300.

(86) Himmelberger, S.; Salleo, A. Engineering Semiconducting Polymers for Efficient Charge Transport. *MRS Commun.* **2015**, *5*, 383–395.

(87) Wu, J.; Cheng, S.; Cheng, Y.; Hsu, C. Donor – Acceptor Conjugated Polymers Based on Multifused Ladder-Type Arenes for Organic Solar Cells. *Chem. Soc. Rev.* **2014**, *44*, 1113–1154.

(88) Savagatrup, S.; Printz, A. D.; O'Connor, T. F.; Zaretski, A. V.; Rodriquez, D.; Sawyer, E. J.; Rajan, K. M.; Acosta, R. I.; Root, S. E.; Lipomi, D. J. Mechanical Degradation and Stability of Organic Solar Cells: Molecular and Microstructural Determinants. *Energy Environ. Sci.* **2015**, *8*, 55–80.

(89) Duan, C.; Huang, F.; Cao, Y. Recent Development of Push-Pull Conjugated Polymers for Bulk-Heterojunction Photovoltaics: Rational Design and Fine Tailoring of Molecular Structures. *J. Mater. Chem.* **2012**, *22*, 10416–10434.

(90) Jemison, R. C.; McCullough, R. D. Techniques for the Molecular Design of Push-Pull Polymers towards Enhanced Organic Photovoltaic Performance. In *Polymer Composites for Energy Harvesting, Conversion, and Storage*; 2014; pp 71–109.

(91) Zhang, S.; Ocheje, M. U.; Huang, L.; Galuska, L.; Cao, Z.; Luo, S.; Cheng, Y.; Ehlenberg, D.; Goodman, R. B.; Zhou, D.; Liu, Y.; Chiu, Y.; Azoulay, J. D.; Rondeau-gagné, S.; Gu, X. The Critical Role of Electron-Donating Thiophene Groups on the Mechanical and Thermal Properties of Donor – Acceptor Semiconducting Polymers. *Adv. Electron. Mater.* **2019**, *5*, 1800898–1800899.

(92) Li, W.; Hendriks, K. H.; Wienk, M. M.; Janssen, R. A. J. Diketopyrrolopyrrole Polymers for Organic Solar Cells. *Acc. Chem. Res.* **2016**, *49*, 78–85.

(93) Wienk, M. M.; Turbiez, M.; Gilot, J.; Janssen, R. A. J. Narrow-Bandgap Diketo-Pyrrolo-Pyrrole Polymer Solar Cells: The Effect of Processing on the Performance. *Adv. Mater.* **2008**, *20*, 2556–2560.

(94) Bijleveld, J. C.; Gevaerts, V. S.; Di Nuzzo, D.; Turbiez, M.; Mathijssen, S. C. J.; De Leeuw, D. M.; Wienk, M. M.; Janssen, R. A. J. Efficient Solar Cells Based on an Easily Accessible Diketopyrrolopyrrole Polymer. *Adv. Mater.* **2010**, *22*, 242–246.

(95) Karsten, B. P.; Bijleveld, J. C.; Janssen, R. A. J. Diketopyrrolopyrroles as Acceptor Materials in Organic Photovoltaics. *Macromol. Rapid Commun.* **2010**, *31*, 1554–1559.

(96) Bijleveld, J. C.; Zoombelt, A. P.; Mathijssen, S. G. J.; Wienk, M. M.; Turbiez, M.; De Leeuw, D. M.; Janssen, R. A. J. High-Mobility Ambipolar Transistors and High-Cain Inverters from a Donor-Acceptor Copolymer Semiconductor. *Adv. Mater.* **2010**, *22*, 478–482.

(97) Roberts, M. E.; Queraltó, N.; Mannsfeld, S. C. B.; Reinecke, B. N.; Knoll, W.; Bao, Z. Cross-Linked Polymer Gate Dielectric Films for Low-Voltage Organic Transistors. *Chem. Mater.* **2009**, *21*, 2292–2299.

(98) Sugiyama, F.; Kleinschmidt, A. T.; Kayser, L. V.; Rodriquez, D.; Finn, M.; Alkhadra, M. A.; Wan, J. M. H.; Ramírez, J.; Chiang, A. S. C.; Root, S. E.; Savagatrup, S.; Lipomi, D. J. Effects of

Flexibility and Branching of Side Chains on the Mechanical Properties of Low-Bandgap Conjugated Polymers. *Polym. Chem.* **2018**, *9*, 4354–4363.

(99) Oh, J. Y.; Rondeau-Gagné, S.; Chiu, Y. C.; Chortos, A.; Lissel, F.; Wang, G. J. N.; Schroeder, B. C.; Kurosawa, T.; Lopez, J.; Katsumata, T.; Xu, J.; Zhu, C.; Gu, X.; Bae, W. G.; Kim, Y.; Jin, L.; Chung, J. W.; Tok, J. B. H.; Bao, Z. Intrinsically Stretchable and Healable Semiconducting Polymer for Organic Transistors. *Nature* **2016**, *539*, 411–415.

(100) Mei, J.; Bao, Z. Side Chain Engineering in Solution-Processable Conjugated Polymers. *Chem. Mater.* **2014**, *26*, 604–615.

(101) Ashraf, R. S.; Meager, I.; Nikolka, M.; Kirkus, M.; Planells, M.; Schroeder, B. C.; Holliday, S.; Hurhangee, M.; Nielsen, C. B.; Sirringhaus, H.; McCulloch, I. Chalcogenophene Comonomer Comparison in Small Band Gap Diketopyrrolopyrrole-Based Conjugated Polymers for High-Performing Field-Effect Transistors and Organic Solar Cells. *J. Am. Chem. Soc.* **2015**, *137*, 1314–1321.

(102) Li, C.; Zhang, A.; Feng, G.; Yang, F.; Jiang, X.; Yu, Y.; Xia, D.; Li, W. A Systematical Investigation of Non-Fullerene Solar Cells Based on Diketopyrrolopyrrole Polymers as Electron Donor. *Org. Electron.* **2016**, *35*, 112–117.

(103) Hendriks, K. H.; Heintges, G. H. L.; Gevaerts, V. S.; Wienk, M. M.; Janssen, R. A. J. High-Molecular-Weight Regular Alternating Diketopyrrolopyrrole-Based Terpolymers for Efficient Organic Solar Cells. *Angew. Chemie* **2013**, *125*, 8499–8502.

(104) Savagatrup, S.; Zhao, X.; Chan, E.; Mei, J.; Lipomi, D. J. Effect of Broken Conjugation on the Stretchability of Semiconducting Polymers. *Macromol. Rapid Commun.* **2016**, *37*, 1623–1628.

(105) Stehling, F. C.; Mandelkern, L. The Glass Temperature of Linear Polyethylene. *Macromolecules* **1970**, *3*, 242–252.

(106) Sugiyama, F.; Kleinschmidt, A. T.; Kayser, L. V.; Alkhadra, M. A.; Wan, J. M. H.; Chiang, A. S. C.; Rodriquez, D.; Root, S. E.; Savagatrup, S.; Lipomi, D. J. Stretchable and Degradable Semiconducting Block Copolymers. *Macromolecules* **2018**, *51*, 5944–5949.

(107) Zhao, Y.; Zhao, X.; Zang, Y.; Di, C. A.; Diao, Y.; Mei, J. Conjugation-Break Spacers in Semiconducting Polymers: Impact on Polymer Processability and Charge Transport Properties. *Macromolecules* **2015**, *48*, 2048–2053.

(108) Melenbrink, E. L.; Hilby, K. M.; Alkhadra, M. A.; Samal, S.; Lipomi, D. J.; Thompson, B. C. Influence of Systematic Incorporation of Conjugation-Break Spacers into Semi-Random Polymers on Mechanical and Electronic Properties. *ACS Appl. Mater. Interfaces* **2018**, *10*, 32426–32434.

(109) Melenbrink, E. L.; Hilby, K. M.; Choudhary, K.; Samal, S.; Kazerouni, N.; McConn, J. L.; Lipomi, D. J.; Thompson, B. C. Influence of Acceptor Side-Chain Length and Conjugation-Break Spacer Content on the Mechanical and Electronic Properties of Semi-Random Polymers. *ACS Appl. Polym. Mater.* **2019**, *1*, 1107–1117.

(110) Alkhadra, M. A.; Root, S. E.; Hilby, K. M.; Rodriquez, D.; Sugiyama, F.; Lipomi, D. J. Quantifying the Fracture Behavior of Brittle and Ductile Thin Films of Semiconducting Polymers. *Chem. Mater.* **2017**, *29*, 10139–10149.

(111) Savagatrup, S.; Printz, A. D.; Rodriquez, D.; Lipomi, D. J. Best of Both Worlds: Conjugated Polymers Exhibiting Good Photovoltaic Behavior and High Tensile Elasticity. *Macromolecules* **2014**, *47*, 1981–1992.

(112) Gargallo, L.; Hamidi, N.; Radić, D. Effect of the Side Chain Structure on the Glass Transition Temperature. 2. Poly(o-Alkylphenyl Methacrylate)S. *Thermochim. Acta* **1987**, *114*, 319–328.

(113) Zhang, S.; Alesadi, A.; Selivanova, M.; Cao, Z.; Qian, Z.; Luo, S.; Galuska, L.; I, C.; Ocheje, M. U.; Mason, G. T.; St. Onge, P. B. J.; Zhou, D.; Rondeau-Gagné, S.; Xia, W.; Gu, X. Toward the

Prediction and Control of Glass Transition Temperature for Donor–Acceptor Polymers. *Adv. Funct. Mater.* **2020**, *30*, 1–9.

(114) Kim, J.; Noh, J.; Choi, H.; Lee, J.; Kim, T. Mechanical Properties of Polymer − Fullerene Bulk Heterojunction Films : Role of Nanomorphology of Composite Films. *Chem. Mater.* **2017**, *29*, 3954–3961.

(115) Savagatrup, S.; Rodriquez, D.; Printz, A. D.; Sieval, A. B.; Hummelen, J. C.; Lipomi, D. J. PCBM and Incompletely Separated Grades of Methanofullerenes Produce Bulk Heterojunctions with Increased Robustness for Ultra-Flexible and Stretchable Electronics. *Chem. Mater.* **2015**, *27*, 3902–3911.

(116) Rodriquez, D.; Savagatrup, S.; Valle, E.; Proctor, C. M.; McDowell, C.; Bazan, G. C.; Nguyen, T. Q.; Lipomi, D. J. Mechanical Properties of Solution-Processed Small-Molecule Semiconductor Films. *ACS Appl. Mater. Interfaces 8*, 11649–11657.

(117) Kausch, H. H.; Devries, K. L. Molecular Aspects of High Polymer Fracture as Investigated by ESR-Technique. *Int. J. Fract.* **1975**, *11*, 727–759.

(118) Hedley, G. J.; Ward, A. J.; Alekseev, A.; Howells, C. T.; Martins, E. R.; Serrano, L. A.; Cooke, G.; Ruseckas, A.; Samuel, I. D. W. Determining the Optimum Morphology in High-Performance Polymer-Fullerene Organic Photovoltaic Cells. *Nat. Commun.* **2013**, *4*, 1–10.

(119) Liu, F.; Zhao, W.; Tumbleston, J. R.; Wang, C.; Gu, Y.; Wang, D.; Briseno, A. L.; Ade, H.; Russell, T. P. Understanding the Morphology of PTB7:PCBM Blends in Organic Photovoltaics. *Adv. Energy Mater.* **2014**, *4*, 1–9.

(120) Shin, N.; Richter, L. J.; Herzing, A. A.; Kline, R. J.; DeLongchamp, D. M. Effect of Processing Additives on the Solidification of Blade-Coated Polymer/Fullerene Blend Films via in-Situ Structure Measurements. *Adv. Energy Mater.* **2013**, *3*, 938–948.

(121) Facchetti, A. Polymer Donor-Polymer Acceptor (All-Polymer) Solar Cells. *Mater. Today* **2013**, *16*, 123–132.

(122) Kang, H.; Lee, W.; Oh, J.; Kim, T.; Lee, C.; Kim, B. J. From Fullerene − Polymer to All-Polymer Solar Cells : The Importance of Molecular Packing , Orientation , and Morphology Control. *Acc. Chem. Res.* **2016**, No. ii.

(123) Kim, T.; Kim, J.; Kang, T. E.; Lee, C.; Kang, H.; Shin, M.; Wang, C.; Ma, B.; Jeong, U.; Kim, T.; Kim, B. J. Flexible , Highly Efficient All-Polymer Solar Cells. *Nat. Commun.* **2015**, *6*, 1–7.

(124) Kim, W.; Choi, J.; Kim, J.; Kim, T.; Lee, C.; Lee, S.; Kim, M.; Kim, B. J.; Kim, T. Comparative Study of the Mechanical Properties of All-Polymer and Fullerene − Polymer Solar Cells : The Importance of Polymer Acceptors for High Fracture Resistance. *Chem. Mater.* **2018**, *30*, 2102–2111.

(125) Kim, T.; Choi, J.; Kim, H. J.; Lee, W.; Kim, B. J. Comparative Study of Thermal Stability, Morphology, and Performance of All-Polymer, Fullerene-Polymer, and Ternary Blend Solar Cells Based on the Same Polymer Donor. *Macromolecules* **2017**, *50*, 6861–6871.

(126) Yin, J.; Zhou, W.; Zhang, L.; Xie, Y.; Yu, Z.; Shao, J.; Ma, W.; Zeng, J.; Chen, Y. Improved Glass Transition Temperature towards Thermal Stability via Thiols Solvent Additive versus DIO in Polymer Solar Cells. *Macromol. Rapid Commun.* **2017**, *38*, 1–8.

(127) Ong, B. S.; Wu, Y.; Liu, P.; Gardner, S. High-Performance Semiconducting Polythiophenes for Organic Thin-Film Transistors. *J. Am. Chem. Soc.* **2004**, *126*, 3378–3379.

(128) Bjerring, M.; Nielsen, J. S.; Nielsen, N. C.; Krebs, F. C. Polythiophene by Solution Processing. *Macromolecules* **2007**, *40*, 6012–6013.

(129) Manceau, M.; Helgesen, M.; Krebs, F. C. Thermo-Cleavable Polymers: Materials with Enhanced Photochemical Stability. *Polym. Degrad. Stab.* **2010**, *95*, 2666–2669.

(130) Mcculloch, I.; Heeney, M.; Chabinyc, M. L.; Delongchamp, D.; Kline, R. J.; Cölle, M.; Duffy, W.; Fischer, D.; Gundlach, D.; Hamadani, B.; Hamilton, R.; Richter, L.; Salleo, A.; Shkunov, M.; Sparrowe, D.; Tierney, S.; Zhang, W. Semiconducting Thienothiophene Copolymers: Design, Synthesis, Morphology, and Performance in Thin-Film Organic Transistors. *Adv. Mater.* **2009**, *21*, 1091–1109.

(131) Kline, R. J.; DeLongchamp, D. M.; Fischer, D. A.; Lin, E. K.; Richter, L. J.; Chabinyc, M. L.; Toney, M. F.; Heeney, M.; McCulloch, I. Critical Role of Side-Chain Attachment Density on the Order and Device Performance of Polythiophenes. *Macromolecules* **2007**, *40*, 7960–7965.

(132) McCulloch, I.; Heeney, M.; Bailey, C.; Genevicius, K.; MacDonald, I.; Shkunov, M.; Sparrowe, D.; Tierney, S.; Wagner, R.; Zhang, W.; Chabinyc, M. L.; Kline, R. J.; McGehee, M. D.; Toney, M. F. Liquid-Crystalline Semiconducting Polymers with High Charge-Carrier Mobility. *Nat. Mater.* **2006**, *5*, 328–333.

(133) Wang, G. J. N.; Zheng, Y.; Zhang, S.; Kang, J.; Wu, H. C.; Gasperini, A.; Zhang, H.; Gu, X.; Bao, Z. Tuning the Cross-Linker Crystallinity of a Stretchable Polymer Semiconductor. *Chem. Mater.* **2019**, 6465–6475.

(134) Liang, Z.; Cabarcos, O. M.; Allara, D. L.; Wang, Q. Hydrogen-Bonding-Directed Layer-by-Layer Assembly of Conjugated Polymers. *Adv. Mater.* **2004**, *16*, 823–827.

(135) Oh, J. Y.; Son, D.; Katsumata, T.; Lee, Y.; Kim, Y.; Lopez, J.; Wu, H. C.; Kang, J.; Park, J.; Gu, X.; Mun, J.; Wang, N. G. J.; Yin, Y.; Cai, W.; Yun, Y.; Tok, J. B. H.; Bao, Z. Stretchable Self-Healable Semiconducting Polymer Film for Active-Matrix Strain-Sensing Array. *Sci. Adv.* **2019**, *5*.

(136) Gumyusenge, A.; Tran, D. T.; Luo, X.; Pitch, G. M.; Zhao, Y.; Jenkins, K. A.; Dunn, T. J.; Ayzner, A. L.; Savoie, B. M.; Mei, J. Semiconducting Polymer Blends That Exhibit Stable Charge

Transport at High Temperatures. *Science*. **2018**, *362*, 1131–1134.

(137) Qiu, L.; Lee, W. H.; Wang, X.; Kim, J. S.; Lim, J. A.; Kwak, D.; Lee, S.; Cho, K. Organic Thin-Film Transistors Based on Polythiophene Nanowires Embedded in Insulating Polymer. *Adv. Mater.* **2009**, *21*, 1349–1353.

(138) Song, E.; Kang, B.; Choi, H. H.; Sin, D. H.; Lee, H.; Lee, W. H.; Cho, K. Stretchable and Transparent Organic Semiconducting Thin Film with Conjugated Polymer Nanowires Embedded in an Elastomeric Matrix. *Adv. Electron. Mater.* **2016**, *2*, 1–8.

(139) Lu, G.; Bu, L.; Li, S.; Yang, X. Bulk Interpenetration Network of Thermoelectric Polymer in Insulating Supporting Matrix. *Adv. Mater.* **2014**, *26*, 2359–2364.

(140) Lu, G.; Blakesley, J.; Himmelberger, S.; Pingel, P.; Frisch, J.; Lieberwirth, I.; Salzmann, I.; Oehzelt, M.; Pietro, R. Di; Salleo, A.; Koch, N.; Neher, D. Moderate Doping Leads to High Performance of Semiconductor/Insulator Polymer Blend Transistors. *Nat. Commun.* **2013**, *4*, 1588.

(141) Tekin, E.; Egbe, D. A. M.; Kranenburg, J. M.; Ulbricht, C.; Rathgeber, S.; Birckner, E.; Rehmann, N.; Meerholz, K.; Schubert, U. S. Effect of Side Chain Length Variation on the Optical Properties of PPE-PPV Hybrid Polymers. *Chem. Mater.* **2008**, *20*, 2727–2735.

Chapter 2. Comparison of the Mechanical Properties of a Conjugated Polymer Deposited using Spin Coating, Interfacial Spreading, Solution Shearing, and Spray Coating

2.1 Introduction

Semiconducting (π-conjugated) polymers are amenable to the manufacture of devices covering large areas in part because of their ability to be deposited from solution. That is, polymer-based solar cells, solid-state lighting, wearable sensors, display technologies, and other devices have the potential to be manufactured using processes analogous to ink-based printing.[1–3] One requirement central to all envisioned applications of devices intended for use in these flexible form factors is mechanical robustness. The mechanical properties of a polymer are dependent not only on its molecular structure, but also on its morphology. The morphology in the solid state is the result of an interplay of processes, which include the kinetics of solidification and the forces present during deposition.[4] However, the majority of mechanical data for conjugated polymer films has been obtained from films prepared by spin coating,[5–7] which is not amenable to large-area deposition or deposition on flexible substrates.[8] It is not clear how the mechanical properties are influenced by processes of deposition that have the potential for scalability, such as interfacial spreading, solution shearing, and spray coating (**Figure 2.1**). The purpose of this work is to elucidate how the mechanical properties of a conjugated polymer film—as mediated by its morphology—are influenced by different deposition processes.

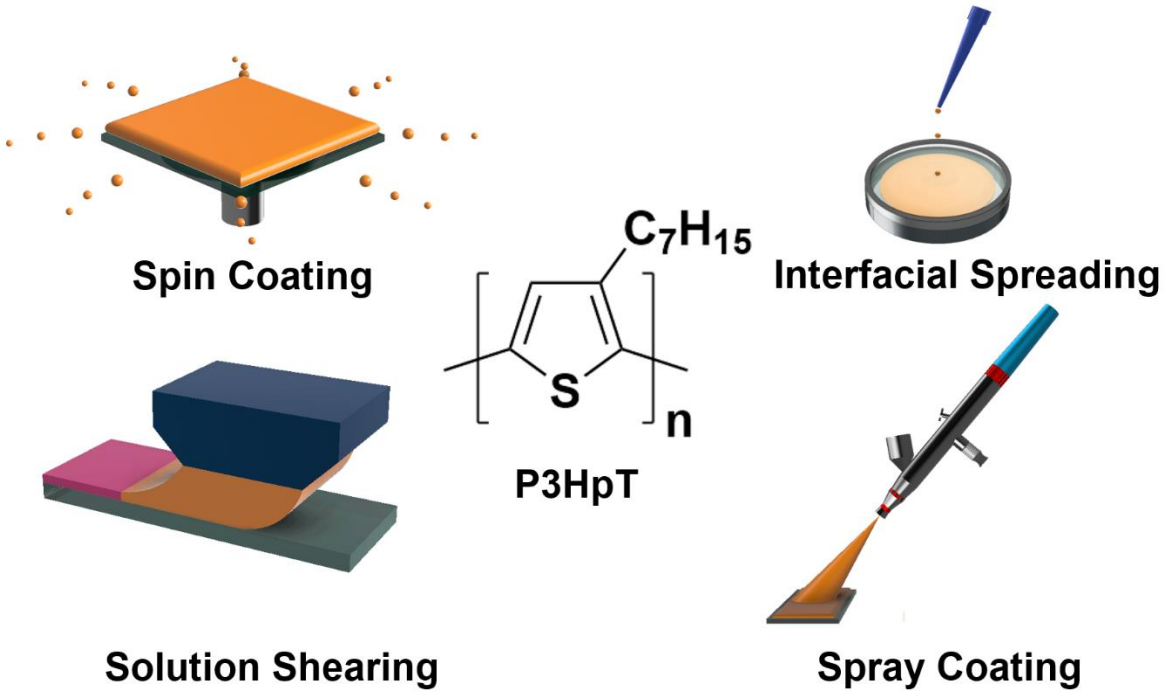

Figure 2.1. Films of poly(3-heptylthiophene) (P3HpT) were cast using four different deposition processes: spin coating, interfacial spreading, solution shearing, and spray coating.

2.2 Background

The manner in which a material is processed is crucial to its physical properties in an engineering application. For polymeric materials, the processing conditions influence the crystallinity, density, glass transition temperature, extent of entanglement, topography, texture, and defects.[9] For semiconducting polymers, these characteristics determine not only the mechanical response, but also the electronic properties.[10–12] Most studies on the mechanical properties of conjugated polymers use molecular characteristics as the independent variables in experiments.[13–15] That is, parameters such as side chain length, molecular weight, or single atoms in the backbone are altered systematically. In most of these studies, with few exceptions,[16–18] the films are deposited using spin coating, which cannot be readily scaled.

Nevertheless, among the first to study the role of solution processing on the mechanical properties of semiconducting polymers was the O'Connor group, who modified the speed and concentration during spin coating to manipulate the kinetics of solidification of bulk heterojunction films of poly(3-

hexylthiophene) and [6,6]-phenyl-C61-butyric methyl ester (P3HT:PCBM).[4] Films spun at lower speeds had greater short-range order in photophysical aggregates (as determined by the weakly interacting H-aggregate model).[19] Films with greater order had higher elastic moduli (i.e., increased stiffness) but lower fracture strains (i.e., extensibility). In molecular dynamics simulations performed in our laboratory, Root et al. found that processes designed to mimic solidification from the melt phase had a larger density of entanglements and an increased modulus compared to those modeled to be solidified from solution in a poor solvent.[20] However, such simulations are currently unable to predict the formation of crystallites and micron-scale defects, which are of critical importance to the mechanical properties of the solid film.

This work seeks to elucidate how scalable, roll-to-roll compatible deposition processes affect the morphology and mechanical properties of a polymer film. To guarantee a wide range of morphologies—and thus mechanical properties—we explored four solution-phase deposition processes which rely on different processing conditions: spin coating, interfacial spreading, solution shearing, and spray coating. Unlike spin coating, the other three processes (spreading, shearing, and spraying) have the potential to be used in continuous forms of deposition, i.e., roll-to-roll manufacturing.[21]

2.3 Experimental Design

2.3.1 Choice of Deposition Processes

We chose three deposition processes which have the potential for scalability—interfacial spreading (i.e., "floating film transfer method"), solution shearing (i.e., "blade coating"), and spray coating—and compared the mechanical properties to films produced by spin coating. Interfacial spreading ("floating film transfer method") is a process in which a polymer solution is drop cast on the surface of a liquid with a high surface tension, typically water.[22] The process relies on Marangoni spreading and results in solidification upon evaporation of the solvent.[23,24] The resulting films are air-stable once solidified, and can then be transferred (e.g., "stamped") directly from the water bath to planar or textured substrates.[25–27] Interfacial

spreading also allows for sequential film deposition from orthogonal solvents by stamping coatings layer by layer.[28,29]

Solution shearing is a process by which a blade attached to a linear actuator is used to spread solution over a substrate. Shearing has been shown to induce alignment of polymer backbones[30,31] and influence the lattice spacing in the solid film.[32,33] The shearing process resembles that of slot-die coating, a process common in industrial manufacturing of inks and polymeric thin films.[8]

Finally, spray coating uses an airbrush to deposit films on a surface, which enables two-dimensional patterning of the solid film using shadow masks. Spray coated films are characterized by their granular topography, which is due to the pressurized atomization of solution droplets.[34,35] Previous studies have shown that spray coated films are more disordered than their spin coated counterparts, yet are able to retain the same hole mobilities in thin-film transistors and power-conversion efficiencies in solar cells.[36–38]

2.3.2 Choice of Polymer and Solvent

As a test material, we chose regioregular poly(3-heptylthiophene) (P3HpT). Compared to its more widely used analogue, poly(3-hexylthiophene) (P3HT), P3HpT has a lower glass transition temperature (T_g) and greater deformability.[39] Chlorobenzene was used as the solvent due to the favorable spreading parameter on water (for interfacial spreading) and ability to solubilize P3HpT without clogging the airbrush used in spray coating.[23,24] Because the glass transition temperature of P3HpT is below room temperature, we did not explore the effects of thermal annealing. However, previous studies have suggested that annealing has a significant impact on the morphology and mechanical properties.[40,41]

2.3.3 Mechanical Testing

Stress-strain measurements of thin films were obtained using a pseudo-freestanding tensile test, i.e., “film-on-water”.[42] In this method, the ends of the dogbone-shaped film are adhered to

polydimethylsiloxane (PDMS) slabs on a linear actuator by van der Waals forces, and the load of the polymer film is measured as it is elongated.

2.3.4 Morphological Characterization

Optical microscopy was used to investigate global uniformity of the film, and atomic force microscopy (AFM) was used to investigate nanoscale surface structure. Aggregation in conjugated polymers provides short-range order and has the potential to contribute to inter-chain charge transport in conjugated polymers,[43] and was determined using ultraviolet-visible spectroscopy (UV-vis). UV-vis was also used to determine the dichroic ratio of sheared films. Grazing incidence X-ray diffraction (GIXD) measurements were performed to measure the atomic spacing, anisotropy of the domains, relative degree of crystallinity, coherence length, and texture of the crystallites (i.e., edge-on vs. face-on).

2.3.5 Thermal Characterization

To investigate how the deposition processes affects the glass transition temperature of the deposited thin film, we used a technique previously developed by our research group in which the UV-vis spectrum of a film is continuously scanned at increasing temperatures until a change in the spectrum is observed.[44] However, these measurements would be difficult to perform for P3HpT because its glass transition temperature below room temperature.[39,44] Thus, we chose to use poly(3-butylthiophene) (P3BT), which has a higher glass transition temperature (~65 °C, due to the shorter alkyl chain length),[45] as a proxy.

2.3.6 Electronic Characterization

To understand how morphological changes induced by different deposition processes affect the electronic performance, we obtained measurements of hole mobility from bottom-gate bottom-contact transistors. The electrode material for the source and drain contact was gold. The substrates were modified with an octadecyltrichlorosilane (ODTS) surface treatment, which has been shown to enhance the growth

of crystallites on the substrate.[46] In addition, the polymer films were annealed at 100 °C for 1 h in a nitrogen-filled glove box in order to remove any residual solvent trapped in the film and to improve the morphology of the film.[40] Previous work has shown that stamping an interfacially spread film from above (e.g., from the polymer-air interface) or below (e.g., from the polymer-water interface) influences the mobility of the resulting OFET device.[23] Semiconducting polymer films have been shown to have better mobilities in OFET devices when the transport layer is formed at the polymer-air interface.[23,47] For this reason, we chose to fabricate our interfacially spread OFET devices by stamping the P3HpT film from the polymer-air interface.

2.4 Results and Discussion

2.4.1 Optical Microscopy

Films produced by spin coating (**Figure 2.2a**) and shearing (**Figure 2.2c**) were uniform at the scale observable by optical microscopy. This finding is in contrast to interfacial spreading (**Figure 2.2b**) and spray coating (**Figure 2.2d**), which produced inhomogeneous films. Spread films showed alternating light and dark bands, corresponding to thinner and thicker regions.[26,27] Spray coating results in a granular surface (**Figure 2.2d**) due to the atomization of solution from the airbrush.[34,35]

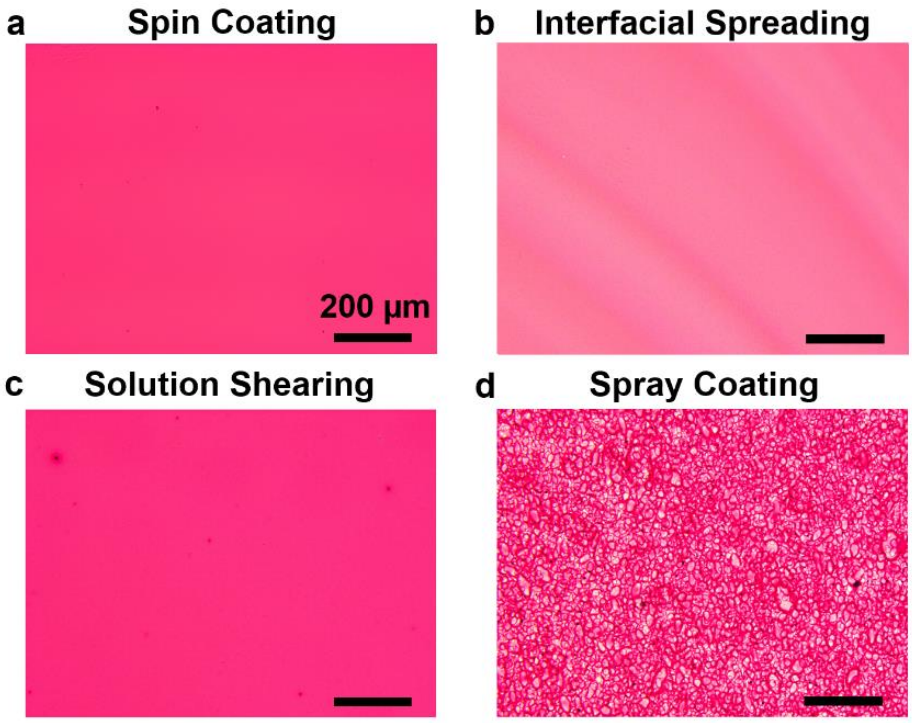

Figure 2.2. Optical microscopy images of (**a**) spin coated, (**b**) interfacially spread, (**c**) sheared, and (**d**) spray coated films. Spray coated films have a granular topography, while spread films have regions of lamellar zones of uneven thicknesses.

2.4.2 Mechanical Properties of Films Obtained using Different Deposition Processes

The mechanical response of the films produced by the four different deposition processes is shown in **Figure 2.3**. The most prominent features of the data are (1) the low apparent strength and modulus, and high brittleness, of the spray coated films, (2) the high extensibilities (and overall similar mechanical response) of the spin coated and spread films, and (3) the high modulus and strength of the sheared films. The mechanical behavior of spray coated films appeared to be dominated by the accumulation of stress around inhomogeneities that serve as point defects that concentrate stress (**Figure B1**). Spin coated and spread films displayed similar mechanical responses. The slightly lower measured modulus of the spread films is possibly due to its inhomogeneous thickness (which in turn could possibly be a consequence of the relatively high concentration of polymer solution) or the influence of the aqueous substrate during the film formation process (**Figure 2.2b**). (The average and standard deviation of the thickness for each sample was

measured using UV-vis as shown in **Figure B2**.) The lower modulus and higher fracture strain of spread films relative to spin coated films is consistent with the results of an earlier study by our laboratory,[26] as well previous studies elucidating effects of thickness on the mechanical properties of ultrathin polymer films.[6,48] Finally, sheared films had the greatest modulus, tensile strength, and toughness, despite the topographies of sheared films being indistinguishable from those of spin coated films (**Figure 2.2**).

The directionality of the shearing process suggested to us that chain alignment might play a role in the increased modulus and strength of sheared films.[49] Ultimately, AFM images, dichroic ratio measurements, and GIXD line plots along the parallel and perpendicular axes all suggest that shearing did not produce observable anisotropy (**Figure B3**). Likewise, although previous studies have suggested that interfacial spreading can produce anisotropic films,[50,51] our dichroic measurements of spread P3HpT films do not show evidence of anisotropy (**Figure B4**). While spread and sheared films can show chain alignment (i.e., anisotropy), producing anisotropic films often requires optimization of the processing parameters (e.g., solvent boiling point, concentration, deposition or annealing temperature).[50] For example, in sheared films, the degree of anisotropy can be a function of shear speed and annealing temperature.[30,32]

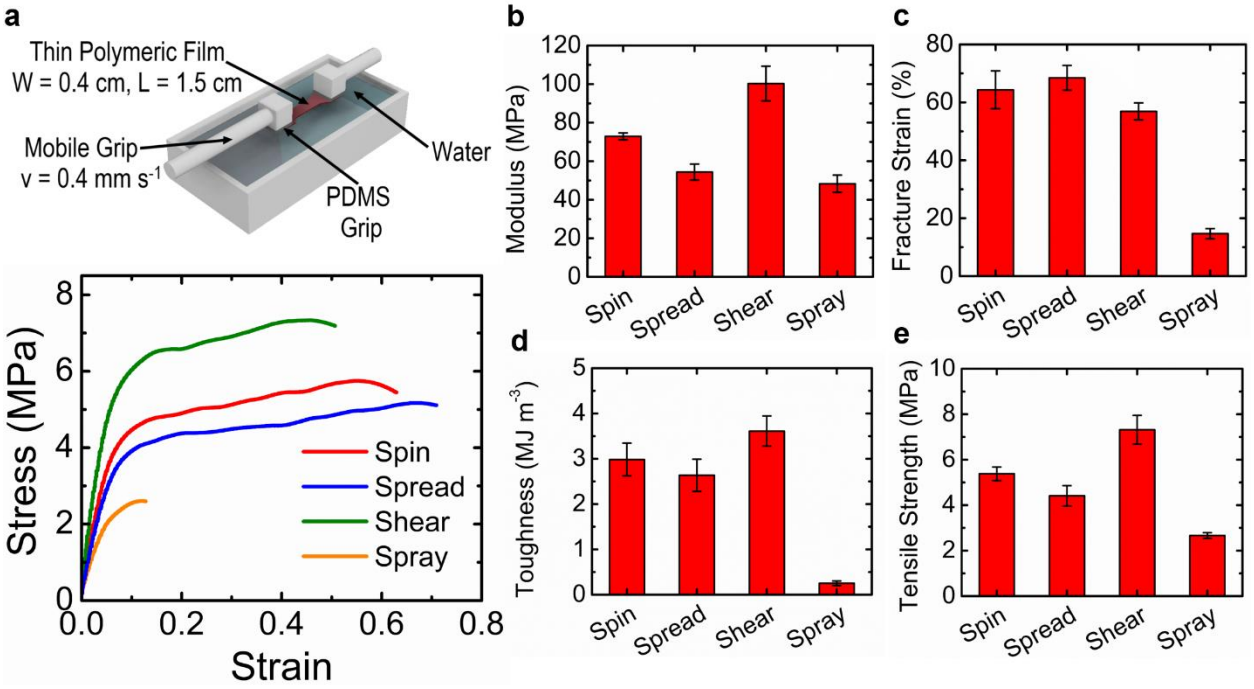

Figure 2.3. Mechanical properties of P3HpT films (120 nm) measured using the film-on-water tensile testing technique. (**a**) Top: schematic of the tensile testing setup. Bottom: representative stress-strain curves of P3HpT films cast using different deposition processes. Mechanical properties extracted from the stress-strain curves are (**b**) fracture strain, (**c**) elastic modulus, (**d**) toughness, and (**e**) ultimate tensile strength. Standard deviations are calculated from a minimum of four stress-strain measurements per deposition process.

2.4.3 Effect of Deposition Process on Glass Transition Temperature

We examined other characteristics associated with mechanical robustness in order to elucidate (1) the high modulus, strength, and toughness of sheared films and (2) the high extensibility of interfacially spread films. A film with high strength and modulus generally has a high glass transition temperature (T_g) as a result of greater packing density and decreased free volume (i.e., between polymer chains in amorphous domains).[6,7] Therefore, we hypothesized that the differences in mechanical behavior between spin coated and sheared films could be due to the deposition process affecting the density (i.e., free volume, and therefore also the glass transition temperature). Likewise, we reasoned that films with greater fracture strains likely also have a greater number of entanglements between polymer chains,[6] which possibly also affects the density. The key role of T_g in predicting the thermomechanical properties of poly(3-

alkylthiophenes) is well known.[6,14,39,45] To test our hypothesis, we used UV-vis spectroscopy to compare the glass transition temperature of films produced using shearing, spreading, and spin coating (**Figure 2.4, B5**).[44] However, the low T_g of P3HpT (approximately –12 °C)[45] would make this experiment difficult, as the film would have to be cast at a temperature below the glass transition temperature. For this reason, we performed our thermal and mechanical measurements on poly(3-butylthiophene) (P3BT) (**Figure 2.4**). The purpose of using P3BT as opposed to P3HpT is twofold. First, P3BT has a shorter alkyl chain length, and thus a glass transition temperature above room temperature (**Figure 2.4**).[45] Second, we use P3BT as a model polymer in order to elucidate whether the mechanical effects we observe with P3HpT are reproducible with a higher-T_g polymer.

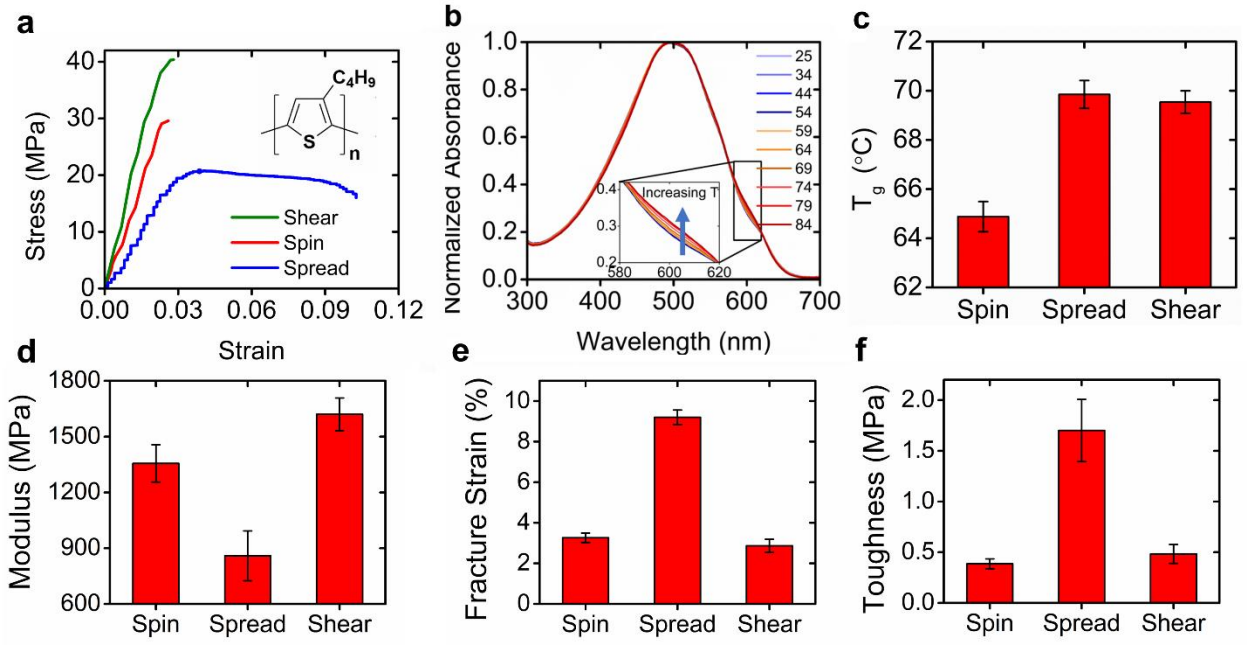

Figure 2.4. Mechanical and thermal properties of poly(3-butylthiophene) (P3BT) films cast using spin coating and solution shearing. (**a**) Stress-strain curves show that sheared films had a greater modulus and tensile strength than those produced using spin coating, while spread films had greater fracture strains. Chemical structure of P3BT is shown in the inset. (**b**) The progression of absorption spectra for a reference P3BT film relative to annealing temperature. Inset shows the progression of aggregation as the annealing temperature is increased. The sample spectra shown above are of a spin coated film of P3BT. (**c**) The glass transition temperature of both sheared and spread films were approximately 5 °C greater than their spin coated counterparts. The (**d**) modulus, (**e**) fracture strain, and (**f**) toughness are extracted from the stress-strain curves.

When comparing spin coating, interfacial spreading, and solution shearing, the mechanical response of P3BT mirrors that obtained for P3HpT. That is, sheared films, again, show higher modulus, strength, and toughness than their spin coated counterparts (**Figure 2.4a, 2.4d**). Likewise, spread films again show a lower modulus and higher fracture strain (**Figure 2.4a, 2.4d, 2.4e**). Encouragingly, this finding suggests that the effect of the deposition process on the tensile response is consistent for both higher-T_g and lower-T_g P3ATs. We note that the thickness of spread P3BT films (~80 nm) differed greatly from their spun (~110 nm) and sheared (~110 nm) counterparts (**Figure B6**). This difference is attributed to the difficulty of spreading uniform P3BT films of comparable thicknesses without inhomogeneities or wrinkles (**Figure B7**).

From the temperature that corresponds to the onset of aggregation by UV-vis spectroscopy (**Figure 2.4b, B5**), we see that the T_g of sheared and spread films were approximately 5 °C higher than that of spin coated films (**Figure 2.4c**). Increased T_g is associated with a reduction in free volume, an increase in van der Waals forces and a concomitant increase in cohesive energy density, and possibly also an increase in density of entanglements.[6,15,45] Based on these findings for P3BT, it is likely that similar morphological differences (i.e., decreased free volume) account for the increased elastic modulus and tensile strength for sheared P3HpT films (**Figure 2.3b, 2.3e**).

Interestingly, spread P3BT films showed a higher T_g despite having a lower modulus than spin coated films. This suggests to us that the film formation process on an aqueous substrate affects the amorphous morphology of the film, which in turn is a cause of the greater fracture strains. Notably, spread P3BT films showed fracture strains approximately three times that of spun and sheared films (**Figure 2.4e**), resulting in films with the greatest toughness (**Figure 2.4f**). Therefore, we see that solution shearing and interfacial spreading both result in a significant difference in amorphous morphology relative to spin coated films, and that their decreased free volumes manifest in their respective tensile responses in two different ways: a high strength and modulus for sheared films and a high fracture strain for spread films, both of which able to improve the toughness of the film.

2.4.4 Effect of Aggregation and Time of Solidification

Previous work from our group has suggested that faster solidification may be correlated with an increase in free volume within the polymer film, which corresponds with a decrease in modulus.[20,26] This finding is consistent with our comparison of spun and sheared films, in which we show that sheared films have the lowest free volume and slowest solidification rate (**Figure 2.4c, 2.5a**), which then corresponds to the highest modulus (**Figure 2.3b**). Studies have also pointed to a correlation of aggregation behavior on the mechanical properties of conjugated polymers.[4,39] We determined the fraction of aggregation in P3HpT and P3BT films using the weakly interacting H-aggregate model developed by Spano and coworkers (**Figure 2.5a**).[19] This model approximates the aggregates of P3ATs in a solid film as weakly interacting H-aggregates by comparing the relative peak intensities of the 0-0 and 0-1 vibronic transitions.[19] These vibronic transitions are represented as Gaussian distributions fitted to the measured aggregate absorption of the deconvoluted spectra.[19] However, this correlation was weak: the aggregate fraction of all P3HpT films was similar (~0.55), with the exception of those that were spray coated (**Figure 2.5a**). Interestingly, the process with the fastest solidification, spray coating, also had the highest fraction of aggregation. The similarity in aggregate fraction of the spun, sheared, and spread P3HpT films—which nevertheless have disparate mechanical behavior—suggests that other morphological features are responsible for differentiating the mechanical response.

Work from the O'Connor group has suggested that faster film formation (i.e., faster spin speeds) results in films with lower aggregate fractions.[4] However, we see no significant differences in aggregate fraction between spun, spread, and sheared films despite differing solidification times. The similarity in aggregation behavior itself may be a consequence of the low T_g of P3HpT (–12 °C).[39] The positioning of this second-order phase transition below room temperature may allow for some degree of equilibration between aggregated and non-aggregated domains during film formation. Our hypothesis is validated by a comparison of aggregate fraction in P3BT films (**Figure 2.5b**), which show the same trends between spun,

spread, and sheared films, yet with a far greater correlation (i.e., quantifiable differences in aggregation). (For example, a difference of ~0.02 between the aggregate fractions of spun and spread P3HpT films compared to a difference of ~0.13 between P3BT films prepared using the same two methods). Likewise, a comparison of the aggregate fractions of spun and spread films suggest that the low aggregation of spread films could possibly contribute to their low modulus and tensile strength. That is to say, the relative difference between both the aggregation and the modulus of spun films and sheared films is much greater for P3BT (**Figure 2.5b, 2.4d**) than for P3HpT (**Figure 2.5b, 2.3b**).

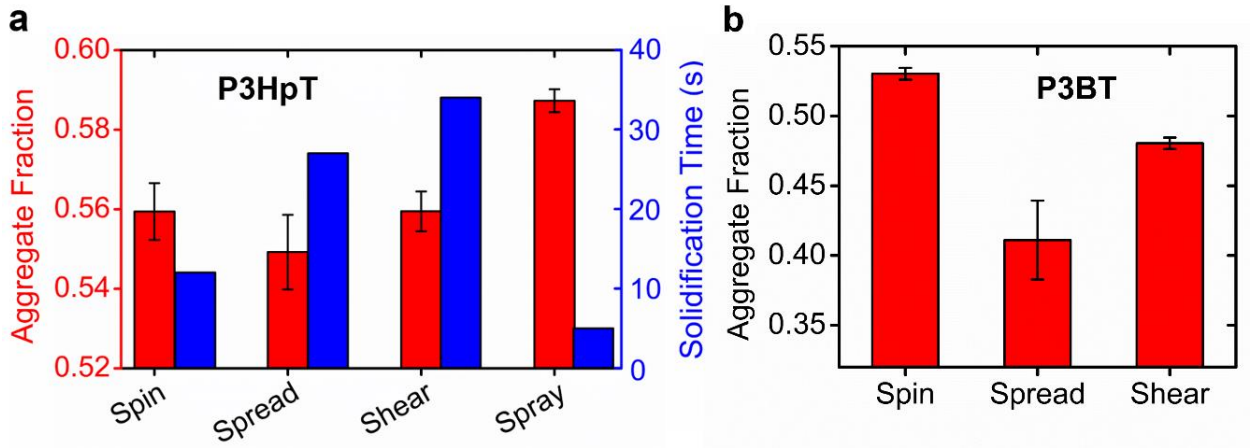

Figure 2.5. (**a**) Solidification time (blue) and aggregate fraction (red) relative to the deposition process used for P3HpT films. Solidification time was qualitatively determined as the time necessary for >90% of the P3HpT solution (bright orange) to form a film (dark red) after deposition. (**b**) Aggregate fraction of P3BT films.

2.4.5 Correlation of Mechanical and Structural Data with Charge-Transport Properties

In some types of conjugated polymer, e.g., polythiophenes, charge transport and mechanical deformability have been found to be antithetical.[52,53] Recently, however, numerous studies have shown that synthetic approaches to obtaining favorable charge transport and mechanical deformability can be successful.[54,55] To determine the effect of the deposition process on the transport properties of P3HpT—as mediated by the morphology of the resulting film—we fabricated bottom-gate, bottom-contact field effect transistors (OFETs, **Figure 2.6**).

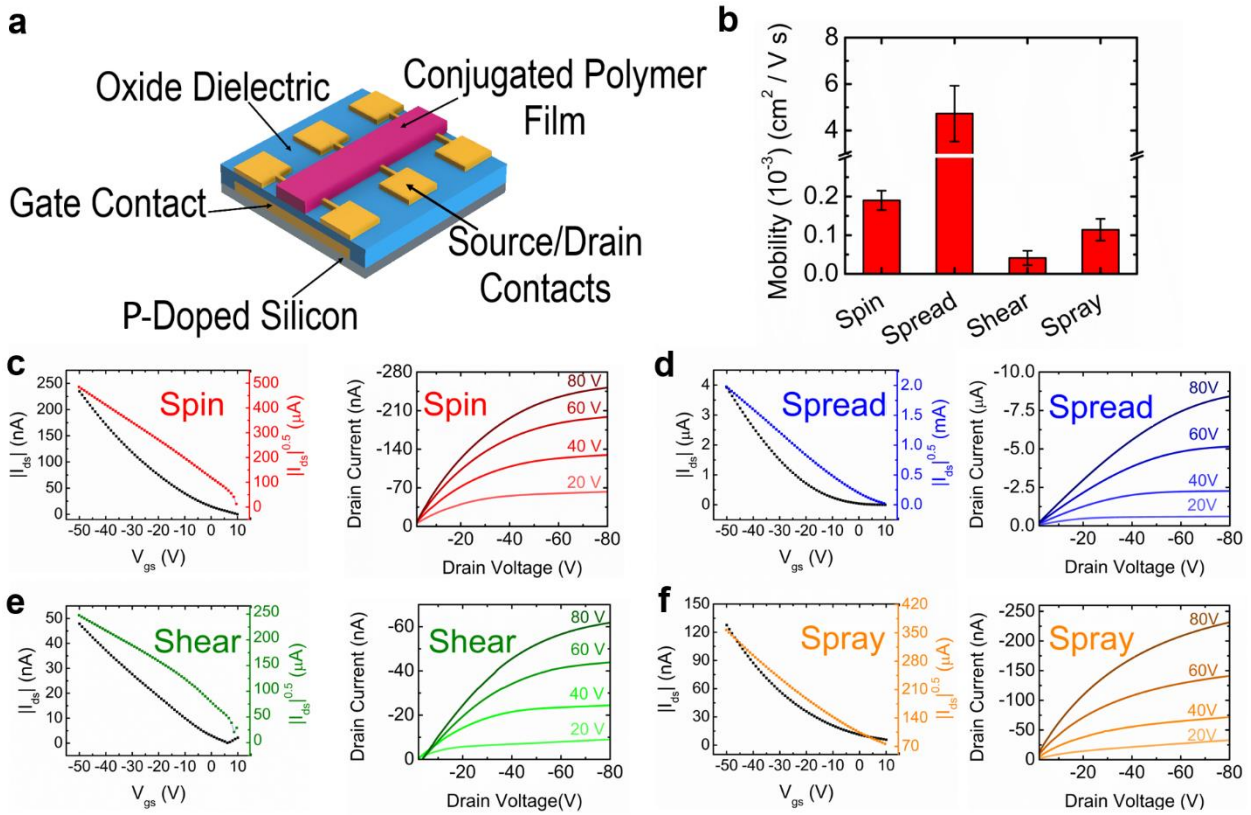

Figure 2.6. Charge-transport properties of P3HpT films. (**a**) Schematic of bottom-gate, bottom-contact transistors used to measure the mobility of P3HpT films cast from different deposition techniques. (**b**) The deposition process has a significant effect on the mobility of the device as shown by the transfer (left) and output (right) characteristics across (**c**) spin coated, (**d**) spread, (**e**) sheared, and (**f**) spray coated films.

Spin coated, spray coated, and sheared films all had hole mobilities near 0.1 × 10^{-3} cm^2 V^{-1} s^{-1} (**Figure 2.6b**, with output and transfer characteristics shown in **Figures 2.6c-f** and mobility extractions from all device measurements found in **Figure B8**). Sheared films showed the lowest mobilities amongst the four deposition processes. Spray coated films had mobilities comparable to spin coated films, which is consistent with previous results reported in literature.[36–38] However, the most notable observation is that films formed by interfacial spreading demonstrated the highest hole mobilities by over one magnitude (**Figure 2.6b**). The high mobility of spread films relative to their spin coated counterparts has been observed previously.[22,47,51] This increase in mobility has been attributed to increased edge-on texturing in spread films,[22,28,51,56] as well as an increase in crystallinity.[27,51]

2.4.6 Influence of Crystalline Features on the Mechanical and Electronic Properties of P3HpT Films

To elucidate the effect of crystalline features in P3HpT films on the mechanical and electronic properties, we performed grazing incidence X-ray diffraction (GIXD) measurements (**Figure 2.7**). Spin coated, spread, and sheared films showed similar Bragg reflections with three distinct lamellar peaks along the Q_z axis (100, 200, 300) and a π-stacking peak (010) near 1.6 $Å^{-1}$. Spray coated films showed much weaker intensities of higher-order lamellar reflections (the (200) and (300) peaks) as is evident from 2D-images (**Figure 2.7a**) as well as the orientationally averaged I-Q plot (**Figure 2.7e**). While all four films had similar π-stacking distances, there were more observable differences in lamellar packing distances (**Figure 2.7b**). Such a result is not surprising, considering that π-π interactions are stronger than the relatively weaker van der Waals forces between the aliphatic side chains of the polymer that govern lamellar spacing.[65–67]

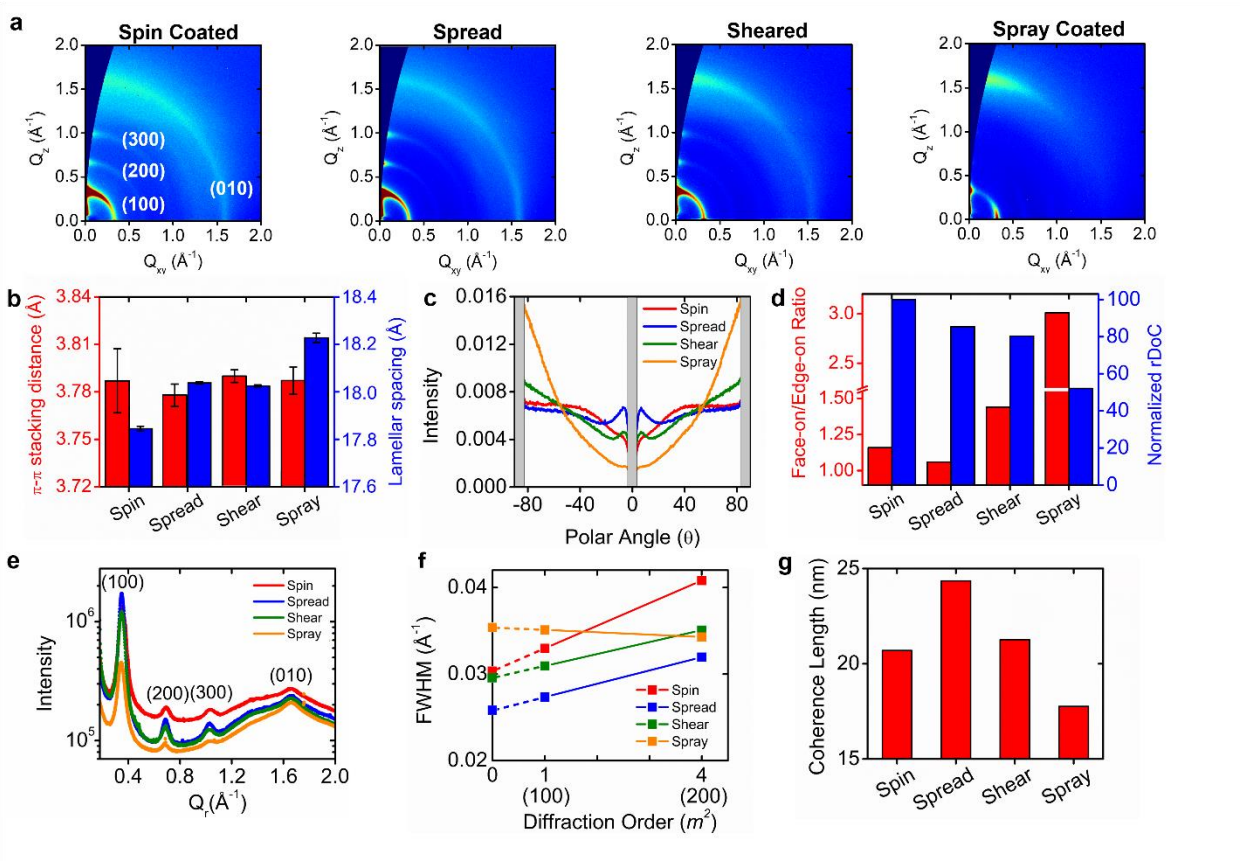

Figure 2.7. Grazing-incidence X-ray diffraction (GIXD) was used to obtain crystallographic information for P3HpT films cast using different deposition processes. (**a**) Diffraction images of spin coated, spread, sheared, and spray coated films. (**b**) Variations in π-π stacking distance and lamellar packing distance across the different films. (**c**) The crystallite orientation distribution function (ODF) was obtained from the (100) Bragg peak for each film and used to calculate both the (**d**) face-on to edge-on population ratio and normalized relative degree of crystallinity (rDoC). (**e**) Reduced $I(Q_r)$ vs Q_r (where Q_r is the scattering vector length) plots were determined from the diffraction images and used to calculate the (**f**) full width at half maximum (FWHM) of the (100) and (200) peaks, which is shown as a function of the square of the diffraction order (m^2). The y-intercept of the FWHM-m^2 relationship was used to calculate the (**g**) coherence length in the different films.

Additionally, it is possible that differences in crystallite orientation—i.e., texture— with respect to the film geometry and substrate plane have an effect on the mechanical[49] and electronic responses.[57] From the orientation distribution function (ODF) of scattering intensities for the (100) signatures relative to polar angle (**Figure 2.7c**), we are able to quantify texture exhibited by each film (**Figure 2.7c**). Spray coated films differed from the other three in that they displayed high scattering intensities at higher angles (near ±90°) and low scattering intensities at low angles (~0°), suggesting that spray coated films preferentially

form face-on crystallites (i.e., where the side chain is aligned parallel to the substrate and π-stacking is out-of-plane). In contrast, spin coated, spread, and sheared films all showed more uniform intensities across all angles (aside from a sharp increase in intensity for spread films near 0°). These distributions indicate that for these films, crystalline domains are more edge-on (i.e., where the side chain is perpendicular to the substrate) than in spray coated films. Indeed, spray coated films had the highest ratio of face-on to edge-on crystallites at ~3. Spin coated and sheared films had face-on to edge-on ratios of 1.15 and 1.44 respectively, while spread films had the lowest ratio amongst the four deposition processes (~1.0) (**Figure 2.7d**). The high edge-on texturing in spread films has previously been attributed to the migration of low-surface energy side chains to the polymer-air interface during the evaporation process.[47,58] As such, solution spreading with high boiling point solvents thermodynamically favors the formation of edge-on oriented crystallites at the dielectric-polymer interface.[22,23,50,56]

We also quantified the relative proportion of crystalline domains by calculating the relative degree of crystallinity (rDoC) for each film (**Figure 2.7d**). These values were then normalized to the relative degree of crystallinity for spin coated films, which had the highest degree of crystallinity. Spread and sheared films were almost identical in rDoC, differing by only 5%. Spray coated films were the least crystalline with a normalized rDoC of ~50%.

Lastly, we compared the progression of paracrystalline disorder in crystallites by analyzing the full width at half maximum (FWHM) and coherence length as determined from the (100) and (200) peaks (**Figure 2.7e-g**).[59] For spin, spread, and sheared films, the FWHM of the lamellar peak increased with diffraction order (m), which is indicative of cumulative disorder in the crystalline domains (**Figure 2.7f**). The variations in the FWHM across different deposition processes ultimately influence the coherence length (**Figure 2.7g**), which refers to the distance over which long-range order persists in the crystalline domains. The greater coherence length of spread films relative to spin coated films has previously only been observed for P3HT nanowires,[60] but here we show the improvement in long-range order occurs in P3HpT films as well.

Interestingly, our findings suggest that spray coated films have comparable mobilities to spin coated films despite a lower proportion of edge-on texturing and rDoC (**Figure 2.7d**), as well as a shorter coherence length (**Figure 2.7g**). A previous study comparing spun and sprayed films of polythieno[3,4-*b*]-thiophene-co-benzodithiophene:[6,6]-phenyl-C_{71}-butyric acid methyl ester (PTB7:$PC_{71}BM$) also suggested that spray coating results in significantly reduced order of molecular packing.[34] Together, our results suggest that the high mobility of spray coated films likely arises from the presence of favorable short-range order (as indicated by the high aggregate fraction, **Figure 2.5**) rather than long-range order in crystalline domains. X-ray diffraction measurements also reveal several morphological differences that could contribute to the high mobility of interfacially spread films. First, our calculations of face-on to edge-on population ratios suggest that spread films have the greatest proportion of edge-on texturing (**Figure 2.7d**), which agrees with previous studies on interfacial spreading.[22,23,50,56]. Edge-on texturing has been shown to be the preferred orientation for good mobility in transistors (though recent studies have shown that crystallite orientation alone does not determine mobility[61,62]).[63,64] Second, spread films have the greatest coherence length (~15% greater than sheared and spin coated films, **Figure 2.7g**), which is also consistent with previous observations.[60] Third, we note that additional GIXD measurements suggest that spread films tend to show more intense scattering intensities along the π-stacking (010) direction, which could also play a role in the higher mobilities (**Figure B9**). Unfortunately, it is unclear from our morphological characterization why sheared films have the lowest mobilities despite a relatively large coherence length (**Figure 2.7g**), high edge-on texturing, and high rDoC(**Figure 2.7d**).

This interrogation of the crystalline morphologies offers an explanation for the improved mobilities of interfacially spread and spray coated films. However, we find that the mechanical properties of P3HpT films do not seem to be influenced by the crystalline domains of the film. No clear correlation was observed between crystallographic features (i.e., atomic packing distances, relative degree of crystallinity, coherence length) and the mechanical responses of the films. Previous studies have elucidated the effect of secondary interactions (like Van der Waals forces and π-stacking interactions) on the mechanical properties of a

semiconducting film,[7,65–67] suggesting that increased lamellar spacing and π-π spacing is expected to result in a weaker and less stiff film. Likewise, work from the O'Connor and DeLongchamp laboratories have shown that biaxial strain can be utilized to reorient the texturing of P3HT films (from predominantly edge-on to predominantly face-on),[61,68] thus suggesting that molecular texture is influenced by strain. (The Gu group has shown a similar result with a donor-acceptor polymer.[69]) Additionally, work by Kim and coworkers has shown that decreasing the crystallinity of P3HT, by decreasing the regioregularity, results in a weaker, less stiff, and more extensible film.[70] However, we observed no correlation between secondary interactions, crystallinity, or paracrystalline disorder and the mechanical responses of the films, perhaps because the proportion of crystalline domains in P3HpT films is too small to influence the mechanical properties. As such, these results reinforce the idea that crystalline domains predominantly dictate the electronic properties of P3HpT films, while the amorphous domains predominantly dictate the mechanical response of P3HpT films. We summarize our morphological characterization in **Figure 2.8,** below**.**

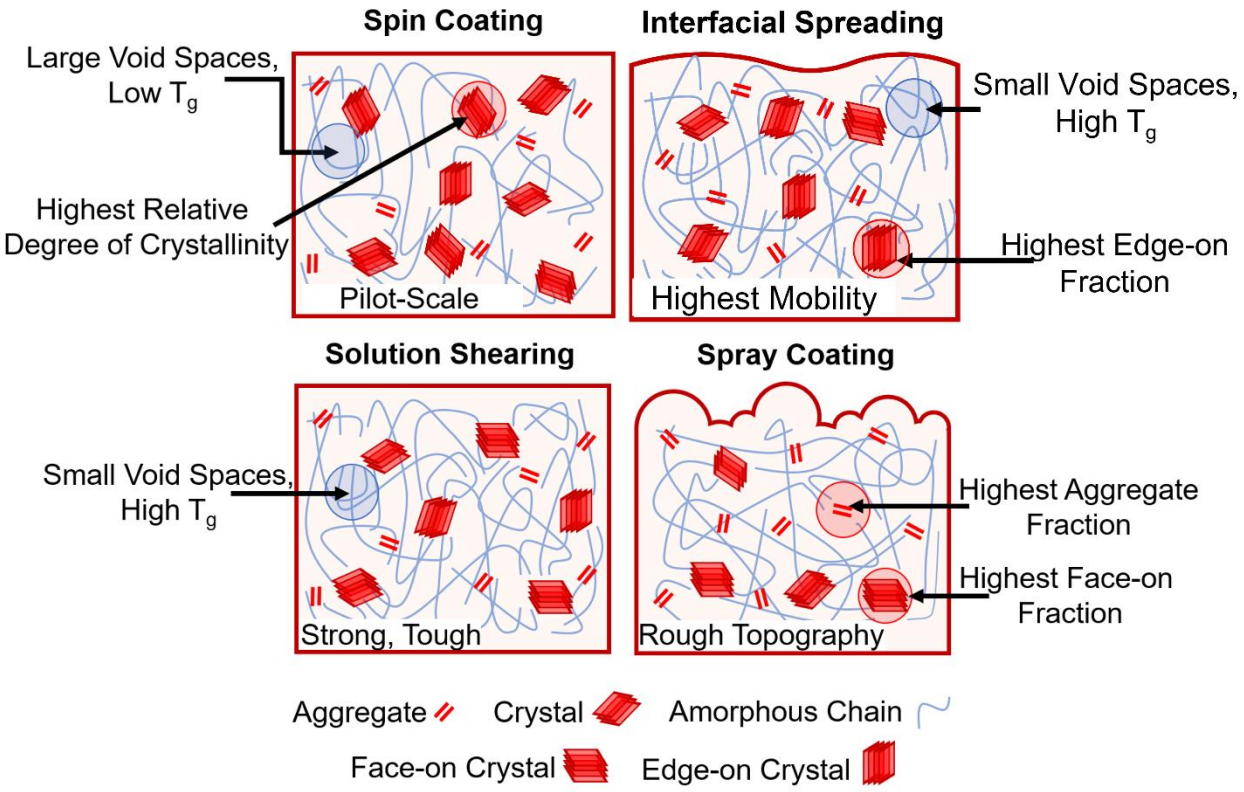

Figure 2.8. Schematic diagrams highlighting differences in morphology and topography for P3HpT films deposited using the four processes studied in this work. The number of aggregates and crystalline domains are representative of the aggregate fraction and relative degree of crystallinity in these films. The primary features are (1) the topographical differences in spread and spray coated films, (2) the predominantly face-on texturing of spray coated films, and (3) the high density (low free volume, as depicted by the greater number of chains in the amorphous regions) of sheared films.

2.5 Conclusion

This study examines how the mechanical properties and charge-transport properties of P3HpT are mediated by morphology, as influenced by the deposition process (**Figure 2.9**). When comparing these deposition processes, we draw five significant conclusions. First, interfacially spread P3HpT films have the greatest deformability (among films formed from scalable deposition processes) and the highest mobilities. Thus, for applications requiring mechanical compliance, interfacially spread films thus appear to offer "the best of both worlds." Second, sheared P3HpT films are the most mechanically robust in that they have the highest modulus, strength, and toughness. Thus, solution shearing should be preferred for applications that must withstand mechanical insult. Third, spray coated films demonstrate very poor mechanical behavior in

all respects. However, spray coating is the least expensive process, and it is unique among all studied processes in this work in that it enables patterning through stencil masks. Therefore, further efforts should be made in studying how spray coating can be used in conjunction with semiconducting polymers to obtain films of higher quality. Fourth, we observe that spin coating provides a "middle-of-the-road" for all measurements. Along with its affordability and ease of use, these "representative" measurements make spin coating a powerful tool at the pilot scale. Last, our comparison of P3HpT and P3BT films suggest that effects of the deposition process on the tensile response of the polymer films possibly hold true for both lower-T_g and higher-T_g polymers. Therefore, we find that the deposition process and their processing parameters can have a significant effect on the mechanical properties, electronic properties, and morphology of conjugated polymers.

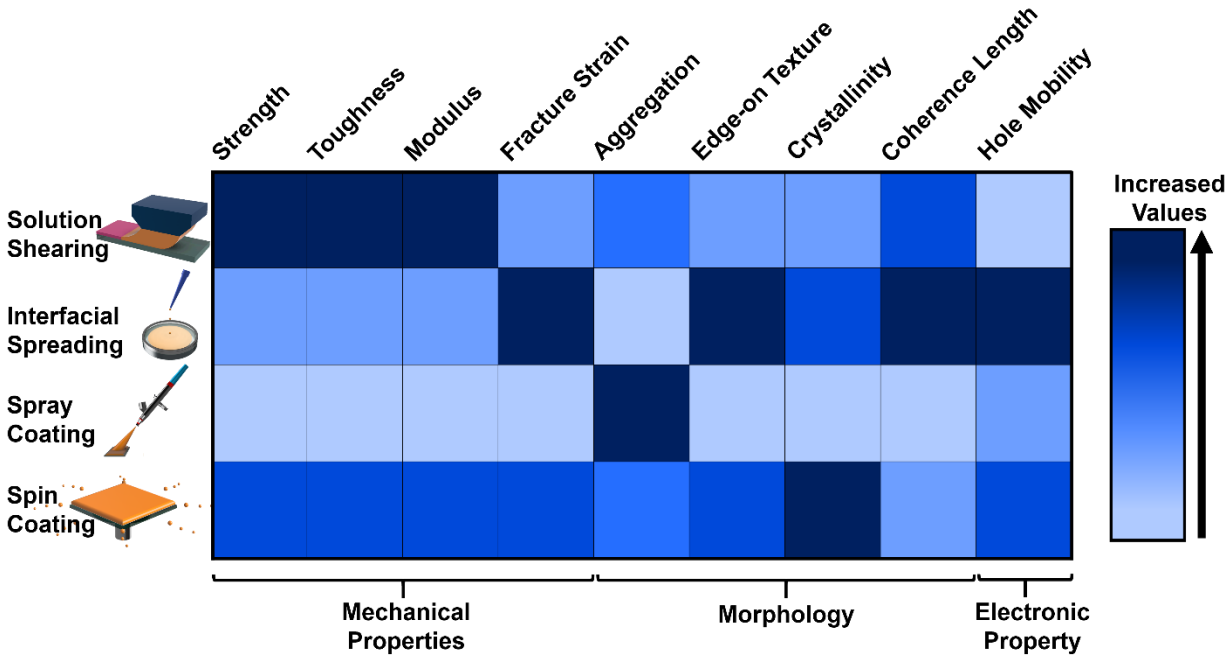

Figure 2.9. A summary of the findings from this work comparing P3HpT films deposited from four deposition processes.

One limitation of this study is that it used only one set of conditions for each deposition process. In reality, the parameters of each process could be tuned to allow a semi-infinite set of permutations. While

our experimental choices were born out of a desire to obtain a tractable data set (i.e., to characterize films of comparable thicknesses), such decisions have practical as well as scientific consequences. For example, our GIXD results revealed no correlation between parameters associated with the crystalline regions and the mechanical properties. It is, however, possible that the characteristics of the crystalline phases do indeed affect the mechanical response, but in ways that are counterbalanced by other characteristics considered in this paper—e.g., T_g, free volume, and surface topography. A second potential limitation of this study is the choice of polymer. Although polythiophenes are commonly used as models for other semiconducting polymers, interest in the last decade or so has shifted significantly to donor–acceptor (D–A) polymers.[7] There has been considerable interest in D–A polymers synthesized to have low glass transition temperatures by means of structural modification (e.g., conjugation break spacers, side chain modifications), blending with elastomers or non-conjugated polymers, or polymerization of block copolymers with non-conjugated segments.[6,15] However, most D–A polymers have high glass transition temperatures and greatly different chemical structures, and the same effects on crystalline morphology have yet to be compared using a high-T_g D–A polymer. Our initial results, however, do suggest that the effects of the deposition process on the mechanical responses of P3HpT and P3BT films are consistent. Considering the scarcity of process-property studies on the mechanical properties of semiconducting polymers, we believe that this study offers a good starting framework for future work in this research area.

2.6 Acknowledgements

This work was supported by the Air Force Office of Scientific Research (AFOSR) grant no. FA9550-19-1-0278. K.C. acknowledges additional support as a Hellman Scholar and an Intel Scholar provided through the Academic Enrichment Program (AEP) at UCSD through the following awards: The Undergraduate Research Scholarship and Semiconductor Research Corporation Scholarship. In addition, R.R. received support from the National Science Foundation Graduate Research Fellowship (NSF GRFP) under grant no. DGE-1144086. D.P.F. acknowledges financial support from the California Energy

Commission (EPC-19-004). A.L.A. acknowledges financial support from the National Science Foundation under grant no. 1848069. This work was performed in part at the San Diego Nanotechnology Infrastructure (SDNI) of UC San Diego, a member of the National Nanotechnology Coordinated Infrastructure, which is supported by the National Science Foundation (Grant ECCS-1542148). Use of the Stanford Synchrotron Radiation Light Source, SLAC National Accelerator Laboratory, is supported by the U.S. Department of Energy, Office of Science, and Office of Basic Energy Sciences under Contract DEAC02-76SF00515. The authors would also like to thank Julian Ramirez, Mickey Finn, and Guillermo Esparza for insightful discussions.

2.7 References

(1) Amb, C. M.; Dyer, A. L.; Reynolds, J. R. Navigating the Color Palette of Solution-Processable Electrochromic Polymers†. *Chem. Mater.* **2010**, *23* (3), 397–415. https://doi.org/10.1021/CM1021245.

(2) Inal, S.; Rivnay, J.; Suiu, A.-O.; Malliaras, G. G.; McCulloch, I. Conjugated Polymers in Bioelectronics. *Acc. Chem. Res.* **2018**, *51* (6), 1368–1376. https://doi.org/10.1021/ACS.ACCOUNTS.7B00624.

(3) Facchetti, A. π-Conjugated Polymers for Organic Electronics and Photovoltaic Cell Applications†. *Chem. Mater.* **2010**, *23* (3), 733–758. https://doi.org/10.1021/CM102419Z.

(4) Awartani, O.; Lemanski, B. I.; Ro, H. W.; Richter, L. J.; DeLongchamp, D. M.; O'Connor, B. T. Correlating Stiffness, Ductility, and Morphology of Polymer:Fullerene Films for Solar Cell Applications. *Adv. Energy Mater.* **2013**, *3* (3), 399–406. https://doi.org/10.1002/AENM.201200595.

(5) Zhang, S.; Ocheje, M. U.; Luo, S.; Ehlenberg, D.; Appleby, B.; Weller, D.; Zhou, D.; Rondeau-Gagné, S.; Gu, X. Probing the Viscoelastic Property of Pseudo Free-Standing Conjugated Polymeric Thin Films. *Macromol. Rapid Commun.* **2018**, *39* (14), 1800092. https://doi.org/10.1002/MARC.201800092.

(6) Chen, A. X.; Kleinschmidt, A. T.; Choudhary, K.; Lipomi, D. J. Beyond Stretchability: Strength, Toughness, and Elastic Range in Semiconducting Polymers. *Chem. Mater.* **2020**, *32* (18), 7582–7601. https://doi.org/10.1021/ACS.CHEMMATER.0C03019.

(7) Root, S. E.; Savagatrup, S.; Printz, A. D.; Rodriquez, D.; Lipomi, D. J. Mechanical Properties of Organic Semiconductors for Stretchable, Highly Flexible, and Mechanically Robust Electronics. *Chem. Rev.* **2017**, *117* (9), 6467–6499. https://doi.org/10.1021/ACS.CHEMREV.7B00003.

(8) Diao, Y.; Shaw, L.; Bao, Z.; Mannsfeld, S. C. B. Morphology Control Strategies for Solution-Processed Organic Semiconductor Thin Films. *Energy Environ. Sci.* **2014**, *7* (7), 2145–2159.

https://doi.org/10.1039/C4EE00688G.

(9) Fenner, R. T. Processing Properties of Polymers. *Princ. Polym. Process.* **1979**, 16–32. https://doi.org/10.1007/978-1-349-16234-5_3.

(10) Li, Y.; Sun, H.; Shi, Y.; Tsukagoshi, K. Patterning Technology for Solution-Processed Organic Crystal Field-Effect Transistors. *Sci. Technol. Adv. Mater.* **2014**, *15* (2). https://doi.org/10.1088/1468-6996/15/2/024203.

(11) Beaujuge, P. M.; Reynolds, J. R. Color Control in π-Conjugated Organic Polymers for Use in Electrochromic Devices. *Chem. Rev.* **2010**, *110* (1), 268–320. https://doi.org/10.1021/CR900129A.

(12) Søndergaard, R.; Hösel, M.; Angmo, D.; Larsen-Olsen, T. T.; Krebs, F. C. Roll-to-Roll Fabrication of Polymer Solar Cells. *Mater. Today* **2012**, *15* (1–2), 36–49. https://doi.org/10.1016/S1369-7021(12)70019-6.

(13) Whitesides, G. M. Physical-Organic Chemistry: A Swiss Army Knife. *Isr. J. Chem.* **2016**, *56* (1), 66–82. https://doi.org/10.1002/IJCH.201500061.

(14) Qian, Z.; Cao, Z.; Galuska, L.; Zhang, S.; Xu, J.; Gu, X. Glass Transition Phenomenon for Conjugated Polymers. *Macromol. Chem. Phys.* **2019**, *220* (11), 1900062. https://doi.org/10.1002/MACP.201900062.

(15) Higashihara, T. Strategic Design and Synthesis of π-Conjugated Polymers Suitable as Intrinsically Stretchable Semiconducting Materials. *Polym. J. 2021* **2021**, 1–11. https://doi.org/10.1038/s41428-021-00510-1.

(16) Balar, N.; Xiong, Y.; Ye, L.; Li, S.; Nevola, D.; Dougherty, D. B.; Hou, J.; Ade, H.; O'Connor, B. T. Role of Polymer Segregation on the Mechanical Behavior of All-Polymer Solar Cell Active Layers. *ACS Appl. Mater. Interfaces* **2017**, *9* (50), 43886–43892. https://doi.org/10.1021/ACSAMI.7B13719.

(17) Wang, Y.; Zhu, Q.; Naveed, H. B.; Zhao, H.; Zhou, K.; Ma, W. Sequential Blade-Coated Acceptor and Donor Enables Simultaneous Enhancement of Efficiency, Stability, and Mechanical Properties

for Organic Solar Cells. *Adv. Energy Mater.* **2020**, *10* (7), 1903609. https://doi.org/10.1002/AENM.201903609.

(18) Lin, B.; Zhang, L.; Zhao, H.; Xu, X.; Zhou, K.; Zhang, S.; Gou, L.; Fan, B.; Zhang, L.; Yan, H.; Gu, X. D.; Ying, L.; Huang, F.; Cao, Y.; Ma, W. Molecular Packing Control Enables Excellent Performance and Mechanical Property of Blade-Cast All-Polymer Solar Cells. *Nano Energy* **2019**, *59*, 277–284. https://doi.org/10.1016/J.NANOEN.2019.02.046.

(19) Spano, F. C.; Silva, C. H- and J-Aggregate Behavior in Polymeric Semiconductors. *Annu. Rev. Phys. Chem.* **2014**, *65*, 477–500. https://doi.org/10.1146/ANNUREV-PHYSCHEM-040513-103639.

(20) Root, S. E.; Jackson, N. E.; Savagatrup, S.; Arya, G.; Lipomi, D. J. Modelling the Morphology and Thermomechanical Behaviour of Low-Bandgap Conjugated Polymers and Bulk Heterojunction Films. *Energy Environ. Sci.* **2017**, *10* (2), 558–569. https://doi.org/10.1039/C6EE03456J.

(21) Helgesen, M.; Søndergaard, R.; Krebs, F. C. Advanced Materials and Processes for Polymer Solar Cell Devices. *J. Mater. Chem.* **2009**, *20* (1), 36–60. https://doi.org/10.1039/B913168J.

(22) Morita, T.; Singh, V.; Nagamatsu, S.; Oku, S.; Takashima, W.; Kaneto, K. Enhancement of Transport Characteristics in Poly(3-Hexylthiophene) Films Deposited with Floating Film Transfer Method. *Appl. Phys. Express* **2009**, *2* (11), 111502. https://doi.org/10.1143/APEX.2.111502.

(23) Choi, G.; Lee, K.; Oh, S.; Seo, J.; Kim, C.; An, T. K.; Lee, J.; Lee, H. S. Understanding Marangoni Flow-Driven Solidification of Polymer Semiconducting Films on an Aqueous Substrate. *J. Mater. Chem. C* **2020**, *8* (29), 10010–10020. https://doi.org/10.1039/D0TC02339F.

(24) Sung, Y.; Shin, E.-Y.; Noh, Y.-Y.; Lee, J.-Y. Flexible Bottom-Gated Organic Field-Effect Transistors Utilizing Stamped Polymer Layers from the Surface of Water. *ACS Appl. Mater. Interfaces* **2020**, *12* (22), 25092–25099. https://doi.org/10.1021/ACSAMI.0C03612.

(25) Esparza, G. L.; Lipomi, D. J. Solid-Phase Deposition: Conformal Coverage of Micron-Scale Relief Structures with Stretchable Semiconducting Polymers. *ACS Mater. Lett.* **2021**, 988–995.

https://doi.org/10.1021/ACSMATERIALSLETT.1C00213.

(26) Runser, R.; Root, S. E.; Ober, D. E.; Choudhary, K.; Chen, A. X.; Dhong, C.; Urbina, A. D.; Lipomi, D. J. Interfacial Drawing: Roll-to-Roll Coating of Semiconducting Polymer and Barrier Films onto Plastic Foils and Textiles. *Chem. Mater.* **2019**, *31* (21), 9078–9086. https://doi.org/10.1021/ACS.CHEMMATER.9B03343.

(27) Noh, J.; Jeong, S.; Lee, J.-Y. Ultrafast Formation of Air-Processable and High-Quality Polymer Films on an Aqueous Substrate. *Nat. Commun. 2016 71* **2016**, *7* (1), 1–9. https://doi.org/10.1038/ncomms12374.

(28) Pandey, M.; Sadakata, S.; Nagamatsu, S.; Pandey, S. S.; Hayase, S.; Takashima, W. Layer-by-Layer Coating of Oriented Conjugated Polymer Films towards Anisotropic Electronics. *Synth. Met.* **2017**, *227*, 29–36. https://doi.org/10.1016/J.SYNTHMET.2017.02.018.

(29) Nawaz, A.; Tavares, A. C. B.; Do, T. T.; Patil, B. B.; Sonar, P.; Hümmelgen, I. A. Experimental and Modeling Study of Low-Voltage Field-Effect Transistors Fabricated with Molecularly Aligned Copolymer Floating Films. *Flex. Print. Electron.* **2018**, *3* (1), 015006. https://doi.org/10.1088/2058-8585/AAA97B.

(30) Shaw, L.; Hayoz, P.; Diao, Y.; Reinspach, J. A.; To, J. W. F.; Toney, M. F.; Weitz, R. T.; Bao, Z. Direct Uniaxial Alignment of a Donor–Acceptor Semiconducting Polymer Using Single-Step Solution Shearing. *ACS Appl. Mater. Interfaces* **2016**, *8* (14), 9285–9296. https://doi.org/10.1021/ACSAMI.6B01607.

(31) Smilgies, D.-M.; Li, R.; Giri, G.; Chou, K. W.; Diao, Y.; Bao, Z.; Amassian, A. Look Fast: Crystallization of Conjugated Molecules during Solution Shearing Probed in-Situ and in Real Time by X-Ray Scattering. *Phys. status solidi – Rapid Res. Lett.* **2013**, *7* (3), 177–179. https://doi.org/10.1002/PSSR.201206507.

(32) Giri, G.; DeLongchamp, D. M.; Reinspach, J.; Fischer, D. A.; Richter, L. J.; Xu, J.; Benight, S.; Ayzner, A.; He, M.; Fang, L.; Xue, G.; Toney, M. F.; Bao, Z. Effect of Solution Shearing Method

on Packing and Disorder of Organic Semiconductor Polymers. *Chem. Mater.* **2015**, *27* (7), 2350–2359. https://doi.org/10.1021/CM503780U.

(33) Giri, G.; Verploegen, E.; Mannsfeld, S. C. B.; Atahan-Evrenk, S.; Kim, D. H.; Lee, S. Y.; Becerril, H. A.; Aspuru-Guzik, A.; Toney, M. F.; Bao, Z. Tuning Charge Transport in Solution-Sheared Organic Semiconductors Using Lattice Strain. *Nat. 2011 4807378* **2011**, *480* (7378), 504–508. https://doi.org/10.1038/nature10683.

(34) Al-Hussein, M.; Herzig, E. M.; Schindler, M.; Löhrer, F.; Palumbiny, C. M.; Wang, W.; Roth, S. V.; Müller-Buschbaum, P. Comparative Study of the Nanomorphology of Spray and Spin Coated PTB7 Polymer: Fullerene Films. *Polym. Eng. Sci.* **2016**, *56* (8), 889–894. https://doi.org/10.1002/PEN.24317.

(35) Noebels, M.; Cross, R. E.; Evans, D. A.; Finlayson, C. E. Characterization of Spray-Coating Methods for Conjugated Polymer Blend Thin Films. *J. Mater. Sci. 2014 4912* **2014**, *49* (12), 4279–4287. https://doi.org/10.1007/S10853-014-8123-5.

(36) Bielecka, U.; Lutsyk, P.; Janus, K.; Sworakowski, J.; Bartkowiak, W. Effect of Solution Aging on Morphology and Electrical Characteristics of Regioregular P3HT FETs Fabricated by Spin Coating and Spray Coating. *Org. Electron.* **2011**, *12* (11), 1768–1776. https://doi.org/10.1016/J.ORGEL.2011.06.027.

(37) Khim, D.; Baeg, K.-J.; Yu, B.-K.; Kang, S.-J.; Kang, M.; Chen, Z.; Facchetti, A.; Kim, D.-Y.; Noh, Y.-Y. Spray-Printed Organic Field-Effect Transistors and Complementary Inverters. *J. Mater. Chem. C* **2013**, *1* (7), 1500–1506. https://doi.org/10.1039/C2TC00085G.

(38) Scarratt, N. W.; Griffin, J.; Wang, T.; Zhang, Y.; Yi, H.; Iraqi, A.; Lidzey, D. G. Polymer-Based Solar Cells Having an Active Area of 1.6 Cm2 Fabricated via Spray Coating. *APL Mater.* **2015**, *3* (12), 126108. https://doi.org/10.1063/1.4937553.

(39) Savagatrup, S.; Printz, A. D.; Wu, H.; Rajan, K. M.; Sawyer, E. J.; Zaretski, A. V.; Bettinger, C. J.; Lipomi, D. J. Viability of Stretchable Poly(3-Heptylthiophene) (P3HpT) for Organic Solar

Cells and Field-Effect Transistors. *Synth. Met.* **2015**, *203*, 208–214. https://doi.org/10.1016/J.SYNTHMET.2015.02.031.

(40) Savikhin, V.; Jagadamma, L. K.; Purvis, L. J.; Robertson, I.; Oosterhout, S. D.; Douglas, C. J.; Samuel, I. D. W.; Toney, M. F. Morphological, Chemical, and Electronic Changes of the Conjugated Polymer PTB7 with Thermal Annealing. *iScience* **2018**, *2*, 182–192. https://doi.org/10.1016/J.ISCI.2018.03.002.

(41) Selivanova, M.; Zhang, S.; Billet, B.; Malik, A.; Prine, N.; Landry, E.; Gu, X.; Xiang, P.; Rondeau-Gagné, S. Branched Polyethylene as a Plasticizing Additive to Modulate the Mechanical Properties of π-Conjugated Polymers. *Macromolecules* **2019**, *52* (20), 7870–7877. https://doi.org/10.1021/ACS.MACROMOL.9B01697.

(42) Kim, J.-H.; Nizami, A.; Hwangbo, Y.; Jang, B.; Lee, H.-J.; Woo, C.-S.; Hyun, S.; Kim, T.-S. Tensile Testing of Ultra-Thin Films on Water Surface. *Nat. Commun. 2013 41* **2013**, *4* (1), 1–6. https://doi.org/10.1038/ncomms3520.

(43) Wang, S.; Fabiano, S.; Himmelberger, S.; Puzinas, S.; Crispin, X.; Salleo, A.; Berggren, M. Experimental Evidence That Short-Range Intermolecular Aggregation Is Sufficient for Efficient Charge Transport in Conjugated Polymers. *Proc. Natl. Acad. Sci.* **2015**, *112* (34), 10599–10604. https://doi.org/10.1073/PNAS.1501381112.

(44) Root, S. E.; Alkhadra, M. A.; Rodriquez, D.; Printz, A. D.; Lipomi, D. J. Measuring the Glass Transition Temperature of Conjugated Polymer Films with Ultraviolet–Visible Spectroscopy. *Chem. Mater.* **2017**, *29* (7), 2646–2654. https://doi.org/10.1021/ACS.CHEMMATER.7B00242.

(45) Xie, R.; Weisen, A. R.; Lee, Y.; Aplan, M. A.; Fenton, A. M.; Masucci, A. E.; Kempe, F.; Sommer, M.; Pester, C. W.; Colby, R. H.; Gomez, E. D. Glass Transition Temperature from the Chemical Structure of Conjugated Polymers. *Nat. Commun. 2020 111* **2020**, *11* (1), 1–8. https://doi.org/10.1038/s41467-020-14656-8.

(46) Ito, Y.; Virkar, A. A.; Mannsfeld, S.; Oh, J. H.; Toney, M.; Locklin, J.; Bao, Z. Crystalline

Ultrasmooth Self-Assembled Monolayers of Alkylsilanes for Organic Field-Effect Transistors. *J. Am. Chem. Soc.* **2009**, *131* (26), 9396–9404. https://doi.org/10.1021/JA9029957.

(47) Wei, Q.; Miyanishi, S.; Tajima, K.; Hashimoto, K. Enhanced Charge Transport in Polymer Thin-Film Transistors Prepared by Contact Film Transfer Method. *ACS Appl. Mater. Interfaces* **2009**, *1* (11), 2660–2666. https://doi.org/10.1021/AM9005572.

(48) Lee, J.-H.; Chung, J. Y.; Stafford, C. M. Effect of Confinement on Stiffness and Fracture of Thin Amorphous Polymer Films. *ACS Macro Lett.* **2011**, *1* (1), 122–126. https://doi.org/10.1021/MZ200090A.

(49) Moulton, J.; Smith, P. Electrical and Mechanical Properties of Oriented Poly(3-Alkylthiophenes): 2. Effect of Side-Chain Length. *Polymer (Guildf).* **1992**, *33* (11), 2340–2347. https://doi.org/10.1016/0032-3861(92)90525-2.

(50) Pandey, M.; Kumari, N.; Nagamatsu, S.; Pandey, S. S. Recent Advances in the Orientation of Conjugated Polymers for Organic Field-Effect Transistors. *J. Mater. Chem. C* **2019**, *7* (43), 13323–13351. https://doi.org/10.1039/C9TC04397G.

(51) Yang, Y.; Liu, Z.; Chen, J.; Cai, Z.; Wang, Z.; Chen, W.; Zhang, G.; Zhang, X.; Chi, L.; Zhang, D. A Facile Approach to Improve Interchain Packing Order and Charge Mobilities by Self-Assembly of Conjugated Polymers on Water. *Adv. Sci.* **2018**, *5* (11), 1801497. https://doi.org/10.1002/ADVS.201801497.

(52) O'Connor, B.; Chan, E. P.; Chan, C.; Conrad, B. R.; Richter, L. J.; Kline, R. J.; Heeney, M.; McCulloch, I.; Soles, C. L.; DeLongchamp, D. M. Correlations between Mechanical and Electrical Properties of Polythiophenes. *ACS Nano* **2010**, *4* (12), 7538–7544. https://doi.org/10.1021/NN1018768.

(53) Printz, A. D.; Lipomi, D. J. Competition between Deformability and Charge Transport in Semiconducting Polymers for Flexible and Stretchable Electronics. *Appl. Phys. Rev.* **2016**, *3* (2), 021302. https://doi.org/10.1063/1.4947428.

(54) Zheng, Y.; Wang, G.-J. N.; Kang, J.; Nikolka, M.; Wu, H.-C.; Tran, H.; Zhang, S.; Yan, H.; Chen, H.; Yuen, P. Y.; Mun, J.; Dauskardt, R. H.; McCulloch, I.; Tok, J. B.-H.; Gu, X.; Bao, Z. An Intrinsically Stretchable High-Performance Polymer Semiconductor with Low Crystallinity. *Adv. Funct. Mater.* **2019**, *29* (46), 1905340. https://doi.org/10.1002/ADFM.201905340.

(55) Ding, Z.; Liu, D.; Zhao, K.; Han, Y. Optimizing Morphology to Trade Off Charge Transport and Mechanical Properties of Stretchable Conjugated Polymer Films. *Macromolecules* **2021**, *54* (9), 3907–3926. https://doi.org/10.1021/ACS.MACROMOL.1C00268.

(56) Pandey, M.; Gowda, A.; Nagamatsu, S.; Kumar, S.; Takashima, W.; Hayase, S.; Pandey, S. S. Rapid Formation and Macroscopic Self-Assembly of Liquid-Crystalline, High-Mobility, Semiconducting Thienothiophene. *Adv. Mater. Interfaces* **2018**, *5* (6), 1700875. https://doi.org/10.1002/ADMI.201700875.

(57) Osaka, I.; Takimiya, K. Backbone Orientation in Semiconducting Polymers. *Polymer (Guildf).* **2015**, *59*, A1–A15. https://doi.org/10.1016/J.POLYMER.2014.12.066.

(58) Hao X.T., Hosokai T., Mitsuo N., Okudaira N.N., Mase K., Ueno N. Control of the Interchain Π–π Interaction and Electron Density Distribution at the Surface of Conjugated Poly(3-Hexylthiophene) Thin Films. *J. Phys. Chem. B* **2007**, *111* (35), 10365–10372. https://doi.org/10.1021/JP0732209.

(59) Rivnay, J.; Mannsfeld, S. C. B.; Miller, C. E.; Salleo, A.; Toney, M. F. Quantitative Determination of Organic Semiconductor Microstructure from the Molecular to Device Scale. *Chem. Rev.* **2012**, *112* (10), 5488–5519. https://doi.org/10.1021/CR3001109.

(60) Kim, Y.-J.; Jung, H.-T.; Ahn, C. W.; Jeon, H.-J. Simultaneously Induced Self-Assembly of Poly(3-Hexylthiophene) (P3HT) Nanowires and Thin-Film Fabrication via Solution-Floating Method on a Water Substrate. *Adv. Mater. Interfaces* **2017**, *4* (19), 1700342. https://doi.org/10.1002/ADMI.201700342.

(61) Gargi, D.; Kline, R. J.; DeLongchamp, D. M.; Fischer, D. A.; Toney, M. F.; O'Connor, B. T.

Charge Transport in Highly Face-On Poly(3-Hexylthiophene) Films. *J. Phys. Chem. C* **2013**, *117* (34), 17421–17428. https://doi.org/10.1021/JP4050644.

(62) Rivnay, J.; Toney, M. F.; Zheng, Y.; Kauvar, I. V.; Chen, Z.; Wagner, V.; Facchetti, A.; Salleo, A. Unconventional Face-On Texture and Exceptional In-Plane Order of a High Mobility n-Type Polymer. *Adv. Mater.* **2010**, *22* (39), 4359–4363. https://doi.org/10.1002/ADMA.201001202.

(63) Schuettfort, T.; Thomsen, L.; McNeill, C. R. Observation of a Distinct Surface Molecular Orientation in Films of a High Mobility Conjugated Polymer. *J. Am. Chem. Soc.* **2013**, *135* (3), 1092–1101. https://doi.org/10.1021/JA310240Q.

(64) Kim, G.; Kang, S.-J.; Dutta, G. K.; Han, Y.-K.; Shin, T. J.; Noh, Y.-Y.; Yang, C. A Thienoisoindigo-Naphthalene Polymer with Ultrahigh Mobility of 14.4 Cm2/V·s That Substantially Exceeds Benchmark Values for Amorphous Silicon Semiconductors. *J. Am. Chem. Soc.* **2014**, *136* (26), 9477–9483. https://doi.org/10.1021/JA504537V.

(65) Li, Y.; Tatum, W. K.; Onorato, J. W.; Zhang, Y.; Luscombe, C. K. Low Elastic Modulus and High Charge Mobility of Low-Crystallinity Indacenodithiophene-Based Semiconducting Polymers for Potential Applications in Stretchable Electronics. *Macromolecules* **2018**, *51* (16), 6352–6358. https://doi.org/10.1021/ACS.MACROMOL.8B00898.

(66) Postema, A. R.; Liou, K.; Wudl, F.; Smith, P. Highly Oriented Low-Modulus Materials from Liquid-Crystalline Polymers: The Ultimate Penalty for Solubilizing Alkyl Side Chains. *Macromolecules* **2002**, *23* (6), 1842–1845. https://doi.org/10.1021/MA00208A048.

(67) Sommerville, P. J. W.; Li, Y.; Dong, B. X.; Zhang, Y.; Onorato, J. W.; Tatum, W. K.; Balzer, A. H.; Stingelin, N.; Patel, S. N.; Nealey, P. F.; Luscombe, C. K. Elucidating the Influence of Side-Chain Circular Distribution on the Crack Onset Strain and Hole Mobility of Near-Amorphous Indacenodithiophene Copolymers. *Macromolecules* **2020**, *53* (17), 7511–7518. https://doi.org/10.1021/ACS.MACROMOL.0C00512.

(68) O'Connor, B.; Kline, R. J.; Conrad, B. R.; Richter, L. J.; Gundlach, D.; Toney, M. F.;

DeLongchamp, D. M. Anisotropic Structure and Charge Transport in Highly Strain-Aligned Regioregular Poly(3-Hexylthiophene). *Adv. Funct. Mater.* **2011**, *21* (19), 3697–3705. https://doi.org/10.1002/ADFM.201100904.

(69) Zhang, S.; Alesadi, A.; Mason, G. T.; Chen, K.-L.; Freychet, G.; Galuska, L.; Cheng, Y.-H.; Onge, P. B. J. St.; Ocheje, M. U.; Ma, G.; Qian, Z.; Dhakal, S.; Ahmad, Z.; Wang, C.; Chiu, Y.-C.; Rondeau-Gagné, S.; Xia, W.; Gu, X. Molecular Origin of Strain-Induced Chain Alignment in PDPP-Based Semiconducting Polymeric Thin Films. *Adv. Funct. Mater.* **2021**, *31* (21), 2100161. https://doi.org/10.1002/ADFM.202100161.

(70) Kim, J.-S.; Kim, J.-H.; Lee, W.; Yu, H.; Kim, H. J.; Song, I.; Shin, M.; Oh, J. H.; Jeong, U.; Kim, T.-S.; Kim, B. J. Tuning Mechanical and Optoelectrical Properties of Poly(3-Hexylthiophene) through Systematic Regioregularity Control. *Macromolecules* **2015**, *48* (13), 4339–4346. https://doi.org/10.1021/ACS.MACROMOL.5B00524.

Chapter 3. Increasing the Strength, Hardness, and Survivability of Semiconducting Polymers by Crosslinking

3.1 Introduction

π-Conjugated polymers exhibit the electronic functionality of conductors and semiconductors. Ideally, they would also have the mechanical robustness of engineering plastics, as the mechanical properties of semiconducting polymers are a crucial determinant for device applications. However, the majority of research on the mechanical properties of semiconducting polymers has been focused on increasing the parameters associated with "softness"—i.e., low modulus and high fracture strain.[1] This focus has been primarily driven by an interest in stretchable devices, such as flexible thin-film transistors, solar cells, and sensors. The emphasis on increasing the softness is incompatible with a number of compelling applications for semiconducting polymers, in which strength and hardness are desirable. For example, thin-film solar cells integrated with rooftops, roads, sidewalks, parking lots, and vehicle and aeronautic surfaces; heads-up displays in eyeglasses, windshields, and cockpits; and integration with textiles, especially in physically demanding contexts (military, rescue, and medical workers). Here, we examine the use of a four-armed azide-containing crosslinker as a means of increasing the hardness, strength, and cohesive energy of a library of conjugated polymers. This material, the previously reported "4Bx,"[2] works by crosslinking the aliphatic side chains of the polymer. From this library, we select three which are promising for organic bulk heterojunction solar cells. By measuring the performance of these devices, we determine that it should be possible to increase the robustness of previously reported and commercially available materials.

There are many approaches to modulating the mechanical properties of solid films of conjugated polymers. These approaches range from physical blending[3–12] to chemical modification and re-engineering of the backbone and side chains.[1,4,6,13–15] One approach, which is well known in polymer engineering yet less explored in the field of conjugated polymers, is crosslinking. In their pioneering work, Kim et al. showed that a four-armed perfluorophenyl azide crosslinker (4Bx) could be used to crosslink a

diketopyrrolopyrrole (DPP)-based polymer (by enabling solvent orthogonality) to fabricate arrays of all-photopatterned organic transistors.[2] Moreover, the authors showed that low loadings (1 wt%) of 4Bx could increase the strength, toughness, and fracture strain of a crosslinked DPP polymer film without decreasing the charge-carrier mobility. Likewise, work by Zheng et al. showed that crosslinking can yield films with high intrinsic elasticity. Stretchable semiconducting matrices were formed by crosslinking diketopyrrolopyrrole-based or indacenodithiophene-based polymers (i.e., IDTBT) using a perfluorophenyl azide end-capped polybutadiene crosslinker.[16] By crosslinking IDTBT in a rubber matrix, Zheng et al. were able to produce ultrathin films with an intrinsic elasticity of 70%, which could maintain hole mobilities of 1 $cm^2\ V^{-1}s^{-1}$ after 1000 cycles of stretching to 50% strain.

Likewise, the Anthopoulos group has shown that the chemical structure of the crosslinker plays an important role in determining the mechanical properties.[17] For example, Dauzon et al. crosslinked fullerene acceptors in P3HT:PCBM bulk heterojunctions using three bisazide crosslinkers: 1,12-diazidododecane ($C_{12}N_3$), 1,11-diazido-3,6,9-trioxaundecane (PEG_3N_3), and poly(ethylene glycol) bisazide (PEG_NN_3).[17] Increasing the crosslinker loading and increasing the carbon chain length of the crosslinker both resulted in a decrease in the elastic modulus. Encouragingly, the authors also showed that small loadings of crosslinker (5 wt%) could be incorporated in a P3HT:PCBM solar cell without reducing the power conversion efficiency (PCE). Similarly, work from the Shao group showed that 2,6-bis(4-azidobenzylidene)cyclohexanone (BAC) could be used to crosslink PM6, a benzodithiophene-based low-bandgap polymer.[18] Increasing the BAC loading in crosslinked PM6 films resulted in a continuous increase in the mechanical robustness (e.g., fracture strain, tensile strength, and toughness). At 10 wt% BAC, the crosslinked PM6 film showed a significant increase in the plastic regime, resulting in an increased fracture strain (5% vs 20%), tensile strength (30 MPa vs 50 MPa), and toughness (~0.5 MJ m^{-3} vs 8 MJ m^{-3}) compared to a non-crosslinked PM6 film. Thus, the crosslinker structure and loading are significant determinants of both the mechanical and electronic properties of the active layer in an organic solar cell (OSC).

In addition to increasing the mechanical robustness, crosslinking may also stabilize the morphology of a bulk heterojunction solar cell and increase the lifespan of the device. A significant body of this literature focuses on crosslinking polymer-fullerene blends using a variety of strategies, as have been discussed by Rumer and McCulloch.[19] In most of this work, the crosslinking process is non-selective (e.g., can occur between polymer/polymer, polymer/fullerene, and fullerene/fullerene).[20] While increased lifespan and thermal stability of crosslinked devices often comes at the cost of a lower initial PCE,[19] this tradeoff is not guaranteed.[20–23] For example, Hong et al. has shown that crosslinking a fullerene derivative (PCBSD) in a tertiary bulk heterojunction with a benzodithiophene-based donor and a fused-ring electron acceptor (PBDBTF:Y6:*c*-PCBSD) can increase the PCE from 15.1 to 16.1% while improving device stability.[21] In spite of the foundational work on polymer-fullerene devices, there is significant interest in both all-polymer[24–26] blends and non-fullerene acceptors.[27–30] Some of this arises from the presumed superior mechanical reliability of all-polymer blends[1,31,32] and the high PCEs enabled by non-fullerene acceptors.[33,34] In three studies,[35–37] authors showed that crosslinked bulk heterojunction films containing D–A polymers outperformed their non-crosslinked counterparts in both PCE and device stability.

In this work, we used 4Bx as a crosslinker for a library of 11 semiconducting polymers (spanning a wide range of chemical structures) as a means of increasing the mechanical robustness. The azide moiety of 4Bx undergoes C–H insertion in the presence of heat or UV light,[2,38] thus rendering this crosslinking strategy universal for all polymers with aliphatic side chains. A subset of the polymers tested were selected for use in two all-polymer bulk heterojunction solar cells. Both blends incorporate a poly(naphthalene diimide) derivative (N2200) as the acceptor polymer and a benzodithiophene (BDT)-derivative as a donor polymer (J51, PTB7-Th). In doing so, we elucidate how crosslinking modulates the mechanical properties of semiconducting polymer films, as well as how crosslinking affects the mechanical and electronic properties of all-polymer bulk heterojunctions for OSC applications.

3.2 Experimental Design

Selection of Materials. For this study, we investigated the effect of crosslinking on a library of eleven semiconducting polymers: DPP-C3,[39] DPP-C9,[39] PTB7, PTB7-Th, J51, P3HpT, TQ1, IDTBT,[40,41] 2DPP-2CNTVT,[42] N2200, and PZ1.[43] For solar cells, we selected two donor polymers (PTB7-Th, J51) and one acceptor polymer (N2200) comprising two different bulk heterojunctions, J51:N2200 and PTB7-Th:N2200. The two selected polymer blends have similar benzodithiophene (BDT)-based donor polymers that pair with N2200 as the acceptor. These polymer blends were selected because recipes for such devices were well-documented in existing literature.[44,45] Likewise, the ratios of donor to acceptor polymer for J51:N2200 (1:2)[44] and PTB7-Th:N2200 (2:1)[45] were chosen from existing literature. Similarly, recipes with different ratios were chosen to elucidate how the composition of the bulk heterojunction (e.g., whether it contained more p-type or n-type material) would change the effect of crosslinking. As the crosslinker, we used (2,2-bis(((4-azido2,3,5,6-tetrafluorobenzoyl)oxy)methyl)propane-1,3-diyl bis(4-azido-2,3,5,6-tetrafluorobenzoate) (4Bx), which is reactive toward the aliphatic side chains of nearly all conjugated polymers. Previous work suggested that 4Bx could be used to crosslink isolated polymers at low loadings with no loss in mobility.[2] We reasoned that 4Bx could possibly be applied to crosslink bulk heterojunctions (i.e., polymer blends) without severe inhibition of the photovoltaic properties.

Mechanical Testing. To determine the tensile behavior the films, we used a pseudo free-standing tensile testing method (i.e., film-on-water, FOW).[1,46] The compressive properties (e.g., modulus, hardness) of crosslinked and non-crosslinked polymer films were measured from nanoindentation[47–55] using the Oliver-Pharr method[56] (with an approximation of the Poisson ratio[57]). Finally, a cohesive fracture test was done using a double cantilever beam (DCB) setup[58] in order to determine the energy required to propagate a crack along that interface (G_C). Following fracture, X-ray photoelectron spectroscopy (XPS) was used to determine the interface at which the device stack fractured.

Solar Cells. We fabricated solar cells in order to directly probe physical changes within the bulk heterojunction. In these bulk heterojunction films, we added 1,8-diiodooctane (DIO), which is commonly used to make the morphology of the solid film more amenable to charge separation and transport. Residual DIO in the bulk heterojunction acts as a photoacid that is harmful to the photovoltaic properties,[59,60] and was removed by annealing at an elevated temperature (175 °C for 1 h). Instead of using top contacts based on evaporated metal, we elected to use eutectic gallium indium (EGaIn).[61] The use of removable drops of liquid EGaIn, while not practical for large-area devices, made it possible to measure the properties of underlying conjugated polymer films before and after photovoltaic measurements (e.g., without degradation at a polymer-metal interface for devices with evaporated contacts). We made this decision fully aware that performance metrics of the resulting "devices" would be lower than they would be with evaporated contacts.

Degradation Testing. Several degradation tests were performed to understand how crosslinking with 4Bx affects the physical performance of J51:N2200 and PTB7-Th:N2200 blends. Accelerated degradation tests were conducted by 1) annealing solar cells at 60 °C and 2) ageing solar cells in a 50 °C, 50% relative humidity chamber. Likewise, we evaluated the solvent resistance of the crosslinked active layer by immersion of solar cells in chloroform. Finally, the abrasion resistance was evaluated two ways. First, a bath sonicator was used to physically abrade polymer films using high frequency sound waves in water. Second, the scouring (rougher) surface of a dish sponge was used to abrade the bulk heterojunction films when incorporated in photovoltaic devices.

Morphological Characterization. Fourier-transform infrared (FTIR) spectroscopy was used to qualitatively observe the crosslinking of 4Bx in conjugated polymer films. Crosslinking was verified by reduction of the azide peak (2160-2120 cm^{-1}) using FTIR (**Figure C1**). Ultraviolet-visible (UV-vis) spectroscopy was used to determine 1) the change in thickness in polymer films during sonication abrasion tests and 2) the change in aggregation[62] (e.g., short-range order) in crosslinked and non-crosslinked poly(3-heptylthiophene)

(P3HpT) films (**Figure C2**). P3HpT is used as a proxy polymer because the aggregation behavior of poly(3-alkylthiophene)s has been extensively studied by Spano and coworkers.[62,63]

3.3 Results and Discussion

The library of polymers investigated in this work differed greatly in chemical structure (**Figure 3.1**) and morphology, both of which can possibly affect the crosslinking (and thus mechanical properties) of the solid film. Particular attention was given to diketopyrrolopyrrole (DPP)-based (e.g., DPP-C3, DPP-C9, and 2DPP-2CNTVT) and benzodithiophene (BDT)-based polymers (e.g., PTB7, PTB7-Th, J51), which are motifs common to the design and synthesis of semiconducting polymers used for both solar cells and transistors. Within each family, these polymers differ primarily in terms of backbone structure, electronegativity of donor-acceptor moieties, and backbone rigidity. Most polymers used are semi-crystalline (e.g., DPP-based and BDT-based materials), apart from the inclusion of IDTBT and TQ1, which are primarily amorphous (e.g., with low crystallinity). Detailed studies elucidating the morphology of each polymer can be found elsewhere.[39,42,70–72,43,45,64–69]

For all 11 polymers, the addition of 1 wt% 4Bx as a crosslinker resulted in an increase in the ultimate tensile strength, toughness, and resilience of the solid film, as determined by tensile testing of pseudo free-standing films (**Figure 3.2a, 3.2b, 3.2e**). In most cases, crosslinking also resulted in a similar or greater fracture strain and linear elasticity compared to the non-crosslinked film (**Figure 3.2c, 3.2f**). These findings are consistent with previous results in which the tensile properties of a DPP-based polymer were studied,[2] and can generally be attributed to the greater amounts of energy dissipation allowed by the crosslinks formed at the optimal 1 wt% loading. However, the elastic modulus between crosslinked and non-crosslinked conjugated polymers remained similar (**Figure 3.2d**). One of the most significant differences was between the tensile behavior of the non-crosslinked and crosslinked DPP-C3 and DPP-C9 films. With the lowest molecular weight (M_n ~ 9.4 kDa, **Appendix C.3**), non-crosslinked DPP-C3 was extremely brittle with a low tensile strength, toughness, and fracture strain. Crosslinking with 4Bx greatly

increased the values of these properties (along with the resilience and linear elasticity), likely due to an increase in the effective degree of polymerization and entanglement density. The same was true for DPP-C9, which had the second lowest molecular weight (M_n ~ 13.9 kDa, **Appendix C.3**). In contrast, crosslinking PTB7 (the second highest molecular weight polymer studied, with an M_n ~ 83 kDa, **Appendix C.3**) resulted primarily in an increase in the fracture strain. Coupled with the small increase in tensile strength, this increase in the extensibility resulted in a significant increase in the toughness of the crosslinked film. Interestingly, crosslinked PTB7-Th films showed only a small increase in the overall mechanical robustness (i.e., tensile strength, toughness, and fracture strain), but resulted in a significantly greater resilience due to the increased range of linear elasticity. Thus, the manner in which crosslinking with 4Bx affects the tensile properties of a semiconducting polymer film is also dependent on chemical structure and molecular characteristics (e.g., degree of polymerization, density of entanglements).

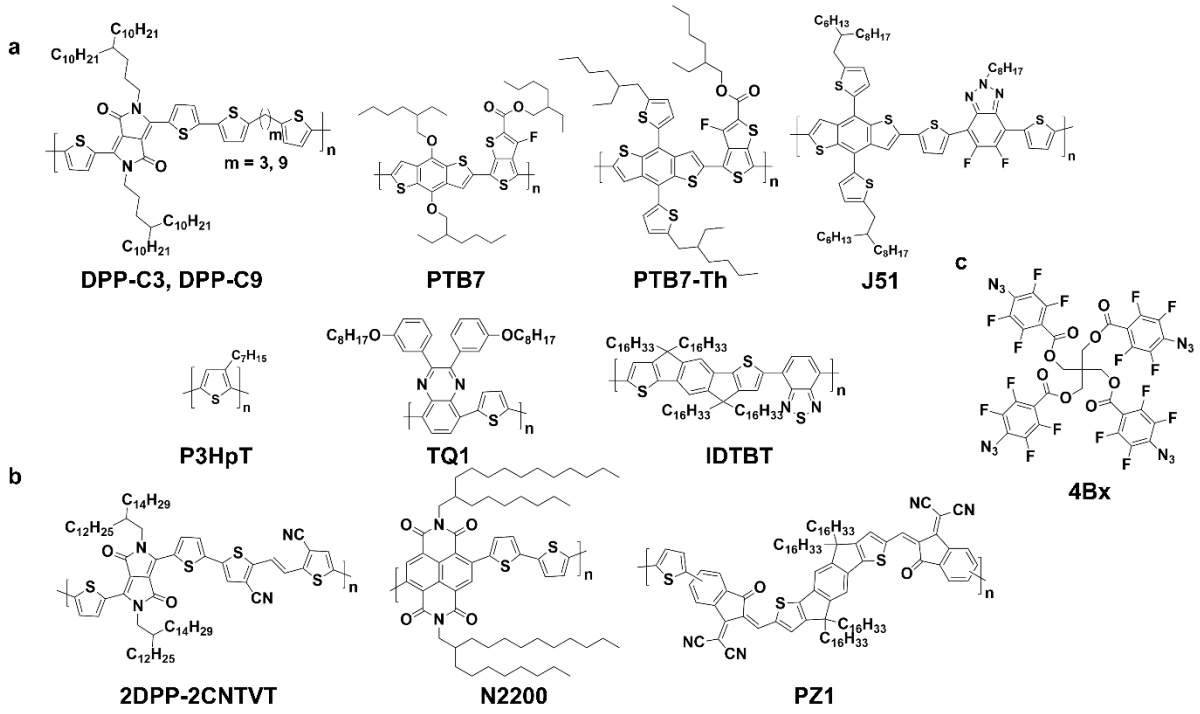

Figure 3.1. The (**a**) p-type and (**b**) n-type semiconducting polymers and (**c**) crosslinker ("4Bx") used in this study.

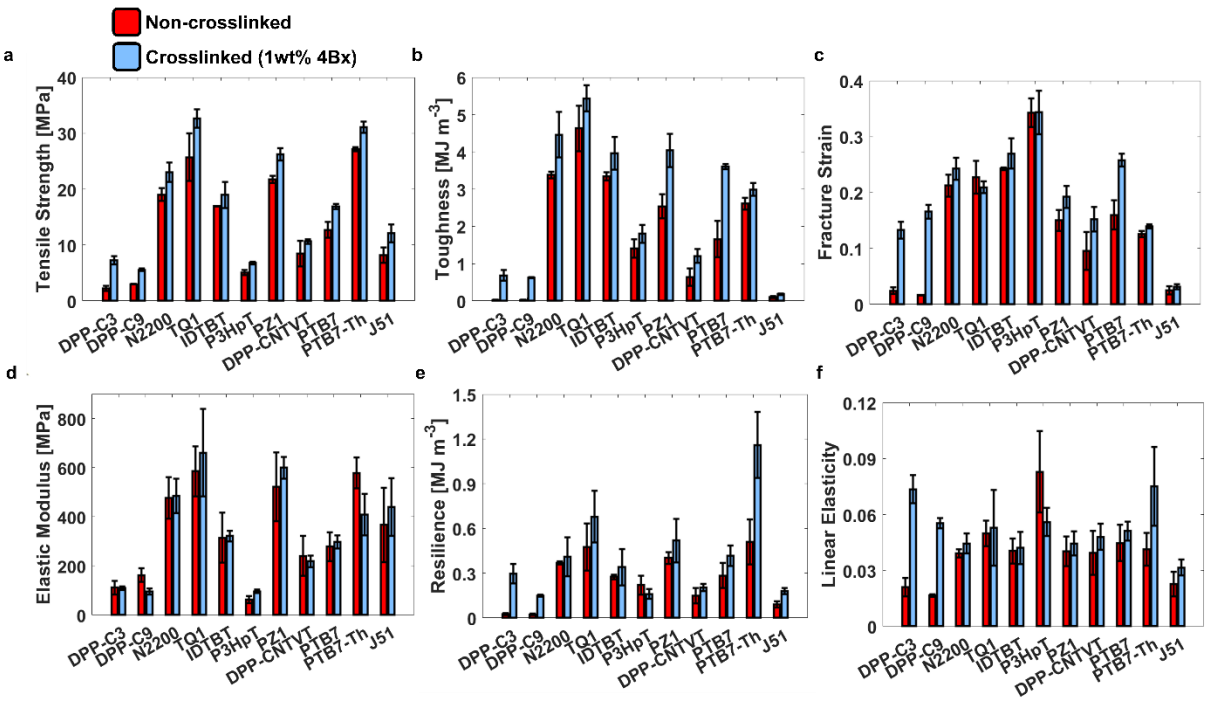

Figure 3.2. Mechanical properties of interest were extracted from stress-strain curves produced by tensile tests of 11 semiconducting polymers. Differences between non-crosslinked (red) polymers and polymers crosslinked with 1 wt% 4Bx (blue) are shown for (**a**) tensile strength, (**b**) toughness, (**c**) fracture strain, (**d**) elastic modulus, (**e**) resilience, and (**f**) linear elasticity.

From this library, we selected three polymers common in the field of organic photovoltaics to incorporate in the bulk heterojunction of OSCs. Devices were fabricated with two different blends: J51:N2200 (1:2)[42] and PTB7-Th:N2200 (2:1).[45] To elucidate how crosslinking affects the mechanical properties of each blend, film-on-water (FOW) tensile tests were conducted on J51:N2200 and PTB7-Th:N2200 films with varied 4Bx loadings (**Figure 3.3**). We observed somewhat different effects of crosslinking for the two different blends. For J51:N2200, as the 4Bx loading increased from 0 wt% to 1 wt%, the strength, modulus, toughness, and fracture strain all increased. A further increase in 4Bx loading to 2 wt% slightly embrittled the film and decreased the fracture strain, but the strength of the film was increased further. However, at 2 wt%, the crosslinked film showed greater tensile strength at the expense of the fracture strain (0.086), which was less than that of the non-crosslinked film (0.12). Therefore, for J51:N2200, our findings suggest that 1 wt% 4Bx can be incorporated to optimize the fracture strain while

increasing the strength and toughness. In contrast, there was a clear mechanical tradeoff for PTB7-Th:N2200 relative to increasing crosslinker loading. Increasing the loading of 4Bx generally resulted in increased strength but decreased fracture strain.

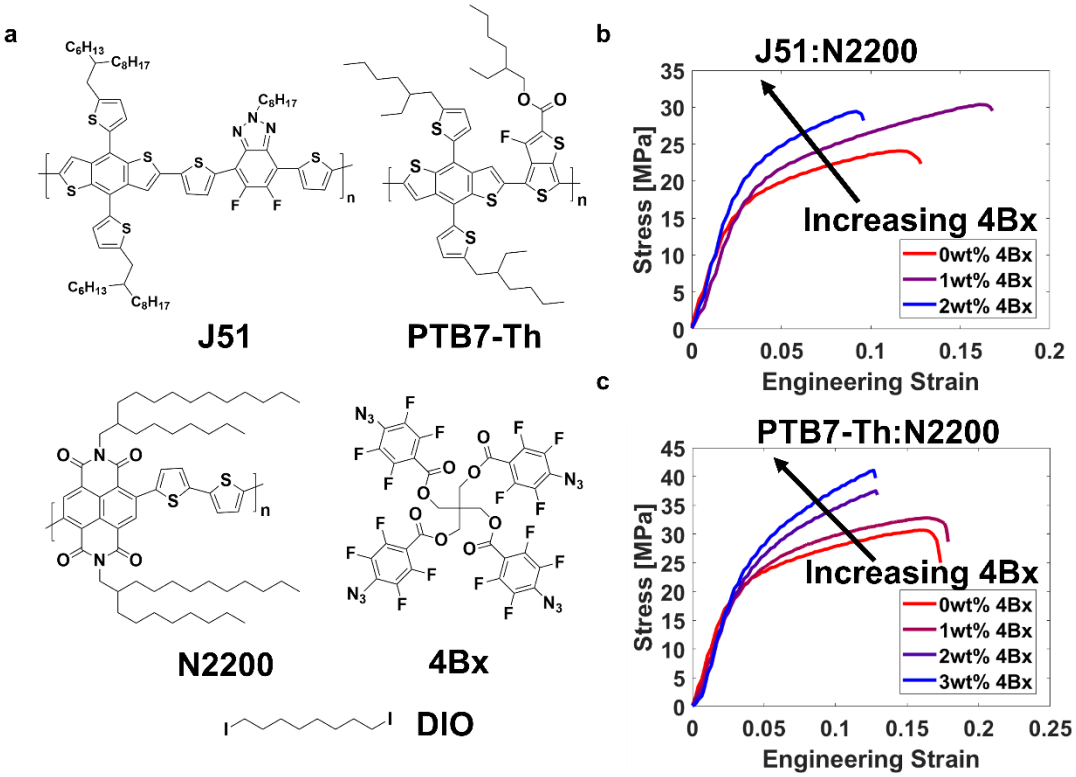

Figure 3.3. (**a**) Chemical structures of J51, PTB7-Th, N2200, 4Bx, and DIO. J51 and PTB7-Th are used as the donor polymers in a bulk heterojunction with N2200, an acceptor polymer. DIO is added as a small molecule additive to improve the morphology for each bulk heterojunction. 4Bx is added to each bulk heterojunction as a crosslinker. Pseudo-free standing tensile tests are conducted on (**b**) 12 mg mL^{-1} (1:2) J51:N2200 (3 vol% DIO) and (**c**) 12 mg mL^{-1} (2:1) PTB7-Th:N2200 (2 vol% DIO) thin films to measure the tensile response. Films are annealed at 175 °C for 60 minutes in order to initiate crosslinking and remove residual DIO. Representative stress-strain curves are shown in (**b**) and (**c**).

The two types of blends differ in two aspects: the chemical structure of the donor polymer, and the ratio of donor to acceptor polymer (derived from the literature for giving the optimized device performance[44,45]). The extracted tensile properties for all polymers and polymer blends are shown in **Table C1**. For all three neat polymers (**Figure C3**), crosslinking with 1 wt% 4Bx resulted in an increase in the fracture strain and tensile strength (though J51 failed by brittle fracture while PTB7-Th and N2200 failed by ductile fracture). Additionally, crosslinked films of J51 were stiffer (i.e., a greater elastic modulus) than

their non-crosslinked counterparts. In PTB7-Th and N2200, crosslinking primarily resulted in a drawn-out plastic regime prior to fracture, and a corresponding increase in toughness. In the elastic regime, both PTB7-Th and N2200 also showed similar behaviors. Crosslinking with 4Bx resulted in an extension of the elastic regime (i.e., linear elasticity, resilience, and yield stress) of the film with little difference in modulus.

In the J51:N2200 bulk heterojunction, one significant observation is the ductile behavior, despite the apparent brittleness of J51 on its own. This plastic behavior is likely due to the relatively high loading of N2200 (1:2 ratio) in the polymer blend (as well as an increased density of entanglements from the blending of two polymers[73–75]). Similar to the isolated ductile polymers, crosslinking J51:N2200 with 1 wt% 4Bx generally resulted in the same changes to the plastic regime: greater fracture strain, greater tensile strength, and greater toughness. The modulus remained similar to the non-crosslinked film, but increased when the 4Bx loading was increased to 2 wt%. Interestingly, the PTB7-Th:N2200 blend with 1 wt% 4Bx showed similar tensile behavior to the J51:N2200 counterpart. Further addition of 4Bx (up to 3 wt%) resulted in a monotonic increase in both the tensile strength and the modulus of the polymer film. Notably, in both J51:N2200 and PTB7-Th:N2200, the tensile strength of the crosslinked blend was greater than that of any isolated polymer. Again, this effect can likely be attributed to the greater entanglement density within a polymer blend.[73–75]

To elucidate how crosslinking affects the photovoltaic properties of the two bulk heterojunctions, we fabricated solar cells with the architecture shown in **Figure 3.4**. For both J51:N2200 and PTB7-Th:N2200 devices, we find that an increase in 4Bx loading generally corresponded to lower J_{sc} and FF, which resulted in a lower PCE. This change in photovoltaic behavior was due to an increase in series resistance. Likewise, the addition of 4Bx also resulted in an increased V_{oc}, although this was not sufficient to offset the PCE lost in either bulk heterojunction. Additionally, crosslinked PTB7-Th:N2200 devices without DIO showed a greater decrease in electronic performance when compared to devices containing DIO, largely due to a greater decrease in FF (**Figure C4**). This comparison suggests that the increased V_{oc} is possibly due to changes in the chemical composition of the bulk heterojunction with the addition of both

DIO and 4Bx. It is possible that small amounts of DIO remained crosslinked in the bulk heterojunction without being removed. These results validate prior studies suggesting that incorporation of an azide-mediated crosslinker into the bulk heterojunction of an organic solar cell can result in a decreased initial PCE.[19] UV-vis of a proxy polymer, poly(3-heptylthiophene) (P3HpT), suggested that crosslinking with 4Bx decreases the short-range order (i.e., aggregation) of the polymer film, which possibly contributes to the decreased electronic performance (**Figure C2**).

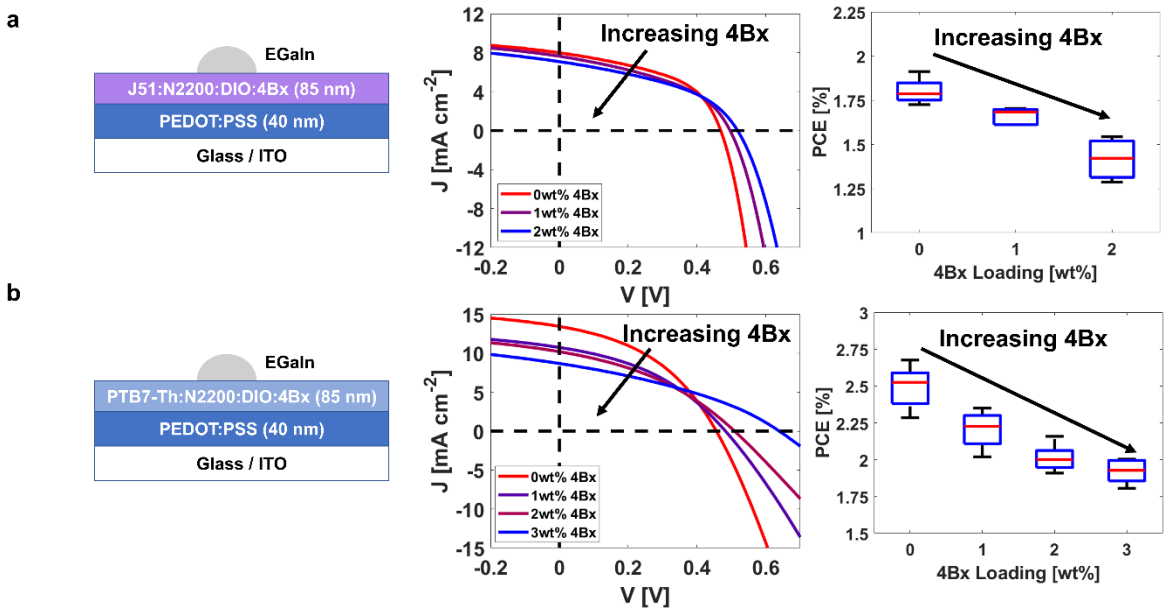

Figure 3.4. Photovoltaic properties of EGaIn solar cells with (**a**) J51:N2200 and (**b**) PTB7-Th:N2200 bulk heterojunctions relative to increasing 4Bx loading. Device structure and representative inverted J-V curves are shown for each bulk heterojunction, along with the change in power conversion efficiency (PCE) relative to 4Bx loading. The red lines in the boxplots represent the average PCE for each loading of 4Bx. A total of 6 EGaIn measurements were made on each device.

We demonstrate that crosslinking the bulk heterojunction increases the survivability of the solar cell for four different degradation tests (**Figure 3.5**). First, we show that the increased mechanical robustness of a crosslinked J51:N2200 bulk heterojunction can increase the survivability of solar cells subject to physical (e.g., scratch and abrasion) damage (**Figures 3.5a, C5**). Second, we show that the insolubility of a crosslinked PTB7-Th:N2200 bulk heterojunction increases the resistance to organic solvents, even when directly exposed to chloroform (**Figures 3.5b, C6**). Third, to evaluate the thermal

stability of crosslinked J51:N2200 cells, we subjected devices to thermal ageing at 60 °C for 400 h in a nitrogen environment (**Figures 3.5c, C7**). Finally, we accelerate the degradation of PTB7-Th:N2200 solar cells using heat (50 °C), moisture (50% relative humidity), and oxygen (e.g., in atmospheric conditions, with unencapsulated devices) (**Figures 3.5d, C8**). The mechanisms by which water, heat, and oxygen accelerate degradation in OSCs has been investigated by others.[76–78] Detailed photovoltaic properties and J-V curves for each degradation test and all crosslinker loadings can be found in **Figures C5-C8**.

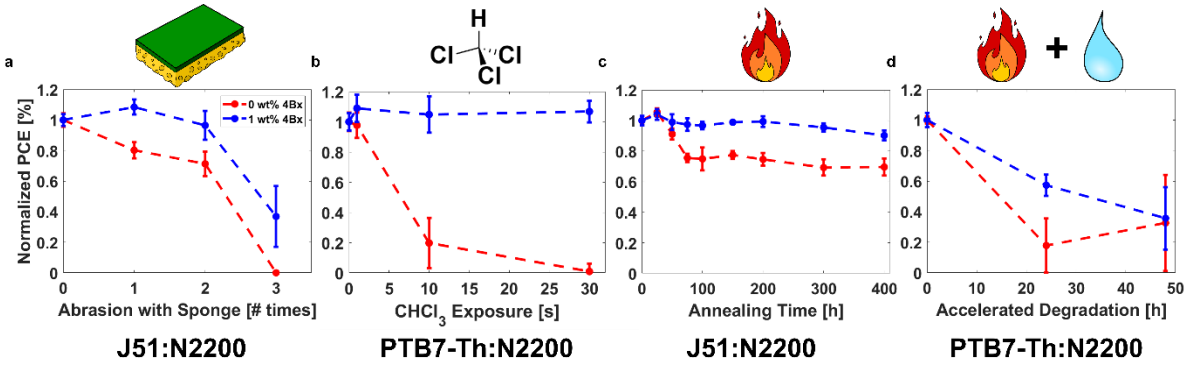

Figure 3.5. Normalized power conversion efficiencies of crosslinked and non-crosslinked EGaIn solar cells subject to (**a**) abrasion tests using a sponge, (**b**) direct exposure to chloroform, (**c**) thermal ageing at 60 °C, and (**d**) accelerated degradation in atmospheric conditions at 50 °C and 50% relative humidity.

Non-crosslinked films of semiconducting polymers can be easily damaged by relatively innocuous forces. That is, many semiconducting polymer films can be removed from a substrate by rubbing with a gloved finger. We used the abrasive side of a standard kitchen sponge (loaded with a 20 g weight to ensure contact) to gradually damage crosslinked and non-crosslinked J51:N2200 solar cells. We measured the photovoltaic properties every time the sponge was dragged over the film using a linear actuator. As expected, crosslinked solar cells showed greater survivability than their non-crosslinked counterparts. After both cells were abraded once, the crosslinked device showed little change in photovoltaic performance, with a similar J_{sc} and PCE to the pristine device (**Figures 3.5a, C5**). In comparison, the non-crosslinked device showed noticeably lower PCE due to the decreased J_{sc}. From optical microscopy, we observed many scratches on the active layer of the non-crosslinked device (**Figure C9**). Although some scratches were present on the

crosslinked J51:N2200 device, these were fewer and smaller. The non-crosslinked device failed after three abrasion cycles (short circuit, **Figure C5**), at which point the crosslinked device still remained functional.

In addition to the locked morphology, crosslinking renders the bulk heterojunction insoluble to organic solvents. To demonstrate the increased solvent resistance of crosslinked bulk heterojunction films, PTB7-Th:N2200 cells were fabricated and directly exposed to chloroform. When the non-crosslinked device was dipped in chloroform, the active layer dissolved, resulting in the J_{sc}, V_{oc}, FF, and PCE monotonically decreasing until the active layer was completely removed (**Figure C6, Figure C10**). In contrast, crosslinked bulk heterojunctions showed little change in photovoltaic performance. Exposure of the crosslinked bulk heterojunctions to chloroform for approximately 1 s dissolved any remaining non-crosslinked polymer and crosslinker, resulting in a small change in photovoltaic properties. After that initial change, all three crosslinked bulk heterojunctions (1–3 wt% 4Bx) remained highly resistant to the chloroform treatment and unchanged in terms of photovoltaic properties for immersions of up to 30 s.

Other studies have suggested that crosslinking the active layer of an OSC increases the thermal stability of the device.[19] Thus, we fabricated J51:N2200 cells and thermally aged crosslinked and non-crosslinked devices at 60 °C. Previous studies have shown that short annealing is beneficial for improving the crystallization, and thus charge transport, of bulk heterojunction films.[76] However, continuous heating may have the opposite effect in that it drives the morphology of the bulk heterojunction towards thermodynamic equilibrium (i.e., as opposed to a metastable morphology most favorable to charge transport).[76] In polymer:fullerene blends, previous studies have suggested that thermal ageing results in greater phase separation.[77,79,80] As a result, larger polymer and fullerene domains are formed, reducing the effective surface area of donor-acceptor interfaces and reducing charge transfer.[79]

In the non-crosslinked J51:N2200 device, gradual annealing over 400 h resulted in significant changes in the photovoltaic properties of the bulk heterojunction (**Figure 3.5c**). The non-crosslinked device only maintained 68% of PCE after 400 h. In comparison, the 1 wt% 4Bx crosslinked device maintained ~100% of its PCE over 200 h and 94% of its PCE over 400 h. Similarly, the device crosslinked with 2 wt%

4Bx maintained 100% of its PCE over 400 h. Previous studies have suggested that an Arrhenius model could relate the accelerated thermal ageing to the expected lifespan of the device at room temperature.[81] For P3HT:PCBM, ageing a device for 200 h at 60 °C approximately corresponds to a lifespan of 1000 h at 25 °C.[81] Using this model, our findings suggest that the 1 wt% J51:N2200:4Bx bulk heterojunction would show no change in overall PCE for ~1000 h at room temperature, while the 2 wt% bulk heterojunction would show no change for ~2000 h.

Finally, PTB7-Th:N2200 devices were subjected to accelerated degradation conditions in a purpose-built chamber held at 50 °C and 50% relative humidity (RH) in atmosphere. Devices were tested every 24 h and showed significant changes in the photovoltaic performance (**Figure 3.5d**). All cells showed significantly worsened photovoltaic properties after 24 h. Diagnostically, photovoltaic properties were worsened due to increased series resistance and failure was observed to occur by shunting (**Figure C8)**. This behavior was likely due to degradation of the PEDOT:PSS, which is partially solubilized in the presence of water.[82,83] It is likely this ingress of moisture resulted in physical degradation (e.g., delamination of the ITO/PEDOT:PSS interface or PEDOT:PSS/PTB7-Th:N2200 interface) that resulted in increased series resistance (and shunting).. Crosslinking with 2% 4Bx impeded this ingress, and thus the crosslinked device lasted longer. Thus, the observed changes to the photovoltaic properties of these devices were most likely a consequence of degradation of the PEDOT:PSS layer. For example, the 3 wt% device completely shunted after 48 h in the degradation chamber, likely because the device was placed closest to the water vapor inlet. However, the non-crosslinked device was placed on the row furthest away from the water vapor valve (along with the 1 and 2 wt% devices), yet still showed the worst performance after 24 h.

Next, we investigated the stability of crosslinked films of J51:N2200 bulk heterojunction films to withstand physical agitation using sonication (**Figure 3.6**). J51:N2200 films were placed in Hellendahl-type glass staining dishes, submerged in water, and sonicated for 1 h. Photographs of the films after each time interval showed significantly greater removal of non-crosslinked J51:N2200 films from the glass substrate in comparison to their crosslinked counterparts (**Figure 3.6a**). To quantify the physical damage

done to each film, we used UV-vis to monitor changes in film thickness (**Figures 3.6b, C11**) and image analysis (i.e., color thresholding) to approximate film coverage on the substrate (**Figure 3.6c**). We found that sonicating a semiconducting polymer film results in both adhesive and cohesive damage. The photographs and subsequent image analysis show a gradual reduction in surface coverage, suggesting that the sonication resulted in adhesive failure due to delamination of the film from the glass substrate. Moreover, for regions in which film remained, UV-vis spectra suggest that the thickness also decreased. After 1 h, the crosslinked film lost only ~20% of the total film volume, compared to ~90% of the non-crosslinked film.

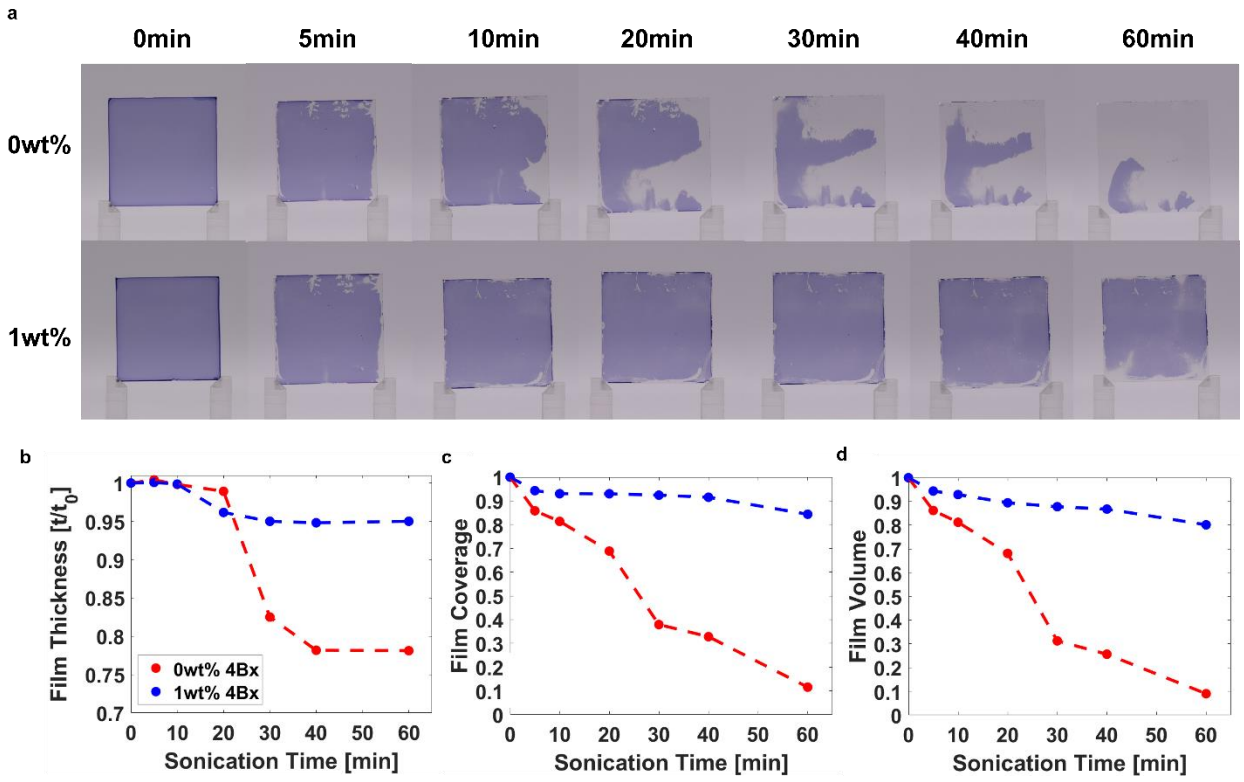

Figure 3.6. (**a**) Crosslinked and non-crosslinked J51:N2200 films were sonicated in a bath sonicator for 1 h. Photographs of the films were taken periodically in order to compare the damage from physical agitation to the crosslinked and non-crosslinked films. Likewise, UV-vis measurements were taken of non-crosslinked crosslinked J51:N2200 films after each time interval of sonication. The absorbance peak at ~390 nm for each spectrum was used to determine (**b**) the change in film thickness relative to sonication time (for regions on the glass substrate where the film remained). Photographs of each film were taken after each time interval in order to approximate the (**c**) the surface area of the film using color thresholding. These changes in film thickness and surface area were used to approximate (**d**) the total volume of the film removed due to agitation from the bath sonicator.

To quantify the way in which crosslinking affects both the cohesive and adhesive properties of the films, we performed debonding tests using a double cantilever beam (DCB) setup (**Figure 3.7**). Both non-crosslinked and crosslinked J51:N2200 film stacks required similar amounts of energy to propagate fracture (**Figure 3.7a**), yet exhibited different debonding behavior (**Figure 3.7b**). In contrast, the PTB7-Th:N2200 film stacks fractured within the same layer (**Figure 3.7c**), while the crosslinked active layer required 5% more energy to propagate fracture.

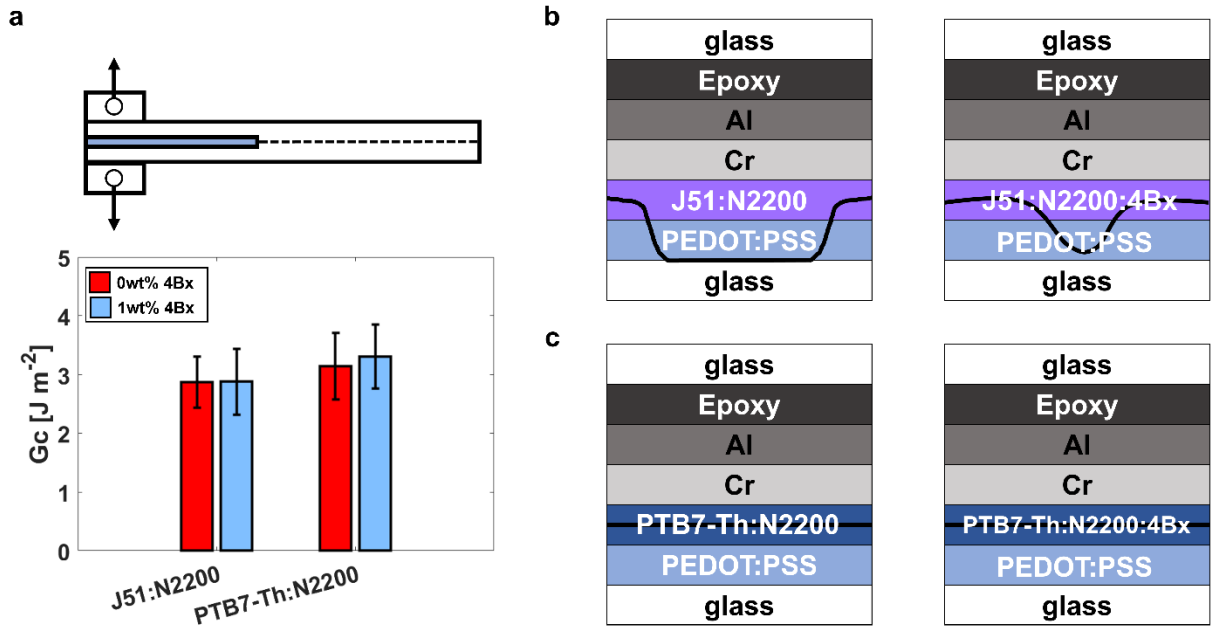

Figure 3.7. (**a**) Cohesive fracture tests were conducted using double cantilever beam (DCB) measurements in order to measure the fracture energy of a glass/PEDOT:PSS/BHJ/Cr/Al stack. X-ray photoelectron spectroscopy (XPS) was conducted after fracturing DCB samples in order to determine the interface of fracture for sample stacks with non-crosslinked and crosslinked films of (**b**) J51:N2200 and (**c**) PTB7-Th:N2200.

XPS measurements were conducted on opposing surfaces of each sample stack after fracture to identify the interface of fracture (**Figure C12, C13**). For PTB7-Th:N2200, both the crosslinked and non-crosslinked films resulted in cohesive failure within the PTB7-Th:N2200 layer. In contrast, the J51:N2200 films experienced both adhesive and cohesive failure: adhesive failure at the PEDOT:PSS/J51:N2200 interface and cohesive failure within the J51:N2200 film. The adhesive failure likely occurred due to domains of J51 serving as fracture (e.g., embrittling) pathways into the PEDOT:PSS layer. When

crosslinked, XPS suggested that samples with a J51:N2200:4Bx active layer primarily underwent cohesive failure within the active layer. For these J51:N2200:4Bx samples, polymer chains were crosslinked to one another, likely reducing the embrittling effect of J51 domains. Likewise, crosslinking with 4Bx increased the adhesion to the PEDOT:PSS layer (e.g., possibly due to cross reactivity with the PEDOT:PSS interface). However, fracture still propagated through some available pathways within the bulk heterojunction, suggesting that some regions within the J51:N2200 were less crosslinked than others. Similarly, it is possible that the meandering fracture path of the non-crosslinked J51:N2200 film resulted in an increase in the measured fracture energy.[84] Therefore, the measured fracture energy between the non-crosslinked and crosslinked samples remained approximately the same. Thus, XPS suggests that crosslinking with low loadings of 4Bx reduces (but does not necessarily eliminate) the number of paths for fracture to propagate from the polymer blend into the PEDOT:PSS (i.e., across layers). These findings validate previous experiments observing that the crosslinked J51:N2200 film showed a smaller decrease in film thickness over 1 h of sonication. Fracture tests suggest that this decreased loss can be attributed to the increase in cohesion due to the crosslinked network within the solid film (**Figure 3.7b**).

In contrast, sample stacks with both non-crosslinked and crosslinked active layers of PTB7-Th:N2200 experienced cohesive failure within the active layer. The crosslinked PTB7-Th:N2200:4Bx samples had an average Gc ~5% greater than the non-crosslinked PTB7-Th:N2200 samples. This difference suggests that crosslinking with 4Bx increased the cohesive strength of the PTB7-Th:N2200 active layer and possibly the adhesive strength of the PTB7-Th:N2200/PEDOT:PSS interface. However, the difference was not significant enough to change the interface of fracture. Previous work done by the O'Connor group showed that the fracture energy of an all-polymer blend is largely dictated by the tougher polymer (i.e., N2200).[73] Thus, when fracture is unable to propagate to the PEDOT:PSS layer (as for J51:N2200), the increase in the toughness of N2200 when crosslinked (**Table C1**) translates to an active layer that requires a greater amount of energy to propagate fracture.

To quantify the abrasion resistance of the crosslinked bulk heterojunction films, we measured the hardness, modulus, and elastic work in compression using nanoindentation (**Figure 3.8a, C14**). These measurements showed that the polymer films increased in hardness as a function of 4Bx loading (**Figure 3.8b**), which is consistent with the increase in resilience derived from the tensile behavior (**Figure 3.3**). Compressive measurements likewise show similar changes in the elastic modulus (**Figure 3.8c**). All films of J51:N2200 (0–2 wt% 4Bx) resulted in similar moduli. In contrast, films of PTB7-Th:N2200 had similar moduli for both 0 and 1 wt% 4Bx, but a greater modulus for 2 wt% 4Bx. Similarly, the loss modulus remained constant despite increasing 4Bx loading for both J51:N2200 and PTB7-Th:N2200 (**Figure C15**). These differences agreed with the embrittlement previously observed in the tensile behavior of PTB7-Th:N2200 relative to increasing 4Bx loading (**Figure 3.3c**). In both J51:N2200 (**Figure 3.8d**) and PTB7-Th:N2200 (**Figure 3.8e**), the elastic work measured by nanoindentation slightly increased as the crosslinker loading increased. For J51:N2200, the plastic work remained similar between 0 and 1 wt% 4Bx, and then decreased at 2 wt% 4Bx. This compressive behavior is consistent with the tensile behavior observed in **Figure 3.3b**, in which 1 wt% 4Bx seemed to be the optimal loading for maintaining fracture strain and toughness (i.e., plastic behavior). After 1 wt% 4Bx, embrittlement resulted in a tradeoff between decreasing fracture strain and increasing tensile strength. In contrast, the plastic work continuously decreased while the elastic work monotonically increased for PTB7-Th:N2200, which is again consistent with the observed tensile behavior (**Figure 3.3c**). Due to the decreased plastic behavior, the storage modulus of PTB7-Th:N2200 increased while the loss modulus remained similar (**Figure C15**). This change in the viscoelastic behavior resulted in a slightly lower tan δ (i.e., ratio between loss and storage modulus) relative to increasing 4Bx loading (**Figure C15**).

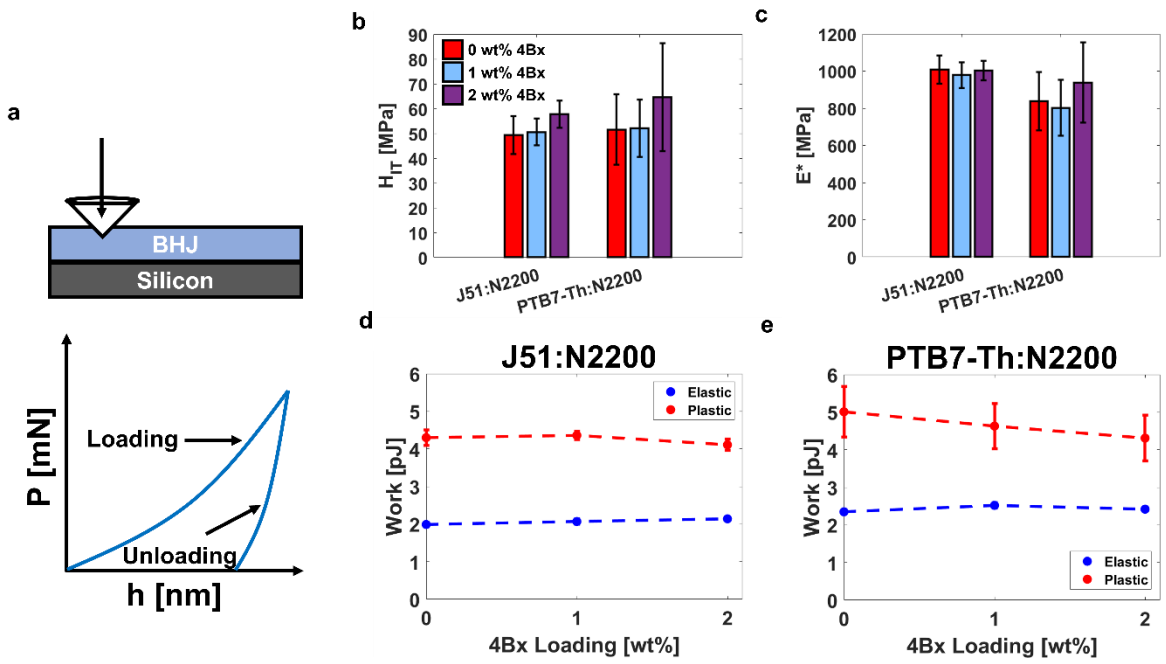

Figure 3.8. (**a**) Compressive properties of J51:N2200 and PTB7-Th:N2200 with 0, 1, or 2 wt% 4Bx were measured using nanoindentation (Sinus indentation) with a Berkovich tip in order to extract the (**b**) indentation hardness (H_{IT}) and (**c**) elastic modulus (E*). From the load-unloading curves, the elastic and plastic work for (**d**) J51:N2000 and (**e**) PTB7-Th:N2200 were extracted.

3.4 Conclusion

In this study, we use a four-armed azide crosslinker ("4Bx") to crosslink a library of semiconducting polymers, with special attention paid to two different bulk heterojunction films used in all-polymer solar cells (J51:N2200 and PTB7-Th:N2200) . We show that 4Bx can be used to modulate the mechanical properties of these films, particularly for increasing the tensile strength, hardness, and cohesive strength. To directly probe how crosslinking affects the photovoltaic properties of the bulk heterojunction, we fabricated all-polymer solar cells. We find that crosslinked bulk heterojunctions showed significant improvements in abrasion resistance, likely in part due to the increased cohesive strength. This increased abrasion resistance translates to a more survivable device when subject to mild abrasion and scratches. Likewise, crosslinking the bulk heterojunction results in a device with increased solvent resistance (30 s of chloroform exposure) and thermal stability (>200 h at 60 °C), but with somewhat lower performance. Nevertheless, it is our hope that devices made from conjugated polymers can be afforded greater

environmental stability by simple strategies like the one explored here. In particular, solar cells with greater strength, hardness, and abrasion resistance could enable energy harvesting from surfaces subject to continuous mechanical insults.

Our work suggests the importance of investigating crosslinkers more ideally suited to conjugated polymers than is 4Bx. For example, the presence of 4Bx increases the insulating fraction of a crosslinked film relative to a pristine film. There may be an opportunity to explore conjugated crosslinkers, or those which are less likely to disrupt lamellar packing within ordered domains. Thus, rational design of both conjugated polymers and crosslinkers for the purposes of increasing the mechanical robustness could also allow for greater crosslinker loading with a reduced deleterious effect on the electronic properties.

Finally, this work focuses on a relatively small subset of conjugated polymers, most of which are structurally distinct from one another. However, systematic exploration on the effect of crosslinking should be done with the many assorted families of conjugated polymers that are widely in use today. In conjunction with structure-property studies of the crosslinker structure on the physical properties of conjugated polymer, further studies could yield a deeper understanding of how the mechanical and electronic properties of conjugated polymers can be modified to better suit applications expected to survive rigorous environmental conditions.

3.5 Acknowledgements

This work was supported by the Air Force Office of Scientific Research (AFOSR) grant no. FA9550-19-1-0278. K.C. acknowledges additional support as a Hellman Scholar and an Intel Scholar provided through the Academic Enrichment Program (AEP) at UCSD through the following awards: The Undergraduate Research Scholarship and Semiconductor Research Corporation Scholarship. R.R. acknowledges support from the National Science Foundation Graduate Research Fellowship (NSF GRFP) under grant no. DGE-1144086. The authors acknowledge the use of facilities and instrumentation supported by NSF through the UC San Diego Materials Research Science and Engineering Center (UCSD MRSEC), grant DMR-2011924. This work was performed in part at the San Diego Nanotechnology Infrastructure (SDNI) of UCSD, a member of the National Nanotechnology Coordinated Infrastructure, which is supported by the National Science Foundation (Grant ECCS-2025752). We thank the Department of Chemistry and Biochemistry at The University of Arizona for support of the Laboratory for Electron Spectroscopy and Surface Analysis.

3.6 References

(1) Chen, A. X.; Kleinschmidt, A. T.; Choudhary, K.; Lipomi, D. J. Beyond Stretchability: Strength, Toughness, and Elastic Range in Semiconducting Polymers. *Chem. Mater.* **2020**, *0*.

(2) Kim, M. J.; Lee, M.; Min, H.; Kim, S.; Yang, J.; Kweon, H.; Lee, W.; Kim, D. H.; Choi, J. H.; Ryu, D. Y.; Kang, M. S.; Kim, B. S.; Cho, J. H. Universal Three-Dimensional Crosslinker for All-Photopatterned Electronics. *Nat. Commun.* **2020**, *11*, 1–11.

(3) Peng, Z.; Xian, K.; Cui, Y.; Qi, Q.; Liu, J.; Xu, Y.; Chai, Y.; Yang, C.; Hou, J.; Geng, Y.; Ye, L. Thermoplastic Elastomer Tunes Phase Structure and Promotes Stretchability of High-Efficiency Organic Solar Cells. *Adv. Mater.* **2021**, *33*, 1–14.

(4) Wang, G. J. N.; Gasperini, A.; Bao, Z. Stretchable Polymer Semiconductors for Plastic Electronics. *Adv. Electron. Mater.* **2018**, *4*, 1–21.

(5) Qian, Y.; Zhang, X.; Xie, L.; Qi, D.; Chandran, B. K.; Chen, X.; Huang, W. Stretchable Organic Semiconductor Devices. *Adv. Mater.* **2016**, *28*, 9243–9265.

(6) Savagatrup, S.; Printz, A. D.; O'Connor, T. F.; Zaretski, A. V.; Lipomi, D. J. Molecularly Stretchable Electronics. *Chem. Mater.* **2014**, *26*, 3028–3041.

(7) Ocheje, M. U.; Charron, B. P.; Nyayachavadi, A.; Rondeau-Gagné, S. Stretchable Electronics: Recent Progress in the Preparation of Stretchable and Self-Healing Semiconducting Conjugated Polymers. *Flex. Print. Electron.* **2017**, *2*.

(8) Kim, D. C.; Shim, H. J.; Lee, W.; Koo, J. H.; Kim, D. H. Material-Based Approaches for the Fabrication of Stretchable Electronics. *Adv. Mater.* **2020**, *32*, 1–29.

(9) Han, J.; Bao, F.; Huang, D.; Wang, X.; Yang, C.; Yang, R.; Jian, X.; Wang, J.; Bao, X.; Chu, J. A Universal Method to Enhance Flexibility and Stability of Organic Solar Cells by Constructing Insulating Matrices in Active Layers. *Adv. Funct. Mater.* **2020**, *30*, 1–13.

(10) Ashizawa, M.; Zheng, Y.; Tran, H.; Bao, Z. Intrinsically Stretchable Conjugated Polymer Semiconductors in Field Effect Transistors. *Prog. Polym. Sci.* **2020**, *100*, 101181.

(11) Zhang, S.; Cheng, Y. H.; Galuska, L.; Roy, A.; Lorenz, M.; Chen, B.; Luo, S.; Li, Y. T.; Hung, C. C.; Qian, Z.; St. Onge, P. B. J.; Mason, G. T.; Cowen, L.; Zhou, D.; Nazarenko, S. I.; Storey, R. F.; Schroeder, B. C.; Rondeau-Gagné, S.; Chiu, Y. C.; Gu, X. Tacky Elastomers to Enable Tear-Resistant and Autonomous Self-Healing Semiconductor Composites. *Adv. Funct. Mater.* **2020**, *30*, 1–10.

(12) Oh, J. Y.; Son, D.; Katsumata, T.; Lee, Y.; Kim, Y.; Lopez, J.; Wu, H. C.; Kang, J.; Park, J.; Gu, X.; Mun, J.; Wang, N. G. J.; Yin, Y.; Cai, W.; Yun, Y.; Tok, J. B. H.; Bao, Z. Stretchable Self-Healable Semiconducting Polymer Film for Active-Matrix Strain-Sensing Array. *Sci. Adv.* **2019**, *5*.

(13) Xie, R.; Weisen, A. R.; Lee, Y.; Aplan, M. A.; Fenton, A. M.; Masucci, A. E.; Kempe, F.; Sommer, M.; Pester, C. W.; Colby, R. H.; Gomez, E. D. Glass Transition Temperature from the Chemical Structure of Conjugated Polymers. *Nat. Commun.* **2020**, *11*, 1–8.

(14) Kim, M. J.; Jung, A. R.; Lee, M.; Kim, D.; Ro, S.; Jin, S. M.; Nguyen, H. D.; Yang, J.; Lee, K. K.; Lee, E.; Kang, M. S.; Kim, H.; Choi, J. H.; Kim, B.; Cho, J. H. Structure-Property Relationships of Semiconducting Polymers for Flexible and Durable Polymer Field-Effect Transistors. *ACS Appl. Mater. Interfaces* **2017**, *9*, 40503–40515.

(15) Zheng, Y.; Ashizawa, M.; Zhang, S.; Kang, J.; Nikzad, S.; Yu, Z.; Ochiai, Y.; Wu, H.-C.; Tran, H.; Mun, J.; Zheng, Y.-Q.; Tok, J. B.-H.; Gu, X.; Bao, Z. Tuning the Mechanical Properties of a Polymer Semiconductor by Modulating Hydrogen Bonding Interactions. *Chem. Mater.* **2020**.

(16) Zheng, Y.; Yu, Z.; Zhang, S.; Kong, X.; Michaels, W.; Wang, W.; Chen, G.; Liu, D.; Lai, J.; Prine, N.; Zhang, W.; Nikzad, S.; Cooper, C. B.; Zhong, D.; Mun, J.; Zhang, Z.; Kang, J.; Tok, J. B.; Mcculloch, I.; Qin, J.; Gu, X.; Bao, Z. A Molecular Design Approach towards Elastic and Multifunctional Polymer Electronics. *Nat. Commun.* **2021**, 1–11.

(17) Dauzon, E.; Sallenave, X.; Plesse, C.; Goubard, F.; Amassian, A.; Anthopoulos, T. D. Versatile Methods for Improving the Mechanical Properties of Fullerene and Non-Fullerene Bulk

Heterojunction Layers to Enable Stretchable Organic Solar Cells. *J. Mater. Chem. C* **2022**, *10*, 3375–3386.

(18) Wang, Z.; Zhang, D.; Xu, M.; Liu, J.; He, J.; Yang, L.; Li, Z.; Gao, Y.; Shao, M. Intrinsically Stretchable Organic Solar Cells with Simultaneously Improved Mechanical Robustness and Morphological Stability Enabled by a Universal Crosslinking Strategy. *Small* **2022**, *2201589*, 1–10.

(19) Rumer, J. W.; McCulloch, I. Organic Photovoltaics: Crosslinking for Optimal Morphology and Stability. *Mater. Today* **2015**, *18*, 425–435.

(20) Rumer, J. W.; Ashraf, R. S.; Eisenmenger, N. D.; Huang, Z.; Meager, I.; Nielsen, C. B.; Schroeder, B. C.; Chabinyc, M. L.; McCulloch, I. Dual Function Additives: A Small Molecule Crosslinker for Enhanced Efficiency and Stability in Organic Solar Cells. *Adv. Energy Mater.* **2015**, *5*, 5–10.

(21) Hong, L.; Yao, H.; Cui, Y.; Yu, R.; Lin, Y.; Chen, T.; Xu, Y.; Qin, J.; Hsu, C.; Ge, Z.; Hou, J. Simultaneous Improvement of Efficiency and Stability of Organic Photovoltaic Cells by Using a Cross-Linkable Fullerene Derivative. *Small* **2021**, *2101133*, 2101133.

(22) Cheng, Y. J.; Hsieh, C. H.; Li, P. J.; Hsu, C. S. Morphological Stabilization by in Situ Polymerization of Fullerene Derivatives Leading to Efficient, Thermally Stable Organic Photovoltaics. *Adv. Funct. Mater.* **2011**, *21*, 1723–1732.

(23) Qian, D.; Xu, Q.; Hou, X.; Wang, F.; Hou, J.; Tan, Z. Stabilization of the Film Morphology in Polymer: Fullerene Heterojunction Solar Cells with Photocrosslinkable Bromine-Functionalized Low-Bandgap Copolymers. *J. Polym. Sci. Part A Polym. Chem.* **2013**, *51*, 3123–3131.

(24) Lee, C.; Lee, S.; Kim, G. U.; Lee, W.; Kim, B. J. Recent Advances, Design Guidelines, and Prospects of All-Polymer Solar Cells. *Chem. Rev.* **2019**, *119*, 8028–8086.

(25) Facchetti, A. Polymer Donor-Polymer Acceptor (All-Polymer) Solar Cells. *Mater. Today* **2013**, *16*, 123–132.

(26) Wang, G.; Melkonyan, F. S.; Facchetti, A.; Marks, T. J. All-Polymer Solar Cells: Recent Progress, Challenges, and Prospects. *Angew. Chemie - Int. Ed.* **2019**, *58*, 4129–4142.

(27) Zhu, L.; Zhang, M.; Zhong, W.; Leng, S.; Zhou, G.; Zou, Y.; Su, X.; Ding, H.; Gu, P.; Liu, F.; Zhang, Y. Progress and Prospects of the Morphology of Non-Fullerene Acceptor Based High-Efficiency Organic Solar Cells. *Energy Environ. Sci.* **2021**, *14*, 4341–4357.

(28) Wang, J.; Zhan, X. Fused-Ring Electron Acceptors for Photovoltaics and Beyond. *Acc. Chem. Res.* **2021**, *54*, 132–143.

(29) Zhang, Y.; Ji, Y.; Zhang, Y.; Zhang, W.; Bai, H.; Du, M. Recent Progress of Y6-Derived Asymmetric Fused Ring Electron Acceptors. **2022**, *2205115*, 1–18.

(30) Dey, S. Recent Progress in Molecular Design of Fused Ring Electron Acceptors for Organic Solar Cells. *Small* **2019**, *15*, 1–38.

(31) Root, S. E.; Savagatrup, S.; Printz, A. D.; Rodriquez, D.; Lipomi, D. J. Mechanical Properties of Organic Semiconductors for Stretchable, Highly Flexible, and Mechanically Robust Electronics. *Chem. Rev.* **2017**, *117*, 6467–6499.

(32) Kang, H.; Lee, W.; Oh, J.; Kim, T.; Lee, C.; Kim, B. J. From Fullerene − Polymer to All-Polymer Solar Cells : The Importance of Molecular Packing , Orientation , and Morphology Control. *Acc. Chem. Res.* **2016**, No. ii.

(33) Wen, Z. C.; Yin, H.; Hao, X. T. Recent Progress of PM6:Y6-Based High Efficiency Organic Solar Cells. *Surfaces and Interfaces* **2021**, *23*, 100921.

(34) Guo, Q.; Guo, Q.; Geng, Y.; Tang, A.; Zhang, M.; Du, M.; Sun, X.; Zhou, E. Recent Advances in PM6:Y6-Based Organic Solar Cells. *Mater. Chem. Front.* **2021**, *5*, 3257–3280.

(35) Wu, S.-C.; Strover, L. T.; Yao, X.; Chen, X. Q.; Xiao, W. J.; Liu, L. N.; Wang, J.; Visoly-Fisher, I.; Katz, E. A.; Li, W. S. UV-Cross-Linkable Donor-Acceptor Polymers Bearing a Photostable Conjugated Backbone for Efficient and Stable Organic Photovoltaics. *ACS Appl. Mater. Interfaces* **2018**, *10*, 35430–35440.

(36) Kwon, N. Y.; Park, S. H.; Kang, H.; Kim, Y. U.; Chau, H. D.; Harit, A. K.; Woo, H. Y.; Yoon, H. J.; Cho, M. J.; Choi, D. H. Improved Stability of All-Polymer Solar Cells Using Crosslinkable Donor and Acceptor Polymers Bearing Vinyl Moieties in the Side-Chains. *ACS Appl. Mater. Interfaces* **2021**, *13*, 16754–16765.

(37) Yang, F.; Zhao, W.; Zhu, Q.; Li, C.; Ma, W.; Hou, J.; Li, W. Boosting the Performance of Non-Fullerene Organic Solar Cells via Cross-Linked Donor Polymers Design. *Macromolecules* **2019**, *52*, 2214–2221.

(38) Schock, M.; Bräse, S. Reactive & Efficient: Organic Azides as Cross-Linkers in Material Sciences. *Molecules* **2020**, *25*.

(39) Zhao, X.; Zhao, Y.; Ge, Q.; Butrouna, K.; Diao, Y.; Graham, K. R.; Mei, J. Complementary Semiconducting Polymer Blends: The Influence of Conjugation-Break Spacer Length in Matrix Polymers. *Macromolecules* **2016**, *49*, 2601–2608.

(40) Wadsworth, A.; Chen, H.; Thorley, K. J.; Cendra, C.; Nikolka, M.; Bristow, H.; Moser, M.; Salleo, A.; Anthopoulos, T. D.; Sirringhaus, H.; McCulloch, I. Modification of Indacenodithiophene-Based Polymers and Its Impact on Charge Carrier Mobility in Organic Thin-Film Transistors. *J. Am. Chem. Soc.* **2020**, *142*, 652–664.

(41) Zhang, W.; Smith, J.; Watkins, S. E.; Gysel, R.; McGehee, M.; Salleo, A.; Kirkpatrick, J.; Ashraf, S.; Anthopoulos, T.; Heeney, M.; McCulloch, I. Indacenodithiophene Semiconducting Polymers for High-Performance, Air-Stable Transistors. *J. Am. Chem. Soc.* **2010**, *132*, 11437–11439.

(42) Kim, H. S.; Huseynova, G.; Noh, Y. Y.; Hwang, D. H. Modulation of Majority Charge Carrier from Hole to Electron by Incorporation of Cyano Groups in Diketopyrrolopyrrole-Based Polymers. *Macromolecules* **2017**, *50*, 7550–7558.

(43) Zhang, Z. G.; Yang, Y.; Yao, J.; Xue, L.; Chen, S.; Li, X.; Morrison, W.; Yang, C.; Li, Y. Constructing a Strongly Absorbing Low-Bandgap Polymer Acceptor for High-Performance All-Polymer Solar Cells. *Angew. Chemie - Int. Ed.* **2017**, *56*, 13503–13507.

(44) Runser, R.; Root, S. E.; Ober, D. E.; Choudhary, K.; Chen, A. X.; Dhong, C.; Urbina, A. D.; Lipomi, D. J. Interfacial Drawing: Roll-to-Roll Coating of Semiconducting Polymer and Barrier Films onto Plastic Foils and Textiles. *Chem. Mater.* **2019**, *31*, 9078–9086.

(45) Chen, C. P.; Tsai, Y. Y.; Chen, Y. C.; Li, Y. H. High-Performance and Long-Term Stable Inverted Ternary Solar Cells Based on PTB7-Th/N2200/PC71BM Blends. *Sol. Energy* **2018**, *176*, 170–177.

(46) Kim, J. H.; Nizami, A.; Hwangbo, Y.; Jang, B.; Lee, H. J.; Woo, C. S.; Hyun, S.; Kim, T. S. Tensile Testing of Ultra-Thin Films on Water Surface. *Nat. Commun.* **2013**.

(47) Vanlandingham, M. R.; Chang, N. K.; Drzal, P. L.; White, C. C.; Chang, S. H. Viscoelastic Characterization of Polymers Using Instrumented Indentation. I. Quasi-Static Testing. *J. Polym. Sci. Part B Polym. Phys.* **2005**, *43*, 1794–1811.

(48) White, C. C.; Vanlandingham, M. R.; Drzal, P. L.; Chang, N. K.; Chang, S. H. Viscoelastic Characterization of Polymers Using Instrumented Indentation. II. Dynamic Testing. *J. Polym. Sci. Part B Polym. Phys.* **2005**, *43*, 1812–1824.

(49) Lu, H.; Wang, B.; Ma, J.; Huang, G.; Viswanathan, H. Measurement of Creep Compliance of Solid Polymers by Nanoindentation. *Mech. Time-Dependent Mater.* **2003**, *7*, 189–207.

(50) Wang, Y.; Shang, L.; Zhang, P.; Yan, X.; Zhang, K.; Dou, S.; Zhao, J.; Li, Y. Measurement of Viscoelastic Properties for Polymers by Nanoindentation. *Polym. Test.* **2020**, *83*, 106353.

(51) Odegard, G. M.; Gates, T. S.; Herring, H. M. Characterization of Viscoelastic Properties of Polymeric Materials through Nanoindentation. *Exp. Mech.* **2005**, *45*, 130–136.

(52) Klapperich, C.; Komvopoulos, K.; Pruitt, L. Nanomechanical Properties of Polymers Determined from Nanoindentation Experiments. *J. Tribol.* **2001**, *123*, 624–631.

(53) Chakravartula, A.; Komvopoulos, K. Viscoelastic Properties of Polymer Surfaces Investigated by Nanoscale Dynamic Mechanical Analysis. *Appl. Phys. Lett.* **2006**, *88*, 28–31.

(54) Li, H.; Randall, N. X.; Vlassak, J. J. New Methods of Analyzing Indentation Experiments on Very Thin Films. *J. Mater. Res.* **2010**, *25*, 728–734.

(55) Mahouche-Chergui, S.; Boussaboun, Z.; Oun, A.; Kazembeyki, M.; Hoover, C. G.; Carbonnier, B.; Ouellet-Plamondon, C. M. Sustainable Preparation of Graphene-like Hybrid Nanomaterials and Their Application for Organic Dyes Removal. *Chem. Eng. Sci.* **2021**, *236*, 116482.

(56) Oliver, W. C.; Pharr, G. M. An Improved Technique for Determining Hardness and Elastic Modulus Using Load and Displacement Sensing Indentation Experiments. *J. Mater. Res.* **1992**, *7*, 1564–1583.

(57) Root, S. E.; Savagatrup, S.; Pais, C. J.; Arya, G.; Lipomi, D. J. Predicting the Mechanical Properties of Organic Semiconductors Using Coarse-Grained Molecular Dynamics Simulations. *Macromolecules* **2016**, *49*, 2886–2894.

(58) Kanninen, M. F. An Augmented Double Cantilever Beam Model for Studying Crack Propagation and Arrest. *Int. J. Fract.* **1973**, *9*, 83–92.

(59) Doumon, N. Y.; Wang, G.; Qiu, X.; Minnaard, A. J.; Chiechi, R. C.; Koster, L. J. A. 1,8-Diiodooctane Acts As a Photo-Acid in Organic Solar Cells. *Sci. Rep.* **2019**, *9*, 1–14.

(60) Zusan, A.; Gieseking, B.; Zerson, M.; Dyakonov, V.; Magerle, R.; Deibel, C. The Effect of Diiodooctane on the Charge Carrier Generation in Organic Solar Cells Based on the Copolymer PBDTTT-C. *Sci. Rep.* **2015**, *5*.

(61) Savagatrup, S.; Printz, A. D.; O'Connor, T. F.; Kim, I.; Lipomi, D. J. Efficient Characterization of Bulk Heterojunction Films by Mapping Gradients by Reversible Contact with Liquid Metal Top Electrodes. *Chem. Mater.* **2017**, *29*, 389–398.

(62) Spano, F. C.; Silva, C. H- and J-Aggregate Behavior in Polymeric Semiconductors. *Annu. Rev. Phys. Chem.* **2014**.

(63) Spano, F. C. Modeling Disorder in Polymer Aggregates: The Optical Spectroscopy of Regioregular Poly(3-Hexylthiophene) Thin Films. *J. Chem. Phys.* **2005**.

(64) Gao, L.; Zhang, Z. G.; Xue, L.; Min, J.; Zhang, J.; Wei, Z.; Li, Y. All-Polymer Solar Cells Based on Absorption-Complementary Polymer Donor and Acceptor with High Power Conversion

Efficiency of 8.27%. *Adv. Mater.* **2016**, *28*, 1884–1890.

(65) Choudhary, K.; Chen, A. X.; Pitch, G. M.; Runser, R.; Urbina, A.; Dunn, T. J.; Kodur, M.; Kleinschmidt, A. T.; Wang, B. G.; Bunch, J. A.; Fenning, D. P.; Ayzner, A. L.; Lipomi, D. J. Comparison of the Mechanical Properties of a Conjugated Polymer Deposited Using Spin Coating, Interfacial Spreading, Solution Shearing, and Spray Coating. *ACS Appl. Mater. Interfaces* **2021**, *13*, 51436–51446.

(66) Zheng, Y.; Wang, G. J. N.; Kang, J.; Nikolka, M.; Wu, H. C.; Tran, H.; Zhang, S.; Yan, H.; Chen, H.; Yuen, P. Y.; Mun, J.; Dauskardt, R. H.; McCulloch, I.; Tok, J. B. H.; Gu, X.; Bao, Z. An Intrinsically Stretchable High-Performance Polymer Semiconductor with Low Crystallinity. *Adv. Funct. Mater.* **2019**, *29*, 1–12.

(67) Zhang, Q.; Chen, Z.; Ma, W.; Xie, Z.; Liu, J.; Yu, X.; Han, Y. Efficient Nonhalogenated Solvent-Processed Ternary All-Polymer Solar Cells with a Favorable Morphology Enabled by Two Well-Compatible Donors. *ACS Appl. Mater. Interfaces* **2019**, *11*, 32200–32208.

(68) Yi, X.; Gautam, B.; Constantinou, I.; Cheng, Y.; Peng, Z.; Klump, E.; Ba, X.; Ho, C. H. Y.; Dong, C.; Marder, S. R.; Reynolds, J. R.; Tsang, S. W.; Ade, H.; So, F. Impact of Nonfullerene Molecular Architecture on Charge Generation, Transport, and Morphology in PTB7-Th-Based Organic Solar Cells. *Adv. Funct. Mater.* **2018**, *28*, 1–9.

(69) Xia, Y.; Musumeci, C.; Bergqvist, J.; Ma, W.; Gao, F.; Tang, Z.; Bai, S.; Jin, Y.; Zhu, C.; Kroon, R.; Wang, C.; Andersson, M. R.; Hou, L.; Inganäs, O.; Wang, E. Inverted All-Polymer Solar Cells Based on a Quinoxaline-Thiophene/Naphthalene-Diimide Polymer Blend Improved by Annealing. *J. Mater. Chem. A* **2016**, *4*, 3835–3843.

(70) Park, S. H.; Kim, Y.; Kwon, N. Y.; Lee, Y. W.; Woo, H. Y.; Chae, W. S.; Park, S.; Cho, M. J.; Choi, D. H. Significantly Improved Morphology and Efficiency of Nonhalogenated Solvent-Processed Solar Cells Derived from a Conjugated Donor–Acceptor Block Copolymer. *Adv. Sci.* **2020**, *7*.

(71) Yuan, J.; Guo, W.; Xia, Y.; Ford, M. J.; Jin, F.; Liu, D.; Zhao, H.; Inganäs, O.; Bazan, G. C.; Ma, W. Comparing the Device Physics, Dynamics and Morphology of Polymer Solar Cells Employing Conventional PCBM and Non-Fullerene Polymer Acceptor N2200. *Nano Energy* **2017**, *35*, 251–262.

(72) Sharma, A.; Singh, R.; Kini, G. P.; Hyeon Kim, J.; Parashar, M.; Kim, M.; Kumar, M.; Kim, J. S.; Lee, J. J. Side-Chain Engineering of Diketopyrrolopyrrole-Based Hole-Transport Materials to Realize High-Efficiency Perovskite Solar Cells. *ACS Appl. Mater. Interfaces* **2021**, *13*, 7405–7415.

(73) Balar, N.; Rech, J. J.; Henry, R.; Ye, L.; Ade, H.; You, W.; O'Connor, B. T. The Importance of Entanglements in Optimizing the Mechanical and Electrical Performance of All-Polymer Solar Cells. *Chem. Mater.* **2019**, *31*, 5124–5132.

(74) Sun, T.; Scott, J. I.; Wang, M.; Kline, R. J.; Bazan, G. C.; Connor, B. T. O. Plastic Deformation of Polymer Blends as a Means to Achieve Stretchable Organic Transistors. **2017**, *201600388*, 1–10.

(75) Scott, J. I.; Xue, X.; Wang, M.; Kline, R. J.; Hoffman, B. C.; Dougherty, D.; Zhou, C.; Bazan, G.; O'Connor, B. T. Significantly Increasing the Ductility of High Performance Polymer Semiconductors through Polymer Blending. *ACS Appl. Mater. Interfaces* **2016**, *8*, 14037–14045.

(76) Xu, X.; Li, D.; Yuan, J.; Zhou, Y.; Zou, Y. Recent Advances in Stability of Organic Solar Cells. *EnergyChem* **2021**, *3*, 100046.

(77) Jørgensen, M.; Norrman, K.; Krebs, F. C. Stability/Degradation of Polymer Solar Cells. *Sol. Energy Mater. Sol. Cells* **2008**, *92*, 686–714.

(78) Lee, J.; Kim, J. W.; Park, S. A.; Son, S. Y.; Choi, K.; Lee, W.; Kim, M.; Kim, J. Y.; Park, T. Study of Burn-In Loss in Green Solvent-Processed Ternary Blended Organic Photovoltaics Derived from UV-Crosslinkable Semiconducting Polymers and Nonfullerene Acceptors. *Adv. Energy Mater.* **2019**, *9*.

(79) Jo, J.; Kim, S. S.; Na, S. I.; Yu, B. K.; Kim, D. Y. Time-Dependent Morphology Ewolution by

Annealing Processes on Polymer:Fullerene Blend Solar Cells. *Adv. Funct. Mater.* **2009**, *19*, 866–874.

(80) Motaung, D. E.; Malgas, G. F.; Arendse, C. J. Insights into the Stability and Thermal Degradation of P3HT:C60 Blended Films for Solar Cell Applications. *J. Mater. Sci.* **2011**, *46*, 4942–4952.

(81) De Bettignies, R.; Leroy, J.; Firon, M.; Sentein, C. Accelerated Lifetime Measurements of P3HT:PCBM Solar Cells. *Synth. Met.* **2006**, *156*, 510–513.

(82) Modarresi, M.; Mehandzhiyski, A.; Fahlman, M.; Tybrandt, K.; Zozoulenko, I. Microscopic Understanding of the Granular Structure and the Swelling of PEDOT:PSS. *Macromolecules* **2020**, *53*, 6267–6278.

(83) Bießmann, L.; Kreuzer, L. P.; Widmann, T.; Hohn, N.; Moulin, J.-F.; Müller-Buschbaum, P. Monitoring the Swelling Behavior of PEDOT:PSS Electrodes under High Humidity Conditions. *ACS Appl. Mater. Interfaces* **2018**, *10*, 9865–9872.

(84) Watson, B. L.; Rolston, N.; Printz, A. D.; Dauskardt, R. H. Scaffold-Reinforced Perovskite Compound Solar Cells. *Energy Environ. Sci.* **2017**, *10*, 2500–2508.

Chapter 4. Adhesive Properties of Semiconducting Polymers: Poly(3-alkylthiophene) as an Ersatz Glue

4.1 Introduction

The promise of π-conjugated (semiconducting) polymers is to combine the electronic functionality of conventional semiconductors with the processability and deformability of plastics. Conjugated polymers are widely investigated as active components in organic bioelectronic and optoelectronic devices.[1–9] These materials are especially attractive for applications that must withstand the rigors of wearability and the outdoor environment. Thus, their usability and functionality depend on the ability of the polymer to store or dissipate mechanical energy without failure of the device.[10] For this reason, a significant body of literature is dedicated to understanding the mechanical properties of conventional polymers and engineering plastics.[11] Work by Seitz has shown that mechanical properties of a solid polymer film can often be predicted from five molecular properties: the molecular weight,[12] van der Waals volume, length and number of rotational bonds in the monomer structure, and glass transition temperature.[13] However, for semiconducting polymers, which are composed of π-conjugated backbones that discourage deformation—along with pendant groups that encourage it—such simple models have failed to predict the subtleties of the thermomechanical behavior, particularly as the length of the pendant group increases. Moreover, thermomechanical stability must be balanced with electronic performance.

Several recent strategies, including crosslinking of the side chains,[14–18] aggregation of polymer molecules into coiled nanofibers,[19–21] and copolymerization,[22–31] have succeeded in many ways to combine electronic function and mechanical deformability. Despite this success, there remain important questions as to what structural parameters should be engineered to obtain specific mechanical outcomes. Of course, the polymer must have sufficient cohesive energy to retain favorable charge-transport properties when bent or deformed. However, conjugated polymer films must also have strong mechanical interfaces with other layers in multilayer devices. The semiconducting film thus acts as an "ersatz glue"; it must function as an adhesive within a device, despite not being designed to do so.

The way in which mechanical energy is absorbed and dissipated within a semiconducting polymer film is governed by its molecular structure and a way that structure assembles itself in the solid state.[32] For a device stack comprising multiple polymeric films which are deposited sequentially, the interactions between the layers—including physical interpenetration and electrostatic effects—also influence the adhesive strength at the interface.[32,33] As in a purpose-designed adhesive (e.g., sticky tape), mechanical work can also be dissipated by the viscoelastic behavior of the semiconducting polymer. Adhesive properties[34] are thus determined by both the properties of the bulk and of the interfaces.[32,35,36] For semiconducting polymers, adhesive properties having their origins in electrostatics[37] (e.g., van der Waals forces) are influenced by the presence of polar and polarizable groups, the ratio of saturated to unsaturated bonds, the packing density of the film, and possibly the molecular orientation (texture) at the surface.[33] Adhesive properties arising from molecular dynamics—including interpenetration and viscoelasticity—are influenced by molecular weight and dispersity, as well as the inclusion of tackifiers, plasticizers, and dopants.[38–40] The mechanical properties are also influenced extrinsically by processing methods, operating temperature, and thermal history.[32,35,38]

The type of fracture obtained depends on the details of energy dissipation at the crack tip, which depends both on molecular structure and extensive parameters (e.g., thickness). For example, Dauskardt and coworkers measured greater energies of decohesion as the thickness of the poly(3-hexylthiophene):[6,6]-phenyl-C_{61}-butyric acid methyl ester (P3HT:PCBM) film increased (for P3HT with molecular weights of 53 – 100 kDa). The reason for this increase in measured energies was attributed to the larger plastic zone at the crack tip in thicker films, which allows for the dissipation of mechanical work, thus impeding the growth of the crack.[41] However, for P3HT with a molecular weight of 28 kDa, the authors found that the decohesion energy was not affected by the film thickness due to the decreased plasticity (and viscoelasticity) of the film at the crack tip.[41,42] The mechanisms associated with the de-adhesion of viscoelastic materials are also dependent on, e.g., the angle of the peel, the rigidity of the substrate, and the rigidity of the adherend.[43–45] Previous work from our laboratory has shown that in roll-to-roll printed devices,

encapsulation allows P3HT:PCBM solar cells to withstand thousands of cycles of torsion and bending.[46] However, mechanical delamination eventually occurs due to crazing near the rough perimeter edges of the barrier layer, which propagates under continued deformation and results in adhesive failure at the interface between the PEDOT:PSS and the active layer as well as decohesion within the active layer.

The alkyl pendant groups attached to the main chain of conjugated polymers are significant determinants of the thermomechanical properties of the solid polymer film. Rigid π-conjugated backbones have limited conformational flexibility, and thus the entropic driving force for solubility is limited. The presence of alkyl chains affords greater conformational freedom and thus increased solubility.[47] In the solid state, the side chains increase the free volume and decrease the van der Waals energy between the π-conjugated main chains. These effects combine to reduce the activation energy required to translate the chains past one another. Likewise, the greater free volume also contributes to greater conformational mobility (e.g., twisting, bending) along the backbone.[48] Thus, an increase in alkyl chain length leads to a decrease in the glass transition temperature (T_g)[49,50]—i.e., the α-transition temperature—of the backbone and thus elastic modulus.[51,52] In contrast, the thermal transition associated with relaxation of the pendant group (i.e., β-transition) increases with increasing side chain length.[49,53,54] At an operating temperature above the T_g, secondary thermal relaxation mechanisms are dependent on both the α-transition and β-transition temperatures, and allow for dissipation of kinetic energy in both the disordered (amorphous) and ordered phases (e.g., relaxation of aggregates, chain slip in crystallites).[48,55] Additional transitions are likely to be present in polymers with structures more complex than P3ATs, e.g., donor-acceptor polymers, which have two or more monomer subunits and may have branched side chains.[56]

Here, we used the well-known class of semiconducting polymer, regioregular poly(3-alkythiophene) (P3AT), as a model polymer. A number of studies have elucidated the effect on the linear side chain length on the mechanical properties in P3ATs.[57] For example, our laboratory has investigated the effects of side chain length and molecular weight on the scratch resistance and tensile behavior of P3AT thin films.[58–60] Progressive-load scratch testing determined that an increase in the alkyl chain length led to a decrease in

both cohesion and adhesion on silicon substrates.[58] Likewise, our group and others have used the buckling methodology[61] and quasi-free-standing tensile testing methodology (film-on-water)[62,63] to measure the elastic modulus relative to increasing length of the alkyl chain; the modulus was found to decrease monotonically. With regard to optoelectronic properties, studies have shown that a longer side chains in P3ATs typically corresponds to a decreased conductivity,[64] increased luminescence,[64–66] decreased hole mobility (as measured using organic field-effect transistors[67–69], although the effect is not always monotonic[70,71]), and increased barriers to hole injection.[72] In solar cells, the side chain length of P3ATs have been shown to be a significant determinant of the photovoltaic properties of P3AT:fullerene[51,73–75] (and P3AT:non-fullerene[76–78]) heterojunctions, all-polymer heterojunctions,[79,80] and perovskite solar cells.[81]

A comparatively smaller body of literature has studied the adhesive properties of P3ATs (or other conjugated polymers). A notable exception has been the work of Dauskardt and coworkers, who have made extensive use of the four-point-bend and double cantilever beam tests to understand how the morphology and composition of layers within an organic solar cell control adhesive and cohesive debonding behavior.[41,82–90] For example, Bruner and Dauskardt found that the cohesion energy[41] and resistance to decohesion growth[82] of a P3HT:PCBM bulk heterojunction increased from ~2 J m^{-2} to ~17 J m^{-2} as the molecular weight of P3HT increased. Choi et al. later extended this work to an acceptor-type polymer, which also exhibited increased fracture energy with increasing molecular weight.[88] Dupont et al. found that the presence of moisture drove the cohesive debonding of PEDOT:PSS films, which are commonly used as hole transporting layers in organic solar cells.[89] Brand et al. determined that debonding in a P3HT:PCBM solar cell always occurred cohesively within the bulk heterojunction, with an increasing mass ratio of P3HT (up to 75%) corresponding to an increase in fracture energy.[42] This fracture mechanism within the P3HT:PCBM bulk heterojunction has been attributed to tensile strain resulting in the delamination of P3HT chains from the fullerene interface, resulting in crazing.[91] Bruner et al. has shown that molecular intercalation of fullerene acceptors in organic bulk heterojunctions increases the cohesion energy, but increasing mass ratio of the fullerene decreases the cohesion energy.[92] Other work has studied the effect of

processing conditions (e.g., deposition processes,[83,93] humidity,[94] thermal annealing,[94–96] UV irradiation[94]) on the adhesive and cohesive properties. For example, Dupont et al. have found that thermal annealing can be used to modulate the interdiffusion at the P3HT:PCBM and PEDOT:PSS interface and increase the fracture energy.[94–96]

In this study, we probe the effect of the length of the alkyl side chain[57] (n = butyl, pentyl, hexyl, heptyl, octyl, and decyl) on the tensile, compressive, viscoelastic, and adhesive properties of P3AT films. Here, we use the film-on-water test, combined with three other tests conventionally used for coatings and adhesives but not generally applied to conjugated polymers: compressive nanoindentation (quasi-static and oscillatory), lap-joint (shear) tests, and peel tests. We use peel tests (rather than, e.g., double-cantilever beam tests) to evaluate the effect of a flexible adherend on the debonding behavior of the film, as conjugated polymers are likely to be used in flexible and stretchable form factors, as opposed to rigid ones.

4.2 Experimental Design

Material selection and mechanical testing. Poly(3-alkylthiophene)s were used as model polymers because they are widely studied in literature and readily available from commercial vendors. In order to reduce the effect of entanglement density on the measured properties, we used P3ATs with comparable molecular weights as reported by the vendors (and remeasured by us using gel permeation chromatography[97]), degrees of polymerization, and regioregularity (**Table D3**). Likewise, the molecular weight of all P3ATs were selected to be above the entanglement molecular weight of P3HT (typically ~10-20 kDa).[10,98] Detailed descriptions about the materials used are contained in **Appendix D**. We chose several modes of mechanical measurement because envisioned applications of semiconducting polymers are likely to be subjected to tensile, compressive, shearing, and peeling forces. Thus, we measured the mechanical properties five ways: a pseudo-free standing tensile test (tensile properties), nanoindentation (compressive properties),[99–103] lap joint shear tests (shear properties), 180° peel tests for a glass/P3AT interface (adhesive peel force), and 90° peel tests for a PEDOT:PSS/P3AT interface (peel force, debonding behavior). We

choose to use peel tests to evaluate the debonding behavior from a flexible adherend (e.g., adhesive tape) rather than a rigid adherend (e.g., a glass substrate).

Tensile tests and 90° peel tests were conducted with spin coated films. However, because nanoindentation required thicker films (as to reduce the impact of the silicon substrate on the measurement), drop casting was used to form the films (yielding films with thicknesses of ~4 μm). For adhesion measurements (i.e., lap joint shear tests and 180° peel tests), blade coating was used to deposit films on top of rectangular glass substrates, for which the measured adhesion is dependent on both layers (e.g., both the polymer film and the substrate). Here, we selected glass as the substrate in order to ensure a sharp interface with weak molecular force (i.e., with no covalent bonds or chemical interactions).[32] The goal of this selection was to evaluate the functionality of these films as viscoelastic adhesives (in which the dissipation of energy is mediated by chain reptation, entropy, intermolecular forces, and the stretching and breakage of covalent bonds). However, in device applications, the conjugated polymer film is likely to interface with another thin, flexible layer. Semiconducting polymers are incorporated in a variety of devices, and thus a broad range of interfaces must be considered. (Trends in adhesive and debonding behavior are unlikely to be universal, as adhesion is dependent on both surfaces in contact.) In this study, we conducted 90° peel tests where P3AT films are deposited on top of a PEDOT:PSS layer, which is ubiquitously used as a hole transport layer in organic solar cells.

Theoretical Calculations. Semi-empirical relationships between the mechanical properties and molecular characteristics of conventional (non-conjugated) polymers were developed by Seitz.[13] Here, we used methods developed by Seitz[13] and Fedors[104] (and later applied to conjugated polymers by Tahk et al.[105] and Savagatrup et al.[106]) to calculate the theoretical tensile modulus (E), bulk modulus (B), and cohesive energy (E_{coh}). Measured values for the T_g of each P3AT were extracted from literature[49,107–109] and used in these calculations. These calculated values were used as a guide and comparison for our measurements. Detailed methodologies are included in the Supporting Information (**Figure D1, Table D1, Table D2**).

Characterization of P3AT films. Characterization of the morphological and molecular characteristics of each P3AT film were performed to elucidate how such characteristics govern the bulk and interfacial properties of P3ATs. Gel permeation chromatography (GPC) was used to measure the molecular weight and dispersity of each P3AT (**Table D3**), while ultraviolet-visible (UV-vis) spectroscopy was used to determine the aggregation. The surface energy was calculated from contact angle measurements with water and diiodomethane using the harmonic mean Wu model.[110] Finally, atomic force spectroscopy (AFM) was used to elucidate changes in film topography relative to side chain length.

4.3 Results and Discussion

We summarize the mechanical characterization conducted in this work on a series of poly(3-alkylthiophene)s (P3ATs) in **Figure 4.1**. The mechanical properties were compared using two modes of deformation: tension and compression. Likewise, the adhesive behavior was evaluated using three measurements: lap joint shear tests, 180° peel tests (glass/P3AT/tape) and 90° peel tests (glass/PEDOT:PSS/P3AT/tape). We elected to use P3ATs with comparable number-average molecular weights (with the caveat that Koch et al. has shown that gel permeation chromatography, when calibrated with polystyrene standards, overestimates the molecular weight of P3HT by a factor of 1.67[111]) and degrees of polymerization (X_n) in order to isolate the effect of chemical structure on the mechanical properties (**Figure 4.1b, Table D3**).

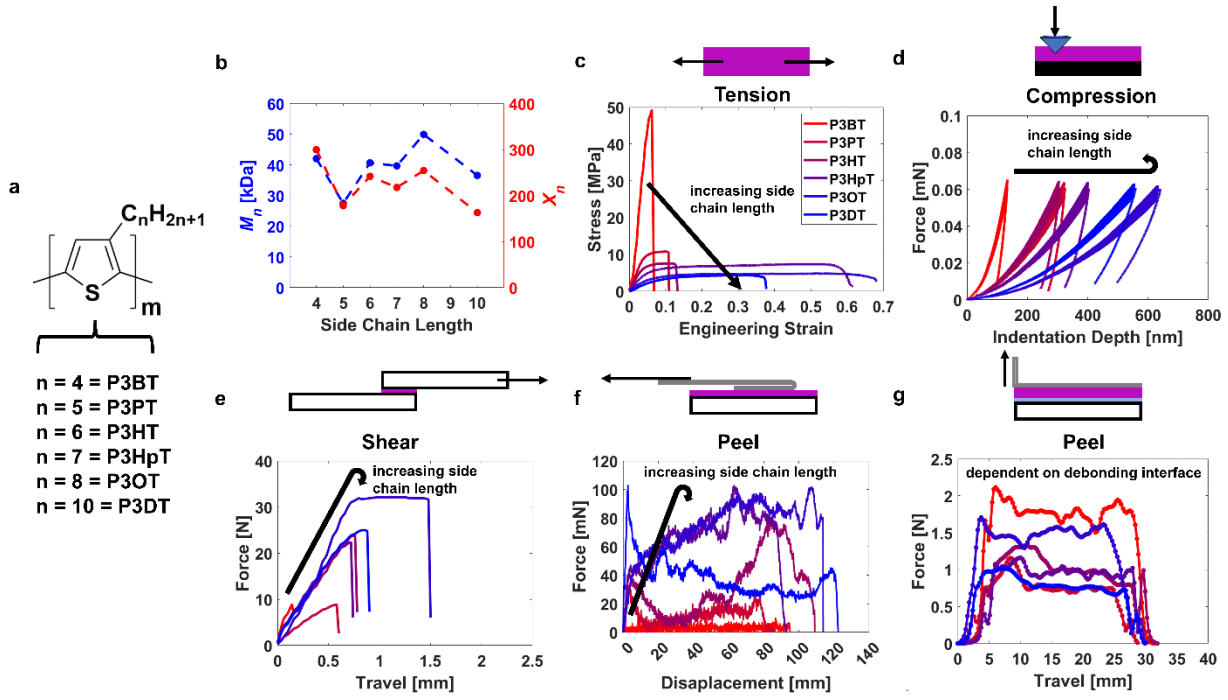

Figure 4.1. (**a**) Chemical structure of the poly(3-alkylthiophene) (P3AT) library investigated in this study. (**b**) Number-averaged molecular weight (M_n) and degree of polymerization (X_n) for each polymer in the library. (**c-g**) Summary of the (**c**) tensile, (**d**) compressive (oscillatory), (**e**) lap joint shear, (**f**) 180° peel (glass/P3AT/tape), and (**g**) 90° peel (glass/PEDOT:PSS/P3AT/tape) measurements performed in this study. Representative data are shown in each plot. The black arrows in (**c-f**) are to guide the eye to the trends in the data.

The tensile properties, as extracted from the stress-strain curves (**Figure 4.1c**), are shown in **Figure 4.2**. An increase in the side chain length makes it more favorable (i.e., requiring less mechanical energy) for a polythiophene chain to stretch and deform, which corresponds to a monotonic decrease in the elastic modulus (**Figure 4.2a, Table D4**), tensile strength (**Figure 4.2b**), and resilience (**Figure 4.2c**) of the solid film, along with a monotonic increase in linear elasticity (**Figure 4.2d**). We find the chemical structure to be a dominant determinant in the storage of energy (i.e., entropic elasticity for low-T_g P3ATs, molecular stiffness and Lennard-Jones interactions for high-T_g P3ATs) from which emerge monotonic relationships between the elastic parameters and the side chain length (**Figure 4.2a-d**).

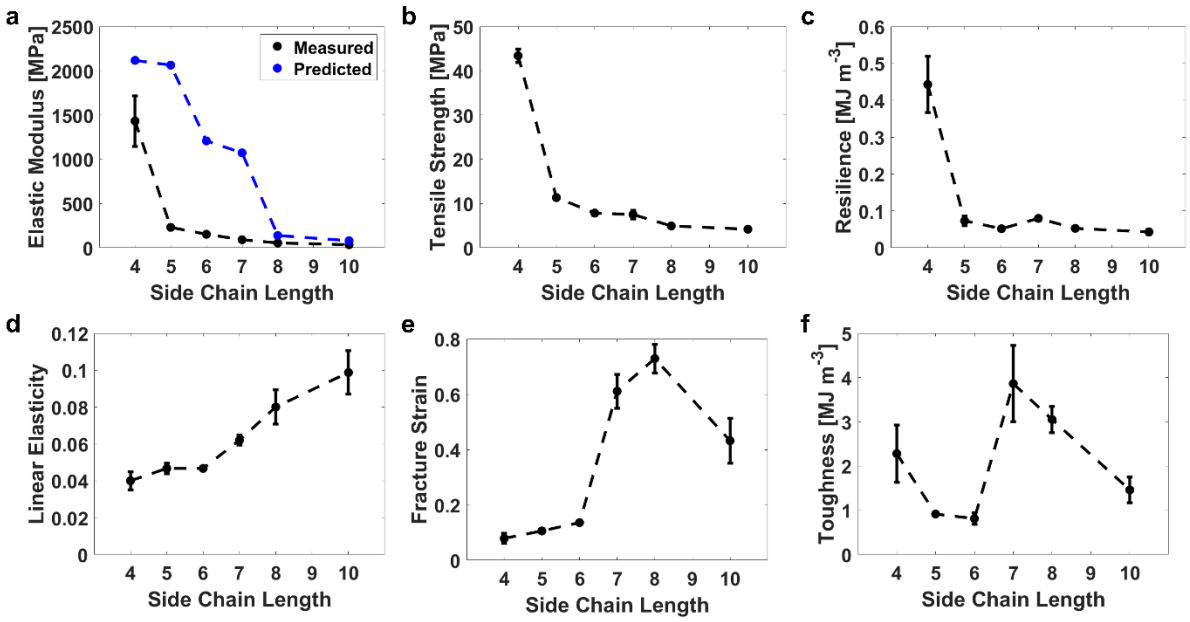

Figure 4.2. (**a**) Elastic modulus (measured and predicted), (**b**) tensile strength, (**c**) resilience, (**d**) linear elasticity, (**e**) fracture strain, and (**f**) toughness relative to side chain length as extracted from tensile measurements.

We find that the measured tensile modulus was lower than predicted for all P3ATs (**Figure 4.2a, Table D2, Table D4**). The predicted model agrees best for P3ATs with the shortest (P3BT) and longest (P3OT, P3DT) alkyl chains, with calculations suggesting moduli about twice that of measured values. However, the moduli for P3PT, P3HT, and P3HpT differed significantly between experiment and theory, by about one order of magnitude (**Table D2**). These observed differences suggest that empirical correlations determined from the mechanical behavior of conventional polymers do not apply perfectly to conjugated materials, particularly for those with glass transitions near the operating temperature (~37 °C to –12 °C for P3PT to P3HpT), and thus likely demonstrate both glassy and rubbery behavior (**Figure D2**). One reason for this misalignment could be the significantly greater difference between the thermal transitions associated with the backbone and the side chain for conjugated polymers as opposed to polymers with non-conjugated backbones.

When deformation extends beyond the elastic regime, dissipation of energy is manifested as plastic deformation, cracking, or fracture of the polymer film. Here, dissipation occurs by the disruption of

intermolecular interactions (e.g., π-π stacking), active slip (e.g., along the (100) and (010) planes),[112] chain pullout, and by the breaking of covalent bonds. Previous studies have shown that increasing the length of the alkyl side chain can allow for greater ordering, as well as the formation of interdigitated (e.g., "Form II") structures, which can in some circumstances lead to brittle behavior.[113,114] However, the usual result of an increase in the alkyl chain length is to increase the lamellar spacing[115] and to decrease the π-π stacking.[67,69,116] These effects suggest a weakening of van der Waals forces between polymer chains.

Whereas the parameters associated with elasticity exhibited monotonic relationships with the length of the alkyl side chain (**Figure 4.2a-d**), those associated with plasticity—namely fracture strain and toughness (**Figure 4.2e-f**), exhibited maxima. First, there was a significant increase in fracture strain from P3HT (n = 6) to P3HpT (n = 7), likely due to the T_g of P3HpT being significantly lower than room temperature. Second, there appeared to be diminishing returns to increasing the fracture strain as the side chain length increases. An increase in side chain length from P3HpT (n = 7) to P3OT (n = 8) resulted in a similar fracture strain, while that of P3DT (n = 10) was lower. It is possible the decrease in fracture strain is in part due to a comparatively low degree of polymerization for P3DT relative to P3OT (**Table D3**). However, AFM experiments by Jaing et al. investigating the unfolding behavior of P3AT chains show that a single P3OT chain can extend further than a single P3DT chain (ΔL of ~14 nm compared to ~12 nm).[117] Likewise, buckling experiments by Printz et al. suggest that both the fracture strain and yield point of P3OT are greater than that of P3DDT (n = 12).[118] Thus, previous literature suggests that the decrease in fracture strain from n = 8 to n = 10 cannot solely be explained here by differences in degree of polymerization. Rather, the maximum in fracture strain (which occurs around n = 7 to 8) may represent a compromise between competing effects. That is, as the side chain is lengthened, the glass transition temperature decreases and the film becomes more ductile. However, increase the length of the alkyl chain too much and the volume fraction of load-bearing covalent bonds in the main chain is diluted to the point where the solid becomes waxy and loses its cohesion.

The toughness, taken as the energy density absorbed by a solid prior to fracture, exhibits a similar maximum around n = 7 to 8 (**Figure 4.2f**) owing to the large extensibility of these two entries in the series. Interestingly, the toughness of P3BT (n = 4) is nearly as high. We attribute this behavior to the extraordinarily large tensile strength exhibited by the glassiest (T_g ~ 65 °C[107]) of P3ATs tested (**Figure 4.1c**, red curve). At an operating temperature significantly below the glass transition, the brittleness (and high strength) stems from the glassy nature of the polymer. Nevertheless, we observed some plastic flow beyond the regime of linear elasticity for P3BT (**Figure D3**), suggesting some mobility despite the kinetically frozen structure.[48]

The compressive properties, as extracted from nanoindentation measurements (**Figure 4.1d**), are shown in **Figure 4.3**. Again, we found essentially monotonic relationships between the elastic properties (elastic modulus, hardness, elastic work) and the alkyl chain length (**Figures 4.3a-c**), for both quasi-static and dynamic (oscillatory) measurements. However, we do observe a greater modulus (and decreased elastic work) for P3DT in comparison to P3OT. Previous studies have observed greater crystalline fractions in n = 10, 12 compared to n = 8,[54] which likely result in this increased modulus. It is also possible that the slow drying kinetics (due to the solidification process of a drop cast film) and long alkyl side chain allow for the formation of morphological structures (e.g., nanowhiskers and nanoribbons resulting in greater π-π stacking[119]) that contribute to this difference in mechanical behavior. Under compression, the measured moduli were significantly greater than those extracted from tensile measurements (**Figure 4.3a, Table D4**). We attribute this difference to the decrease in film volume under compression in comparison to an increase under tension (i.e., the elastic modulus is related to the compressive modulus by the Poisson's ratio[13]). Under real (i.e., non-theoretical) measurements, larger differences between the compressive and tensile moduli can be observed due to the behavior of defects within the solid film under the two modes of measurement.[59] For example, under tension, void spaces are stretched, propagating fracture as the size of the defect grows (i.e., crazing). Under compression, while localized deformation still occurs, some cracks and fracture interfaces can be closed, slowing down compaction and preventing fracture from propagating

across larger length scales.[120] Previous work has shown similar increases in measured elastic modulus (and tensile strength) for films of poly(methyl methacrylate) between measurements under tension and compression.[121]

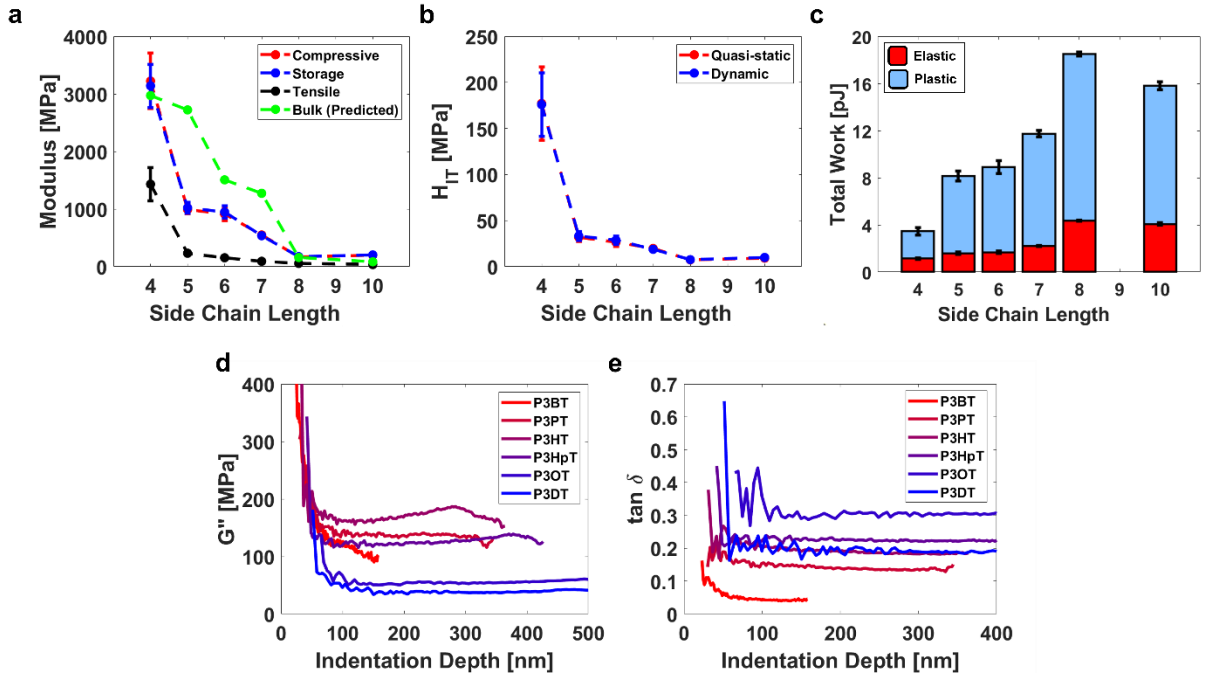

Figure 4.3. (**a**) Elastic modulus (measured and predicted) and (**b**) indentation hardness were extracted from quasi-static nanoindentation measurements, while (**c**) work, (**d**) loss modulus, and (**e**) tan δ were extracted from dynamic (oscillatory) measurements. The tensile modulus is included in the comparison of moduli for reference.

As such, our findings agree with empirical relationships that predict the compressive (bulk) modulus to be greater than the tensile modulus in non-conjugated polymers (**Figure D4**).[13] We also observed greater agreement between the calculated and measured values of the compressive modulus compared to the tensile modulus (**Table D2, D4**), with the caveat that there was still a significant difference between the two for polymers with glass transitions near room temperature (P3PT, P3HT, and P3HpT, see discussion in the Supporting Information).

From oscillatory indentation measurements, storage modulus (**Figure 4.3a, D5**), loss modulus (**Figure 4.3d**), and tan δ (**Figure 4.3e**) were extracted. Under dynamic conditions, we see significant differences between the loss modulus measured for polymers with glass transition temperatures above and

below the operating temperature. Previous work on polycarbonate has shown that the deformation phenomena of the solid film is in part determined by the crazing (deformation resulting from an increase in volume, e.g., formation of void spaces by chain scission or disentanglement) and shear yield (deformation without a change in volume, e.g., chain slippage) transitions.[122,123] Kramer and Berger showed that such transitions are associated with the glass transition temperature, for which the transition between crazing and shear yield occurs approximately 28 °C below the T_g for polycarbonate.[122,124] Thus, changes in deformation behavior could possibly provide insight as to the differences between n = 4–5 and n = 6–10 (where there is a monotonic decrease in G"). The damping behavior (tan δ) is calculated as the ratio of the loss and storage (elastic) modulus, for which there was a monotonic increase (from ~0.05 to ~0.3) relative to alkyl chain length for n = 4–8. The tan δ is dependent on the operating temperature of the film (here, room temperature) relative to the thermal transitions[48] associated with the polymer film (e.g., glass transition, for which there was a constant decrease as n increased[49]). Our findings were consistent with data reported by the Gu group on the thermal behavior of P3PT and P3HT using dynamic mechanical analysis (DMA) of glass fiber mesh samples.[125] However, the tan δ of P3DT (n = 10) was measured to be 0.2, similar to that of P3HT. This difference is attributed to an increase in the storage modulus (G') (**Figure 4.3a, D5**), which possibly stems from an increase in morphological ordering.[54,106,119]

For indentation of all P3AT films, plastic work was greater than elastic work, both under tension (**Figure D3**) and compression (**Figure 4.3c**). The elastic work dissipated increased relative to increasing side chain length, which was counter to the trend observed for resilience under tension (yet similar to that of linear elasticity) (**Figure 4.2c, 4.2d**). The one outlier was P3OT, which exhibited both the greatest amount of plastic and elastic work. As such, both measurements in tension and in compression suggest that the plastic behavior of P3AT films is dependent, non-monotonically, on the side chain length.

To elucidate the effect of the side chain length on the adhesive properties of P3ATs, lap shear (**Figures 4.4a-c, D6**), 180° peel test (**Figures 4.4d-e, D7, D8**), and 90° peel test samples (**Figures D8, D9**) were prepared. When subject to shear strain (**Figure 4.4a**), an increase in the alkyl chain length generally

resulted in an increase in the adhesive strength (**Figure 4.4b**) and energy dissipated (**Figure 4.4c**, normalized to the surface area of the lap joint). Due to the debonding behavior of P3OT, the total energy dissipated by the lap joint was significantly greater than that of the rest of the P3ATs. These results correlate strongly with the fracture strains and compressive work, in that P3OT has the greatest fracture strain (**Figure 4.2e**), total work (**Figure 4.3c**) and adhesive strength (**Figure 4.4b**). Likewise, the increase in alkyl chain length from n = 8 to n = 10 resulted in both a decrease in the fracture strain and adhesive strength, suggesting a maximum in the adhesive strength for P3OT.

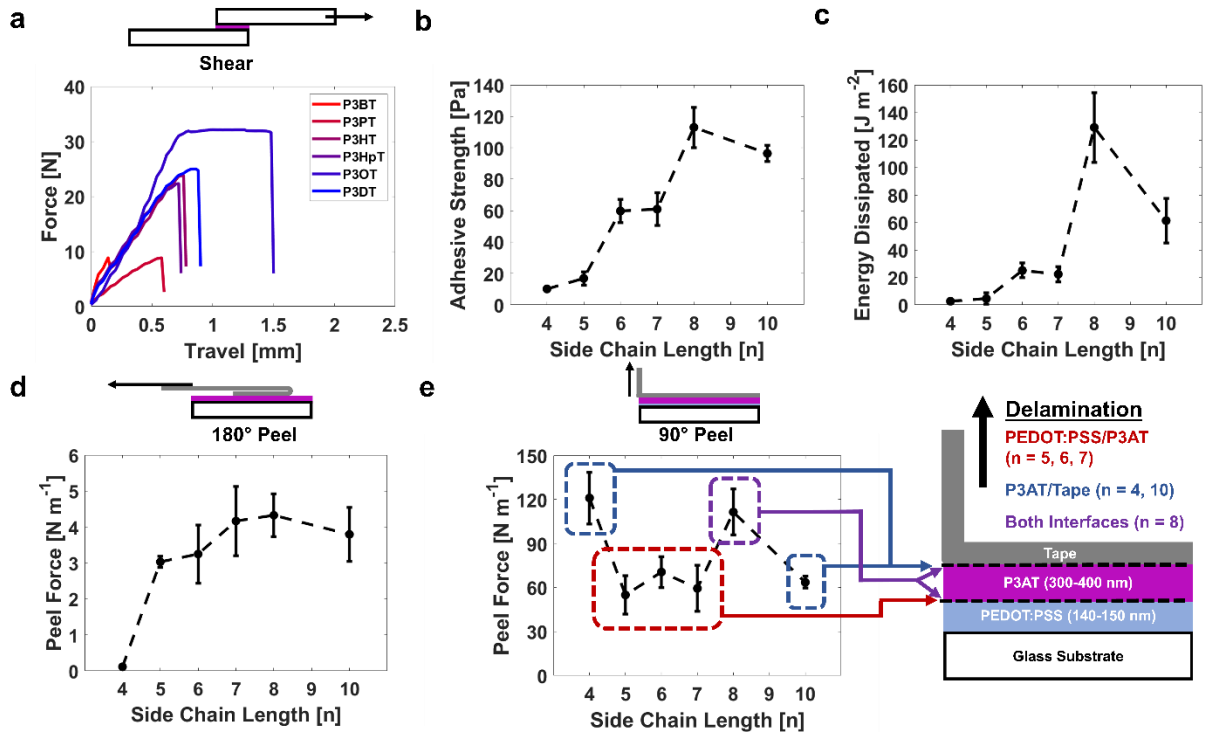

Figure 4.4. (**a**) Lap joint shear tests were conducted on glass substrates glued together by each P3AT film (for which representative force-displacement curves are shown) from which the (**b**) adhesive strength and (**c**) energy dissipated by the adhesive material are extracted (**Figure D6**). Likewise, 180° peel test samples were measured by peeling P3AT films off using adhesive tape (**Figure D7**). From force-displacement curves, the (**d**) adhesive peel force (normalized to the width of the tape) was measured relative to the side chain length (**Figure D8**). (**e**) Finally, 90° peel tests were performed on glass/PEDOT:PSS/P3AT stacks using adhesive tape, from which the peel force was measured and debonding interface was photographed (**Figures D8, D9**). The thickness of the 180° peel test films ranged from 100-150 nm in thickness while the P3AT films used for 90° peel tests were between 300-400 nm (**Figure D8**).

With an operating temperature significantly below the glass transition, P3BT chains are highly immobile (glassy) at room temperature, and thus cannot rearrange to encourage the dissipation of

mechanical energy throughout the film. Thus, P3BT (n = 4) films showed the least adhesive strength and displacement (~0.15 mm). P3PT, likewise with a glass transition above the operating temperature, showed a comparable adhesive strength. When the side chain is sufficiently long such that the glass transition is below the operating temperature (n > 5), the polymer film functions as a viscoelastic adhesive between rigid substrates.[126] P3ATs with n = 5–7 and n = 10 all failed with a displacement between 0.5 and 1 mm. However, the maximum load applied was low, suggesting that these polymer films have little resistance to flow.[127] Finally, P3OT showed a clear maximum in adhesive strength, which is likely attributed to the greatest amount of viscoelastic dissipation of energy (as suggested by the relatively high value of tan δ, **Figure 4.3e**). The plateau in force relative to increasing displacement (>1 mm) for P3OT suggests that highly mobile polymer chains can undergo significant rearrangement to dissipate the mechanical work (**Figure 4.4a**).

Although a clear trend is present from these lap shear measurements, the calculated adhesive strengths of this P3AT library were extremely low (common polymeric adhesives have adhesive strengths on the order of MPa). Our calculations were likely significant underestimates of the actual adhesive strength, as we assume uniformity of the polymer film. Photographs of representative samples (**Figure D6**) show that the lap joints were primarily held together by a thicker outer border of polymer. A more accurate estimate of the surface area of the adhesive would likely be that corresponding to the thick border of the overlapping lap joint. As such, the calculated adhesive strength should be taken as representative of how these samples were prepared, with more importance being given to the qualitative trend rather than the numerical values. An extended discussion is included in **Appendix D** along with **Figure D6**.

Similar lap shear measurements were conducted on a family of methacrylate-based copolymers with increasing alkyl chain lengths by Payra et al.[128] The authors found a similar maximum when comparing the measured lap shear strength against the glass transition of the synthesized copolymers.[128] Coincidentally, the copolymers with octyl (and 2-ethyl hexyl) side chains also resulted in the greatest lap shear strength (~2.8 MPa). At low glass transitions (T_g ~–55 °C to –40 °C), copolymers with decyl and dodecyl side chains

were highly ductile, which resulted in mobile polymer chains that yielded easily when subject to low loads (e.g., a low tensile strength but a high fracture strain). In contrast, copolymers with methyl and butyl side chains (T_g ~–70 °C to 130 °C) had insufficient ductility due to the glassy nature of the polymer film, which resulted in highly brittle lap joints that, again, failed at low loads once energy storage mechanisms were saturated. Our findings thus suggest that the ability of a conjugated polymer film to function as a lap shear adhesive is dependent on a balance between both a high tensile strength and high fracture strain (as opposed to simply a high toughness, where the strength or ductility could possibly be low).

Additionally, 180° peel tests were conducted to further study the debonding behavior of P3ATs from glass substrates (**Figure 4.4d, D7, D8**). P3BT, with its glassy behavior, required minimal force to delaminate (**Figure D7**). This behavior corresponds well with the low plasticity and low viscoelasticity (i.e., low tan δ). In contrast, the adhesive peel forces for polymers above their glass transition (n > 5) showed a trend of increasing peel force relative to side chain length (despite random fluctuations in force inherent to the measurement technique[32]), with P3DT again behaving counter to the trend. We observed a maximum around n = 7–8, with P3HpT and P3OT measuring comparable peel forces (**Figure 4.4d**). This result agreed with our previous findings, as the progression of the peeling interface results in both tensile and compressive stresses, and depend strongly on the viscoelastic behavior.[32] P3HpT and P3OT films were measured to have the greatest measured toughness (and also plastic dissipation of energy, which is of particular importance to the behavior of the crack growth[129]) under tension and compression, as well as the greatest measured values of tan δ at room temperature (and thus most favorable viscoelastic behavior).

In most envisioned device applications, an applied semiconducting polymer film will likely interface with another transport or sensing layer. In organic solar cells, a polymeric bulk heterojunction is thus often deposited on top of a PEDOT:PSS hole transport layer. We conclude by investigating how an increase in side chain length changes the debonding behavior of a glass/PEDOT:PSS/P3AT/tape stack using 90° peel tests (**Figure 4.4e, D8, D9**). We find that delamination occurs at either the PEDOT:PSS/P3AT (n = 5-7) or P3AT/tape (n = 4, 10) interface, with a transition at n = 8 between the two (**Figure D9**).

Tuning the side chain structure of a conjugated polymer is a common strategy for optimizing the surface energy of the solid film.[130–132] However, alteration of the ratio of saturated to unsaturated groups within the solid film also potentially affects the surface energy, which would affect the adhesion between two films in contact arising from van der Waals forces.[133] Contact angle measurements were used to determine the effect of the alkyl chain length on the surface energy of the resulting polymer film (**Figure 4.5a**). As-cast films showed no coherent trend, with all polymers having an approximate surface energy of ~30 mJ m^{-2} (although complete elimination of the relatively high-boiling solvent, chlorobenzene, was unlikely without thermal treatment). However, when thermally annealed, the surface energy decreased with increasing side chain length. These findings validate previous results showing that the water contact angle increases for P3AT films of increasing side chain length.[106,134] Annealing removes residual solvent and may also promote the reorientation of the polymer chains into domains with edge-on texture (as previous studies have shown with P3HT).[135,136] Thus, this increase in water contact angle (and decrease in measured surface energy) is attributed to the increased presentation of hydrophobic alkyl side chains at the surface.[134] This observation suggests that the adhesion between the tape and the P3AT film decreases as the side chain length increases, which explains the debonding behavior shown in the 90° peel tests (**Figure D9**).

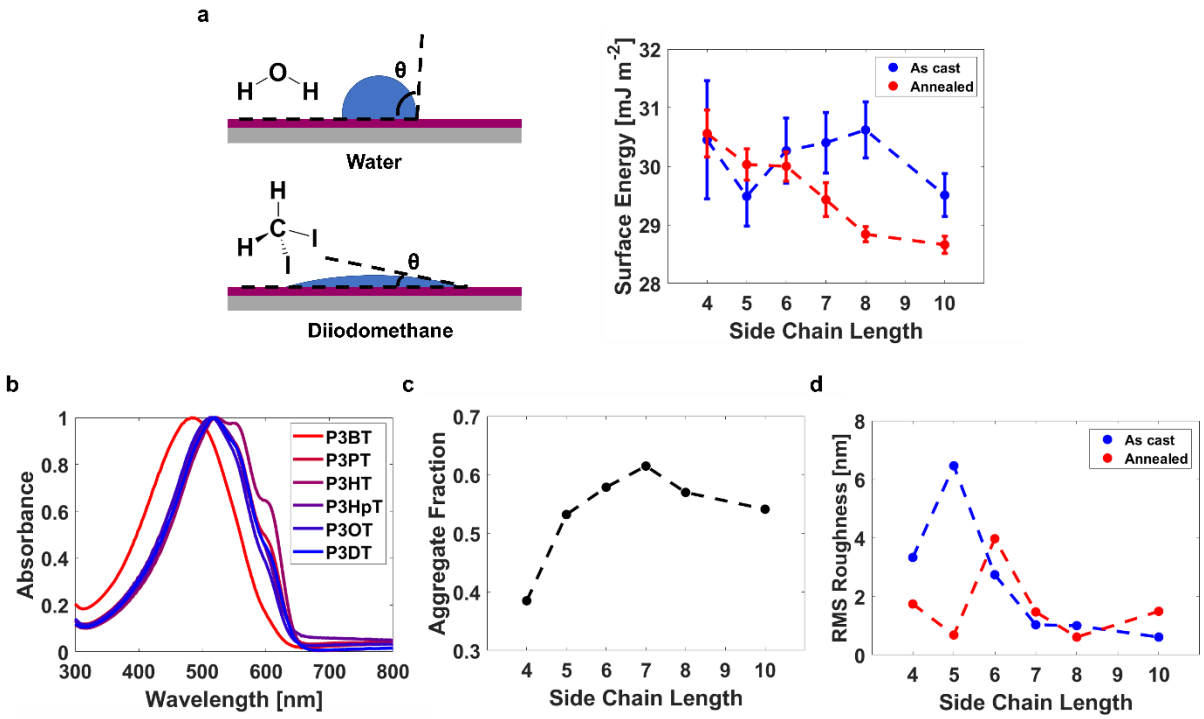

Figure 4.5. (**a**) Surface energy measurements of as-cast and annealed (100 °C, 30 min) P3AT films were made using contact angle measurements of water and diiodomethane. (**b**) UV-vis spectra of P3AT films, from which the (**c**) aggregate fraction was extracted using a model developed by Spano and coworkers. (**d**) The mean square roughness for as cast and annealed P3AT films were measured using AFM (**Figure S10**).

The greatest peel force was measured for P3BT (~120 N m^{-1}), which delaminated at the P3BT/tape interface. While the high surface energy allowed for the best adhesion between the tape and polymer film, the high stiffness and strength of the film likely prevented bending, and thus fracture from propagating throughout the film. The mechanical properties of the PEDOT:PSS layer also likely contributed to this observed debonding behavior. P3BT was the only polymer in the series to have an elastic modulus greater than PEDOT:PSS (~385 MPa[137]), which likely prevented crazing at the PEDOT:PSS/P3BT interface due to elastic mismatch. In contrast, n = 5–7 all delaminated at the PEDOT:PSS/P3AT interface with low measured peel forces (~60 N m^{-1}), which is consistent with findings from the Dauskardt group showing that the PEDOT:PSS/P3HT:PCBM interface is weakest within a device stack.[42,84] At n = 8, there was a transition at which the adhesion between the P3AT/tape interface became weak enough such that it becomes the most favorable debonding interface. However, at this transition, the PEDOT:PSS/P3OT interface was still weak

enough to delaminate, resulting in debonding occurring at both interfaces (**Figure D8b**). This meandering fracture path,[86] as well as the formation of four new surfaces rather than two, likely resulted in a relatively high measured peel force (~110 N m^{-1}). Finally, for P3DT, the P3DT/tape interface was clearly the weakest due to the poor adhesion between the two; the same amount of force needed to delaminate the P3AT film from PEDOT:PSS for n = 5–7 is sufficient to peel tape off the P3DT film. As such, these findings suggest that the length (and structure) of the side chain play a significant role in determining the fracture behavior of a device stack which incorporates a conjugated polymer film. Likewise, the mechanical properties of the P3AT film (as well as the adjacent layers) govern how debonding occurs and how the fracture tip propagates. For example, both P3BT and P3DT delaminated at the P3AT/tape interface, yet for different reasons.

Finally, the aggregation and topography of the P3AT films were characterized using UV-vis (**Figure 4.5b, 4.5c**) and AFM (**Figure 4.5d, D10**) to determine their effects on the observed mechanical behaviors. A comparison of the measured aggregate fraction to the degree of polymerization showed no apparent trend (**Figure D11**). P3BT had the lowest aggregation (~0.4), likely due to the kinetically frozen structure preventing the formation of aggregates, while all other P3ATs had aggregate fractions above 0.5. Interestingly, P3HpT had the greatest fraction of aggregates, which possibly contributed to the significant plastic deformation (e.g., energy dissipated due to the breaking of aggregates) and relatively high fracture strain observed from FOW measurements. Likewise, AFM phase images were used to investigate the topography of P3AT films (**Figure D10**), from which the root-mean roughness are extracted (**Figure 4.5d**), as the adhesion is additionally dependent on the contact area between two surfaces (and thus, the roughness and topography of each surface).[138–140] For example, an increased surface roughness can improve mechanical adhesion by allowing for the interlocking of the two surfaces,[141,142] or significantly reduce adhesion when an elastic solid (e.g., rubber) is in contact with a hard substrate.[143] However, the P3AT films used in this study were similar in surface roughness, and thus not likely to have significantly affected the measurements performed.

4.4 Conclusions

Here, we sought to understand how the length of the alkyl chain side chain affects the mechanical and adhesive properties of a library of poly(3-alkylthiophene) (P3AT) films using four methods: a quasi-free-standing tensile test, compressive nanoindentation, a lap-joint shear test, and adhesive peel tests. We find that the length of the alkyl side chain significantly impacts the elastic storage of energy, plastic dissipation of energy, and surface energy. While elastic properties have a relatively monotonic relationship relative to side chain length, plastic properties are typically non-monotonic. These relationships between mechanical behavior (and electronic performance) and side chain length govern the viscoelasticity of the P3AT film. At a specific operating temperature (here, room temperature), the bulk (e.g., viscoelasticity, plasticity, and elasticity) and surface (e.g., viscoelasticity and surface energy) properties govern the ability of the polymer film to function as an ersatz adhesive within a device stack. For poly(3-alkylthiophene) thin films, we find that the most favorable mechanical properties for stretchable and soft electronics occur with a side chain length of n = 7 (P3HpT) or n = 8 (P3OT). Similarly, the increase in side chain length results in an relatively monotonic tradeoff between increasing deformability ("softness") and decreasing surface energy. As a result, P3OT displays the best adhesive functionality, both as a viscoelastic adhesive gluing together two glass slides and as a polymeric interlayer in an example device stack (e.g., when deposited on top of PEDOT:PSS). We summarize our findings below (**Figure 4.6**).

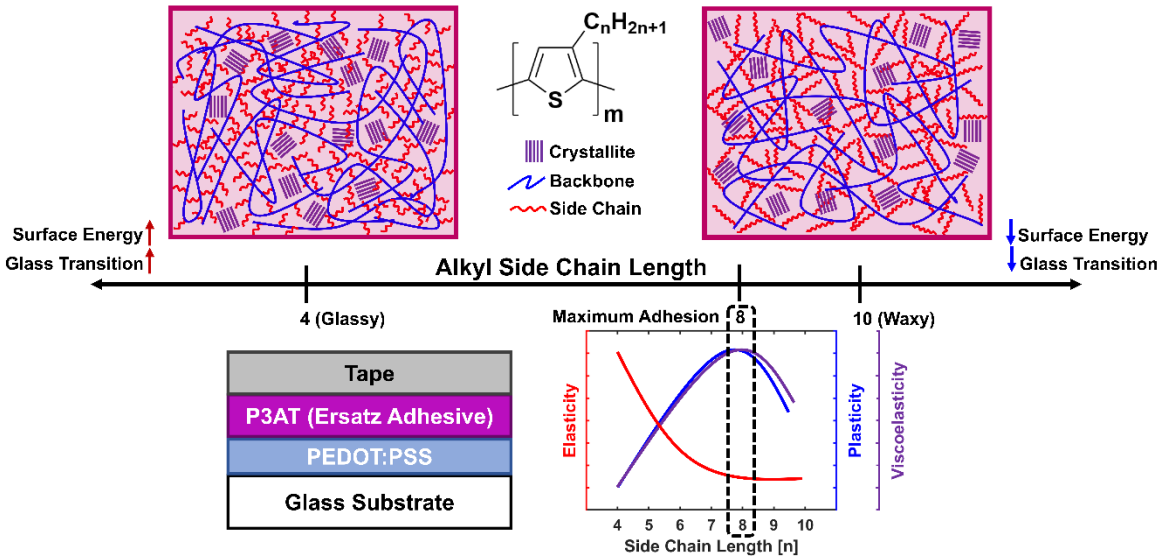

Figure 4.6. Summary of changes in the morphology and mechanical behavior in poly(3-alkylthiophene) thin films as the side chain length increases from n = 4 to n = 10. These monotonic and non-monotonic relationships govern the functionality of the semiconducting polymer film to function as an ersatz adhesive within a device stack.

The envisioned application of semiconducting polymers in flexible and stretchable electronics is dependent on the electronic, mechanical, and adhesive performance, which often have tradeoffs that must be optimized. Here, we demonstrate how methods common to conventional polymers can be used to characterize the mechanical behavior of semiconducting polymers in detail in order to understand these tradeoffs. While our study only evaluates the effect of side chain length on one model family of conjugated polymers (i.e., poly(3-alkylthiophene)), the backbone structure is also a significant determinant of the mechanical and adhesive properties of the solid polymer film. Likewise, while most conjugated polymers still feature linear or branched alkyl side chains, the chemical structure can be rationally designed to improve the mechanical and adhesive performance of the polymer film (functionalization of the side chain with e.g., amines, catechol, hydrogen bonding moieties) within a device stack. Additionally, semiconducting polymers are applied in a broad range of device applications, and thus interface with many types of sensing, transport, and electrode materials. The adhesive and debonding behavior of many of these interfaces are seldom explored, and offer opportunities for improving the mechanical robustness and stability of these devices. For example, the interface of the lap joint shear samples can be changed (e.g., by

depositing PEDOT:PSS on top of the glass substrates) in order to investigate interfaces more relevant to device stacks. Finally, empirical correlations have been developed to relate chemical and molecular structure to elastic modulus in conventional (non-conjugated) polymers, but these correlations do not apply well to conjugated polymers, particularly those operating at a temperature where both glassy and rubbery behavior is demonstrated. As such, our findings motivate further study of how the different electronic, mechanical, and adhesive figures of merit can be tuned be systematically tuned by rational design of the polymer structure.

4.5 Acknowledgements

This work was supported by the Air Force Office of Scientific Research (AFOSR) grant no. FA9550-22-1-0454 to D.J.L. A. X. C. acknowledges support from the UC President's Dissertation Year Fellowship. S.S.P. and C.G.H. acknowledge financial support from the Zimin Institute for Smart and Sustainable Cities at ASU under award no. AWD00034680. The authors acknowledge the use of facilities and instrumentation supported by NSF through the UC San Diego Materials Research Science and Engineering Center (UCSD MRSEC), grant DMR-2011924. This work was performed in part at the San Diego Nanotechnology Infrastructure (SDNI) of UC San Diego, a member of the National Nanotechnology Coordinated Infrastructure, which is supported by the National Science Foundation (Grant ECCS-2025752). The authors would like to thank Ricardo De-luna for support with the GPC measurements and Prof. Shengqiang Cai for helpful discussions.

4.6 References

(1) Kayser, L. V.; Lipomi, D. J. Stretchable Conductive Polymers and Composites Based on PEDOT and PEDOT:PSS. *Adv. Mater.* **2019**, *31*, 1–13.

(2) Lee, C.; Lee, S.; Kim, G. U.; Lee, W.; Kim, B. J. Recent Advances, Design Guidelines, and Prospects of All-Polymer Solar Cells. *Chem. Rev.* **2019**, *119*, 8028–8086.

(3) Someya, T.; Bao, Z.; Malliaras, G. G. The Rise of Plastic Bioelectronics. *Nature* **2016**, *540*, 379–385.

(4) Heeger, A. J. Semiconducting Polymers: The Third Generation. *Chem. Soc. Rev.* **2010**, *39*, 2354–2371.

(5) Forrest, S. R.; Thompson, M. E. Introduction: Organic Electronics and Optoelectronics. *Chem. Rev.* **2007**, *107*, 923–925.

(6) Khau, B. V.; Scholz, A. D.; Reichmanis, E. Advances and Opportunities in Development of Deformable Organic Electrochemical Transistors. *J. Mater. Chem. C* **2020**, *8*, 15067–15078.

(7) Liang, Y.; Wu, Y.; Feng, D.; Tsai, S. T.; Son, H. J.; Li, G.; Yu, L. Development of New Semiconducting Polymers for High Performance Solar Cells. *J. Am. Chem. Soc.* **2009**, *131*, 56–57.

(8) Liang, Y.; Yu, L. A New Class of Semiconducting Polymers for Bulk Heterojunction Solar Cells with Exceptionally High Performance. *Acc. Chem. Res.* **2010**, *43*, 1227–1236.

(9) Lee, G. H.; Moon, H.; Kim, H.; Lee, G. H.; Kwon, W.; Yoo, S.; Myung, D.; Yun, S. H.; Bao, Z.; Hahn, S. K. Multifunctional Materials for Implantable and Wearable Photonic Healthcare Devices. *Nat. Rev. Mater.* **2020**, *5*, 149–165.

(10) Root, S. E.; Savagatrup, S.; Printz, A. D.; Rodriquez, D.; Lipomi, D. J. Mechanical Properties of Organic Semiconductors for Stretchable, Highly Flexible, and Mechanically Robust Electronics. *Chem. Rev.* **2017**, *117*, 6467–6499.

(11) Nielsen, L. E.; Landel, R. F. *Mechanical Properties of Polymers and Composites*, 2nd editio.; CRC Press, 1993.

(12) Cooper, A. R. Mechanical Properties of Polymers: The Influence of Molecular Weight and Molecular Weight Distribution. *J. Macromol. Sci. Part C* **1972**, *8*, 57–199.

(13) Seitz, J. T. The Estimation of Mechanical Properties of Polymers from Molecular Structure. *J. Appl. Polym. Sci.* **1993**, *49*, 1331–1351.

(14) Chen, A. X.; Hilgar, J. D.; Samoylov, A. A.; Pazhankave, S. S.; Bunch, J. A.; Choudhary, K.; Esparza, G. L.; Lim, A.; Luo, X.; Chen, H.; Runser, R.; Mcculloch, I.; Mei, J.; Hoover, C.; Printz, A. D.; Romero, N. A.; Lipomi, D. J. Increasing the Strength, Hardness, and Survivability of Semiconducting Polymers by Crosslinking. *ACS Appl. Mater. Interfaces* **2022**, *10*, 2202503.

(15) Wang, Z.; Zhang, D.; Xu, M.; Liu, J.; He, J.; Yang, L.; Li, Z.; Gao, Y.; Shao, M. Intrinsically Stretchable Organic Solar Cells with Simultaneously Improved Mechanical Robustness and Morphological Stability Enabled by a Universal Crosslinking Strategy. *Small* **2022**, *2201589*, 1–10.

(16) Kim, M. J.; Lee, M.; Min, H.; Kim, S.; Yang, J.; Kweon, H.; Lee, W.; Kim, D. H.; Choi, J. H.; Ryu, D. Y.; Kang, M. S.; Kim, B. S.; Cho, J. H. Universal Three-Dimensional Crosslinker for All-Photopatterned Electronics. *Nat. Commun.* **2020**, *11*, 1–11.

(17) Rumer, J. W.; McCulloch, I. Organic Photovoltaics: Crosslinking for Optimal Morphology and Stability. *Mater. Today* **2015**, *18*, 425–435.

(18) Zheng, Y.; Yu, Z.; Zhang, S.; Kong, X.; Michaels, W.; Wang, W.; Chen, G.; Liu, D.; Lai, J.; Prine, N.; Zhang, W.; Nikzad, S.; Cooper, C. B.; Zhong, D.; Mun, J.; Zhang, Z.; Kang, J.; Tok, J. B.; Mcculloch, I.; Qin, J.; Gu, X.; Bao, Z. A Molecular Design Approach towards Elastic and Multifunctional Polymer Electronics. *Nat. Commun.* **2021**, 1–11.

(19) Xu, J.; Wang, S.; Wang, G. N.; Zhu, C.; Luo, S.; Jin, L.; Gu, X.; Chen, S.; Feig, V. R.; To, J. W. F.; Rondeau-gagné, S.; Park, J.; Schroeder, B. C.; Lu, C.; Oh, J. Y.; Wang, Y.; Kim, Y.; Yan, H.; Sinclair, R.; Zhou, D.; Xue, G.; Murmann, B.; Linder, C.; Cai, W.; Tok, J. B. Highly Stretchable Polymer Semiconductor Films through the Nanoconfinement Effect. **2017**, *64*, 59–64.

(20) Wang, S.; Xu, J.; Wang, W.; Wang, G. J. N.; Rastak, R.; Molina-Lopez, F.; Chung, J. W.; Niu, S.; Feig, V. R.; Lopez, J.; Lei, T.; Kwon, S. K.; Kim, Y.; Foudeh, A. M.; Ehrlich, A.; Gasperini, A.; Yun, Y.; Murmann, B.; Tok, J. B. H.; Bao, Z. Skin Electronics from Scalable Fabrication of an Intrinsically Stretchable Transistor Array. *Nature* **2018**, *555*, 83–88.

(21) Xu, J.; Wu, H. C.; Zhu, C.; Ehrlich, A.; Shaw, L.; Nikolka, M.; Wang, S.; Molina-Lopez, F.; Gu, X.; Luo, S.; Zhou, D.; Kim, Y. H.; Wang, G. J. N.; Gu, K.; Feig, V. R.; Chen, S.; Kim, Y.; Katsumata, T.; Zheng, Y. Q.; Yan, H.; Chung, J. W.; Lopez, J.; Murmann, B.; Bao, Z. Multi-Scale Ordering in Highly Stretchable Polymer Semiconducting Films. *Nat. Mater.* **2019**, *18*, 594–601.

(22) Melenbrink, E. L.; Hilby, K. M.; Choudhary, K.; Samal, S.; Kazerouni, N.; McConn, J. L.; Lipomi, D. J.; Thompson, B. C. Influence of Acceptor Side-Chain Length and Conjugation-Break Spacer Content on the Mechanical and Electronic Properties of Semi-Random Polymers. *ACS Appl. Polym. Mater.* **2019**, *1*, 1107–1117.

(23) Sugiyama, F.; Kleinschmidt, A. T.; Kayser, L. V.; Alkhadra, M. A.; Wan, J. M. H.; Chiang, A. S. C.; Rodriquez, D.; Root, S. E.; Savagatrup, S.; Lipomi, D. J. Stretchable and Degradable Semiconducting Block Copolymers. *Macromolecules* **2018**, *51*, 5944–5949.

(24) Lee, Y.; Oh, J. Y.; Xu, W.; Kim, O.; Kim, T. R.; Kang, J.; Kim, Y.; Son, D.; Tok, J. B. H.; Park, M. J.; Bao, Z.; Lee, T. W. Stretchable Organic Optoelectronic Sensorimotor Synapse. *Sci. Adv.* **2018**, *4*, 1–10.

(25) Printz, A. D.; Savagatrup, S.; Burke, D. J.; Purdy, T. N.; Lipomi, D. J. Increased Elasticity of a Low-Bandgap Conjugated Copolymer by Random Segmentation for Mechanically Robust Solar Cells. *RSC Adv.* **2014**, *4*, 13635–13643.

(26) Müller, C.; Goffri, S.; Breiby, D. W.; Andreasen, J. W.; Chanzy, H. D.; Janssen, R. A. J.; Nielsen, M. M.; Radano, C. P.; Sirringhaus, H.; Smith, P.; Stingelin-Stutzmann, N. Tough, Semiconducting Polyethylene-Poly(3-Hexylthiophene) Diblock Copolymers. *Adv. Funct. Mater.* **2007**, *17*, 2674–2679.

(27) Zokaei, S.; Kroon, R.; Gladisch, J.; Paulsen, B. D.; Sohn, W.; Hofmann, A. I.; Persson, G.; Stamm, A.; Syrén, P. O.; Olsson, E.; Rivnay, J.; Stavrinidou, E.; Lund, A.; Müller, C. Toughening of a Soft Polar Polythiophene through Copolymerization with Hard Urethane Segments. *Adv. Sci.* **2021**, *8*, 1–11.

(28) Kayser, L. V.; Russell, M. D.; Rodriquez, D.; Abuhamdieh, S. N.; Dhong, C.; Khan, S.; Stein, A. N.; Ramírez, J.; Lipomi, D. J. RAFT Polymerization of an Intrinsically Stretchable Water-Soluble Block Copolymer Scaffold for PEDOT. *Chem. Mater.* **2018**, *30*, 4459–4468.

(29) Seo, S.; Lee, J.-W.; Kim, D. J.; Lee, D.; Phan, T. N.-L.; Park, J.; Tan, Z.; Cho, S.; Kim, T.-S.; Kim, B. J. Poly(Dimethylsiloxane)-Block-PM6 Polymer Donors for High-Performance and Mechanically-Robust Polymer Solar Cells. *Adv. Mater.* **2023**, 1–54.

(30) Park, S. H.; Kim, Y.; Kwon, N. Y.; Lee, Y. W.; Woo, H. Y.; Chae, W. S.; Park, S.; Cho, M. J.; Choi, D. H. Significantly Improved Morphology and Efficiency of Nonhalogenated Solvent-Processed Solar Cells Derived from a Conjugated Donor–Acceptor Block Copolymer. *Adv. Sci.* **2020**, *7*.

(31) Park, H.; Ma, B. S.; Kim, J.; Kim, Y.; Kim, H. J.; Kim, D.; Yun, H.; Han, J.; Kim, F. S.; Kim, T.; Kim, B. J. Regioregular- Block -Regiorandom Poly(3-Hexylthiophene) Copolymers for Mechanically Robust and High-Performance Thin- Film Transistors. *Macromolecules* **2019**, *52*, 7721–7730.

(32) Wu, S. *Polymer Interface and Adhesion*, 1st Editio.; Taylor & Francis, 1982.

(33) Wang, Z.; Wang, W.; Wang, S. Surface Adhesion Engineering for Robust Organic Semiconductor Devices. *J. Mater. Chem. C* **2022**, *10*, 2516–2526.

(34) Wake, W. C. Theories of Adhesion and Uses of Adhesives: A Review. *Polymer (Guildf).* **1978**, *19*, 291–308.

(35) Creton, C.; Ciccotti, M. Fracture and Adhesion of Soft Materials: A Review. *Reports Prog. Phys.* **2016**, *79*, 46601.

(36) Mittal, K. L. The Role of the Interface in Adhesion Phenomena. *Polym. Eng. Sci.* **1977**, *17*, 467–473.

(37) Derjaguin, B. V.; Smilga, V. P. Electronic Theory of Adhesion. *J. Appl. Phys.* **1967**, *38*, 4609–4616.

(38) Feldstein, M. M.; Siegel, R. A. Molecular and Nanoscale Factors Governing Pressure-Sensitive Adhesion Strength of Viscoelastic Polymers. *J. Polym. Sci. Part B Polym. Phys.* **2012**, *50*, 739–772.

(39) Godwin, A. D. Plasticizers. In *Applied Plastics Engineering Handbook*; William Andrew, 2017; pp 533–553.

(40) Moore, D. F.; Geyer, W. A Review of Adhesion Theories for Elastomers. *Wear* **1972**, *22*, 113–141.

(41) Bruner, C.; Dauskardt, R. Role of Molecular Weight on the Mechanical Device Properties of Organic Polymer Solar Cells. *Macromolecules* **2014**, *47*, 1117–1121.

(42) Brand, V.; Bruner, C.; Dauskardt, R. H. Cohesion and Device Reliability in Organic Bulk Heterojunction Photovoltaic Cells. *Sol. Energy Mater. Sol. Cells* **2012**, *99*, 182–189.

(43) Kinloch, A. J.; Lau, C. C.; Williams, J. G. The Peeling of Flexible Laminates. *Int. J. Fract.* **1994**, *66*, 45–70.

(44) Wei, Y.; Hutchinson, J. W. Interface Strength, Work of Adhesion and Plasticity in the Peel Test. *Int. J. Fract.* **1998**, *93*, 315–333.

(45) Thouless, M. D.; Jensen, H. M. Elastic Fracture Mechanics of the Peel-Test Geometry. *J. Adhes.* **1992**, *38*, 185–197.

(46) Finn, M.; Martens, C. J.; Zaretski, A. V.; Roth, B.; Søndergaard, R. R.; Krebs, F. C.; Lipomi, D. J. Mechanical Stability of Roll-to-Roll Printed Solar Cells under Cyclic Bending and Torsion. *Sol. Energy Mater. Sol. Cells* **2018**, *174*, 7–15.

(47) Postema, A. R.; Liou, K.; Wudl, F.; Smith, P. Highly Oriented, Low-Modulus Materials from

Liquid Crystalline Polymers: The Ultimate Penalty for Solubilizing Alkyl Side Chains. *Macromolecules* **1990**, *23*, 1842–1845.

(48) Balar, N.; Siddika, S.; Kashani, S.; Peng, Z.; Rech, J. J.; Ye, L.; You, W.; Ade, H.; O'Connor, B. T. Role of Secondary Thermal Relaxations in Conjugated Polymer Film Toughness. *Chem. Mater.* **2020**, *32*, 6540–6549.

(49) Müller, C. On the Glass Transition of Polymer Semiconductors and Its Impact on Polymer Solar Cell Stability. *Chem. Mater.* **2015**, *27*, 2740–2754.

(50) Qian, Z.; Cao, Z.; Galuska, L.; Zhang, S.; Xu, J.; Gu, X. Glass Transition Phenomenon for Conjugated Polymers. *Macromol. Chem. Phys.* **2019**, *220*, 1–30.

(51) Savagatrup, S.; Printz, A. D.; Rodriquez, D.; Lipomi, D. J. Best of Both Worlds: Conjugated Polymers Exhibiting Good Photovoltaic Behavior and High Tensile Elasticity. *Macromolecules* **2014**, *47*, 1981–1992.

(52) Savagatrup, S.; Printz, A. D.; Wu, H.; Rajan, K. M.; Sawyer, E. J.; Zaretski, A. V.; Bettinger, C. J.; Lipomi, D. J. Viability of Stretchable Poly(3-Heptylthiophene) (P3HpT) for Organic Solar Cells and Field-Effect Transistors. *Synth. Met.* **2015**, *203*, 208–214.

(53) Pankaj, S.; Beiner, M. Confined Dynamics and Crystallization in Self-Assembled Alkyl Nanodomains. *J. Phys. Chem. B* **2010**, *114*, 15459–15465.

(54) Pankaj, S.; Hempel, E.; Beiner, M. Side-Chain Dynamics and Crystallization in a Series of Regiorandom Poly(3-Alkylthiophenes). *Macromolecules* **2009**, *42*, 716–724.

(55) Sharma, A.; Pan, X.; Bjuggren, J. M.; Gedefaw, D.; Xu, X.; Kroon, R.; Wang, E.; Campbell, J. A.; Lewis, D. A.; Andersson, M. R. Probing the Relationship between Molecular Structures, Thermal Transitions, and Morphology in Polymer Semiconductors Using a Woven Glass-Mesh-Based DMTA Technique. *Chem. Mater.* **2019**, *31*, 6740–6749.

(56) Balar, N.; Rech, J. J.; Siddika, S.; Song, R.; Schrickx, H. M.; Sheikh, N.; Ye, L.; Megret Bonilla, A.; Awartani, O.; Ade, H.; You, W.; O'Connor, B. T. Resolving the Molecular Origin of

Mechanical Relaxations in Donor–Acceptor Polymer Semiconductors. *Adv. Funct. Mater.* **2022**, *32*, 1–13.

(57) Mei, J.; Bao, Z. Side Chain Engineering in Solution-Processable Conjugated Polymers. *Chem. Mater.* **2014**, *26*, 604–615.

(58) Rodriquez, D.; Kohl, J. G.; Morel, P.; Burrows, K.; Favaro, G.; Root, S. E.; Ramírez, J.; Alkhadra, M. A.; Carpenter, C. W.; Fei, Z.; Boufflet, P.; Heeney, M.; Lipomi, D. J. Measurement of Cohesion and Adhesion of Semiconducting Polymers by Scratch Testing: Effect of Side-Chain Length and Degree of Polymerization. *ACS Macro Lett.* **2018**, *7*, 1003–1009.

(59) Rodriquez, D.; Kim, J.; Root, S. E.; Fei, Z.; Bou, P.; Heeney, M.; Kim, T.; Lipomi, D. J. Comparison of Methods for Determining the Mechanical Properties of Semiconducting Polymer Films for Stretchable Electronics. *ACS Appl. Mater. Interfaces* **2017**, *9*, 8855–8862.

(60) Printz, A. D.; Zaretski, A. V; Savagatrup, S.; Chiang, A. S.; Lipomi, D. J. Yield Point of Semiconducting Polymer Films on Stretchable Substrates Determined by Onset of Buckling. *ACS Appl. Mater. Interfaces* **2015**, *7*, 23257–23264.

(61) Stafford, C. M.; Harrison, C.; Beers, K. L.; Karim, A.; Amis, E. J.; Vanlandingham, M. R.; Kim, H. C.; Volksen, W.; Miller, R. D.; Simonyi, E. E. A Buckling-Based Metrology for Measuring the Elastic Moduli of Polymeric Thin Films. *Nat. Mater.* **2004**, *3*, 545–550.

(62) Kim, J.; Nizami, A.; Hwangbo, Y.; Jang, B.; Lee, H.; Woo, C.; Hyun, S.; Kim, T. Tensile Testing of Ultra-Thin Films on Water Surface. *Nat. Commun.* **2013**, *4*, 1–6.

(63) Chen, A. X.; Kleinschmidt, A. T.; Choudhary, K.; Lipomi, D. J. Beyond Stretchability: Strength, Toughness, and Elastic Range in Semiconducting Polymers. *Chem. Mater.* **2020**, *32*, 7582–7601.

(64) Yoshino, K.; Morita, S.; Uchida, M.; Muro, K.; Kawai, T.; Ohmori, Y. Novel Electrical and Optical Properties of Poly(3-Alkylthiophene) as Function of Alkyl Chain Length and Their Functional Applications. *Synth. Met.* **1993**, *55*, 28–35.

(65) Ohmori, Y.; Uchida, M.; Muro, K.; Yoshino, K. Effects of Alkyl Chain Length and Carrier

Confinement Layer on Characteristics of Poly(3-Alkylthiophene) Electroluminescent Diodes. *Solid State Commun.* **1991**, *80*, 605–608.

(66) Yoshino, K.; Manda, Y.; Sawada, K.; Onoda, M.; Sugimoto, R. ichi. Anomalous Dependences of Luminescence of Poly(3-Alkylthiophene) on Temperature and Alkyl Chain Length. *Solid State Commun.* **1989**, *69*, 143–146.

(67) Thankaraj Salammal, S.; Dai, S.; Pietsch, U.; Grigorian, S.; Koenen, N.; Scherf, U.; Kayunkid, N.; Brinkmann, M. Influence of Alkyl Side Chain Length on the In-Plane Stacking of Room Temperature and Low Temperature Cast Poly(3-Alkylthiophene) Thin Films. *Eur. Polym. J.* **2015**, *67*, 199–212.

(68) Park, Y. D.; Kim, D. H.; Jang, Y.; Cho, J. H.; Hwang, M.; Lee, H. S.; Lim, J. A.; Cho, K. Effect of Side Chain Length on Molecular Ordering and Field-Effect Mobility in Poly(3-Alkylthiophene) Transistors. *Org. Electron.* **2006**, *7*, 514–520.

(69) Sauvé, G.; Javier, A. E.; Zhang, R.; Liu, J.; Sydlik, S. A.; Kowalewski, T.; McCullough, R. D. Well-Defined, High Molecular Weight Poly(3-Alkylthiophene)s in Thin-Film Transistors: Side Chain Invariance in Field-Effect Mobility. *J. Mater. Chem.* **2010**, *20*, 3195–3201.

(70) Babel, A.; Jenekhe, S. A. Alkyl Chain Length Dependence of the Field-Effect Carrier Mobility in Regioregular Poly(3-Alkylthiophene)S. *Synth. Met.* **2005**, *148*, 169–173.

(71) Kaneto, K.; Lim, W. Y.; Takashima, W.; Endo, T.; Rikukawa, M. Alkyl Chain Length Dependence of Field-Effect Mobilities in Regioregular Poly(3-Alkylthiophene) Films. *Japanese J. Appl. Physics, Part 2 Lett.* **2000**, *39*, 8–11.

(72) Lee, H. S.; Cho, J. H.; Cho, K.; Park, Y. D. Alkyl Side Chain Length Modulates the Electronic Structure and Electrical Characteristics of Poly(3-Alkylthiophene) Thin Films. *J. Phys. Chem. C* **2013**, *117*, 11764–11769.

(73) O'Connor, T. F.; Zaretski, A. V.; Shiravi, B. A.; Savagatrup, S.; Printz, A. D.; Diaz, M. I.; Lipomi, D. J. Stretching and Conformal Bonding of Organic Solar Cells to Hemispherical Surfaces. *Energy*

Environ. Sci. **2014**, *7*, 370–378.

(74) Oosterbaan, W. D.; Bolsée, J. C.; Gadisa, A.; Vrindts, V.; Bertho, S.; D'Haen, J.; Cleij, T. J.; Lutsen, L.; McNeill, C. R.; Thomsen, L.; Manca, J. V.; Vanderzande, D. Alkyl-Chain-Length-Independent Hole Mobility via Morphological Control with Poly(3-Alkylthiophene) Nanofibers. *Adv. Funct. Mater.* **2010**, *20*, 792–802.

(75) Nguyen, L. H.; Hoppe, H.; Erb, T.; Günes, S.; Gobsch, G.; Sariciftci, N. S. Effects of Annealing on the Nanomorphology and Performance of Poly(Alkylthiophene):Fullerene Bulk-Heterojunction Solar Cells. *Adv. Funct. Mater.* **2007**, *17*, 1071–1078.

(76) Liu, Y.; Xian, K.; Gui, R.; Zhou, K.; Liu, J.; Gao, M.; Zhao, W.; Jiao, X.; Deng, Y.; Yin, H.; Geng, Y.; Ye, L. Simple Polythiophene Solar Cells Approaching 10% Efficiency via Carbon Chain Length Modulation of Poly(3-Alkylthiophene). *Macromolecules* **2021**, *55*, 133–145.

(77) Zheng, C.; Jalan, I.; Cost, P.; Oliver, K.; Gupta, A.; Misture, S.; Cody, J. A.; Collison, C. J. Impact of Alkyl Chain Length on Small Molecule Crystallization and Nanomorphology in Squaraine-Based Solution Processed Solar Cells. *J. Phys. Chem. C* **2017**, *121*, 7750–7760.

(78) Cho, C. H.; Kim, H. J.; Kang, H.; Shin, T. J.; Kim, B. J. The Effect of Side-Chain Length on Regioregular Poly[3-(4-n-Alkyl) Phenylthiophene]/PCBM and ICBA Polymer Solar Cells. *J. Mater. Chem.* **2012**, *22*, 14236–14245.

(79) Huang, W. Y.; Lee, C. C.; Wang, S. G.; Han, Y. K.; Chang, M. Y. Side Chain Effects of Poly(3-Alkylthiophene) on the Morphology and Performance of Polymer Solar Cells. *J. Electrochem. Soc.* **2010**, *157*, B1336.

(80) Friedel, B.; McNeill, C. R.; Greenham, N. C. Influence of Alkyl Side-Chain Length on the Performance of Poly(3-Alkylthiophene)/Polyfluorene All-Polymer Solar Cells. *Chem. Mater.* **2010**, *22*, 3389–3398.

(81) Li, C.; Zhu, R.; Lai, J.; Tan, J.; Luo, Y.; Ye, S. Conformational Order of Alkyl Side Chain of Poly(3-Alkylthiophene) Promotes Hole-Extraction Ability in Perovskite/Poly(3-Alkylthiophene)

Heterojunction. *J. Phys. Chem. Lett.* **2021**, *12*, 11817–11823.

(82) Bruner, C.; Novoa, F.; Dupont, S.; Dauskardt, R. Decohesion Kinetics in Polymer Organic Solar Cells. *ACS Appl. Mater. Interfaces* **2014**, *6*, 21474–21483.

(83) Dupont, S. R.; Voroshazi, E.; Heremans, P.; Dauskardt, R. H. Adhesion Properties of Inverted Polymer Solarcells: Processing and Film Structure Parameters. *Org. Electron. physics, Mater. Appl.* **2013**, *14*, 1262–1270.

(84) Dupont, S. R.; Oliver, M.; Krebs, F. C.; Dauskardt, R. H. Interlayer Adhesion in Roll-to-Roll Processed Flexible Inverted Polymer Solar Cells. *Sol. Energy Mater. Sol. Cells* **2012**, *97*, 171–175.

(85) Lee, I.; Rolston, N.; Brunner, P. L.; Dauskardt, R. H. Hole-Transport Layer Molecular Weight and Doping Effects on Perovskite Solar Cell Efficiency and Mechanical Behavior. *ACS Appl. Mater. Interfaces* **2019**, *11*, 23757–23764.

(86) Watson, B. L.; Rolston, N.; Printz, A. D.; Dauskardt, R. H. Scaffold-Reinforced Perovskite Compound Solar Cells. *Energy Environ. Sci.* **2017**, *10*, 2500–2508.

(87) Rolston, N.; Watson, B. L.; Bailie, C. D.; McGehee, M. D.; Bastos, J. P.; Gehlhaar, R.; Kim, J. E.; Vak, D.; Mallajosyula, A. T.; Gupta, G.; Mohite, A. D.; Dauskardt, R. H. Mechanical Integrity of Solution-Processed Perovskite Solar Cells. *Extrem. Mech. Lett.* **2016**, *9*, 353–358.

(88) Choi, J.; Kim, W.; Kim, S.; Kim, T. S.; Kim, B. J. Influence of Acceptor Type and Polymer Molecular Weight on the Mechanical Properties of Polymer Solar Cells. *Chem. Mater.* **2019**, *31*, 9057–9069.

(89) Dupont, S. R.; Novoa, F.; Voroshazi, E.; Dauskardt, R. H. Decohesion Kinetics of PEDOT:PSS Conducting Polymer Films. *Adv. Funct. Mater.* **2014**, *24*, 1325–1332.

(90) Kim, J. H.; Lee, I.; Kim, T. S.; Rolston, N.; Watson, B. L.; Dauskardt, R. H. Understanding Mechanical Behavior and Reliability of Organic Electronic Materials. *MRS Bull.* **2017**, *42*, 115–123.

(91) Tummala, N. R.; Bruner, C.; Risko, C.; Bredas, J. L.; Dauskardt, R. H. Molecular-Scale

Understanding of Cohesion and Fracture in P3HT:Fullerene Blends. *ACS Appl. Mater. Interfaces* **2015**, *7*, 9957–9964.

(92) Bruner, C.; Miller, N. C.; McGehee, M. D.; Dauskardt, R. H. Molecular Intercalation and Cohesion of Organic Bulk Heterojunction Photovoltaic Devices. *Adv. Funct. Mater.* **2013**, *23*, 2863–2871.

(93) Corazza, M.; Rolston, N.; Dauskardt, R. H.; Beliatis, M.; Krebs, F. C.; Gevorgyan, S. A. Role of Stress Factors on the Adhesion of Interfaces in R2R Fabricated Organic Photovoltaics. *Adv. Energy Mater.* **2016**, *6*, 1–7.

(94) Dupont, S. R.; Voroshazi, E.; Heremans, P.; Dauskardt, R. H. The Effect of Anneal, Solar Irradiation and Humidity on the Adhesion/Cohesion Properties of P3HT:PCBM Based Inverted Polymer Solar Cells. *Conf. Rec. IEEE Photovolt. Spec. Conf.* **2012**, 3259–3262.

(95) Dupont, S. R.; Voroshazi, E.; Nordlund, D.; Dauskardt, R. H. Morphology and Interdiffusion Control to Improve Adhesion and Cohesion Properties in Inverted Polymer Solar Cells. *Sol. Energy Mater. Sol. Cells* **2015**, *132*, 443–449.

(96) Dupont, S. R.; Voroshazi, E.; Nordlund, D.; Vandewal, K.; Dauskardt, R. H. Controlling Interdiffusion, Interfacial Composition, and Adhesion in Polymer Solar Cells. *Adv. Mater. Interfaces* **2014**, *1*, 1–8.

(97) Heffner, G. W.; Pearson, D. S. Molecular Characterization of Poly(3-Hexylthiophene). *Macromolecules* **1991**, *24*, 6295–6299.

(98) Tummala, N. R.; Risko, C.; Bruner, C.; Dauskardt, R. H.; Brédas, J. L. Entanglements in P3HT and Their Influence on Thin-Film Mechanical Properties: Insights from Molecular Dynamics Simulations. *J. Polym. Sci. Part B Polym. Phys.* **2015**, *53*, 934–942.

(99) Mahouche-Chergui, S.; Boussaboun, Z.; Oun, A.; Kazembeyki, M.; Hoover, C. G.; Carbonnier, B.; Ouellet-Plamondon, C. M. Sustainable Preparation of Graphene-like Hybrid Nanomaterials and Their Application for Organic Dyes Removal. *Chem. Eng. Sci.* **2021**, *236*, 116482.

(100) Vanlandingham, M. R.; Chang, N. K.; Drzal, P. L.; White, C. C.; Chang, S. H. Viscoelastic Characterization of Polymers Using Instrumented Indentation. I. Quasi-Static Testing. *J. Polym. Sci. Part B Polym. Phys.* **2005**, *43*, 1794–1811.

(101) White, C. C.; Vanlandingham, M. R.; Drzal, P. L.; Chang, N. K.; Chang, S. H. Viscoelastic Characterization of Polymers Using Instrumented Indentation. II. Dynamic Testing. *J. Polym. Sci. Part B Polym. Phys.* **2005**, *43*, 1812–1824.

(102) Li, H.; Randall, N. X.; Vlassak, J. J. New Methods of Analyzing Indentation Experiments on Very Thin Films. *J. Mater. Res.* **2010**, *25*, 728–734.

(103) Oliver, W. C.; Pharr, G. M. An Improved Technique for Determining Hardness and Elastic Modulus Using Load and Displacement Sensing Indentation Experiments. *J. Mater. Res.* **1992**, *7*, 1564–1583.

(104) Fedors, R. F. Method for Estimating Both the Solubility Parameters and Molar Volumes of Liquids. *JPL Q Tech Rev* **1973**, *3*, 45–53.

(105) Tahk, D.; Lee, H. H.; Khang, D.-Y. Elastic Moduli of Organic Electronic Materials by the Buckling Method. *Macromolecules* **2009**, *42*, 7079–7083.

(106) Savagatrup, S.; Makaram, A. S.; Burke, D. J.; Lipomi, D. J. Mechanical Properties of Conjugated Polymers and Polymer-Fullerene Composites as a Function of Molecular Structure. *Adv. Funct. Mater.* **2014**, *24*, 1169–1181.

(107) Choudhary, K.; Chen, A. X.; Pitch, G. M.; Runser, R.; Urbina, A.; Dunn, T. J.; Kodur, M.; Kleinschmidt, A. T.; Wang, B. G.; Bunch, J. A.; Fenning, D. P.; Ayzner, A. L.; Lipomi, D. J. Comparison of the Mechanical Properties of a Conjugated Polymer Deposited Using Spin Coating, Interfacial Spreading, Solution Shearing, and Spray Coating. *ACS Appl. Mater. Interfaces* **2021**, *13*, 51436–51446.

(108) Xie, R.; Weisen, A. R.; Lee, Y.; Aplan, M. A.; Fenton, A. M.; Masucci, A. E.; Kempe, F.; Sommer, M.; Pester, C. W.; Colby, R. H.; Gomez, E. D. Glass Transition Temperature from the

Chemical Structure of Conjugated Polymers. *Nat. Commun.* **2020**, *11*, 1–8.

(109) Chen, S.-A.; Ni, J.-M. Structure/Properties of Conjugated Conductive Polymers. 1. Neutral Poly(3-Alkylthiophene)S. *Macromolecules* **1992**, *25*, 6081–6089.

(110) Khlyabich, P. P.; Rudenko, A. E.; Burkhart, B.; Thompson, B. C. Contrasting Performance of Donor-Acceptor Copolymer Pairs in Ternary Blend Solar Cells and Two-Acceptor Copolymers in Binary Blend Solar Cells. *ACS Appl. Mater. Interfaces* **2015**, *7*, 2322–2330.

(111) Koch, F. P. V.; Smith, P.; Heeney, M. "Fibonacci's Route" To Regioregular Oligo(3-Hexylthiophene)S. *J. Am. Chem. Soc.* **2013**, *135*, 13695–13698.

(112) Zhao, B.; Awartani, O.; O'Connor, B.; Zikry, M. A. A Direct Correlation of X-Ray Diffraction Orientation Distributions to the in-Plane Stiffness of Semi-Crystalline Organic Semiconducting Films. *Appl. Phys. Lett.* **2016**, *108*, 1–4.

(113) Qiao, X.; Wang, X.; Mo, Z. Effects of Different Alkyl Substitution on the Structures and Properties of Poly(3-Alkylthiophenes). *Synth. Met.* **2001**, *118*, 89–95.

(114) Park, H.; Han, M. J.; Kim, Y.; Kim, E. J.; Kim, H. J.; Yoon, D. K.; Kim, B. J. Regioregularity-Dependent Crystalline Structures and Thermal Transitions in Poly(3-Dodecylthiophene)S. *Chem. Mater.* **2021**, *33*, 3312–3320.

(115) Mcbride, M.; Zhang, G.; Grover, M.; Reichmanis, E. Poly(3-Alkylthiophenes): Controlled Manipulation of Microstructure and Its Impact on Charge Transport. In *Conjugated Polymers: Properties, Processing, and Applications*; 2019; pp 351–389.

(116) Qian, Z.; Luo, S.; Qu, T.; Galuska, L. A.; Zhang, S.; Cao, Z.; Dhakal, S.; He, Y.; Hong, K.; Zhou, D.; Gu, X. Influence of Side-chain Isomerization on the Isothermal Crystallization Kinetics of Poly(3-alkylthiophenes). *J. Mater. Res.* **2021**, *36*, 191–202.

(117) Jiang, K.; Wang, L.; Zhang, X.; Song, Y.; Zhang, W. Side-Chain Length Dependence of Young's Modulus and Strength in Crystalline Poly(3-Alkylthiophene) Nanofibers. *Macromolecules* **2020**, *53*, 10061–10068.

(118) Printz, A. D.; Zaretski, A. V.; Savagatrup, S.; Chiang, A. S. C.; Lipomi, D. J. Yield Point of Semiconducting Polymer Films on Stretchable Substrates Determined by Onset of Buckling. *ACS Appl. Mater. Interfaces* **2015**, *7*, 23257–23264.

(119) Xu, W.; Li, L.; Tang, H.; Li, H.; Zhao, X.; Yang, X. Solvent-Induced Crystallization of Poly(3-Dodecylthiophene): Morphology and Kinetics. *J. Phys. Chem. B* **2011**, *115*, 6412–6420.

(120) Maksimov, R. D.; Plume, E. Z.; Jansons, J. O. Comparative Studies on the Mechanical Properties of a Thermoset Polymer in Tension and Compression. *Mech. Compos. Mater.* **2005**, *41*, 425–436.

(121) Chen, W.; Lu, F.; Cheng, M. Tension and Compression Tests of Two Polymers under Quasi-Static and Dynamic Loading. *Polym. Test.* **2002**, *21*, 113–121.

(122) Deblieck, R. A. C.; Van Beek, D. J. M.; Remerie, K.; Ward, I. M. Failure Mechanisms in Polyolefines: The Role of Crazing, Shear Yielding and the Entanglement Network. *Polymer (Guildf).* **2011**, *52*, 2979–2990.

(123) Donald, A. M.; Kramer, E. J. The Competition between Shear Deformation and Crazing in Glassy Polymers. *J. Mater. Sci.* **1982**, *17*, 1871–1879.

(124) Kramer, E. J.; Berger, L. L. Fundamental Processes of Craze Growth and Fracture. *Adv. Polym. Sci.* **1990**, *2*, 68.

(125) Cao, Z.; Galuska, L.; Qian, Z.; Zhang, S.; Huang, L.; Prine, N.; Li, T.; He, Y.; Hong, K.; Gu, X. The Effect of Side-Chain Branch Position on the Thermal Properties of Poly(3-Alkylthiophenes). *Polym. Chem.* **2020**, *11*, 517–526.

(126) Gent, A. N.; Petrich, R. P. Adhesion of Viscoelastic Materials To Rigid Substrates. *Proc. R. Soc. A.* **1969**, *310*, 433–448.

(127) Krenceski, M. A.; Johnson, J. F.; Temin, S. C. Chemical and Physical Factors Affecting Performance of Pressure-Sensitive Adhesives. *J. Macromol. Sci. Part C* **1986**, *26*, 143–182.

(128) Payra, D.; Fujii, Y.; Das, S.; Takaishi, J.; Naito, M. Rational Design of a Biomimetic Glue with Tunable Strength and Ductility. *Polym. Chem.* **2017**, *8*, 1654–1663.

(129) Hutchinson, J. W.; Evans, A. G. Mechanics of Materials: Top-down Approaches to Fracture. *Acta Mater.* **2000**, *48*, 125–135.

(130) Schmitt, A.; Samal, S.; Thompson, B. C. Tuning the Surface Energies in a Family of Poly-3-Alkylthiophenes Bearing Hydrophilic Side-Chains Synthesized: Via Direct Arylation Polymerization (DArP). *Polym. Chem.* **2021**, *12*, 2840–2847.

(131) Howard, J. B.; Ekiz, S.; Noh, S.; Thompson, B. C. Surface Energy Modification of Semi-Random P3HTT-DPP. *ACS Macro Lett.* **2016**, *5*, 977–981.

(132) Howard, J. B.; Noh, S.; Beier, A. E.; Thompson, B. C. Fine Tuning Surface Energy of Poly(3-Hexylthiophene) by Heteroatom Modification of the Alkyl Side Chains. *ACS Macro Lett.* **2015**, *4*, 725–730.

(133) Maugis, D. Subcritical Crack Growth, Surface Energy, Fracture Toughness, Stick-Slip and Embrittlement. *J. Mater. Sci.* **1985**, *20*, 3041–3073.

(134) Robinson, L.; Isaksson, J.; Robinson, N. D.; Berggren, M. Electrochemical Control of Surface Wettability of Poly(3-Alkylthiophenes). *Surf. Sci.* **2006**, *600*.

(135) Kanai, K.; Miyazaki, T.; Suzuki, H.; Inaba, M.; Ouchi, Y.; Seki, K. Effect of Annealing on the Electronic Structure of Poly(3-Hexylthiophene) Thin Film. *Phys. Chem. Chem. Phys.* **2010**, *12*, 273–282.

(136) Son, S. Y.; Park, T.; You, W. Understanding of Face-On Crystallites Transitioning to Edge-On Crystallites in Thiophene-Based Conjugated Polymers. *Chem. Mater.* **2021**, *33*, 4541–4550.

(137) Blau, R.; Chen, A. X.; Polat, B.; Becerra, L. L.; Runser, R.; Zamanimeymian, B.; Choudhary, K.; Lipomi, D. J. Intrinsically Stretchable Block Copolymer Based on PEDOT:PSS for Improved Performance in Bioelectronic Applications. *ACS Appl. Mater. Interfaces* **2022**, *14*, 4823–4835.

(138) Persson, B. N. J.; Tosatti, E. The Effect of Surface Roughness on the Adhesion of Elastic Solids. *J. Chem. Phys.* **2001**, *115*, 5597–5610.

(139) Gent, A. N.; Lin, C. W. Model Studies of the Effect of Surface Roughness and Mechanical

Interlocking on Adhesion. *J. Adhes.* **1990**, *32*, 113–125.

(140) Katainen, J.; Paajanen, M.; Ahtola, E.; Pore, V.; Lahtinen, J. Adhesion as an Interplay between Particle Size and Surface Roughness. *J. Colloid Interface Sci.* **2006**, *304*, 524–529.

(141) Kim, W. S.; Yun, I. H.; Lee, J. J.; Jung, H. T. Evaluation of Mechanical Interlock Effect on Adhesion Strength of Polymermetal Interfaces Using Micro-Patterned Surface Topography. *Int. J. Adhes. Adhes.* **2010**, *30*, 408–417.

(142) Libanori, R.; Carnelli, D.; Rothfuchs, N.; Binelli, M. R.; Zanini, M.; Nicoleau, L.; Feichtenschlager, B.; Albrecht, G.; Studart, A. R. Composites Reinforced via Mechanical Interlocking of Surface-Roughened Microplatelets within Ductile and Brittle Matrices. *Bioinspiration and Biomimetics* **2016**, *11*, 1–11.

(143) Fuller, K. N. G.; Tabor, D. The Effect of Surface Roughness on the Adhesion of Elastic Solids. *Proc. R. Soc. Lond. A.* **1975**, *345*, 327–342.

Appendix A. Supporting Information for Chapter 1. Beyond Stretchability: Strength, Toughness, and Elastic Range in Semiconducting Polymers

A.1 Effect of Sample Thickness and Strain Rate

The mechanical properties of a semiconducting film are not just dependent on the material itself, but also the physical characteristics of the sample (e.g. thickness, geometry) and the testing parameters (external factors e.g. temperature, strain rate, pressure, humidity). Device design and optimization therefore requires a thorough understanding of how the physical characteristics and external factors affect the mechanical properties. For example, a flexible wearable device must be able to handle a wide range of strain rates. The same is true for other external factors (e.g. humidity, temperature, pressure, etc.). **Figure A1** and **Figure A2** show how the mechanical properties of poly(3-hexylthiophene) (P3HT) and diketopyrrolopyrrole (DPP)–based polymer films change relative to increasing strain rate (**Figure A1**) and increasing thickness (**Figure A2**).

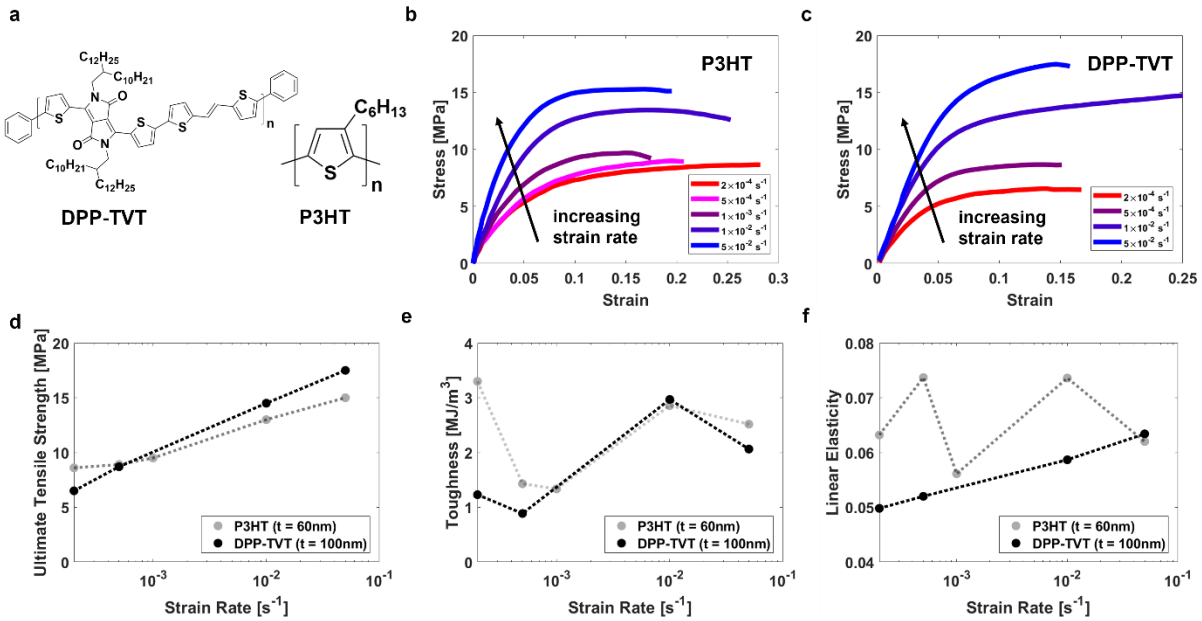

Figure A1. Mechanical properties of P3HT (60 nm) and DPP-TVT (100nm) as a function of tensile-testing strain rate. (**a**) Chemical structures of P3HT and DPP-TVT. (**b**) Stress-strain curves of P3HT and (**c**) DPP-TVT films as a function of strain rate as replotted from Zhang et al. 2018.[1] (**d**) Tensile strength increased as a function of strain rate. (**e**) Toughness remained relatively constant as a function of strain rate. (**f**) The range of linear elasticity increased relative to strain rate for P3HT and remained relatively constant relative to strain rate for DPP-TVT.

Conjugated polymers, much like their nonconjugated counterparts, exhibit rate dependent mechanical behavior.[2] Both P3HT and DPP-TVT are semicrystalline polymers that have glass transition temperatures below room temperature.[1,3] Their low T_g make it so that they exhibit viscoelastic behavior at T > T_g. Higher strain rates give polymer chains less time to arrange themselves in more favorable configurations, thus reducing their conformational degrees of freedom.[1,2] This results in a higher measurement of tensile strength (**Fig A1d**) and related properties (e.g. yield stress) due to the increased resistance to deformation.[1] At lower strain rates, polymer chains are able to dissipate energy by stretching and shifting to more favorable equilibrium positions.[2] For this reason, lower strain rates generally result in a higher fracture strain. An analogous example would be stretching a plastic bag; pulling both sides of the bag quickly results in instantaneous failure of covalent bonds and forcing chain pullout,[4] thus forming a hole immediately. However, pulling the bag slowly results in the plastic getting thinner and thinner as it

stretches, until it eventually tears apart at the weakest (thinnest) point. In these samples, we see that the tensile strength increases as the strain rate increases as expected. However, Zhang et al. noted that the fracture strain is greatly affected by the presence of intrinsic defects in the film, and thus causes deviations in expected behavior.

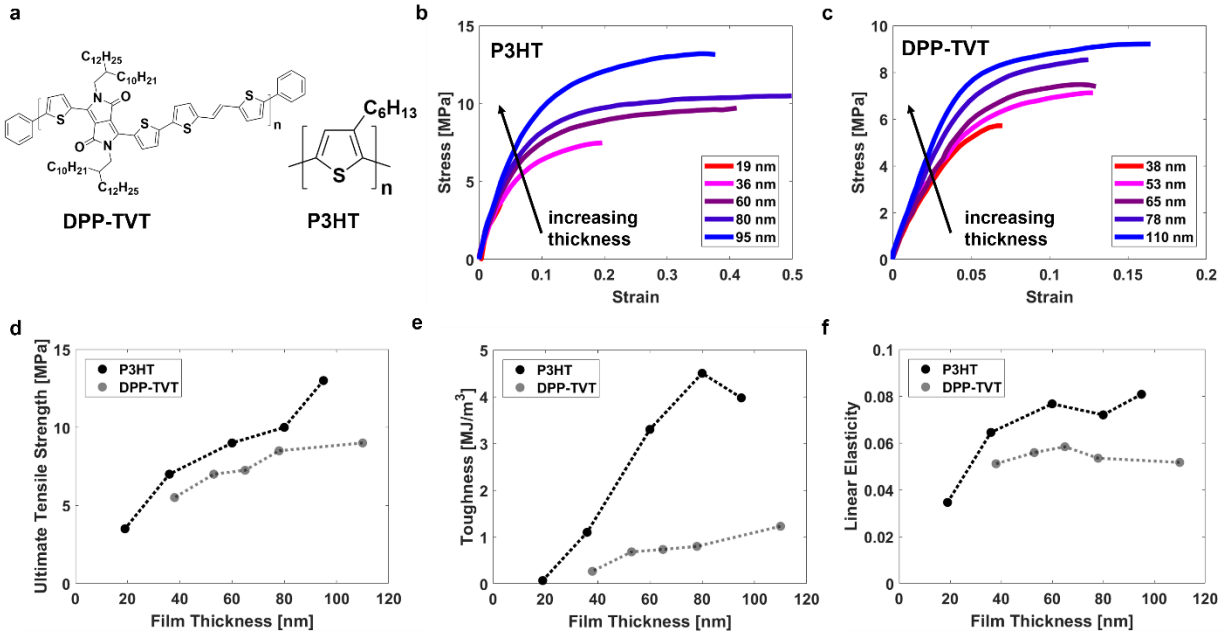

Figure A2. Mechanical properties of P3HT and DPP-TVT as a function of film thickness. (**a**) Chemical structures of P3HT and DPP-TVT. (**b**) Stress-strain curves of P3HT and (**c**) DPP-TVT films as a function of thickness as replotted from Zhang et al. 2018.[1] (**d**) Tensile strength and (**e**) toughness increased relative to increasing film thickness for both P3HT and DPP-TVT. (**f**) The range of linear elasticity increased relative to thickness for DPP-TVT and remained relatively constant relative to thickness for P3HT.

Both P3HT and DPP-TVT show an increase in tensile strength (**Fig A2d**) and fracture strain relative to increasing film thickness. Thus, increasing the thickness of the film consequentially results in an increase in the toughness (**Fig A2e**). The mechanical properties of thin conjugated polymer films are highly dependent on thickness for three main reasons: (1) skin-depth effects (by this, we mean differences between surface and bulk morphology), (2) chain confinement effects, and (3) surface roughness. Due to skin-depth effects, extremely thin films have highly mobile polymer chains and fewer entanglements when the entire sample is "near the surface".[5] As a result, the intermolecular forces between chains are weakened, softening the material. This microstructure additionally results in a lower T_g as well as a lower modulus and fracture

strength.[5] The morphology of the film is also affected by the confinement of the polymer chains between the substrate and the free interface.[6] By this, we mean that the coil conformations and arrangement of the polymer chains become more perturbed as the thickness decreases.[6] Finally, the surface roughness is also a significant consideration for thin films due to its effect on the geometry of the sample. Previous work by Rodriquez et al. has shown that P3HT films with thicknesses between 100 nm – 200 nm can have a peak-to-valley roughness of 25–35 nm.[7] Significant disparities in film thickness can lead to stress concentrating in the thinnest regions of the film, resulting in premature fracture and lower tensile strengths. Likewise, the effect of intrinsic material defects is exacerbated for thinner films with rougher surfaces. In an ideal film, a decreasing thickness generally corresponds to a slight increase in fracture strain due to the increased mobility of the polymer chains.[5] However, this is the opposite of what we see in **Fig A2b-c**. We can attribute this mismatch between theory and data to nonideal testing due to (1) rougher (relatively speaking) surfaces for thinner films, (2) stress concentration in thinner regions or film defects.

A.2 Effect of Solvent

The thermodynamics of polymer solutions has been extensively studied (e.g. Flory–Huggins solution theory,[8–10] Mark–Houwink equation,[11,12] intermolecular forces,[13] kinetic behavior, etc.). It is well known that the structure, conformation, and physical properties of a polymer film are in part dependent on the properties of the solvent.[14] A "good" solvent refers to a polymer-solvent mixture in which interactions between polymer chains and solvent molecules are more energetically favorable, promoting high solubility. This is in contrast to a "poor" solvent, in which polymer-polymer interactions are more energetically favorable, promoting aggregation of polymer chains. In the last few decades, many papers have been dedicated to elucidating how the solvent affects morphology after deposition, and how this in turn affects electronic (and to a lesser extent, mechanical)[15,16] properties.[17–22] **Figure A3** below shows how the mechanical properties of interest for a donor–acceptor (D–A) polymer film change relative to the dielectric constant of the solvent.

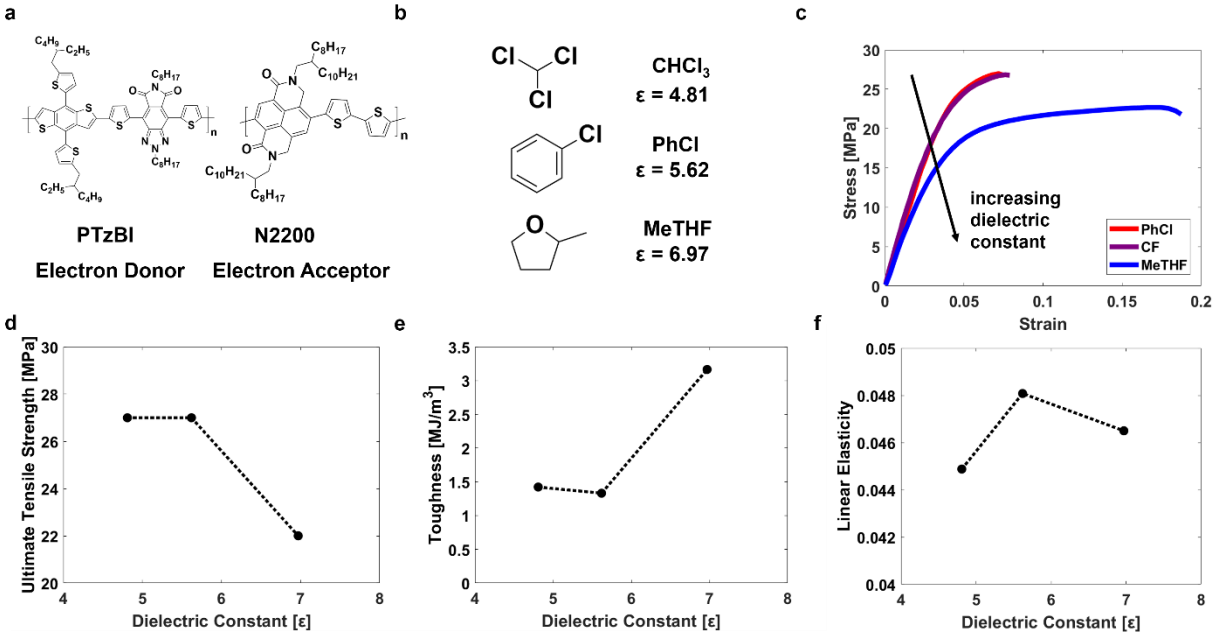

Figure A3. Mechanical properties of PTzBI:N2200 thin films relative to the dielectric constant of the solvent. (**a**) Chemical structures of PTzBI (donor polymer) and N2200 (acceptor polymer). (**b**) The solvents used for the polymer solutions are as follows from top to bottom: chloroform (CF), chlorobenzene (PhCl), and 2-methyltetrahydrofuran (MeTHF). (**c**) Stress-strain curves of PTzBI:N2200 polymer films as replotted from Lin et al. 2019.[16] (**d**) Tensile strength, (**e**) toughness, and (**f**) linear elasticity are shown relative to dielectric constant of the solvent.

For the sake of simplicity, we summarize all property changes associated with varying the solvent (e.g. boiling point, polarity, solubility) as the change in one predominant, systematic variable: the dielectric constant (ε) of the solvent. The dielectric constant is a general measurement of the polarizability (increasing ε corresponds to increasing polarizability) of the solvent, and thus greatly affects the properties and solvent "quality" of the polymer solution. CF and PhCl have relatively similar dielectric constants, and thus similar mechanical properties. In general, a decrease in solvent polarity correlated with a decrease in tensile strength (**Fig A3d**) and increase in toughness (**Fig A3e**). The increase in toughness is largely due to the increased fracture strain for the MeTHF sample. The range of linear elasticity remained approximately constant (**Fig A3f**).

UV-vis absorption spectra showed stronger aggregation of N2200 in MeTHF than in CF and PhCl, which suggests that MeTHF is a poorer solvent. Additional GIWAXS data suggests that the CF and PhCl

films induce strong crystallization and highly ordered films, while the MeTHF indicates weak crystallization and disorder. The authors suggested that this was due to (1) the blade coating deposition process reducing solubility due to the temperature gradient between the high temperature solution and low temperature substrate[16] and (2) MeTHF evaporating faster (due to its lower boiling point), both of which suppress crystalline growth. As a poorer solvent, MeTHF induces a morphological structure more favorable for increasing the extensibility of a film. The opposite is true as well: better solvents like CF and PhCl induce a more favorable morphology for increasing the tensile strength.

The majority of the samples discussed in this Perspective were deposited by spin coating films onto a substrate.[23] These samples, however, were deposited using a blade coating technique. Shearing deposition techniques (e.g. blade coating) induce anisotropy in thin films by promoting chain alignment,[24] and thus the mechanical (and electronic) properties of a blade coated film differ from those of a spun film. Despite this, there have been few if any studies (to the best of our knowledge) comparing how different deposition techniques affect the mechanical properties of semiconducting polymer films.

A.3 Effect of P3HT Nanowire Composition

Nanowires (NWs) are useful structures for many semiconducting polymer applications (e.g. chemical and biological sensing, electrical interconnects, transistors) due to their unique electronic properties and geometry.[25] Their high ratio of area to volume allows for greater surface area for diffusion, adsorption/desorption, and electrical response.[25] However, NWs also offer an opportunity to achieve favorable morphologies for different device applications by altering the microstructure of a polymer film. For example, conjugated polymer nanowires have been used to achieve percolated networks in polymer matrices that are both mechanically stable and improve electronic performance.[26,27] Likewise, semiconducting polymer NWs have been shown to conduct charge even in an insulating polymer matrix.[28] Shown below in **Figure A4** is a comparison of P3HT films blended with varying fractions of P3HT NWs as conducted by Kim et al.[27]

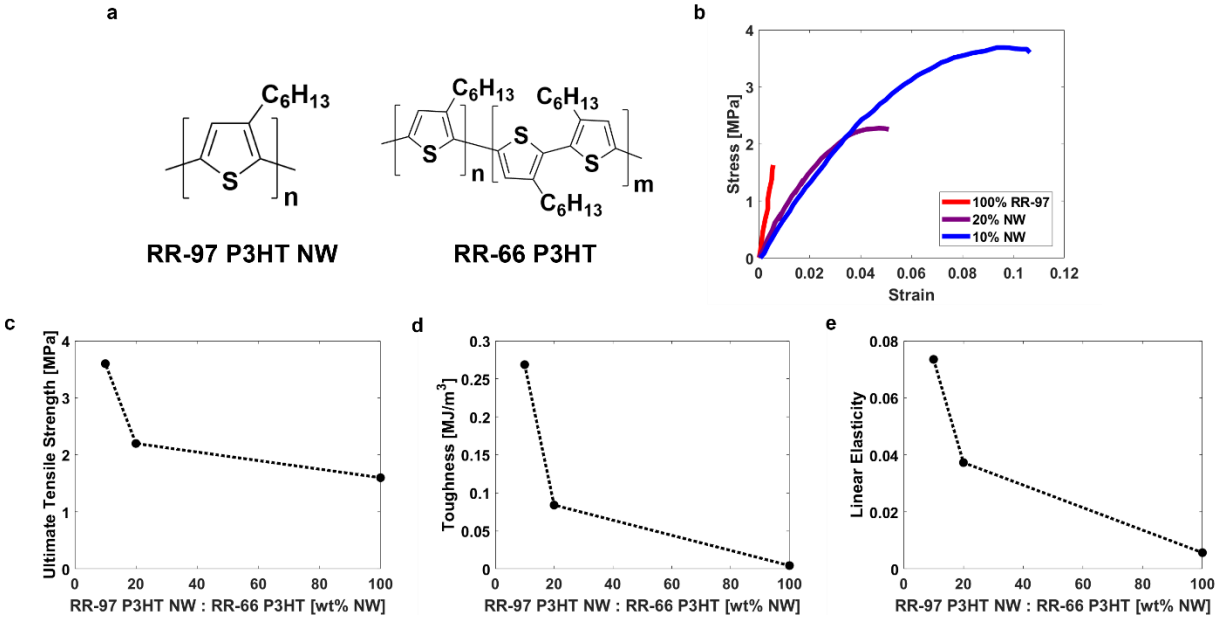

Figure A4. Mechanical properties of P3HT:NW P3HT polymer films. (**a**) Chemical structures of P3HT (66% regioregularity) and P3HT NWs (97% regioregularity). (**b**) Stress-strain curves of P3HT films as a function of nanowire loading as replotted from Kim et al. 2017.[27] Shown in red is a pure RR-97 P3HT film. (**c**) Tensile strength, (**d**) toughness, and (**e**) linear elasticity relative to the fraction of P3HT NWs are shown in the respective plots.

The two main differences between the samples are (1) the average regioregularity of the sample and (2) the weight fraction of highly crystalline P3HT NWs embedded in the amorphous P3HT matrix. The P3HT and P3HT NWs had similar degrees of polymerization, (97% regioregular P3HT: X_n = 111, 66% regioregular P3HT NWs X_n = 102). Likewise, their glass transition temperatures were similar (–20–0 °C).[27] As expected, the P3HT NW: P3HT blends exhibited better mechanical behavior than the pure P3HT film (which had the least favorable mechanical properties by all metrics). However, this data suggests that loading a small fraction of NWs is sufficient for improving the mechanical properties; the tensile strength, toughness, and linear elasticity were all highest for the 10% P3HT NW sample (**Fig A4c-e**).

We can infer that this improvement in mechanical properties can largely be attributed to the change in regioregularity. Embedding crystalline NWs in a relatively amorphous P3HT matrix allows for increased

energy dissipation by decreasing the stress concentration in the crystalline regions. This prevents early breakage of covalent bonds. As a result, the tensile strengths and fracture strains (and thus toughness) of samples with embedded NWs greatly increased (resembling that of the regioregular-*b*-regiorandom P3HT copolymers). However, we are unable to decouple the effect of the nanowires on the mechanical properties from the effect of altering the average regioregularity.

A.4 Effect of Conjugation-Break Spacers

Our main text discusses in detail the Thompson group's work studying the effects of conjugation-break spacers (CBS) on the mechanical properties of semiconducting polymers. However, two of the three libraries of polymers synthesized held the fraction of DPP and CBS units equal. This poses a problem because the mechanical effects of the DPP and CBS monomers cannot be separated from one another. The third library (a library of DPP-based polymers with a 2-ethylhexylDPP (ehDPP) monomer) attempts to isolate the effect of the CBS monomer.[29]

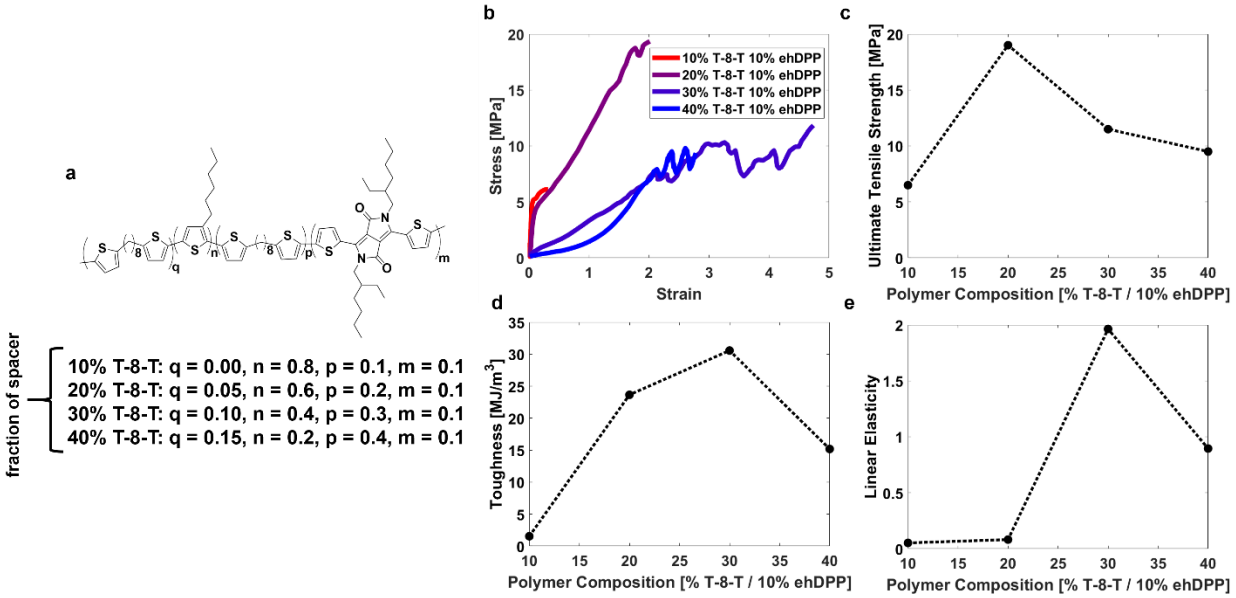

Figure A5. Mechanical properties of modified P3HT-ehDPP polymers relative to conjugation-break spacer length and fraction. (**a**) Chemical structure of the P3HT-ehDPP library used. Spacer fractions ranged from 10% to 40% with a constant fraction of 10% ehDPP. The spacer length likewise remained constant (alkyl length n = 8). (**b**) Stress-strain curves of P3HT-ehDPP polymers relative to increasing CBS fraction as reproduced from Melenbrink et al. 2019.[29] (**c**) Tensile strength, (**d**) toughness, and (**e**) linear elasticity are shown relative to spacer fraction.

This library of P3HT-ehDPP polymers (**Fig A5a**) holds the ehDPP monomer fraction constant at 10% while varying the fraction of the CBS unit to isolate the effect of the spacer unit. The stress-strain behaviors were difficult to interpret due to difficulties in maintaining good solubility (which creates poor quality films and thus poor mechanical measurements) and low degrees of polymerization (**Fig A5b**). The 10% CBS sample had the highest molecular weight, at 19.5 kDa, yet had the lowest tensile strength, toughness, and linear elasticity. This is in contrast to the 20% CBS sample, which had the lowest molecular weight at 8.5 kDa, but the highest tensile strength and relatively high toughness. Likewise, the 30% CBS sample had a fracture strain almost twice that of the 40% CBS sample, yet their molecular weights were relatively similar (12.8 kDa compared to 12.4 kDa). No definitive conclusions can be drawn solely from looking at the calculated strength, toughness, and linear elasticity of these four polymers.

A.5 References

(1) Zhang, S.; Ocheje, M. U.; Luo, S.; Ehlenberg, D.; Appleby, B.; Weller, D.; Zhou, D.; Rondeau-Gagné, S.; Gu, X. Probing the Viscoelastic Property of Pseudo Free-Standing Conjugated Polymeric Thin Films. *Macromol. Rapid Commun.* **2018**, *39*, 1–8.

(2) Siviour, C. R.; Jordan, J. L. High Strain Rate Mechanics of Polymers: A Review. *J. Dyn. Behav. Mater.* **2016**, *2*, 15–32.

(3) Zhang, S.; Ocheje, M. U.; Huang, L.; Galuska, L.; Cao, Z.; Luo, S.; Cheng, Y.; Ehlenberg, D.; Goodman, R. B.; Zhou, D.; Liu, Y.; Chiu, Y.; Azoulay, J. D.; Rondeau-gagné, S.; Gu, X. The Critical Role of Electron-Donating Thiophene Groups on the Mechanical and Thermal Properties of Donor – Acceptor Semiconducting Polymers. *Adv. Electron. Mater.* **2019**, *5*, 1800898–1800899.

(4) Mulliken, A. D.; Boyce, M. C. Mechanics of the Rate-Dependent Elastic-Plastic Deformation of Glassy Polymers from Low to High Strain Rates. *Int. J. Solids Struct.* **2006**, *43*, 1331–1356.

(5) Reynolds, J. R.; Thompson, B. C.; Skotheim, T. A. *Conjugated Polymers: Properties, Processing, and Applications*; **2019**.

(6) Kraus, J.; Müller-Buschbaum, P.; Kuhlmann, T.; Schubert, D. W.; Stamm, M. Confinement Effects on the Chain Conformation in Thin Polymer Films. *Europhys. Lett.* **2000**, *49*, 210–216.

(7) Rodriquez, D.; Kim, J.; Root, S. E.; Fei, Z.; Bou, P.; Heeney, M.; Kim, T.; Lipomi, D. J. Comparison of Methods for Determining the Mechanical Properties of Semiconducting Polymer Films for Stretchable Electronics. *ACS Appl. Mater. Interfaces* **2017**, *9*, 8855–8862.

(8) Sariban, A.; Binder, K. Critical Properties of the Flory-Huggins Lattice Model of Polymer Mixtures. *J. Chem. Phys.* **1987**, *86*, 5859–5873.

(9) Huggins, M. L. Solutions of Long Chain Compounds. *J. Chem. Phys.* **1941**, *9*, 440.

(10) Flory, P. J. Themodynamics of High Polymer Solutions. *J. Chem. Phys.* **1942**, *10*, 51–61.

(11) Wagner, H. L. The Mark-Houwink-Sakurada Equation for the Viscosity of Linear Polyethylene. *J. Phys. Chem. Ref. Data* **1985**, *14*, 611–617.

(12) Scholte, T. G.; Meijerink, N. L. J.; Schoffeleers, H. M.; Brands, A. M. G. Mark–Houwink Equation and GPC Calibration for Linear Short-chain Branched Polyolefines, Including Polypropylene and Ethylene–Propylene Copolymers. *J. Appl. Polym. Sci.* **1984**, *29*, 3763–3782.

(13) Israelachvili, J. N. *Intermolecular and Surface Forces*, 3rd ed.; 2011.

(14) Zverev, M. P.; Zubov, P. I.; Barash, A. N.; Nikonorova, L. P.; Ivanova, L. V. The Properties of Solutions of Polymers in Good and Poor Solvents and of Articles Prepared from These Solutions. *Polym. Sci. U.S.S.R.* **1974**, *16*, 589–598.

(15) Postema, A. R.; Liou, K.; Wudl, F.; Smith, P. Highly Oriented, Low-Modulus Materials from Liquid Crystalline Polymers: The Ultimate Penalty for Solubilizing Alkyl Side Chains. *Macromolecules* **1990**, *23*, 1842–1845.

(16) Lin, B.; Zhang, L.; Zhao, H.; Xu, X.; Zhou, K.; Zhang, S.; Gou, L.; Fan, B.; Zhang, L.; Yan, H.; Gu, X. D.; Ying, L.; Huang, F.; Cao, Y.; Ma, W. Molecular Packing Control Enables Excellent Performance and Mechanical Property of Blade-Cast All-Polymer Solar Cells. *Nano Energy* **2019**, *59*, 277–284.

(17) Grell, M.; Bradley, D. D. C.; Long, X.; Chamberlain, T.; Inbasekaran, M.; Woo, E. P.; Soliman, M. Chain Geometry, Solution Aggregation and Enhanced Dichroism in the Liquid-Crystalline Conjugated Polymer Poly(9,9-Dioctylfluorene). *Acta Polym.* **1998**, *49*, 439–444.

(18) Morgan, B.; Dadmun, M. D. The Importance of Solvent Quality on the Modification of Conjugated Polymer Conformation and Thermodynamics with Illumination. *Soft Matter* **2017**, *13*, 2773–2780.

(19) Nguyen, T. Q.; Doan, V.; Schwartz, B. J. Conjugated Polymer Aggregates in Solution: Control of Interchain Interactions. *J. Chem. Phys.* **1999**, *110*, 4068–4078.

(20) Nguyen, T. Q.; Yee, R. Y.; Schwartz, B. J. Solution Processing of Conjugated Polymers: The Effects of Polymer Solubility on the Morphology and Electronic Properties of Semiconducting Polymer Films. *J. Photochem. Photobiol. A Chem.* **2001**, *144*, 21–30.

(21) Chen, J.; Zhuang, H.; Zhao, J.; Gardella, J. A. Solvent Effects on Polymer Surface Structure. *Surf. Interface Anal.* **2001**, *31*, 713–720.

(22) Schwartz, B. J. Conjugated Polymers as Molecular Materials: How Chain Conformation and Film Morphology Influence Energy Transfer and Interchain Interactions. *Annu. Rev. Phys. Chem.* **2003**, *54*, 141–172.

(23) Chang, C. C.; Pai, C. L.; Chen, W. C.; Jenekhe, S. A. Spin Coating of Conjugated Polymers for Electronic and Optoelectronic Applications. *Thin Solid Films* **2005**, *479*, 254–260.

(24) Dörling, B.; Vohra, V.; Dao, T. T.; Garriga, M.; Murata, H.; Campoy-Quiles, M. Uniaxial Macroscopic Alignment of Conjugated Polymer Systems by Directional Crystallization during Blade Coating. *J. Mater. Chem. C* **2014**, *2*, 3303–3310.

(25) Lipomi, D. J.; Chiechi, R. C.; Dickey, M. D.; Whitesides, G. M. Fabrication of Conjugated Polymer Nanowires by Edge Lithography. *Nano Lett.* **2008**, *8*, 2100–2105.

(26) Qiu, L.; Lee, W. H.; Wang, X.; Kim, J. S.; Lim, J. A.; Kwak, D.; Lee, S.; Cho, K. Organic Thin-Film Transistors Based on Polythiophene Nanowires Embedded in Insulating Polymer. *Adv. Mater.* **2009**, *21*, 1349–1353.

(27) Kim, H. J.; Lee, M. Y.; Kim, J.; Kim, J.; Yu, H.; Yun, H.; Liao, K.; Kim, T.; Oh, J. H.; Kim, B. J. Solution-Assembled Blends of Regioregularity-Controlled Polythiophenes for Coexistence of Mechanical Resilience and Electronic Performance. *ACS Appl. Mater. Interfaces* **2017**, *9*, 14120–14128.

(28) Lu, G.; Bu, L.; Li, S.; Yang, X. Bulk Interpenetration Network of Thermoelectric Polymer in Insulating Supporting Matrix. *Adv. Mater.* **2014**, *26*, 2359–2364.

(29) Melenbrink, E. L.; Hilby, K. M.; Choudhary, K.; Samal, S.; Kazerouni, N.; McConn, J. L.; Lipomi, D. J.; Thompson, B. C. Influence of Acceptor Side-Chain Length and Conjugation-Break Spacer Content on the Mechanical and Electronic Properties of Semi-Random Polymers. *ACS Appl. Polym. Mater.* **2019**, *1*, 1107–1117.

Appendix B. Supplementary Information for Chapter 2. Comparison of the Mechanical Properties of a Conjugated Polymer Deposited using Spin Coating, Interfacial Spreading, Solution Shearing, and Spray Coating

B.1 Experimental Methods

B.1.1 Preparation of Substrates

Glass and silicon substrates were cut into 2.5 cm × 2.5 cm slides (for spin coating and interfacial spreading) using a diamond-tipped scribe or kept as 2.5 cm × 7.5 cm slides (for solution shearing and spray coating). Slides were cleaned by sonicating in Alconox and water, deionized (DI) water, isopropyl alcohol (IPA), and acetone for 10 min each. Prior to deposition, glass slides were dried using compressed air and air plasma treated for 5 min at 200-250 mTorr to increase the wettability of the surface.

B.1.2 Deposition Polymer Films using Different Deposition Processes

Poly(3-heptylthiophene) (P3HpT) (purchased from Rieke Metals, M_n ~ 26.4 kDa, PDI = 2.2, RR = 93%) and was dissolved in chlorobenzene at a concentration of 15 mg mL^{-1} (for spin coated, spread, and sheared films) and 5 mg mL^{-1}. A lower concentration is used for spray coated films to prevent unwanted precipitation of polymer in the airbrush. Poly(3-butylthiophene) (P3BT) (purchased from Sigma Aldrich and manufactured by Rieke Metals, M_n ~ 18.3 kDa, PDI = 3.0, RR = 85%) was dissolved in chlorobenzene at 12 mg mL^{-1} (due to the lower solubility of P3BT). All solutions were stirred for 12-48 h at 80 °C prior to use. The deposition processes outlined below were tailored to form P3HpT films with average thicknesses of approximately 120 nm in order to prevent the influence of skin-depth effects on the mechanical properties of the film.

Spin coating: The polymer solution was deposited directly onto the glass substrate from a syringe fitted with a 0.2 μm Nylon filter and spun at 750 rpm (750 rpm s^{-1} ramp) for 60 s followed by 2000 rpm (1000 rpm s^{-1} ramp) for 30 s.

Interfacial spreading: Glass petri dishes (outer diameter 92 mm) were cleaned using a 3-step rinse (IPA, acetone, DI water) before being filled approximately halfway with DI water. The spreading process was performed by depositing 65 μL of polymer solution onto the surface of water as described by Noh et al.[1] After film solidification (as indicated by a change in color from orange solution to a magenta film), the film was stamped onto glass or silicon substrates.

Solution shearing: The instrument used in this study was a commercial Zehntner ZAA2300 blade coater. Throughout all experiments, the blade applicator was set to a height of 50 ± 5 μm perpendicular to the substrate. The substrate was placed 1 cm away from the applicator before deposition to ensure that the applicator reached steady state velocity before making contact with the polymer solution. The polymer solution (40 μL) was deposited on one end of the substrate and then coated using the applicator moving at a rate of 5 mm s^{-1}. To ensure complete evaporation of any residual solvent, the substrate remained undisturbed for approximately 3 min after deposition.

Spray coating: A Badger 200 NH airbrush with a 20 MPa nitrogen feed was used for spray coating. The airbrush was set at an inclination of 47° relative to the substrate and had a spray diameter of approximately 3 cm (slightly greater than the width of the substrate). The polymer solution (1 mL) was loaded into the feed and sprayed onto the substrate at a flow rate of 0.04 mL min^{-1}. The substrate was rotated after each layer to ensure uniform deposition. Five total layers were deposited, which corresponded to a film thickness of approximately 120 nm.

B.1.3 Mechanical Testing

A water-soluble sacrificial layer is necessary to transfer the polymer film onto the surface of water for tensile testing. Poly(3,4-ethylenedioxythiophene):poly(styrenesulfonate) (PEDOT:PSS) dispersed in water was purchased from Heraeus (Clevios pH 1000) and used as the sacrificial layer. PEDOT:PSS was first deposited onto the substrate until completely covered and spun at 750 rpm (750 rpm s^{-1} ramp) for 90 s followed by 2000 rpm (750 rpm s^{-1} ramp) for 30 s for 2.5 cm × 2.5 cm substrates. On larger substrates (2.5 cm × 7.5 cm), the spin speed was increased to 2000 rpm (2000 rpm s^{-1} ramp) for 90 s followed by 4000 rpm (2000 rpm s^{-1} ramp) for 30 s. After the deposition of the sacrificial layer, P3HpT or P3BT was deposited on top using the same spin conditions outlined (with no treatments made to the PEDOT:PSS surface). The thin films were then scored into dogbone geometries using a 3D-printed stencil. The width at the center of the dogbone was 0.4 cm and the length was 1.5 cm. Thickness measurements were obtained using a Bruker Dektak XT stylus profilometer, operated with a force of 3 mg. The PEDOT:PSS sacrificial layer dissolved when exposed to water, causing the polythiophene film to float off the substrate and onto the surface of water. The film was then aligned and adhered to PDMS slabs, which were taped to the grips of the linear actuator. Films were uniaxially strained at a rate of 6.67×10^{-4} s^{-1} until fracture to obtain a force-displacement curve. Engineering strain was calculated by dividing the change in length of the film by the original length ($\Delta L/L_0$). Engineering stress was calculated by dividing the force by the initial cross-sectional area of the film. Recent work by the Gu group has elucidated the effect of water on the measured tensile properties of ultrathin polymer films.[2] To minimize the presence of residual water inside the solid film, interfacially spread films were dried in a desiccator for between 24 – 48 h after deposition. All other films were tested within 24 – 48 h after deposition. However, the effect of the transport of water into and out of the film during solidification on the mechanical response remains unclear.

B.1.4 Morphological Characterization

Optical microscopy images were obtained using a Leica DM2700M microscope operated with bright-field illumination. Films were imaged at a magnification of 50×. All UV-vis measurements were acquired using an Agilent 8453 UV-vis spectrophotometer, scanning wavelengths from 300 to 800 nm in increments of 1 nm. Dichroic ratio, H-aggregation, and relative degree of crystallinity were determined using a purpose-written script in Matlab R2020b. Atomic force micrographs (AFM) of height and phase images were obtained using a Veeco scanning probe microscope operated in non-contact tapping mode. AFM data analysis was performed using Nanoscope Analysis v1.4.

GIXD measurements were performed at the Stanford Synchrotron Radiation Lightsource (SSRL) on beamline 11-3. The beam energy was 12.7 keV and the sample-detector distance was 315 mm, resulting in an incidence angle of 0.12 degrees. The beam footprint on the sample was 4 mm × 0.15 mm. Each sample was exposed to the beam for 180 s, with images representing the average morphology of three measurements (at different areas) on the same sample. The beam angle was above the critical angle for total external reflection, such that the beam penetrated the entire thickness of the film. The sharp Vineyard-Yoneda peaks which extend from the polar angles of ~ ±85° to ±90° and the forbidden region from ±0° to ±5° were excluded from the normalization of the orientation distribution function (ODF). The definition of the ODF is given as the following equation,

$$ODF = \frac{I(\theta) * sin(\theta)}{\int_{-85^\circ}^{85^\circ} I(\theta) * sin(\theta)\, d\theta} \qquad \textbf{Equation (1)}$$

where θ is the polar angle.

The face-on to edge-on crystallite population ratios were calculated by comparing the fraction of the integrated intensity of the ODF from 5° to 45° (defined as the edge-on contribution) to the integrated intensity from 45° to 85° (face-on contribution). The relative degree of crystallinity (rDoC) was calculated

by computing the integral of the (100) peak intensity over all accepted polar angles (5° to 85°) using a polar angle-dependent correction factor and subtracting an average background from a locally linear baseline fit.[3] Lastly, the progression of disorder was analyzed by looking at the full width at half maximum (FWHM) of the (100) and (200) lamellar peaks as obtained from the reduced I-Q plots, where Q is the scattering vector length. The (300) signature is visible but difficult to isolate from the background due to its low intensity. Therefore, the FWHM of the (300) peak was not calculated. The crystallite coherence length was determined by using the following equation,

$$L_c = \frac{2\pi}{\Delta_q} \qquad \textbf{Equation (2)}$$

where Δ_q is the FWHM when the diffraction order is zero. The value of Δ_q is obtained from the y-intercept of the linear FWHM-diffraction order relationship. The diffraction order (m) refers to the successive set of planes that diffract along a particular axis (i.e., the (100) reflection is first order diffraction, (200) reflection is second order along the general (a00) lamellar direction). This methodology has been described previously by Rivnay et al. for determining the coherence length in materials with substantial paracrystalline disorder.[3]

B.1.5 Thermal and Mechanical Characterization of P3BT

Spin coated and sheared P3BT films were cast using the same parameters outlined previously. For spread films, the deposited solution volume was reduced to 40 μL. This change was primarily made due to significant film wrinkling for films formed from droplet sizes of 65 μL (**Figure B7**). The cast films were placed under active vacuum overnight to remove any residual solvent present in the film. The films were annealed at increasing temperatures, and the UV-vis spectra measured using an Agilent Cary 60 UV-vis spectrophotometer after each annealing step as described in our previous work. The glass transition temperature was calculated by determining the inflection point in the deviation metric, which is defined as:

$$Deviation\ metric = \sum_{\lambda_{min}}^{\lambda_{max}} [I_{RT}(\lambda) - I_{Annealed\ T}(\lambda)]^2 \qquad \textbf{Equation (3)}$$

where λ_{min} and λ_{max} correspond to the wavelengths over which the absorption spectra were taken (300-800 nm). The I_{RT} and $I_{Annealed\ T}$ terms refer to the normalized intensity relative to the peak absorbance spectrum of the polymer at room temperature and at the annealed temperature, respectively.[4]

B.1.6 Electronic Characterization

Prefabricated bottom-gate, bottom-contact transistors (channel width = 1 mm, channel length = 30 μm, electrode material = gold) were purchased from Ossila and used as the substrate for all organic field-effect transistor (OFET) devices. The substrates were rinsed only with IPA and DI water, as acetone and Alconox solution were found to detach the gold from the silicon substrate. To prepare the silane monolayer, octadecyltrichlorosilane (ODTS) (11 μL) was dissolved in trichloroethylene (10 mL) and was allowed to self-assemble on the substrate (e.g., a spin speed of 0 rpm for 10 s followed by 3000 rpm (1500 rpm s^{-1} ramp) for 10 s). The ODTS-treated substrates were then placed in a closed container with 28-30% ammonium hydroxide for 8 h. Prior to deposition of the active layer, substrates were rinsed with DI water, rinsed with toluene, and treated with an air plasma to activate the surface. After deposition, films were immediately transferred into a nitrogen glovebox and annealed at 100 °C for 1 h. Mobility measurements were obtained using a Keithley 4200 semiconductor parameter analyzer. Hole mobility was calculated from the linear fit of the square root of the source-drain current-gate voltage behavior in the saturation regime of the transfer plots.

B.2 Supplementary Figures

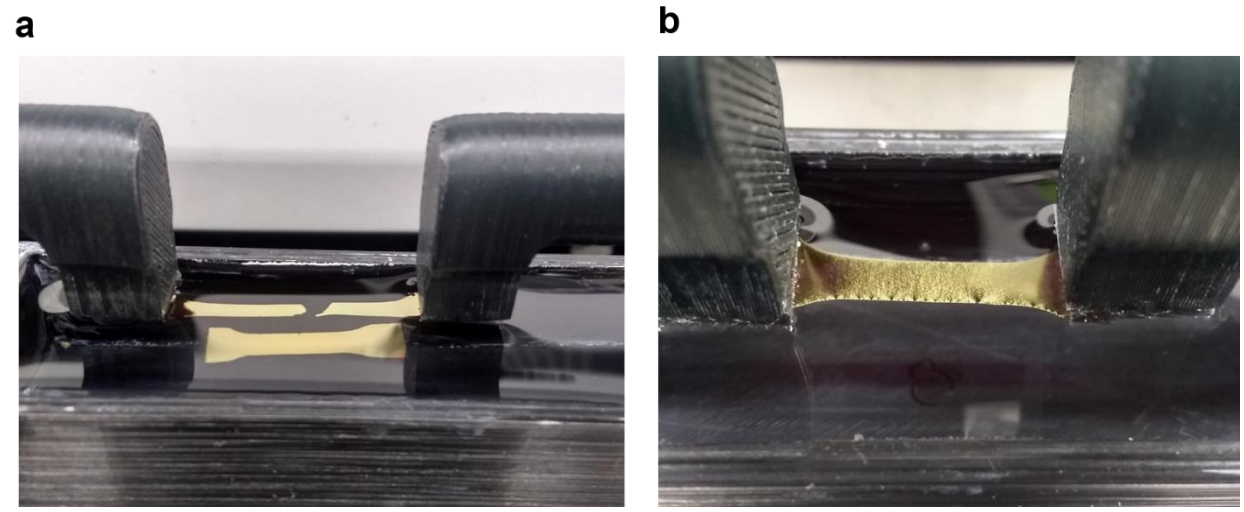

Figure B1. Spray coated films concentrated stress along granular defects. (**a**) While spin, spread, and sheared films underwent necking deformation (a comparison is given with an unstrained film), (**b**) spray coated films underwent weakening mechanisms prior to fracture. The difference in cross-section width of the unstrained film relative to the strained film is characteristic of necking in materials.

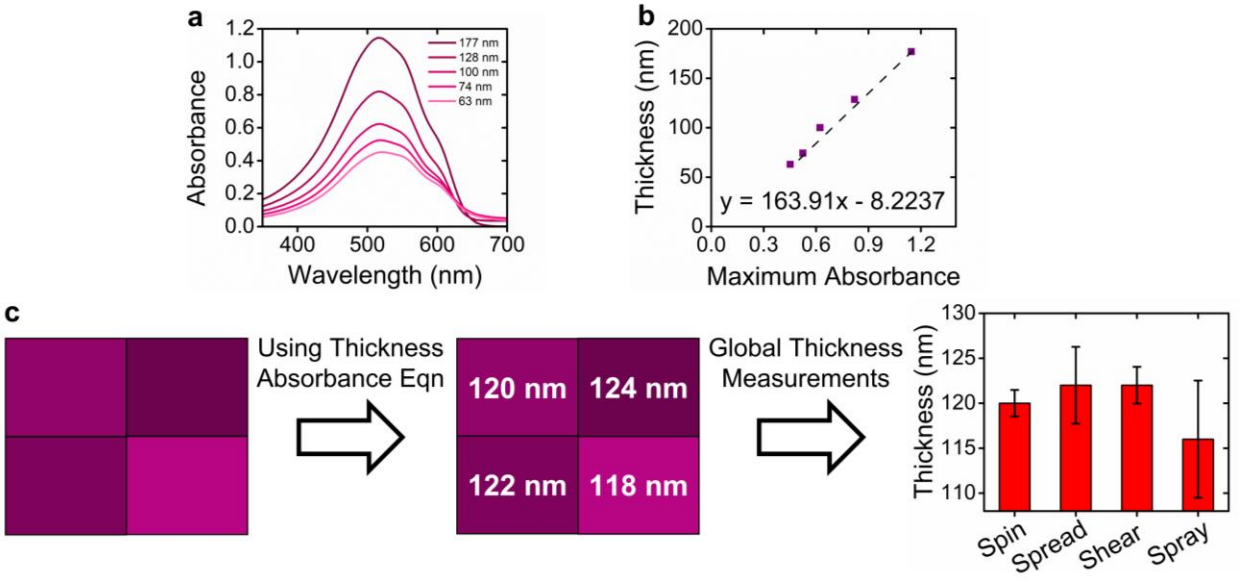

Figure B2: Investigating thickness variations across P3HpT films cast using different deposition techniques. (**a**) The thickness-absorbance relationship for P3HpT films was determined by spin coating films of various thickness by altering the spin speed and measuring their peak absorbance at $\lambda = 515$ nm. (**b**) The thickness-absorbance relationship obtained was a linear fit as expected from Beer's law. (**c**) The absorbance spectra of various regions of the different films were then measured to determine the average and standard deviation of thicknesses across different samples.

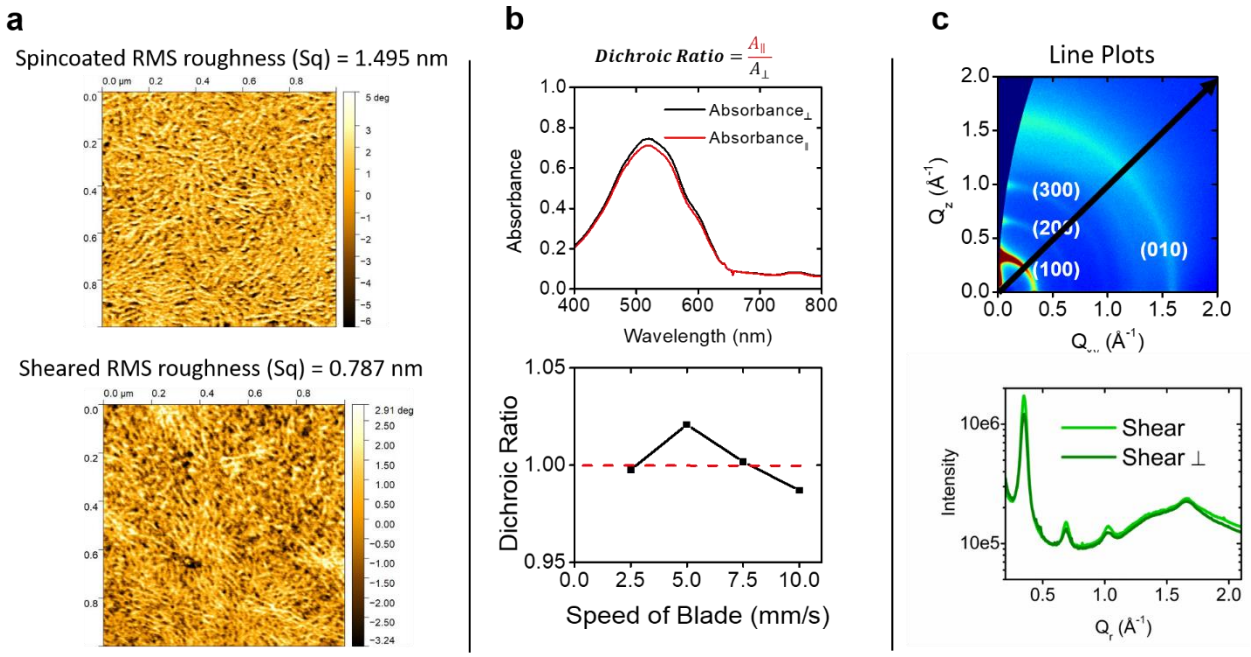

Figure B3. We searched for anisotropy in sheared P3HpT films by (**a**) looking for grain alignment using atomic force microscopy, (**b**) measuring the dichroic ratio of sheared films, and (**c**) taking GIWAXS measurements parallel and perpendicular to the beam axis and plotting the orientationally averaged I-Q plot for sheared films. No alignment was observed using these different characterization methods. The shear speed for AFM, UV-vis, and GIWAXS samples was constant at 5 mm s^{-1}.

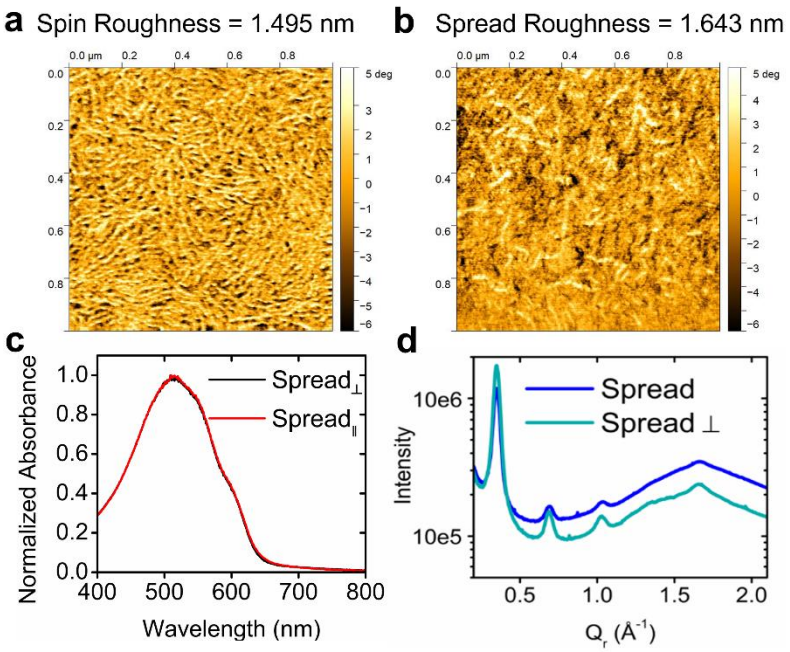

Figure B4. No anisotropy was observed in spread P3HpT films. (**a**) The AFM phase images of spin coated films are provided as a reference of an isotopic sample. (**b**) Similarly, no grain alignment is observed in the phase image of a spread film. (**c**) In addition, the polarized absorption spectroscopy revealed no differences in absorbance of the spread film when oriented in two different directions, further suggesting a lack of anisotropy. (**d**) While GIXD I-Q plots for spread films suggest some orientation dependent intensities, these likely arise from thickness variations rather than chain alignment.

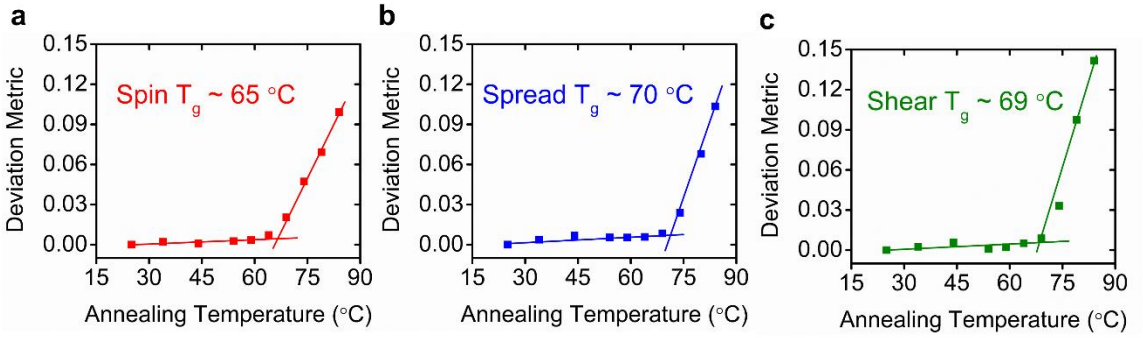

Figure B5. The glass transition temperature was determined by identifying the point of inflection in the deviation metric, calculated from the absorption spectra at each annealing temperature for (**a**) spin coated, (**b**) interfacially spread, and (**c**) solution sheared P3BT films.

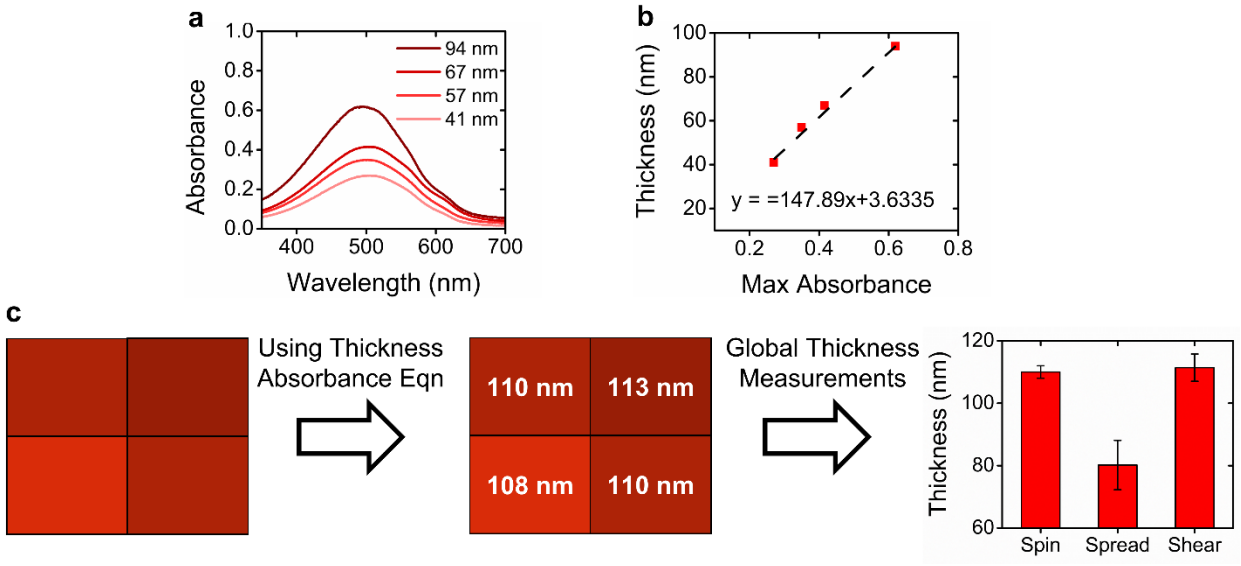

Figure B6: Thickness variations across P3BT films cast using different deposition processes. (**a**) The thickness-absorbance relationship for P3BT films was determined by spin coating films of various thickness and measuring their peak absorbance at λ = 494 nm. (**b**) The thickness-absorbance relationship obtained was a linear fit as expected from Beer's law. (**c**) The absorbance spectra of various regions of the different films were then measured to determine the average and standard deviation of thicknesses across different samples. Spread films of P3BT were significantly thinner than their spun and sheared counterparts due to significant film wrinkling during the solidification process for thick (~100 nm) films.

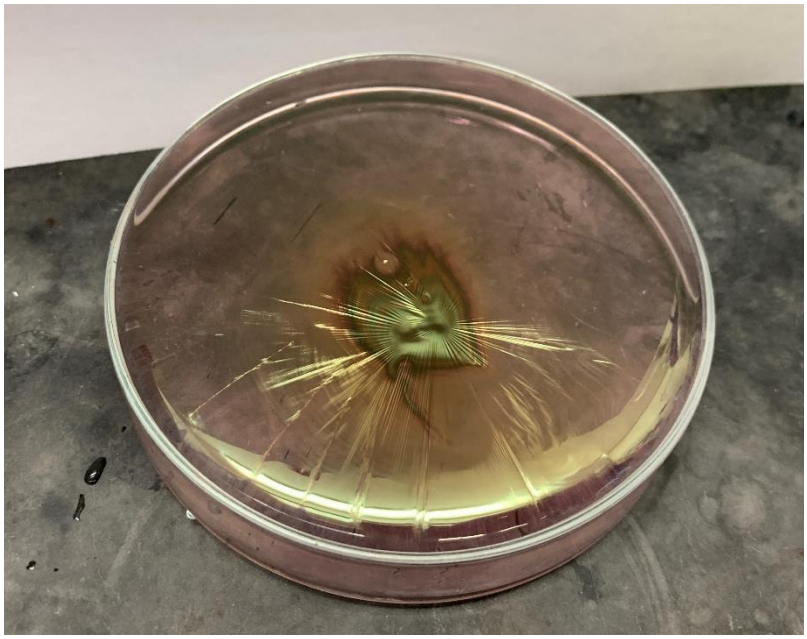

Figure B7. One limitation of interfacial spreading is the difficulty in forming thick (>100 nm for P3BT) polymer films. The resultant film is dependent on the polymer, concentration of polymer solution, solvent, and deposited volume. Unfavorable deposition parameters can result in areas of inhomogeneities (e.g., the dark center region) or wrinkling behavior as shown above.

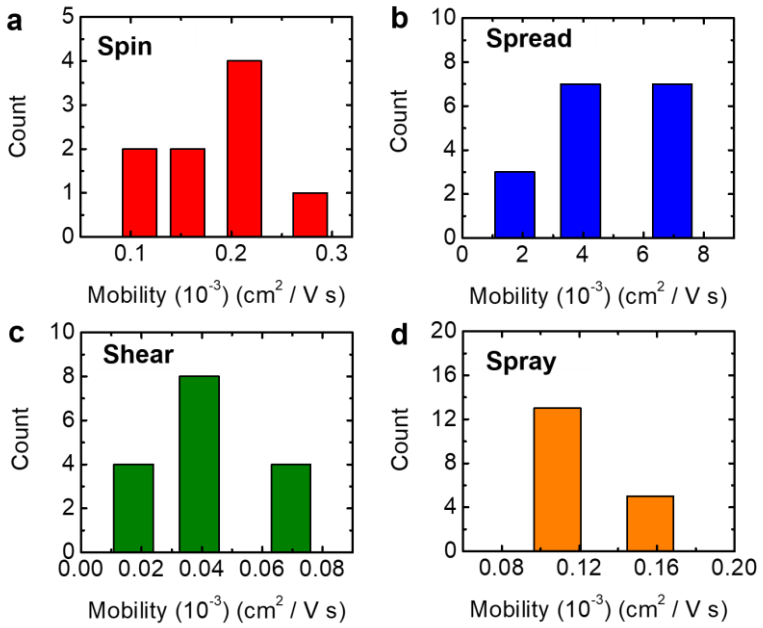

Figure B8. Count-Mobility bar plots for (**a**) spin coated, (**b**) spread, (**c**) shear, and (**d**) spray coated films. Spread films consistently showed mobilities that were one order of magnitude greater than values obtained from films cast using other deposition processes.

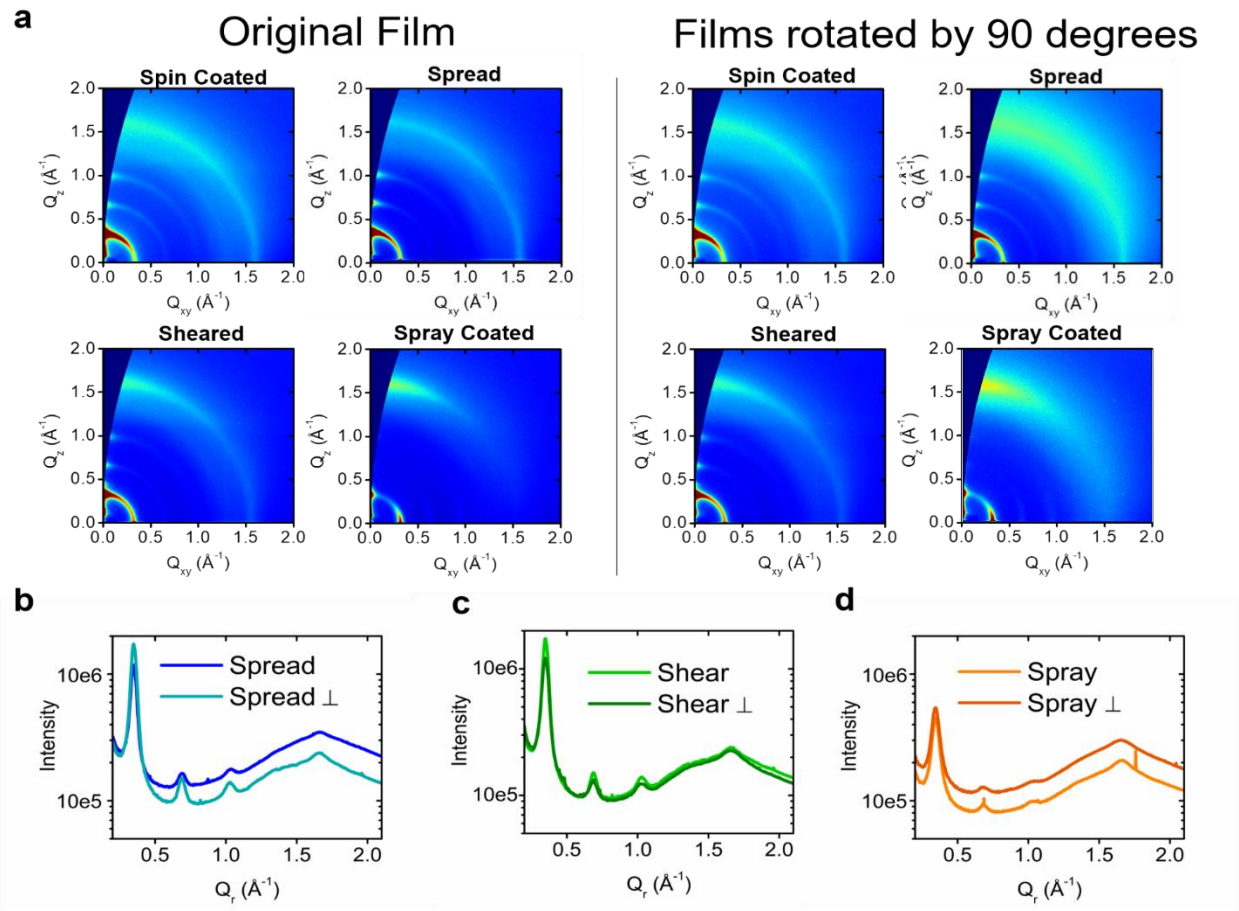

Figure B9. (**a**) Diffraction signatures were obtained from films rotated by 90° to determine whether there was any anisotropy (particularly in sheared samples). We note that spread films often showed high scattering intensities in the π-stacking (010) direction. The resulting I-Q plots were generated for (**b**) spread, (**c**) sheared, and (**d**) spray coated films. Anisotropy could be indicated by variations in peak intensities when the film was rotated. Here, we see no anisotropy in sheared films.

B.3 References

(1) Noh, J.; Jeong, S.; Lee, J.-Y. Ultrafast Formation of Air-Processable and High-Quality Polymer Films on an Aqueous Substrate. *Nat. Commun. 2016 71* **2016**, *7* (1), 1–9. https://doi.org/10.1038/ncomms12374.

(2) Galuska, L. A.; Muckley, E. S.; Cao, Z.; Ehlenberg, D. F.; Qian, Z.; Zhang, S.; Rondeau-Gagné, S.; Phan, M. D.; Ankner, J. F.; Ivanov, I. N.; Gu, X. SMART Transfer Method to Directly Compare the Mechanical Response of Water-Supported and Free-Standing Ultrathin Polymeric Films. *Nat. Commun.* **2021**, *12* (1), 2347. https://doi.org/10.1038/s41467-021-22473-w.

(3) Rivnay, J.; Mannsfeld, S. C. B.; Miller, C. E.; Salleo, A.; Toney, M. F. Quantitative Determination of Organic Semiconductor Microstructure from the Molecular to Device Scale. *Chem. Rev.* **2012**, *112* (10), 5488–5519. https://doi.org/10.1021/CR3001109.

(4) Root, S. E.; Alkhadra, M. A.; Rodriquez, D.; Printz, A. D.; Lipomi, D. J. Measuring the Glass Transition Temperature of Conjugated Polymer Films with Ultraviolet–Visible Spectroscopy. *Chem. Mater.* **2017**, *29* (7), 2646–2654. https://doi.org/10.1021/ACS.CHEMMATER.7B00242.

Appendix C. Supplementary Information for Chapter 3. Increasing the Strength, Hardness, and Survivability of Semiconducting Polymer Films by Crosslinking

C.1 Experimental Methods

C.1.1 Synthesis of 4Bx.

Materials for Synthesis.

Dichloromethane (DCM, Fisher Chemical) was degassed with argon and dried on a solvent purification system (JC Meyer) equipped with activated alumina columns before use. Ethyl acetate (Fisher Chemical) and hexanes (Fisher Chemical) were purchased and used as received. Triethylamine (NEt_3, Sigma-Aldrich) was passed through a column of activated alumina and stored over 4 Å molecular sieves for 24 h before use. Pentaerythritol (Sigma-Aldrich) was finely ground and dried in vacuum oven at 50 °C overnight before use. 4-azido-2,3,5,6-tetrafluorobenzoic acid (TCI Chemicals) and sulfurous dichloride (Sigma-Aldrich) were used as received.

Thin layer chromatography was performed on glass-backed silica TLC plates (SiliaPlate) with F254 indicator and analytes were visualized with a UV-C lamp. Flash chromatography was performed using a Teledyne ISCO CombiFlash NEXTGEN chromatography system with Siliaflash P60 Silica (40-60 μm) as the stationary phase.

NMR spectra were collected on a Bruker Avance-III 300 spectrometer operating at 300 MHz and 282 MHz for ^{1}H and ^{19}F acquisitions, respectively.

Synthesis of 2,2-bis(((4-azido-2,3,5,6-tetrafluorobenzoyl)oxy)methyl)propane-1,3-diyl bis(4-azido-2,3,5,6-tetrafluorobenzoate) (4Bx).

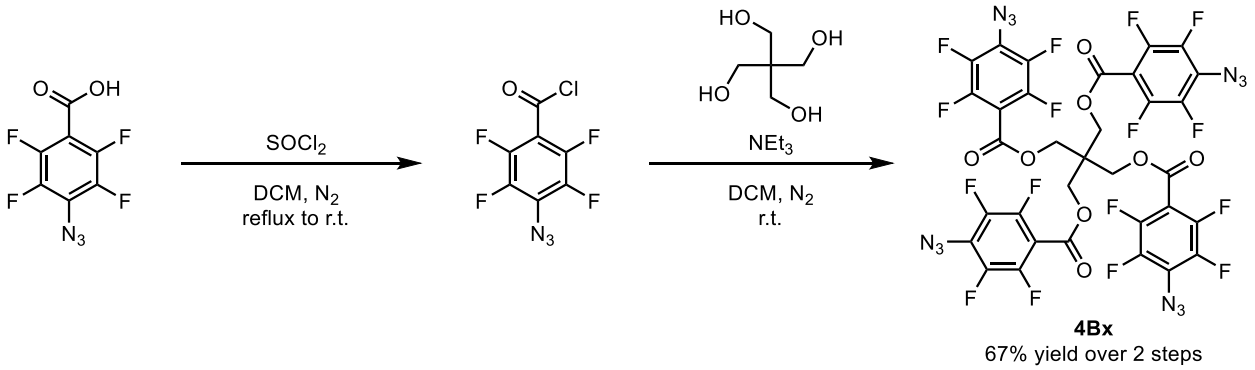

The synthesis of **4Bx** was adapted from the procedure described by Kim et al.[1] A flame-dried Schlenk flask containing a magnetic stir bar was charged with 4-azido-2,3,5,6-tetrafluorobenzoic acid (192 mg, 5.18 eq., 818 µmol) and purged with nitrogen. DCM (6 mL) and sulfurous dichloride (150 µL, 13.1 eq., 2.07 mmol) were added under nitrogen via syringe. The flask was equipped with a reflux condenser and heated to reflux with stirring. After 24 hours, the reaction mixture was cooled to ambient temperature and stirred for an additional 24 hours. Volatiles were removed *in vacuo* to yield the crude acyl chloride as a light yellow oil. The residue was dissolved in 4 mL DCM and transferred via cannula to a separate flame-dried Schlenk flask containing a solution of 2,2-Bis(hydroxymethyl)propane-1,3-diol (pentaerythritol, 21.5 mg, 1.00 eq., 158 µmol) and triethylamine (114 µL, 5.18 eq., 818 µmol) in DCM (4 mL). The resulting mixture was stirred at ambient temperature for 48 hours. Water (10 mL) was added to quench the reaction, and the organic phase was separated. The aqueous phase was extracted with DCM (3 x 10 mL), and the combined organic phases were washed with 30 mL brine, dried over magnesium sulfate, and concentrated in vacuo. The crude residue was purified by chromatography on silica gel with an eluent of hexanes/ethyl acetate (4:1, v/v; R_f = 0.52), followed by recrystallization from warm ethyl acetate/hexanes (ca. 4 mL and 35 mL, respectively) to yield **4Bx** as colorless needles in 106 mg (67% yield). ^{1}H and ^{19}F NMR data matched the literature values.[1]

C.1.2 Preparation of Substrates.

Glass substrates were used as purchased (25mm × 25mm, 1.1 mm thickness, purchased from Biotain Crystal Company) or cut using a diamond-tipped scribe (37.5 mm × 25 mm, 1.1 mm thickness) from 75 mm × 25 mm glass substrates (Fisherbrand, purchased from Fisher Scientific). Silicon substrates were purchased from WaferPro (100 mm N/PH (1-0-0), C04002) and diced into 25 mm × 25 mm squares. Glass, silicon, and unpatterned ITO substrates (25 mm × 25 mm, 100 nm of ITO deposited on top of a 1 mm glass substrate, purchased from Ossila) were cleaned by sonicating in Alconox and water, deionized (DI) water, acetone, and isopropyl alcohol (IPA) for 10 min each. Before deposition of the polymer solution, substrates were dried using compressed air and plasma treated in air (10 min, ~500 mTorr) to increase the wettability of the substrate.

C.1.3 Preparation of Polymer Solutions and Film Formation.

J51 (1-Material, M_n ~25 kDa, PDI ~3), PTB7-Th (Ossila, M_n ~29 kDa, PDI ~1.95), N2200 (Ossila, M_n ~ 90.9 kDa, PDI ~2.2), PTB7 (Ossila, M_n ~ 83 kDa, PDI ~ 2.52), TQ1 (Ossila, M_n ~ 61.5 kDa, PDI ~ 2.44), 2DPP-2CNTVT (1-Material, M_n ~ 24 kDa, PDI ~ 2.5), PZ1 (1-Material, M_n ~ 16.7 kDa, PDI ~ 3), P3HpT (Rieke Metals, M_n ~ 26.4 kDa, PDI = 2.2, RR = 93%), IDTBT (synthesized by H.C. and I.M.,[2,3] M_n ~ 38 kDa, PDI ~ 2.8), DPP-C3 (synthesized by X.L. and J.M.,[4] M_n ~ 9.4 kDa , PDI ~ 1.3), and DPP-C9 (synthesized by X.L. and J.M.,[4] M_n ~ 13.9 kDa , PDI ~ 1.4) were dissolved in chlorobenzene (anhydrous for device fabrication) at a concentration of 10–15 mg mL^{-1}. For J51:N2200 and PTB7-Th:N2200 blends, the ratio of donor polymer to acceptor polymer was 1:2 and 2:1 for each 12 mg mL^{-1} solution, respectively. 4Bx was dissolved in anhydrous chlorobenzene at a concentration of 15 mg mL^{-1}. 4Bx (1–3 wt% with respect to the polymer) and 1,8-diiodooctane (DIO) (purchased from Sigma-Aldrich and used as received) (2–3 vol%) were added to each polymer solution as needed. All solutions were prepared in a nitrogen environment (<0.05% oxygen, ~20% RH). After preparation, polymer solutions were left inside the nitrogen environment to stir overnight (~12–16 h) at 60 °C before use. For polymer films subject to mechanical testing or morphological characterization, films were spun outside of the glove box in atmosphere. The polymer solution was deposited on top of a glass substrate with a syringe fitted with a 0.2

μm Nylon filter. Then, the polymer film was formed by spin coating the sample at 1000–2000 rpm (with a ramp half that of the spin speed, i.e., 500–1000 rpm s^{-1}) for 90 s followed by a 2000 rpm (1000 rpm s^{-1}) step if needed. To initiate crosslinking, polymer films were annealed at 150 °C for 90 min or 175 °C for 60 min on a hot plate in atmosphere. After annealing, the hot plate was turned off in order to let the films slowly cool to room temperature.

C.1.4 Preparation of Polymer Films for Cohesive Fracture Testing and Compressive Mechanical Testing

For fracture testing samples, glass substrates were cut using a diamond-tipped scribe and cleaned as previously described. A layer of poly(3,4-ethylenedioxythiophene):poly(styrenesulfonate) (PEDOT:PSS), purchased from Heraeus (Clevios PH1000), was deposited on top of the glass substrate using a 1 μm glass fiber syringe filter (Chromspec) and spun at 4000 rpm (2000 rpm s^{-1}) for 60 s. Next, a 70–90 nm film of J51:N2200 (3 vol% DIO, 0–1 wt% 4Bx) or PTB7-Th:N2200 (2 vol% DIO, 0–1 wt% 4Bx) was spin coated on top of the PEDOT:PSS at a spin speed of 1800 rpm (1200 rpm s^{-1}) for 90 s followed by 2000 rpm (1200 rpm s^{-1}) for 30 s in atmosphere. All films were annealed at 175 °C for 60 min in atmosphere to initiate crosslinking for polymer blends that included 4Bx as the crosslinker. After annealing, 5 nm of Cr was deposited by thermal evaporation followed by 200 nm of Al by sputter deposition to form an encapsulation layer on top of the polymer film. Finally, a clean glass slide of the same size (37.5 mm × 25 mm) was adhered to the top of the Al layer using Loctite E-20NS HYSOL epoxy. The final fracture testing sample was cured under nitrogen for 12 h at room temperature before use.

For samples used for compressive mechanical testing (i.e., nanoindentation), silicon substrates were diced and cleaned as described. A solution of J51:N2200 (3 vol% DIO, 0–2 wt% 4Bx) or PTB7-Th:N2200 (2 vol% DIO, 0–2 wt% 4Bx) was drop cast (~0.4 mL) on top of silicon substrate in a fume hood. A glass crystallization dish (diameter = 125 mm, height = 65 mm) was used to cover the substrates. The polymer samples were allowed to dry over 48 h to form a solid film (J51:N2200 ~ 4 μm, PTB7-Th:N2200

~ 12 μm). After drying, all polymer films were annealed at 175 °C for 60 min in atmosphere to initiate crosslinking.

C.1.5 Mechanical Testing

Pseudo-Free Standing Tensile Tests ("Film-on-Water")

For FOW tensile tests, a water-soluble sacrificial layer was first deposited on top of the glass substrate before the conjugated polymer film. For the sacrificial layer, a poly(acrylic acid) (PAA) film was used. PAA (purchased from Sigma Aldrich, M_w = 100 kDa, 35 wt% in water) was diluted in DI water at a ratio of 1:15 to form a 2.3 wt% solution. The PAA solution was filtered using a 1 μm glass fiber syringe filter (purchased from Chromatographic Specialties Inc.) before being deposited on top of the glass substrate. PAA sacrificial layers were spun at 500 rpm (250 rpm s^{-1}) for 60 s followed by 2000 rpm (1000 rpm s^{-1}) for 30 s before the conjugated polymer film was deposited using spin conditions described. All films were annealed at 150 °C for 90 min (for J51, PTB7-Th, and N2200) or 175 °C for 60 min (for J51:N2200 and PTB7-Th:N2200). For films containing 4Bx, this annealing step resulted in crosslinking. The polymer films were then scored into a dogbone geometry (length = 1.5 cm, center width = 0.4 cm) using a 3D-printed stencil. The thickness of each polymer film was measured using a Dektak XT stylus profilometer, operated with a force of 3 mg.

To conduct a film-on-water (FOW) tensile test, a dogbone-shaped polymer film was first floated off the glass substrate and onto the surface of water by dissolving the underlying PAA layer. The film was then aligned and adhered to polydimethylsiloxane (PDMS) (Sylgard 184, 1:20 crosslinker to elastomer base ratio) slabs, which were taped to the 3D-printed grips of a Mark-10 linear actuator connected to a 0.5 N force gauge. Films were uniaxially strained at a rate of 6.67×10^{-4} s^{-1} (0.4 mm min^{-1}) until fracture. The resulting force-displacement curve was converted into a stress-strain curve using the dimensions of the dogbone-shaped film as previously described.[5]

Cohesive Fracture Testing

Double Cantilever Beam testing (DCB) was performed in ambient conditions using a thin-film cohesion testing system (Delaminator DTS, Menlo Park, CA) which measured load, *P*, versus displacement, Δ. The initial displacement speed was set to 1 μm s^{-1}, which was increased linearly to accommodate the increasing crack length. The critical fracture energy, G_c (J m^{-2}), was then calculated from equation 1:[6]

$$G_c = \frac{12P_c^2a^2}{b^2E'h^3}\left(1 + 0.64\frac{h}{a}\right)^2 \quad \textbf{(1)}$$

Where P_c is the critical load at which crack growth occurs, a is the crack length, $E'$is the plane-strain elastic modulus, and b and h are the width and half-thickness of the substrates, respectively. The crack length was estimated from elastic compliance ($d\Delta/dP$) using equation 2:

$$a = \left(\frac{d\Delta}{dP} \times \frac{bE'h^3}{8}\right)^{1/3} - 0.64h \quad \textbf{(2)}$$

Nanoindentation

Nanoindentation samples were prepared as described and glued to a steel substrate in order to secure the samples in the grips of the indenter. Nanoindentation measurements (quasistatic[7] and dynamic[8–13]) were performed using an ultra-nanoindentation tester (UNHT^3, Anton Paar) in ambient conditions. An acoustic isolation chamber and piezo vibration isolation table were used to dampen any surface or acoustic vibrations. Indentations were made using a Berkovich tip (total angle = 141.9°). The projected contact area was A_C = 24.5 h_C^2, where h_C is the contact depth of the indenter at maximum load P_{max}.[14] The area shape function A_C was calibrated using a standard silica glass reference prior to testing. Protocol parameters were tuned using pilot tests to ensure accurate surface detection and to determine the loading protocol. For all tests, P_{max} = 0.06 mN was used. The maximum indentation depth (h_{max}) was less than 10% of the sample thickness to reduce the effect of the silicon substrate on the indentation measurement.[15] A minimum of 30 indents were performed on each J51:N2200 sample, while a minimum of 60 indents were performed on PTB7-Th:N2200 samples due to the higher scatter.

In quasistatic testing, samples were loaded in force control up to P_{max}. At P_{max}, the load was held constant for 2 s and was then unloaded quickly. The time to maximum load was chosen such that the maximum load was reached in a minute. The hold and unloading time were set at 1.8s to avoid any time dependent effects while still measuring the unloading curve, down to at 40% P_{max} (as sufficient to calculate the initial unloading slope, S). The output from the measurement was a load (P) versus load point displacement (h) curve at each indentation point, from which Young's modulus (E) and indentation hardness (H_{IT}) was calculated (**Figure C13**). Hardness (i.e., resistance of the material to permanent deformation) was calculated as by dividing P_{max} by the 2D projected contact area (A_c) between the sample and the indenter. The modulus was calculated using the unloading curve (i.e., where it is assumed that only elastic strain energy is being released). Both E and H_{IT} were calculated using the Oliver and Pharr Method encoded in the software provided with UNHT[3] using the following equation, where v is the Poisson ratio (assumed to be 0.35, as for poly(3-hexylthiophene)[16]).[14]

$$\frac{1-v^2}{E} = \frac{2\sqrt{A_c}}{\sqrt{\pi}\,S} - \frac{1-{v_i}^2}{E_i} \qquad \textbf{(3)}$$

In dynamic testing (i.e., the continuous stiffness method), the protocol from the quasistatic testing was modified to include superimposed small harmonic oscillations in the force signal during loading in order to measure the viscoelastic properties of the material (e.g., storage modulus (E'), loss modulus (E''), and phase shift (δ)). The amplitude of force oscillation (F_0) and frequency (f) were set to be 0.01 mN and 10 Hz, respectively.[9] The force amplitude was chosen such that the displacement amplitude (h_0) is much smaller than the indentation depth (h). Dynamic indentation tests generated curves of P vs h, from which the viscoelastic properties were calculated using the following equations encoded in the UNHT[3] software (**Figure C13**).

$$\frac{E'}{1-v^2} = \frac{\sqrt{\pi}}{2\beta\sqrt{A_c}}\left(\frac{F_0}{h_0}\cos\delta + m\omega^2 - K_i\right) \quad (4)$$

$$\frac{E''}{1-v^2} = \frac{\sqrt{\pi}\,\omega}{2\beta\sqrt{A_c}}\left(\frac{F_0}{\omega h_0}\sin\delta - D_i\right) \quad (5)$$

Here, β is the constant depending on the indenter geometry (1.034 for a Berkovich tip), F_0 and h_0 are the force and displacement amplitudes, m is the mass of the indenter, $\omega = 2\pi f$ (where f is the harmonic frequency), K_i is the stiffness coefficient, and D_i is the damping coefficient. This model considers the indenter tip-sample interaction as a spring and dashpot system in parallel.[9] The viscoelastic behavior of each sample can be expressed as $E = E' + iE"$, with the phase shift expressed by $\tan\delta = E"/E'$.

C.1.6 Fabrication and Measurement of EGaIn Solar Cells

EGaIn solar cells (ITO/PEDOT:PSS/BHJ/EGaIn), were fabricated by first depositing poly(3,4-ethylenedioxythiophene):poly(styrenesulfonate) (PEDOT:PSS), purchased from Heraeus (Clevios PH1000), on top of an unpatterned ITO substrate to form a hole-transport layer (HTL). PEDOT:PSS was deposited using a 1 μm glass fiber syringe filter (Chromspec) and spun at 4000 rpm (2000 rpm s^{-1}) for 60 s to form a 35–45 nm film. Following deposition, a third of the PEDOT:PSS layer was wiped away using a foam swab and DI water in order to allow for contact to the ITO electrode. The PEDOT:PSS film was annealed at 120 °C for 30 min in atmosphere before being allowed to cool slowly to room temperature by turning off the hot plate. To form the bulk heterojunction, a 70–90 nm film of J51:N2200 (3 vol% DIO, 0–2 wt% 4Bx) or PTB7-Th:N2200 (2 vol% DIO, 0–3 wt% 4Bx) was spin coated on top of the ITO/PEDOT:PSS inside a nitrogen environment (<0.05% oxygen, ~20% RH) at a spin speed of 1800 rpm (1200 rpm s^{-1}) for 90 s followed by 2000 rpm (1200 rpm s^{-1}) for 30 s. Following deposition, same third of the BHJ layer was wiped away using a foam swab and chloroform, again, to allow for contact to the ITO electrode. The bulk heterojunction was annealed at 175 °C for 60 min in the glove box to 1) crosslink the

BHJ and 2) remove DIO, which can act as a photoacid within the bulk heterojunction. In a solar cell with evaporated contacts, the DIO is generally removed as a consequence of the thermal deposition process, i.e., under high vacuum. For such devices, crosslinking can be initiated at lower temperatures (100–150 °C) for 90–120 min. After annealing, the ITO/PEDOT:PSS/BHJ structure was allowed to slowly cool by turning off the hot plate. After reaching room temperature, a bare copper wire was attached to the bare ITO region using carbon paint. To ensure good contact, mounting tape (3M) was placed on top of the copper wire after the carbon paint dried. Following this step, solar cells were transferred into the antechamber of a glove box and left under vacuum overnight to remove any residual moisture. Solar cells were tested one day after fabrication in a nitrogen glove box environment (<0.5 ppm O_2, <0.5 ppm H_2O).

To form the eutectic gallium-indium (EGaIn) electrode, a bare copper wire was wrapped and adhered to the luer tip of a 2 mL plastic syringe using silver paint as previously described.[17] EGaIn (purchased from Sigma Aldrich and used as received) was drawn into the plastic syringe. The bare copper wires attached to the ITO and EGaIn-filled syringe were connected to alligator clips that were attached to a Keithley 2400 Sourcemeter in a 2-point measurement format.

To form a solar cell, the plunger of the EGaIn-filled syringe was gently tapped to dispense a droplet of EGaIn on top of the bulk heterojunction to form a complete device stack (ITO/PEDOT:PSS/BHJ/EGaIn). The active area of each cell was measured using a camera below the device before each measurement (cell area ~ 0.2–0.65 cm^2). The photovoltaic (i.e., current density versus voltage) characteristics were measured using an ABET Sun 2000 solar simulator (150 W Xe short-arc lamp, AM 1.5G filter) with an irradiance of 100 mW cm^{-2}. A purpose-written LabView program controlling the Keithley 2400 Sourcemeter, sweeping from -0.2 V to 0.7 V with a voltage scan rate of 10 mV s^{-1} was used to control current density (J) versus voltage (V) measurements, as well as extract the photovoltaic properties (J_{sc}, V_{oc}, FF, PCE). The spectral intensity of the solar simulator was calibrated before each set of measurements using a Si reference cell.

C.1.7 Degradation Testing of EGaIn Solar Cells

Accelerated Thermal Degradation

After fabrication, J51:N2200 solar cells were heated on hot plate set at 60 °C in a nitrogen glove box environment (<0.5 ppm O_2, <0.5 ppm H_2O) and periodically tested (every 25 h up to 100 h, then every 50 h up to 200 h, then every 100 h up to 400 h) as described. Before testing, cells were allowed to cool to room temperature slowly by turning off the hot plate. To maximize the measurements that could be obtained from each cell, three measurements were taken at each time interval on the same location on the device by gradually increasing the size of the EGaIn droplet (e.g., from ~0.2 cm^2 to ~0.45 cm^2 to ~0.6 cm^2). For each time interval, a new location on the cell was measured (i.e., to avoid any EGaIn residue remaining from previous measurements from interfering with subsequent measurements). Thus, approximately 9 locations on each device were measured.

Chloroform Exposure

Solar cells containing crosslinked and non-crosslinked PTB7-Th:N2200 bulk heterojunctions were submerged into a beaker of chloroform in a nitrogen environment for 1 s before being annealed on a 100 °C hot plate for 30 min. Following this process, cells were transferred back into the antechamber of the glove box (under vacuum) overnight to remove any residual moisture from the film. J-V measurements were repeated the next day using the EGaIn process as described. This chloroform exposure treatment was repeated twice more for each cell for longer time intervals (10 s, 30 s). For longer exposures, the solar cells were submerged and unperturbed (i.e., no agitation, stirring, or mixing) for the duration of the treatment.

Physical Agitation using Sonication

J51:N2200 films (3 vol% DIO, 0-1% 4Bx) were first spun onto 25 mm × 25 mm glass substrates in atmosphere as described at a spin speed of 1800 rpm (1200 rpm s^{-1}) for 90 s followed by 2000 rpm (1200 rpm s^{-1}) for 30 s. After deposition, all films were annealed on a hot plate in atmosphere at 175 °C for 60 min and allowed to cool slowly back to room temperature. The films were then photographed (Nikon D3300) inside a light box, held upright using 3D-printed stands. After being photographed, each film was measured using a UV-vis spectrophotometer as described. To qualitatively observe the effect of

crosslinking on the abrasion resistance of non-crosslinked and crosslinked films, a Branson 2510 bath sonicator (40 kHz, 120 V) was used to physically abrase the films. J51:N2200 films were placed into glass staining dishes and covered in DI water before being placed in the bath sonicator and sonicated for 5 min. After sonication, the films were carefully removed and gently dried using compressed air, before being photographed and measured using the UV-vis spectrophotometer. To ensure good measurements, the position of the beam (circular, $d \sim 1$ mm) was carefully marked on a clean glass substrate when operating the Cary 60 UV-vis in Zero Order mode (i.e., white light). These UV-vis measurements were repeated 5 times per sonication interval, adjusting the position of the substrate such that the spectrophotometer beam measured regions of intact film. This process was repeated in 5 min intervals up to 10 min, and then 10 min intervals up to 1 h.

The change in film thickness for crosslinked and non-crosslinked films were calculated by comparing the peak absorbance at each time interval to the peak absorbance prior to sonication. The surface coverage of the film was quantified from the photographs of the polymer films using image analysis. For each photograph, the image was exported into Adobe Photoshop and cropped to only display the 25 mm × 25 mm sample. Color thresholding was conducted by selecting the polymer film using the Magic Wand selection tool (tolerance of 35) to determine the proportion of the glass substrate still covered by the polymer film (relative to the total surface area of the substrate). The number of pixels identified using the Magic Wand selection tool was identified by the total number of pixels defining the size of the substrate to approximate the fraction of film coverage remaining. To estimate the total volume of film lost after each sonication step, we assumed that the polymer film still covering the glass substrate remained uniform in thickness. Thus, the change in film volume was approximated by multiplying the fractional surface coverage by the change in film thickness at each time interval.

Physical Abrasion using Sponge

Generic non-scratch scrub sponges (cellulose, 114 mm × 68 mm × 15 mm) were purchased from Target Corporation and dried in a desiccator chamber overnight. The sponge was then cut such that the

width of the sponge (~40 mm) was slightly greater than the width of each solar cell substrate (25 mm). The sponge was then attached to a 10 N force gauge connected to a Mark-10 linear actuator using 3D-printed grips. Solar cells with J51:N2200 bulk heterojunctions (3 vol% DIO, 0–1 wt% 4Bx) were fixed onto a lab jack using strips of mounting tape. J51:N2200 devices were chosen due to the significant increase in mechanical robustness when crosslinked with 1 wt% 4Bx (**Figure 3.3**). The height of the lab jack was adjusted such that the solar cells could be gently grazed by the rough side of the sponge (dark blue). Then, a 20 g weight was placed on the loose end of the sponge. The sponge, pressed down onto the surface of the bulk heterojunction layers from the 20 g weight, was dragged over the solar cells to induce damage from physical abrasion at a velocity of 60 mm min^{-1}. Following abrasion, optical microscopy images of the surfaces of each solar cell were obtained using a Leica DM2700M microscope under bright-field illumination (50× magnification). The cells were then transferred into the antechamber of the glove box overnight under vacuum to remove any residual moisture before being the photovoltaic properties were measured as described. This process was repeated two more times, with the height of the lab jack, position of the sponge, and position of the 20 g weight remaining unchanged between each abrasion treatment.

Accelerated Degradation in 50 °C / 50% RH Chamber

To observe the degradation of our devices under humid environments (e.g., representing no encapsulation), solar cells with PTB7-Th:N2200 bulk heterojunctions (0-3 wt% 4Bx) were put into a testing chamber set at 50 °C and 50% relative humidity (RH). The humidity was controlled by a PID controller regulating the flow of water vapor into the chamber from an attached humidifier. The chamber was relatively small, containing two rows in which samples could be placed. Due to the arrangement of this setup, the 0-2 wt% cells were placed in the row furthest from the water vapor inlet valve, while the 3 wt% cell was placed in the row closest to the valve. After 24 h, the cells were removed and annealed on a hot plate in atmosphere at 100 °C for 30 min before being allowed to slowly cool to room temperature. The cells were then placed into an antechamber under vacuum overnight to remove any residual moisture before

being measured the following day as described. This accelerated degradation treatment was then repeated for another 24 h for a total of 48 h in the degradation chamber.

C.1.8 Morphological Characterization

Ultraviolet-Visible Spectroscopy (UV-Vis)

UV-vis measurements (e.g., absorbance relative to wavelength) were acquired using an Agilent Cary 60 UV-vis spectrophotometer (300–800 nm, 1 nm increments). For P3HpT, H-aggregation was calculated using a purpose-written script in Matlab R2021b.

X-ray Photoelectron Spectroscopy (XPS)

Survey scans (0–1000 eV) were performed on the DCB fracture testing samples with X-ray photoelectron spectroscopy (XPS, Kratos Axis Ultra 165 Hybrid Photoelectron Spectrometer) using monochromatic Al Kα x-ray radiation at 1486.6 eV to determine the composition of chemical species at the surface of the fractured samples after DCB testing. The side of the fractured sample adhered to the slide glued with epoxy is referred to as the ‘‘Epoxy side’’ and the other side is referred to as the “Glass side.” The binding energies associated with silicon, sulfur, fluorine, oxygen, nitrogen, and carbon are highlighted. In particular, the peaks associated with silicon were used to determine presence of the glass substrates, while the peaks associated with fluorine (common only to J51 or PTB7-Th) were used to determine if there was any remaining bulk heterojunction film on the sample surface.

Fourier-Transform Infrared Spectroscopy (FTIR)

Fourier-transform infrared spectroscopy (FTIR) was used to qualitatively observe crosslinking (i.e., the disappearance of the azide peak at 2160-2120 cm^{-1}). A Nicolet6700 FTIR spectrophotometer (ThermoFisher) fixed with a MCT detector was used alongside a diamond ATR attachment. Polymer films were deposited on top of glass substrates, compressed onto the diamond tip, and scanned at a resolution of 2 cm^{-1} for 128 scans per measurement.

C.1.9 Statistical Analysis

EGaIn measurements were conducted at least 5 times on each fabricated solar cell and each data set was used to generate box plots in Matlab R2021b. Tensile measurements were conducted at least 3 times on each polymer film. Compressive measurements were conducted at least 30 times on each polymer blend. Debonding measurements were conducted at least 6 times on each polymer blend. UV-vis measurements were conducted 5 times on each polymer film during abrasion testing between each sonication step and for the aggregation measurements. Reported values in the manuscript are calculated from the mean of each data set, while the error is calculated as the standard deviation. All calculations were conducted in Matlab R2021b or Microsoft Excel.

C.2 Supplementary Figures

Table C1. Summary of tensile properties of J51, PTB7-Th, and N2200 with 4Bx crosslinker.

Polymer(s)	4Bx Loading [wt %]	Elastic Modulus [MPa]	Tensile Strength [MPa]	Resilience [MJ m^{-3}]	Toughness [MJ m^{-3}]	Linear Elasticity [%]	Fracture Strain [%]
J51	0	367 ± 151	8.19 ± 1.41	0.09 ± 0.02	0.10 ± 0.03	2.53 ± 0.71	2.53 ± 0.71
	1	440 ± 118	12.09 ± 1.57	0.18 ± 0.02	0.18 ± 0.02	3.16 ± 0.43	3.16 ± 0.43
PTB7-Th	0	578 ± 63	27.16 ± 0.39	0.51 ± 0.15	2.61 ± 0.16	4.13 ± 0.87	12.62 ± 0.54
	1	409 ± 85	31.05 ± 0.99	1.16 ± 0.42	2.99 ± 0.17	7.51 ± 2.13	13.96 ± 0.41
N2200	0	477 ± 84	19.03 ± 1.12	0.37 ± 0.01	3.38 ± 0.09	3.91 ± 0.28	21.24 ± 2.00
	1	485 ± 71	23.01 ± 1.74	0.41 ± 0.13	4.46 ± 0.61	4.44 ± 0.54	24.27 ± 1.99
J51:N2200 (1:2)	0	501 ± 151	23.82 ± 0.99	0.55 ± 0.28	2.23 ± 0.22	4.70 ± 1.85	12.40 ± 0.69
	1	463 ± 55	30.60 ± 0.63	0.76 ± 0.16	3.88 ± 0.84	5.73 ± 0.95	17.11 ± 3.01
	2	582 ± 133	27.44 ± 1.91	0.65 ± 0.20	1.63 ± 0.42	4.80 ± 1.39	8.58 ± 1.44
PTB7-Th: N2200 (2:1)	0	512 ± 109	30.98 ± 0.74	0.84 ± 0.17	4.35 ± 0.17	5.70 ± 1.32	18.22 ± 0.81
	1	585 ± 3	32.87 ± 0.66	0.73 ± 0.18	4.29 ± 0.64	4.85 ± 0.56	16.76 ± 1.81
	2	629 ± 70	37.03 ± 1.57	0.79 ± 0.18	3.37 ± 0.19	4.92 ± 0.89	12.89 ± 0.73
	3	698 ± 99	38.28 ± 2.68	0.86 ± 0.19	3.69 ± 0.24	4.93 ± 0.92	13.24 ± 0.66

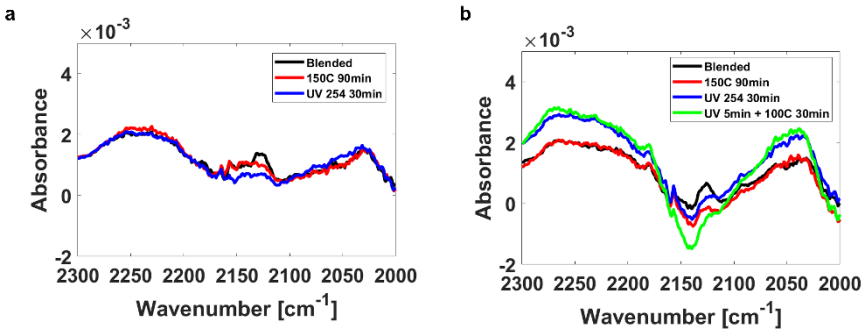

Figure C1. Crosslinking of 4Bx was qualitatively determined using FTIR for (**a**) J51:N2200 and (**b**) PTB7-Th:N2200. Films blended with 1 wt% 4Bx showed a peak corresponding to the azide functional group between 2120–2160 cm^{-1}. After crosslinking using 254 nm wavelength UV light or thermal annealing, FTIR spectra of crosslinked films showed a disappearance of this azide peak.

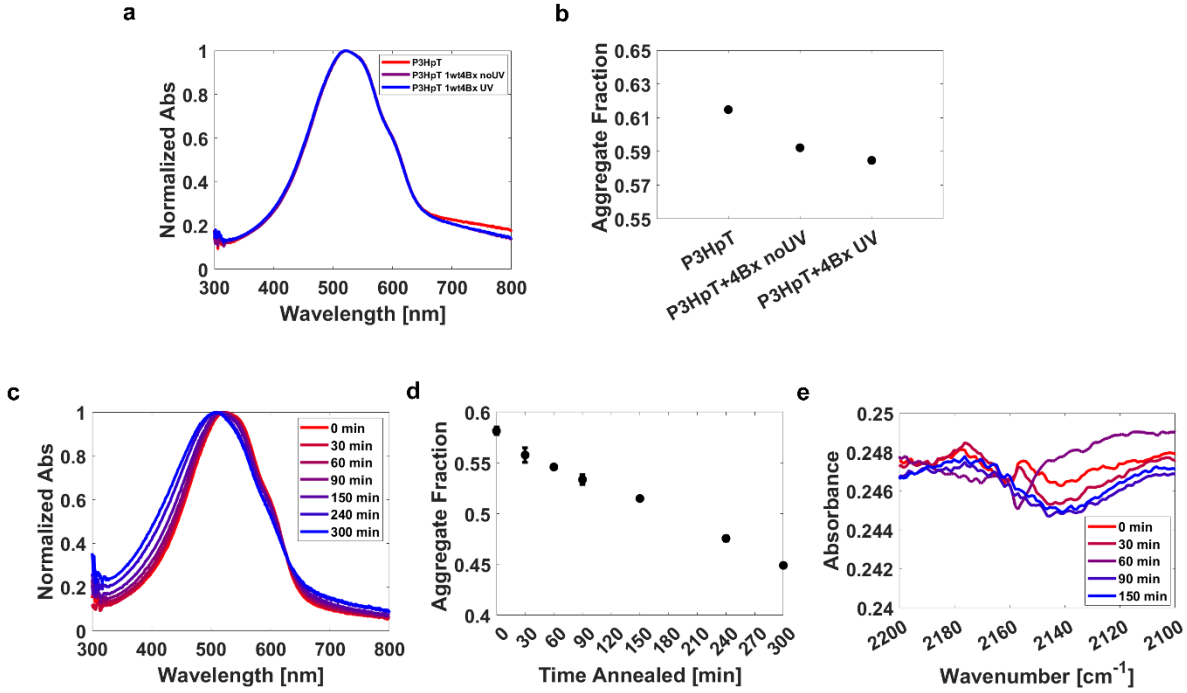

Figure C2. (**a**) UV-vis spectra of P3HpT films as-cast (red), blended with 1 wt% 4Bx (purple), and crosslinked with 4Bx (blue). (**b**) The aggregate fraction was determined from the respective UV-vis spectra using a model developed by Spano and coworkers,[18] and show that crosslinking P3HpT with 4Bx reduces the aggregation in the amorphous domains. To determine the onset of crosslinking with thermal annealing, P3HpT films blended with 1 wt% 4Bx were annealed at 100 °C for between 0–300 min with (**c**) UV-vis spectra taken for each sample, showing a blue shift with increasing annealing time. (**d**) Similarly, these P3HpT samples show a continuous decrease in aggregation relative to annealing time (i.e., as more 4Bx reacts). (**e**) FTIR measurements suggest that the azide peak mostly disappears after approximately 60 min when annealed at 100 °C. Slight differences between the 60 min spectra and the other spectra are present due to the 60 min sample being prepared separate from the others.

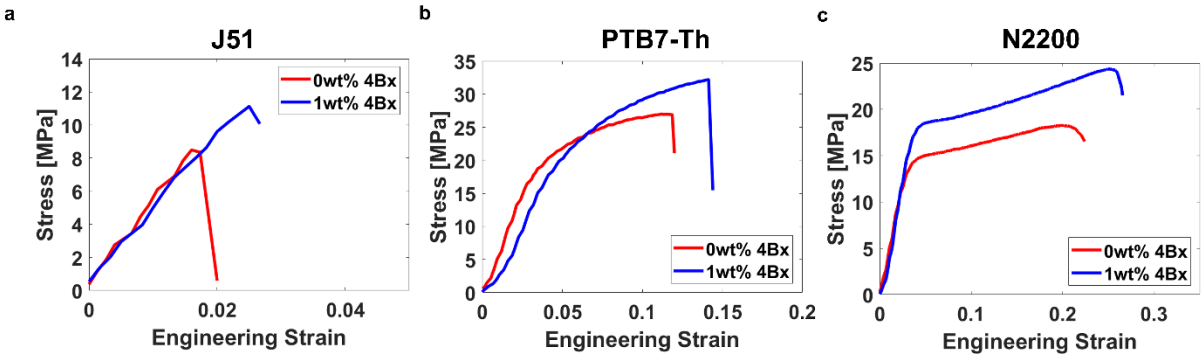

Figure C3. Representative stress-strain curves of (**a**) J51, (**b**) PTB7-Th, and (**c**) N2200 thin films as measured using pseudo-free standing tensile tests.

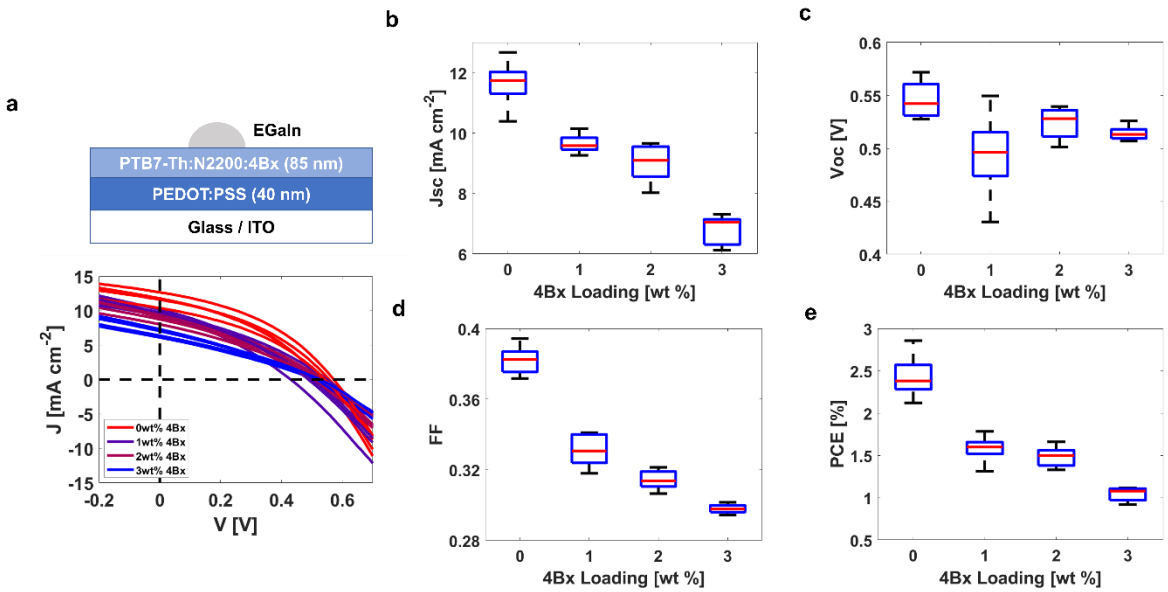

Figure C4. (**a**) J-V curves of PTB7-Th:N2200 devices (without DIO) relative to increasing 4Bx loading. The (**b**) Jsc, (**c**) Voc, (**d**) FF, and (**e**) PCE are extracted from the J-V curves.

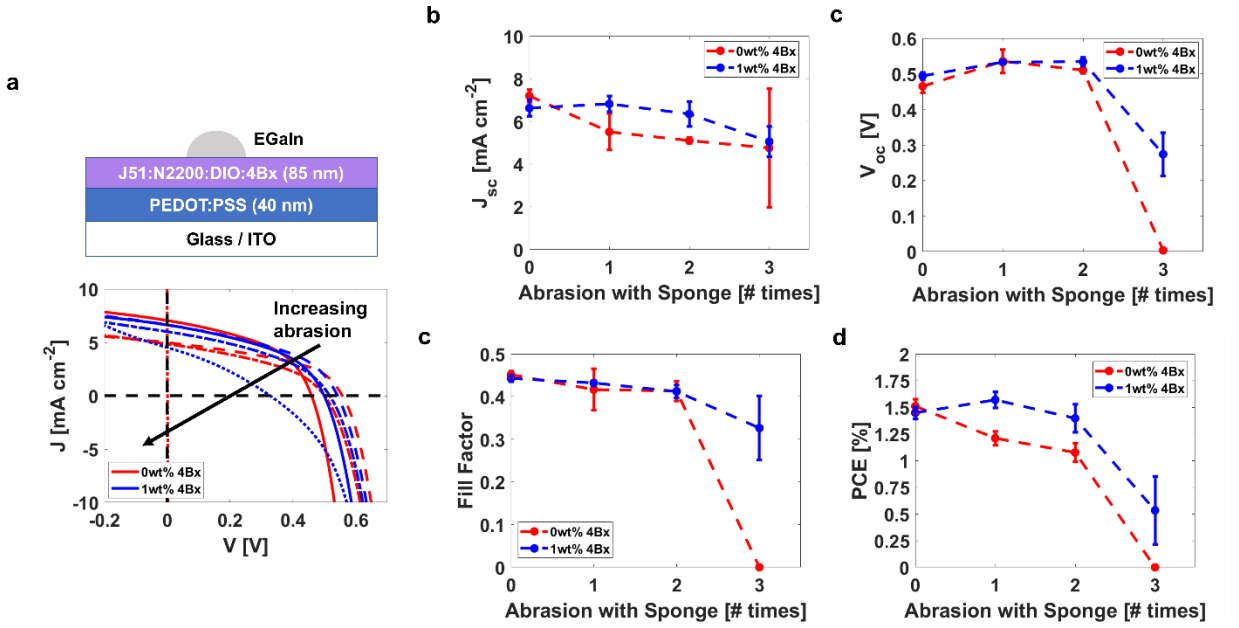

Figure C5. (a) EGaIn solar cells with J51:N2200 bulk heterojunctions were fabricated and subject to abrasion tests using a standard kitchen sponge (where increasingly dotted lines represent greater abrasion). Continuous abrasion resulted in gradual damage to both active layers, resulting in J-V curves with decreasing (**b**) Jsc, (**c**) Voc, (**d**) FF, and (**e**) PCE (where increasingly dotted lines represent greater abrasion) relative to increasing abrasion. However, the solar cell with the crosslinked J51:N2200 active layer (blue) showed greater survivability in comparison to its non-crosslinked counterpart (red).

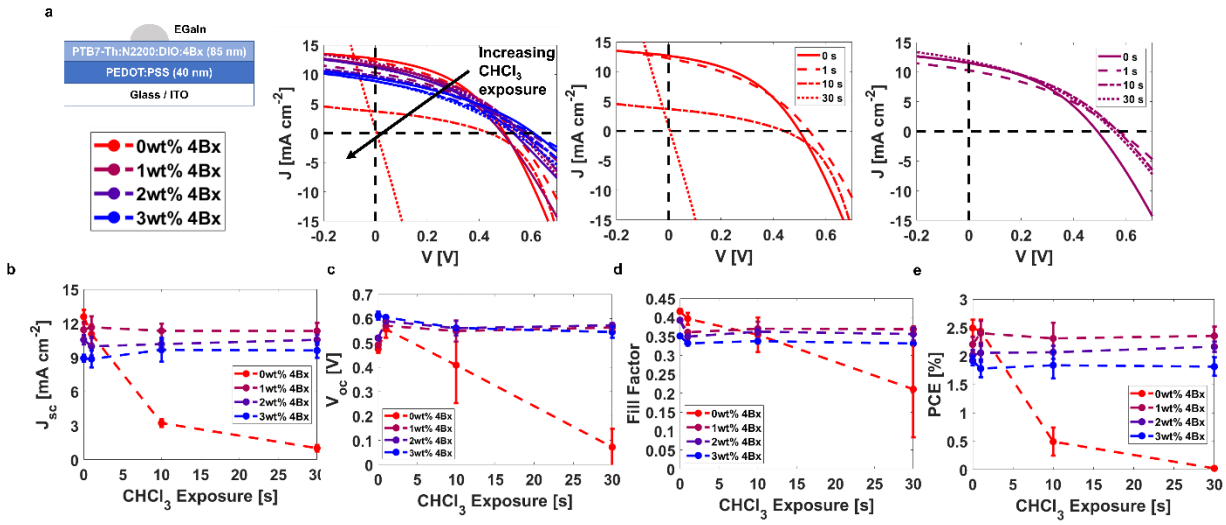

Figure C6. (**a**) J-V curves of EGaIn solar cells with non-crosslinked and crosslinked PTB7-Th:N2200 bulk heterojunctions relative to greater amounts of direct chloroform exposure. The loading of 4Bx crosslinker ranged from 0–3 wt%. An increasing number of dots in the J-V curve refers to an increasing amount of chloroform exposure. The J-V curves for the 0 wt% (red) and 1 wt% (purple) devices are plotted separately to emphasize the change in degradation. The (**b**) J_{sc}, (**c**) V_{oc}, (**d**) FF, and (**e**) PCE are extracted from their respective J-V curves.

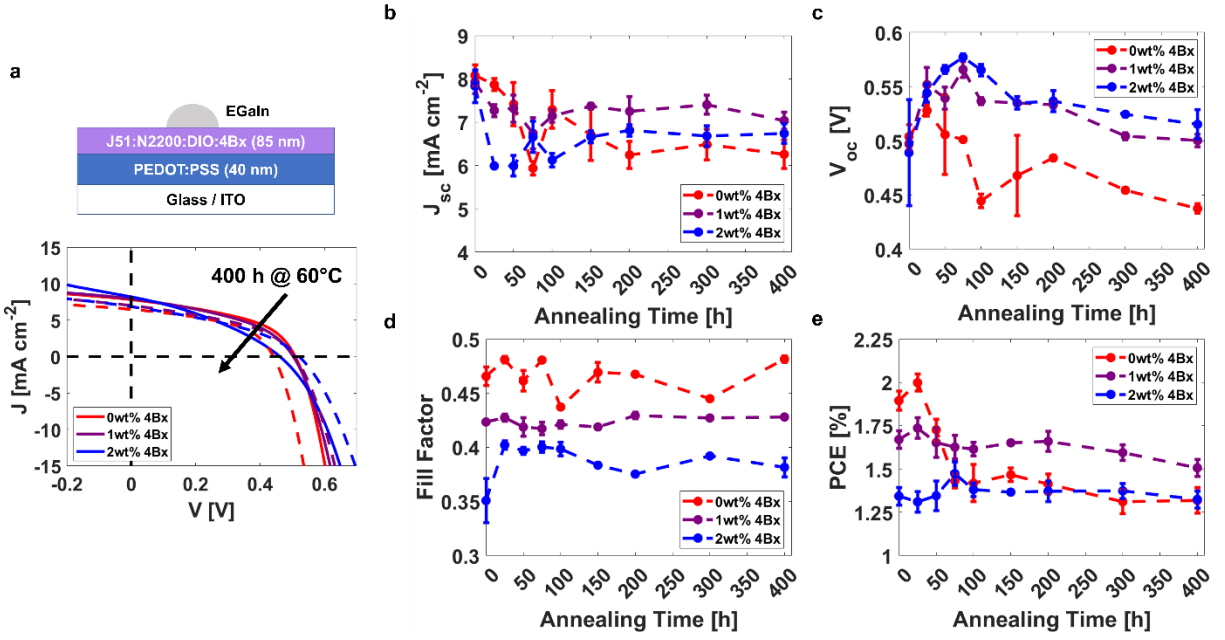

Figure C7. (**a**) The thermal stability and lifespan of crosslinked (1–2 wt%) and non-crosslinked (0 wt%) J51:N2200 EGaIn solar cells were measured using thermal ageing. Devices were thermally annealed over the course of 400 h at 60 °C in order to accelerate degradation. Dotted J-V curves show a representation of the photovoltaic properties of each device after 400 h, while solid lines refer to a pristine device (0 h anneal). The (**b**) J_{sc}, (**c**) V_{oc}, (**d**) FF, and (**e**) PCE are extracted from their respective J-V curves.

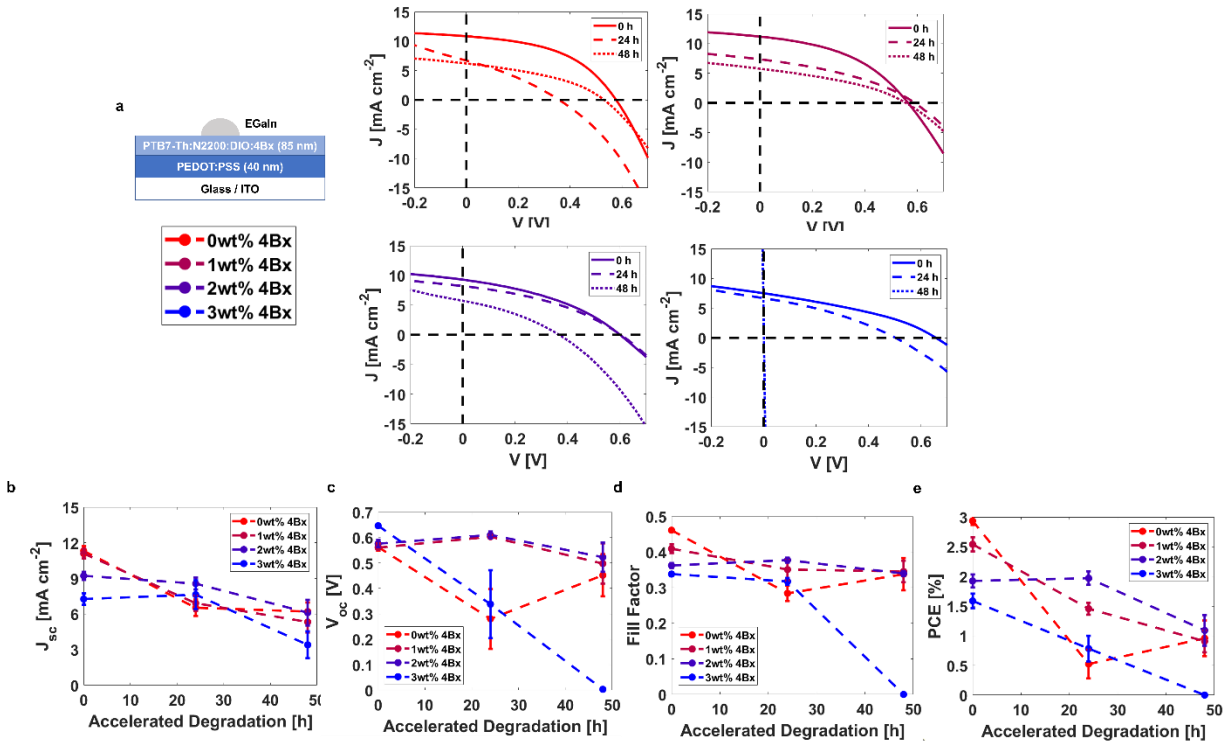

Figure C8. (**a**) EGaIn solar cells with non-crosslinked and crosslinked PTB7-Th:N2200 bulk heterojunctions were fabricated and degraded in a 50 °C and 50% relative humidity (RH) chamber. The loading of 4Bx crosslinker ranged from 0–3 wt%. An increasing number of dots in the J-V curve refers to a greater amount of time spent in the 50/50 degradation chamber. The 3 wt% device (blue) was placed closest to the water vapor inlet, likely resulting in the device shunting after 48 h. In comparison, the 0 wt% device (red) was placed furthest away. The (**b**) J_{sc}, (**c**) V_{oc}, (**d**) FF, and (**e**) PCE are extracted from their respective J-V curves.

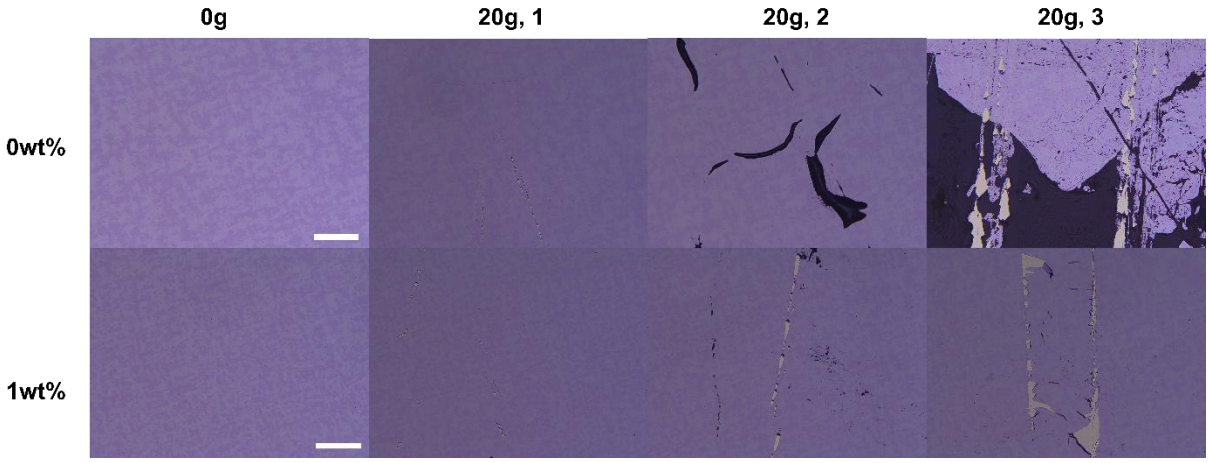

Figure C9. Optical microscopy (bright-field) images taken of J51:N2200 (0–1 wt% 4Bx) EGaIn cells subject to abrasion tests using a standard kitchen sponge. The sponge was weighed down with a 20 g weight in order to make contact with each device. Three abrasion tests (1–3) were done on each device. Dark spots in the images show areas containing EGaIn residue (e.g., filling in any scratches).

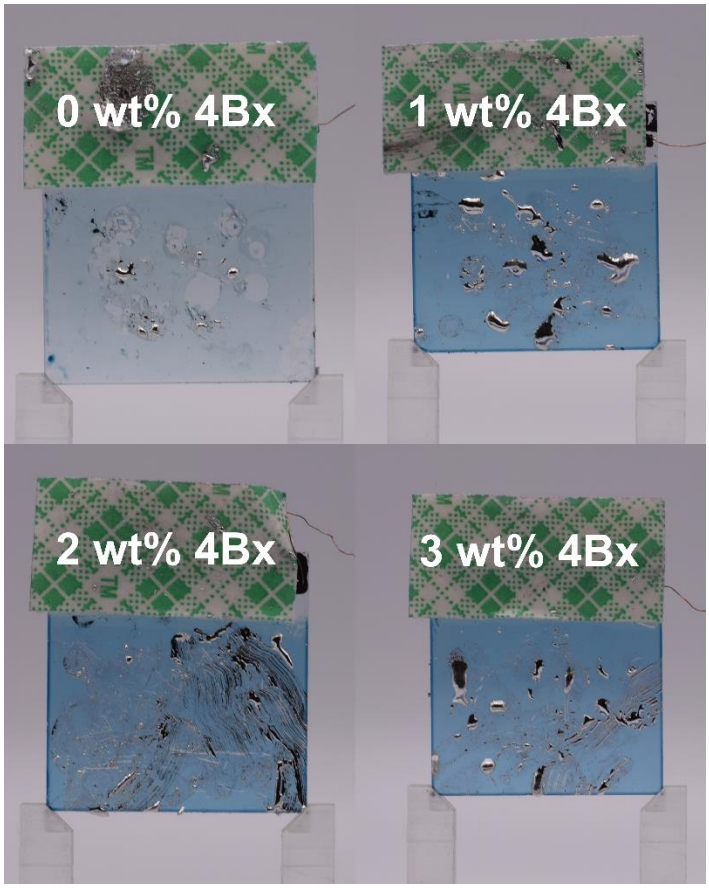

Figure C10. Photographs of PTB7-Th:N2200:4Bx EGaIn solar cells with 0–3 wt% 4Bx after 30 s of direct chloroform exposure. The contrast in color shows a complete removal of the non-crosslinked bulk heterojunction, while the other bulk heterojunctions remained intact.

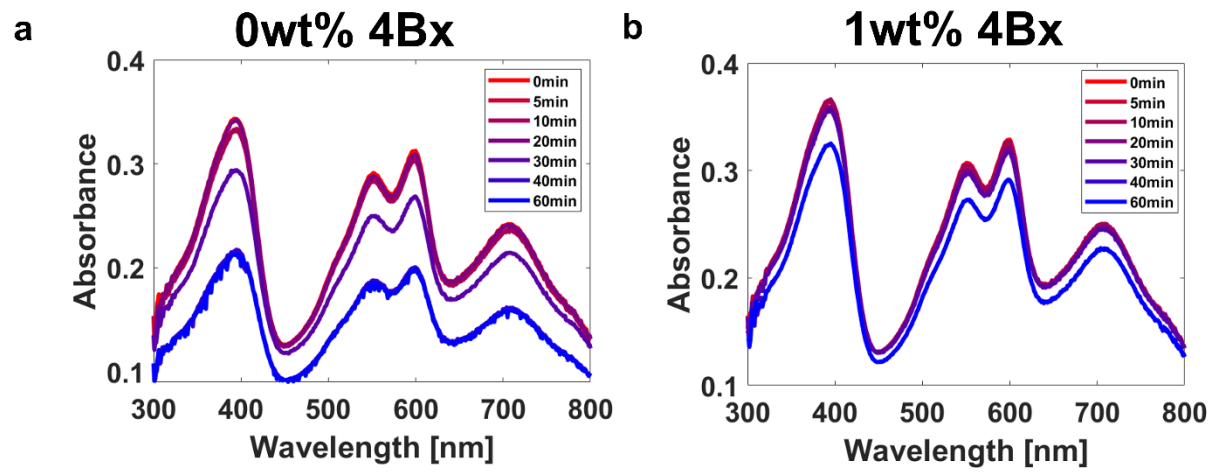

Figure C11. Representative UV-vis spectra of (**a**) non-crosslinked and (**b**) crosslinked J51:N2200 films (2 vol% DIO) taken after each sonication step. Five UV-vis measurements were taken after each sonication in order to approximate the thickness of the remaining regions of polymer film.

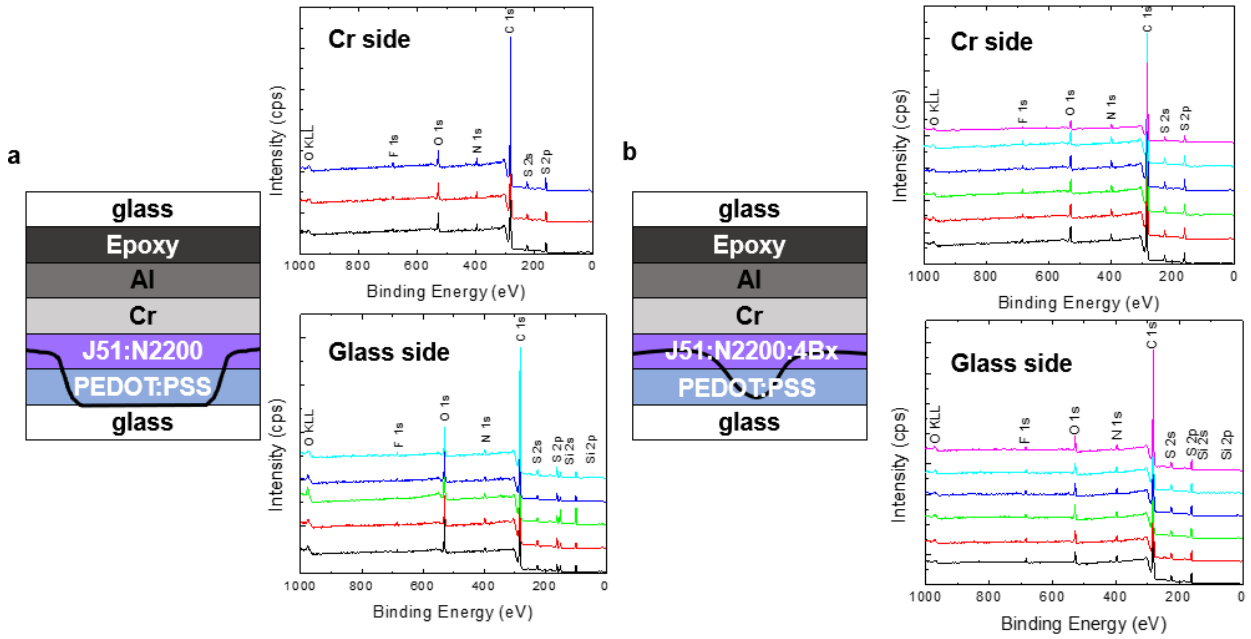

Figure C12. XPS measurements taken after fracture testing of (**a**) J51:N2200 (1:2, 3 vol% DIO) and (**b**) J51:N2200:4Bx (1:2, 1 wt%, 3vol% DIO) sample stacks in order to determine the interface of fracture.

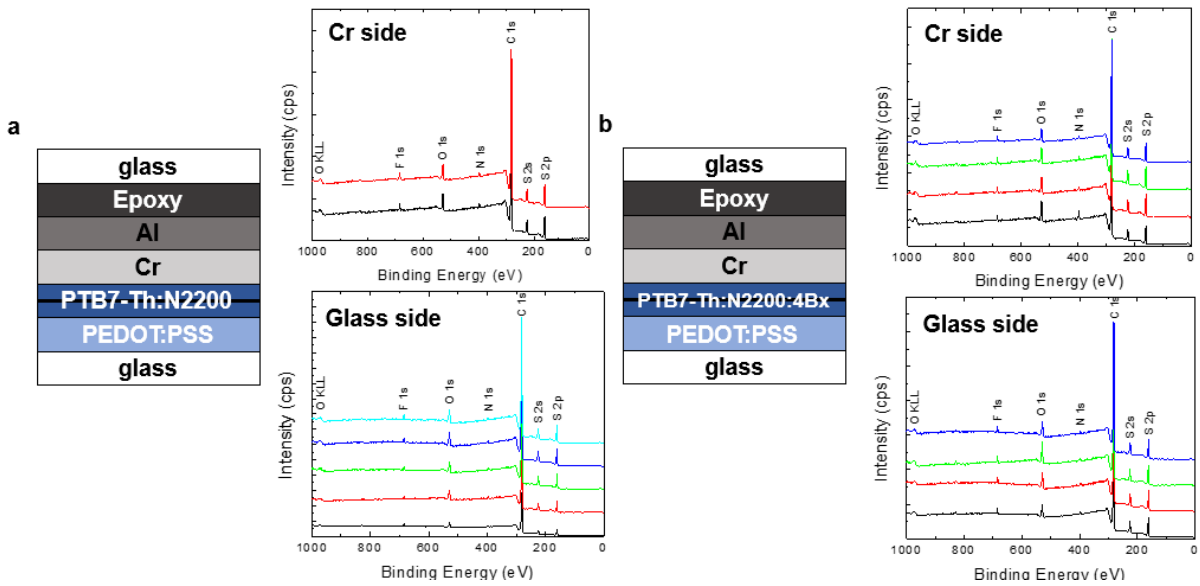

Figure C13. XPS measurements taken after fracture testing of (**a**) PTB7-Th:N2200 (2:1, 3 vol% DIO) and (**b**) PTB7-Th:N2200:4Bx (2:1, 1 wt%, 3vol% DIO) sample stacks in order to determine the interface of fracture.

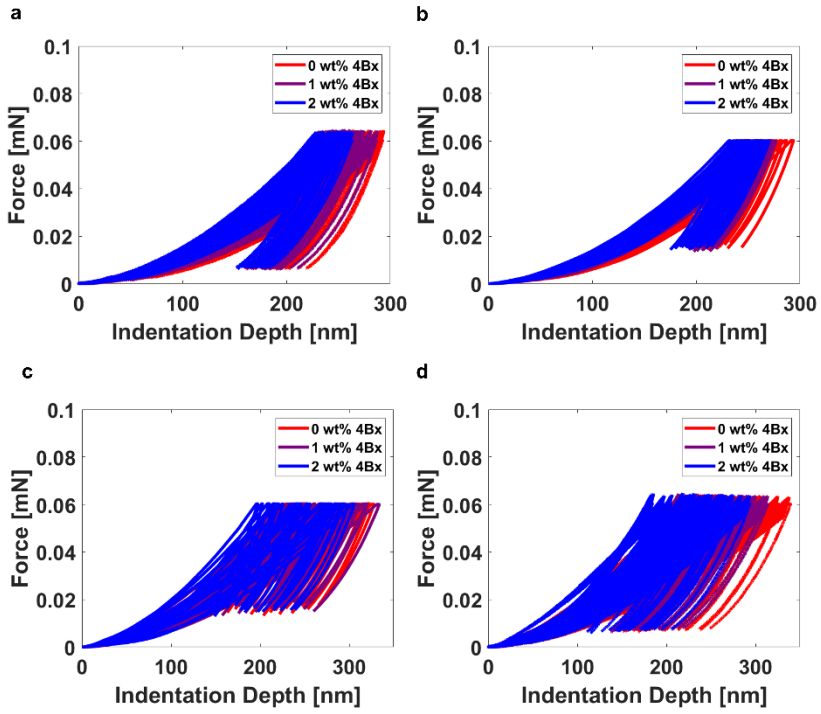

Figure C14. (**a**) Quasi and (**b**) sinus load-unloading curves of J51:N2200 with 0–2 wt% 4Bx collected by nanoindentation. (**c**) Quasi and (**d**) sinus load-unloading curves of PTB7-Th:N2200 with 0–2 wt% 4Bx collected by nanoindentation.

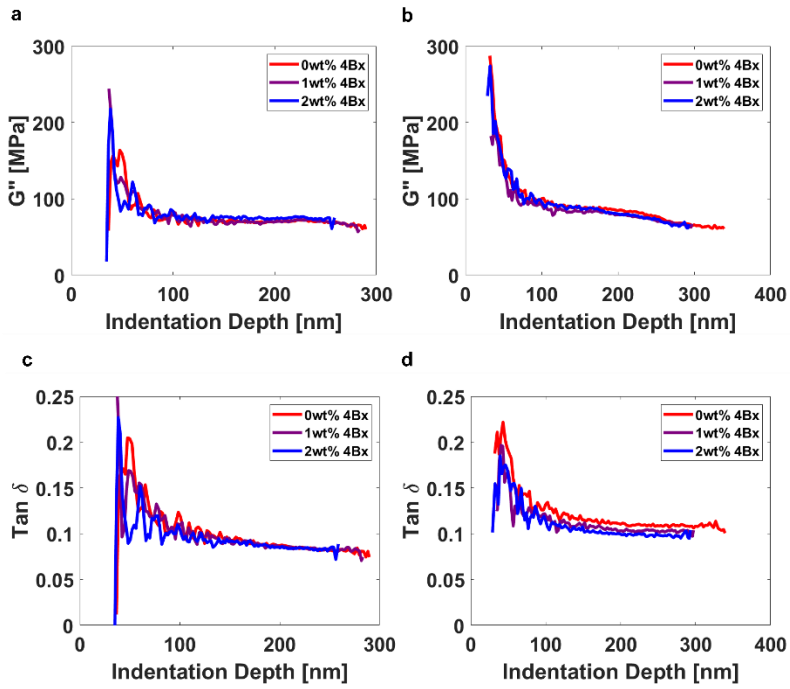

Figure C15. Viscoelastic properties were extracted from sinus measurements using nanoindentation. The (**a**) loss modulus and (**b**) tan δ (i.e., ratio between loss modulus and storage modulus) are shown relative to indentation depth for J51:N2200 relative to increasing 4Bx loading. Likewise, the (**c**) loss modulus and (**d**) tan δ are extracted for PTB7-Th:N2200.

C.3 References

(1) Kim, M. J.; Lee, M.; Min, H.; Kim, S.; Yang, J.; Kweon, H.; Lee, W.; Kim, D. H.; Choi, J. H.; Ryu, D. Y.; Kang, M. S.; Kim, B. S.; Cho, J. H. Universal Three-Dimensional Crosslinker for All-Photopatterned Electronics. *Nat. Commun.* **2020**, *11*, 1–11.

(2) Zhang, W.; Smith, J.; Watkins, S. E.; Gysel, R.; McGehee, M.; Salleo, A.; Kirkpatrick, J.; Ashraf, S.; Anthopoulos, T.; Heeney, M.; McCulloch, I. Indacenodithiophene Semiconducting Polymers for High-Performance, Air-Stable Transistors. *J. Am. Chem. Soc.* **2010**, *132*, 11437–11439.

(3) Wadsworth, A.; Chen, H.; Thorley, K. J.; Cendra, C.; Nikolka, M.; Bristow, H.; Moser, M.; Salleo, A.; Anthopoulos, T. D.; Sirringhaus, H.; McCulloch, I. Modification of Indacenodithiophene-Based Polymers and Its Impact on Charge Carrier Mobility in Organic Thin-Film Transistors. *J. Am. Chem. Soc.* **2020**, *142*, 652–664.

(4) Zhao, X.; Zhao, Y.; Ge, Q.; Butrouna, K.; Diao, Y.; Graham, K. R.; Mei, J. Complementary Semiconducting Polymer Blends: The Influence of Conjugation-Break Spacer Length in Matrix Polymers. *Macromolecules* **2016**, *49*, 2601–2608.

(5) Choudhary, K.; Chen, A. X.; Pitch, G. M.; Runser, R.; Urbina, A.; Dunn, T. J.; Kodur, M.; Kleinschmidt, A. T.; Wang, B. G.; Bunch, J. A.; Fenning, D. P.; Ayzner, A. L.; Lipomi, D. J. Comparison of the Mechanical Properties of a Conjugated Polymer Deposited Using Spin Coating, Interfacial Spreading, Solution Shearing, and Spray Coating. *ACS Appl. Mater. Interfaces* **2021**, *13*, 51436–51446.

(6) Kanninen, M. F. An Augmented Double Cantilever Beam Model for Studying Crack Propagation and Arrest. *Int. J. Fract.* **1973**, *9*, 83–92.

(7) Vanlandingham, M. R.; Chang, N. K.; Drzal, P. L.; White, C. C.; Chang, S. H. Viscoelastic Characterization of Polymers Using Instrumented Indentation. I. Quasi-Static Testing. *J. Polym. Sci. Part B Polym. Phys.* **2005**, *43*, 1794–1811.

(8) Lu, H.; Wang, B.; Ma, J.; Huang, G.; Viswanathan, H. Measurement of Creep Compliance of Solid Polymers by Nanoindentation. *Mech. Time-Dependent Mater.* **2003**, *7*, 189–207.

(9) Odegard, G. M.; Gates, T. S.; Herring, H. M. Characterization of Viscoelastic Properties of Polymeric Materials through Nanoindentation. *Exp. Mech.* **2005**, *45*, 130–136.

(10) White, C. C.; Vanlandingham, M. R.; Drzal, P. L.; Chang, N. K.; Chang, S. H. Viscoelastic Characterization of Polymers Using Instrumented Indentation. II. Dynamic Testing. *J. Polym. Sci. Part B Polym. Phys.* **2005**, *43*, 1812–1824.

(11) Wang, Y.; Shang, L.; Zhang, P.; Yan, X.; Zhang, K.; Dou, S.; Zhao, J.; Li, Y. Measurement of Viscoelastic Properties for Polymers by Nanoindentation. *Polym. Test.* **2020**, *83*, 106353.

(12) Klapperich, C.; Komvopoulos, K.; Pruitt, L. Nanomechanical Properties of Polymers Determined from Nanoindentation Experiments. *J. Tribol.* **2001**, *123*, 624–631.

(13) Chakravartula, A.; Komvopoulos, K. Viscoelastic Properties of Polymer Surfaces Investigated by Nanoscale Dynamic Mechanical Analysis. *Appl. Phys. Lett.* **2006**, *88*, 28–31.

(14) Oliver, W. C.; Pharr, G. M. An Improved Technique for Determining Hardness and Elastic Modulus Using Load and Displacement Sensing Indentation Experiments. *J. Mater. Res.* **1992**, *7*, 1564–1583.

(15) Li, H.; Randall, N. X.; Vlassak, J. J. New Methods of Analyzing Indentation Experiments on Very Thin Films. *J. Mater. Res.* **2010**, *25*, 728–734.

(16) Root, S. E.; Savagatrup, S.; Pais, C. J.; Arya, G.; Lipomi, D. J. Predicting the Mechanical Properties of Organic Semiconductors Using Coarse-Grained Molecular Dynamics Simulations. *Macromolecules* **2016**, *49*, 2886–2894.

(17) Savagatrup, S.; Printz, A. D.; O'Connor, T. F.; Kim, I.; Lipomi, D. J. Efficient Characterization of Bulk Heterojunction Films by Mapping Gradients by Reversible Contact with Liquid Metal Top Electrodes. *Chem. Mater.* **2017**, *29*, 389–398.

(18) Spano, F. C.; Silva, C. H- and J-Aggregate Behavior in Polymeric Semiconductors. *Annu. Rev. Phys. Chem.* **2014**.

Appendix D. Supplementary Information for Chapter 4. Adhesive Properties of Semiconducting Polymers: Poly(3-alkylthiophene) as an Ersatz Glue

D.1 Experimental Methods

Substrate preparation. Pre-cut 25 mm × 25 mm glass substrates were purchased from Agilent, while silicon substrates were diced into 25 mm × 25 mm squares or 10 mm × 10 mm squares. Substrates were cleaned by sonicating in Alconox and water, deionized (DI) water, acetone, and isopropyl alcohol (IPA) for 10 minutes each. Before use, substrates were dried using compressed air and air plasma treated for 10 minutes at 500 mTorr to improve the surface wettability.

Sample preparation and characterization. Regioregular poly(3-alkylthiophenes) (P3ATs) were purchased and used as received. Poly(3-butylthiophene) (P3BT) and poly(3-octylthiophene) (P3OT) were purchased from Sigma Aldrich. Poly(3-pentylthiophene) (P3PT), poly(3-heptylthiophene) (P3HpT), and poly(3-decylthiophene) (P3DT) were purchased from Rieke Metals. Poly(3-hexylthiophene) was purchased from 1-Material. These P3ATs were dissolved in chlorobenzene at a concentration of 10–30 mg mL^{-1}. All solutions were stirred in chlorobenzene at 60 ℃ for 12-48 h prior to use.

To determine the number-average molecular weight (M_n) and dispersity of each commercial polymer, each P3AT was dissolved in HPLC-grade chloroform at a concentration of 1 mg mL^{-1} and characterized using gel permeation chromatography (GPC), for which a miniDAWN SEC-MALS (Wyatt Technology) was used with an Optilab dRI detector (Wyatt Technology) and Shamdzu LC-2050 HPLC. The column used was a Phenogel 10^4 Å GPC/SEC Column (calibrated with polystyrene standards) and run in chloroform. The dn/dc value used to calculate the molecular weight was 0.270 mL g^{-1}.[1]

For contact angle measurements, P3AT solutions of 10 mg mL^{-1} were spun onto cleaned, plasma-treated silicon substrates (25 mm × 25 mm) using a 500 rpm (250 rpm s^{-1} ramp) spin step for 60 s followed by a 2000 rpm (1000 rpm s^{-1} ramp) spin step for 30 s. DI water and diiodomethane (10 uL) were dropped onto

the surface of each film using a micropipette, and the contact angle was measured using a Ramehart goniometer and corresponding DropImage software. The harmonic surface energy was calculated using a two-liquid model (using water and diiodomethane) in DropImage.

For atomic force microscopy (AFM) measurements, the same P3AT solutions were spun onto cleaned, plasma-treated silicon substrates (10 mm × 10 mm) using a 1000 rpm (500 rpm s^{-1} ramp) spin step for 60 s followed by a 2000 rpm (1000 rpm s^{-1} ramp) spin step for 30 s (mimicking tensile samples). These samples were either left as-cast or annealed at 100 °C for 30 min before turning off the hot plate and allowing the film to slowly cool back to room temperature.

Mechanical testing. To determine the tensile response of each P3AT film, a pseudo-freestanding tensile testing method ("film-on-water", "FOW") is used. Poly(3,4-ethylenedioxythiophene):poly(styrenesulfonate) (PEDOT:PSS) dispersed in water was purchased from Heraeus (Clevios PH1000) and first deposited onto the substrate (as a sacrificial layer) through a 1 micron glass fiber syringe filter (Chromspec) until completely covered. The sacrificial layer was spun at 1000 rpm (500 rpm s^{-1} ramp) for 90 s followed by 2000 rpm (1000 rpm s^{-1} ramp) for 30 s onto cleaned, plasma-treated glass substrates. Afterwards, each 15 mg mL^{-1} P3AT solution was spun on top of the sacrificial layer for 500 rpm (250 rpm s^{-1} ramp) for 60 s followed by 2000 rpm (1000 rpm s^{-1} ramp) for 30 s. The films were scored using a 3D-printed stencil to form dogbones with a length of 15 mm and width of 4 mm (at the center). Thickness measurements were obtained using a Bruker Dektak XT stylus profilometer operating at a force of 3 mg. The P3AT films ranged from approximately 100–150 nm in thickness, with PEDOT:PSS layers of approximately 90–110 nm. Each film was transferred onto the surface of water by exposing the PEDOT:PSS sacrificial layer to water. Each film was then adhered to PDMS slabs taped onto the grips of the Mark-10 linear actuator. Films were uniaxially strained at a rate of 6.67×10^{-4} s^{-1} (0.4 mm s^{-1}) until fracture to obtain a force-elongation curve. Engineering strain was calculated by dividing the change in length of the film by the original length ($\Delta L/L_0$). Engineering stress was calculated by dividing the force by

the initial cross-sectional area of the film, i.e., assuming that the width of the film remained constant as the film was elongated. The elastic modulus was determined from the slope of the linear region of the stress-strain curve, where the R^2 (coefficient of determination) of the slope was greater than 0.95. The strain associated with the end of this linear regime was reported as the linear elasticity. Likewise, the resilience was calculated as the area under the curve of the linear regime.

To prepare P3AT films for nanoindentation, each 15 mg mL^{-1} P3AT solution was drop cast on cleaned, plasma-treated silicon substrates and covered with a Pyrex crystallization dish (diameter = 125 mm, height = 65 mm) to decrease the rate of solidification. The films were allowed to solidify over 24 h, resulting in films of approximately 4 μm in thickness. Nanoindentation samples were glued to a steel substrate in order to secure the samples in the grips of the indenter and measurements (quasistatic[2] and dynamic[3,4]) were performed using an ultra-nanoindentation tester (UNHT^3, Anton Paar) in ambient conditions.[5] An acoustic isolation chamber and piezo vibration isolation table were used to dampen any surface or acoustic vibrations. Indentations were made using a Berkovich tip (total angle = 141.9°). The projected contact area was A_C = 24.5 h_C^2, where h_C is the contact depth of the indenter at maximum load P_{max}.[6] The area shape function A_C was calibrated using a standard silica glass reference prior to testing. Protocol parameters were tuned using pilot tests to ensure accurate surface detection and to determine the loading protocol. For all tests, P_{max} = 0.06 mN was used. The maximum indentation depth (h_{max}) was less than 10% of the sample thickness to reduce the effect of the silicon substrate on the indentation measurement.[7] A minimum of 30 indents were performed on each sample. Detailed methodologies are described elsewhere.[8]

For lap joint shear tests, P3AT samples were prepared by depositing a thin polymer film (10 mg mL^{-1} solutions) between the overlapping region of two 25 mm × 75 mm × 1.1 mm glass substrates. These substrates were cleaned and plasma treated as described above. A commercial Zehntner ZAA2300 blade coater was used to deposit the film, with the applicator height set to 1250 μm (150 μm above the substrate surface). After each P3AT solution was filtered, a micropipette was used to deposit 60 μL of solution at

one end of the glass substrate. The solution was coated using the applicator moving at 50 mm s^{-1}. Following this, another glass substrate was quickly placed on top of the thin layer of polymer solution in order to glue the two glass substrates together, such that the overlapping region totaled approximately 12.5 mm in length. Another glass slide was placed at the end of the bottom glass substrate and used to keep the upper glass substrate level. The sample was allowed to remain in this configuration overnight (16–24 h) for the film to solidify. Lap joint shear test samples were loaded vertically onto the Mark-10 linear actuator with appropriate grips attached to a 100 N force gauge. The upper glass substrate was delaminated from the lower glass substrate with the actuator moving at a speed of 1.3 mm min^{-1} (ASTM D1002 standards). The adhesive strength was calculated by dividing the maximum load by the surface area of each lap joint. Similarly, the energy dissipated was calculated by dividing the work (the area under the force-displacement curve) by the surface area of each lap joint. The thickness of the film was relatively non-uniform over the area of the lap joint, resulting in borders of about 20–50 nm of polymer with a significantly thinner center region (**Figure D6**). The thickness of the center of the lap joint was likely limited by the roughness of the glass slides, resulting in film thicknesses varying between 2–10 nm. Thus, these adhesion measurements assumed that the polymer film fractured cohesively.

Peel test samples were prepared two ways. For 180° peel tests, P3AT films were blade coated on the same 25 mm × 75 mm × 1.1 mm glass substrates using different solution concentrations with an applicator height of 1250 μm and a velocity of 7.5 mm s^{-1}, such that the thickness of the film was approximately 100–150 nm. These samples were prepared in a nitrogen-filled chamber with a relative humidity of approximately 20%. Each film remained undisturbed for 3 min after blade coating in order to ensure the film was completely solidified. Following this, a piece of scotch tape (width = 12.7 mm) was carefully placed on each film while attempting to minimize the air bubbles trapped beneath. Each sample was then covered by a large glass dish with two 2 kg aluminum blocks on top in order to ensure that even pressure was being applied on top of all samples. These samples were left under this configuration overnight (16–24 h) before being loaded vertically on the Mark-10 linear actuator in a 180° peel test format with a 10

N force gauge. The samples were peeled upwards at a rate of 30 mm min^{-1}. The thickness of each polymer film was determined by measured the thickness of representative samples (i.e., samples that were blade coated without tape applied on top) using the Dektak XT profilometer.

For 90° peel tests, P3AT solutions were prepared by dissolving polymer in chlorobenzene at a concentration of 30 mg mL^{-1}. PEDOT:PSS (Clevios PH1000) was first deposited on plasma cleaned glass substrates (25 mm × 25 mm × 1.1 mm) by spin coating at 1000 rpm (500 rpm s^{-1} ramp) for 60 s and 2000 rpm (1000 rpm s^{-1} ramp) for 30 s. These PEDOT:PSS films were then annealed at 150 °C for 10 min (in atmosphere) before allowing to slowly cool by turning off the hot plate. The P3AT solutions were filtered using 0.2 micron syringe filters and spun on the PEDOT:PSS films at 500 rpm (250 rpm s^{-1} ramp) for 60 s and 2000 rpm (1000 rpm s^{-1} ramp) for 30 s. These films were allowed to sit under vacuum overnight to remove any residual solvent. The next day, a piece of scotch tape (width = 12.7 mm) was carefully placed on each film while attempting to minimize the air bubbles trapped beneath. Each sample was then covered by a large glass dish with two 2 kg aluminum blocks. These samples were left under this configuration overnight (16–24 h) before being loaded vertically on the Mark-10 linear actuator in a 90° peel test format with a 2.5 N force gauge. The samples were peeled upwards at a rate of 330 mm min^{-1}. The thickness of each polymer film was determined by measured the thickness of representative samples using the Dektak XT profilometer.

Morphological characterization. UV-vis spectra were acquired using an Agilent Cary 60 UV-vis spectrophotometer scanning from 800 nm to 300 nm in increments of approximately 1 nm. H-aggregation was calculated from these spectra using a purpose-written script in Matlab R2019b. Atomic force micrographs (AFM) of height and phase images were obtained using a Veeco scanning probe microscope operated in non-contact tapping mode. AFM data analysis was performed using Nanoscope Analysis v1.4.

D.2 Theoretical Calculations of Mechanical Properties

Mathematical (empirical) correlations between mechanical properties and molecular characteristics were observed by Seitz[9] on conventional (i.e., non-conjugated) polymers. These methods of calculations were initially developed by Seitz,[9] Tahk,[10] and Fedors,[11] and later applied to poly(3-alkylthiophene)s (P3ATs) by Savagatrup.[12] The tensile modulus, *E*, can be determined from the bulk modulus, *B*, and the Poisson's ratio, *υ*, of the material for conventional polymers, and is assumed to apply to conjugated polymers as well. This relationship is mathematically defined as the following:

$$E = 3B(1 - 2\nu). \qquad \textbf{eq (1)}$$

The Poisson's ratio can be calculated from the empirical relationship dependent on the molecular cross-sectional area of the polymer, *A*, where:

$$\nu = 0.513 - 2.37 \times 10^{6}\sqrt{A}. \qquad \textbf{eq (2)}$$

The molecular cross-sectional area is dependent on the van der Waals volume, V_W, and the length of the main chain of the monomer, l_m, such that:

$$A = \frac{V_W}{N_A \times l_m}, \qquad \textbf{eq (3)}$$

where N_A is defined as Avogadro's number. Here, both V_W and l_m are estimated from the chemical structure of the monomer. The calculated length of the main chain is independent of the side chain length, and thus all P3ATs used the same value such that l_m = 0.434 nm (which must be converted to cm in later calculations).[10]

The van der Waals volume (V_W) can be described[10] by the empirical relationship as follows:

$$V_W \approx 3.861803\ {}^{0}\chi + 13.748435\ {}^{1}\chi^{\nu}, \qquad \textbf{eq (4)}$$

where ${}^{0}\chi$ and ${}^{1}\chi^{\nu}$ are the zeroth-order atomic and first-order bond connectivity indices, respectively. These indices can be defined by:

$${}^{0}\chi = \sum_{vertices} \frac{1}{\sqrt{\delta}} \qquad \textbf{eq (5)}$$

and

$$^{1}\chi^{\nu} = \sum_{edges} \frac{1}{\sqrt{\beta^{\nu}}} \qquad \textbf{eq (6)}$$

where δ is defined as the number of non-hydrogen atoms to which a non-hydrogen atom is bonded. β^{ν} is calculated from the valence connectivity index, δ^{ν}, such that:

$$\beta^{\nu} = \delta^{\nu} \times \delta^{\nu} \qquad \textbf{eq (7)}$$

and

$$\delta^{\nu} = \frac{Z^{\nu} - N_H}{Z - Z^{\nu} - 1}. \qquad \textbf{eq (8)}$$

Here, Z^{ν} is the number of valence electrons of an atom, Z is the atomic number, and N_H is the number of hydrogen atoms attached to an atom (i.e., in the chemical structure of the monomer). The manner in which δ and δ^{ν} are defined for P3ATs is shown in **Figure D1** below. The calculated values of l_m, $^{0}\chi$, $^{1}\chi^{\nu}$, V_w, and ν are given in **Table D1** below. From **eq (2)** to **eq (8)**, the Poisson's ratio, ν, can be determined for **eq (1)**.

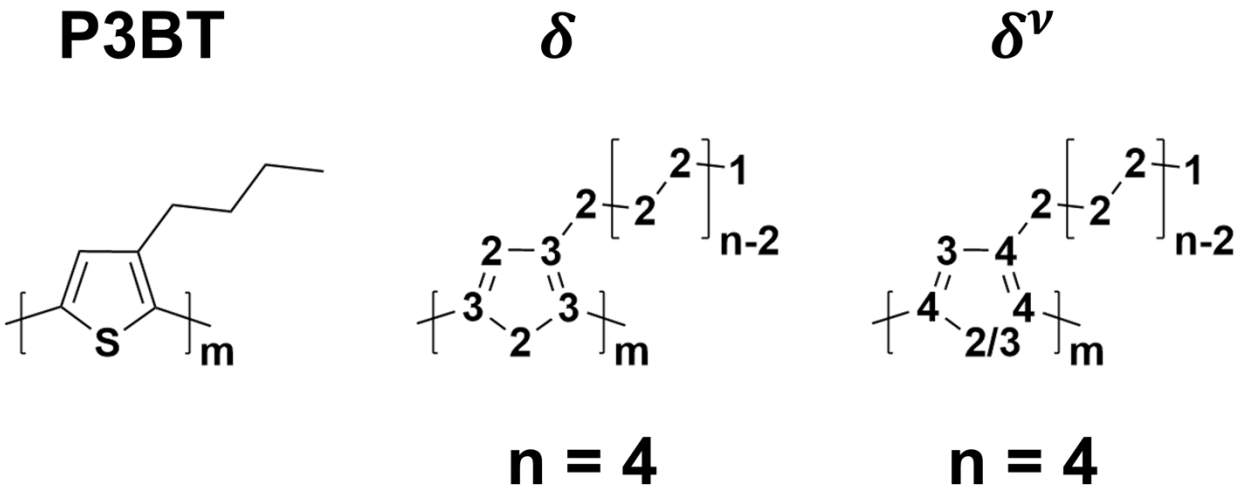

Figure D1. Values of δ and δ^{ν} used in the calculation of tensile modulus based on the monomer structure of each P3AT. Shown above is an example for P3BT (n = 4), which is applicable to all other P3ATs studied in this work (n = 4-10).

Table D1. Parameters used to calculate the Poisson's ratio of poly(3-alkylthiophene)s

	l_m [nm]	${}^0\chi$	${}^1\chi^v$	V_W [cm^3/mol]	ν
P3BT (n=4)	0.434	6.27	4.11	80.71	0.3813
P3PT (n=5)	0.434	6.98	4.61	90.32	0.3737
P3HT (n=6)	0.434	7.68	5.11	99.92	0.3665
P3HpT (n=7)	0.434	8.39	5.61	109.53	0.3596
P3OT (n=8)	0.434	9.10	6.11	119.13	0.3530
P3DT (n=10)	0.434	10.51	7.11	138.34	0.3406

The bulk modulus, B, is a characteristic measuring the resistance of a material to compression (i.e., a change in volume). From Seitz,[9] the bulk modulus is first estimated from the Lennard-Jones potential such that:

$$B = V\frac{\partial^2 U}{\partial^2 V}. \qquad \textbf{eq (9)}$$

Here, V is the molar volume (at the operating temperature), V_0 is the molar volume at T = 0 K, and U is the internal energy. The Lennard-Jones potential can be expressed in terms of the molar volume, where:

$$U = U_0\left[\left(\frac{V_0}{V}\right)^4 - \left(\frac{V_0}{V}\right)^2\right]. \qquad \textbf{eq (10)}$$

The molar volume can be defined in terms of the molar radius, r, and substituted into **eq (10)** such that:

$$\frac{V_0}{V} = \left(\frac{r_0}{r}\right)^3 \qquad \textbf{eq (11)}$$

and

$$U = U_0\left[\left(\frac{r_0}{r}\right)^{12} - \left(\frac{r_0}{r}\right)^6\right]. \qquad \textbf{eq (12)}$$

As such, the internal energy, U, can be defined in terms of the cohesive energy, E_{coh}, such that **eq (12)** becomes:

$$B(T) \approx 8.23333 E_{coh} \left[\frac{5V_0^4}{V(T)^5} - \frac{3V_0^2}{V(T)^3} \right] \quad \textbf{eq (13)}$$

The cohesive energy E_{coh} was empirically estimated by Fedor[11] such that:

$$E_{coh} \approx 9882.5\ {}^1\chi^v + 5021.8. \quad \textbf{eq (14)}$$

Finally, the molar volumes for each P3AT of interest were calculated using glass transition temperatures reported elsewhere (P3BT,[13] P3PT,[14] P3HT,[14] P3HpT,[15] P3OT,[16] P3DT[16]). Three different equations were used, as determined empirically by Seitz,[9] relative to the glass transition temperature of the polymer and the operating temperature (room temperature) of the measurements of comparison. For P3BT and P3PT, with glass transitions above room temperature, the following equation was used:

$$V_{P3BT,P3PT} = V_W \left[0.150 \left(\frac{T}{T_g} \right) + 1.42 \right]. \quad \textbf{eq (15)}$$

For P3HT and P3HpT, with glass transitions near room temperature, the following equation was used:

$$V_{P3HT,P3HpT} = V_W \left[0.225 \left(\frac{T}{T_g} \right) + 1.57 \right]. \quad \textbf{eq (16)}$$

For P3OT and P3DT, with glass transitions below room temperature, the following equation was used:

$$V_{P3OT,P3DT} = V_W \left[0.300 \left(\frac{T}{T_g} \right) + 1.27 \right]. \quad \textbf{eq (17)}$$

The glass transition temperatures used, as well as the calculated values of V, V_0, and E_{coh}, are provided in **Table D2**. **Eq (16)** was used to calculate the molar volume of P3HpT (despite having a glass transition below room temperature) because **eq (17)** resulted in a significantly different calculation of the tensile modulus that disagrees strongly with intuition and experiment. Additionally, **eq (16)** (instead of **eq (15)**) was used to calculate the modulus for P3PT as well (i.e., to account for the glass transition of ~37 °C

being near room temperature). After determining B and ν, the tensile modulus, E, is calculated from **eq (1)**. The calculated values for B and E are also provided in **Table D2**.

Table D2. Parameters used to calculate the bulk and tensile moduli of poly(3-alkylthiophene)s

	T_g [K]	V [cm^3/mol]	V_0 [cm^3/mol]	E_{coh} [kJ/mol]	B [MPa]	E [MPa]
P3BT (n=4)	338.15	125.28	114.61	45.64	2973	2117
P3PT (n=5)	310.15	141.27 161.33*	128.25	50.58	2723 260*	2063 197*
P3HT (n=6)	286.15	180.30 158.13**	156.87	55.52	1507 5465**	1208 4379**
P3HpT (n=7)	261.15	200.09 176.61**	171.95	60.46	1273 4649**	1073 3917**
P3OT (n=8)	259.15	192.41	151.30	65.40	158	139
P3DT (n=10)	251.15	224.96	175.69	75.29	84	80

* Calculated from **eq (16)**
** Calculated from **eq (17)**

D.3 Supplementary Figures

Table D3. Molecular weight and dispersity of the poly(3-alkylthiophene)s used in this study as determined by gel permeation chromatography, as well as the regioregularity of each poly(3-alkylthiophene). Bolded text indicates information provided by the vendor.

	Vendor	M_W [kDa]	M_n [kDa]	Dispersity	Regioregularity [Head-to-Tail]	Degree of Polymerization [X_n]
P3BT (n=4)	Sigma Aldrich*	50.87 **54**	42.05 **23.47**	1.21 **2.3**	**80-90%**	299.71 167.28**
P3PT (n=5)	Rieke Metals	33.81 **37**	27.46 **18.5**	1.23 **2**	**90%**	177.97 119.90**
P3HT (n=6)	1-Material	46.40 **60**	40.67 **24**	1.14 **2.5**	**>90%**	241.65 142.60**
P3HpT (n=7)	Rieke Metals	51.49 **58**	39.67 **26.36**	1.30 **2.2**	**93%**	217.61 144.60**
P3OT (n=8)	Sigma Aldrich*	57.93 **51**	49.93 **26.84**	1.16 **1.9**	**91%**	254.23 173.12**
P3DT (n=10)	Rieke Metals	44.90 **62**	36.56 **29.52**	1.22 **2.1**	**91%**	162.92 131.55**

* Distributed by Sigma Aldrich, product provided by Rieke Metals
** Calculated from information provided by vendor

Table D4. Comparison of measured moduli of poly(3-alkylthiophene)s.

	Tensile [MPa]	Bulk [MPa]	Storage [MPa]
P3BT (n=4)	1432 ± 285.6	3224 ± 482.8	3141 ± 375.1
P3PT (n=5)	231 ± 20.5	991 ± 71.1	1021 ± 94.1
P3HT (n=6)	153 ± 8.8	914 ± 114.8	948 ± 105.2
P3HpT (n=7)	91 ± 6.6	549 ± 15.0	537 ± 22.2
P3OT (n=8)	55 ± 16.4	168 ± 2.4	172 ± 1.6
P3DT (n=10)	35 ± 0.7	198 ± 7.8	202 ± 7.6

Previous work from our laboratory has shown that the calculated tensile moduli correspond well with measurements for P3BT, P3HT, P3OT, and P3DDT (n = 12) using the buckling technique.[12] The reason for this agreement was that buckling measurements yield higher moduli (3–7 times higher for P3HT) than film-on-water measurements (as used in this study).[17] This difference can be in part attributed to the (1) compressive rather than tensile stresses produced by the buckling elastomer, (2) the low strain rate (with greater strain rates yielding increased moduli), and (3) the behavior of defects under compressive stresses rather than tensile stresses.[17]

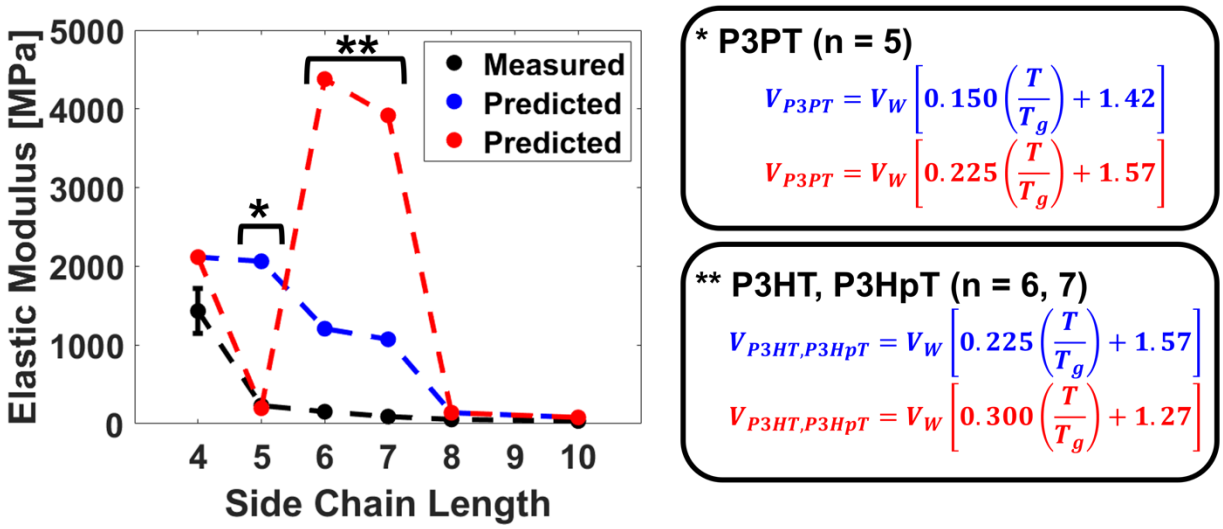

Figure D2. Difference in prediction of elastic modulus for P3AT with glass transition temperatures near room temperature (n = 5 – 7) using different calculated values of the molar volume. Calculated values are provided in **Table D2**.

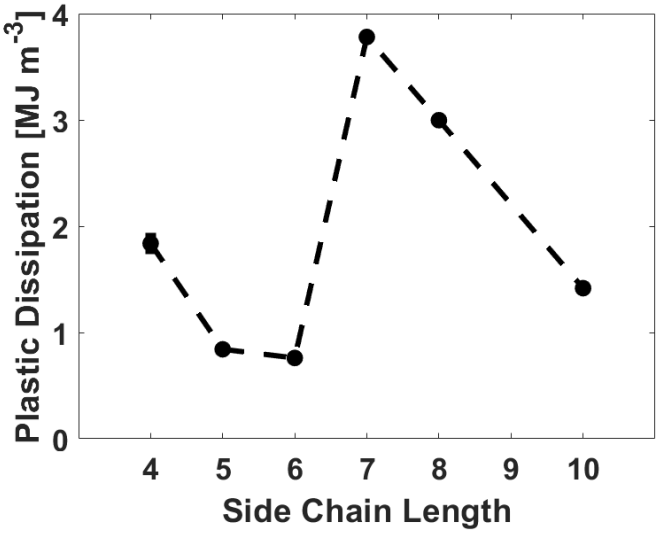

Figure D3. To determine the energy dissipated plastically when under tension, the resilience was subtracted from the toughness. Error bars were determined using error propagation.

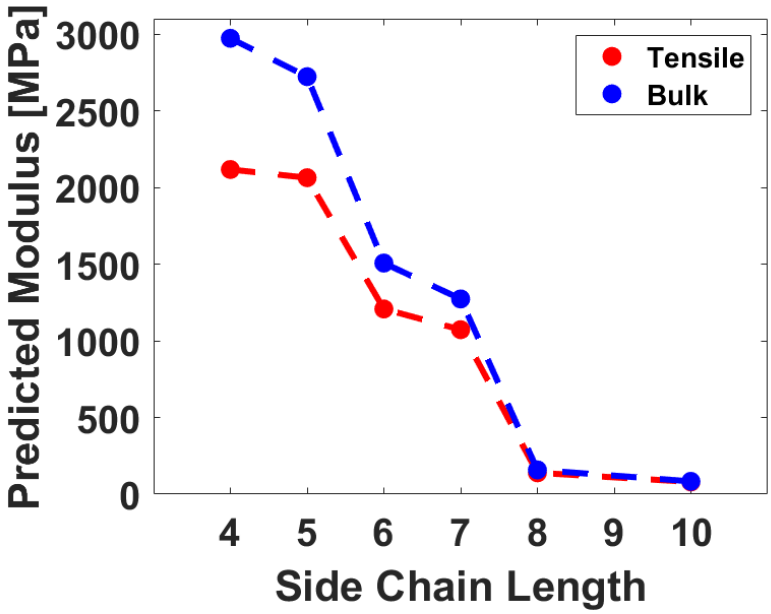

Figure D4. Comparison of the calculated (predicted) bulk (compressive) and tensile modulus for each P3AT.

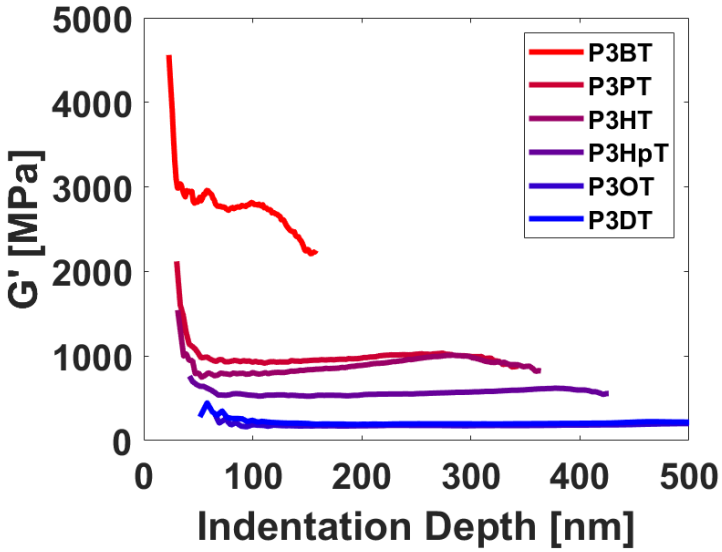

Figure D5. Storage modulus (G') relative to side chain length as determined using oscillatory nanoindentation.

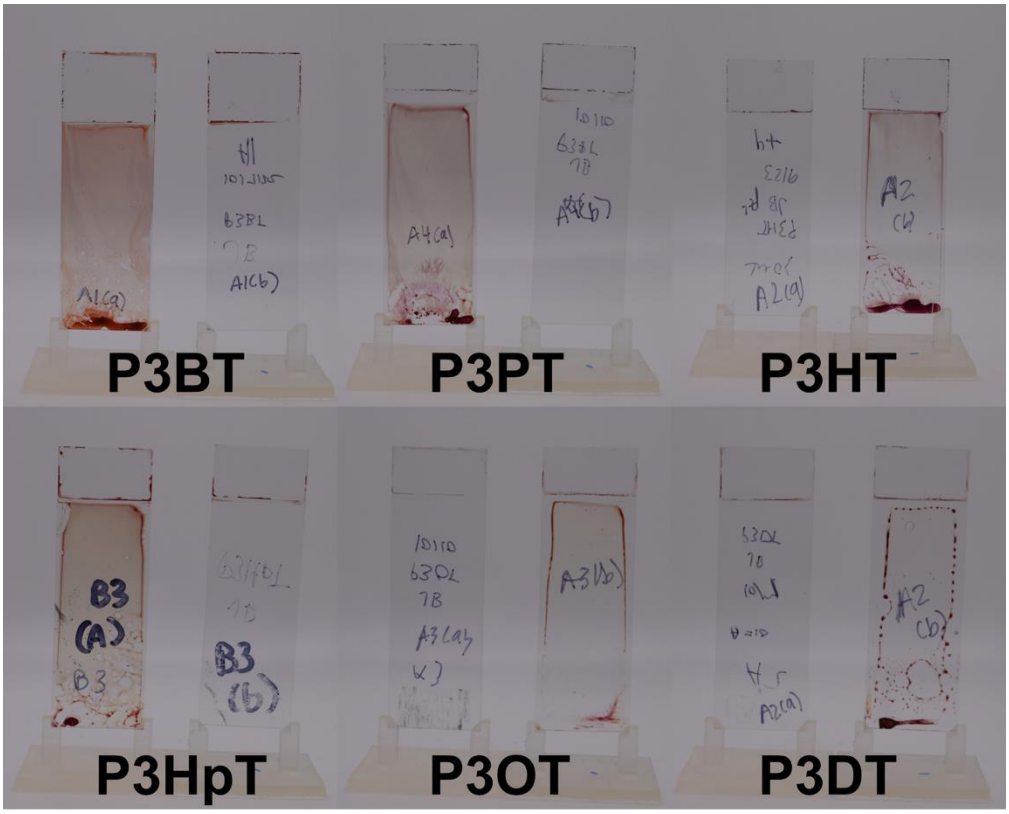

Figure D6. Photographs of representative lap joint shear test samples after fracture.

As discussed here and in Chapter 4, the findings extracted from the lap joint shear samples focus on the qualitative trends relative to polymer structure, rather than quantitative trends (as the assumption that the lap joint is uniform does not hold true). We believe the qualitative trends are of most relevance because the glass/P3AT interface is typically not found in device applications. These samples were prepared in a fume hood environment rather than a glove box, where there is a nitrogen environment, and the humidity can be controlled. (For reference, the humidity of the glove box in which the 180° peel tests samples were prepared was ~15-25%, while the humidity of the fume hood environment is typically ~80%.) Likewise, the blade coating deposition parameters used were those optimized for the 180° peel test samples. It is likely that a more uniform lap joint can be formed by experimenting with the following parameters: different substrate or interface (e.g., silicon, glass/PEDOT:PSS), increased solution concentration (to form a thicker

lap joint), different deposition process (e.g., dip coating or drop casting), different deposition parameters (e.g., blade height and speed), and different solvent (e.g., chloroform).

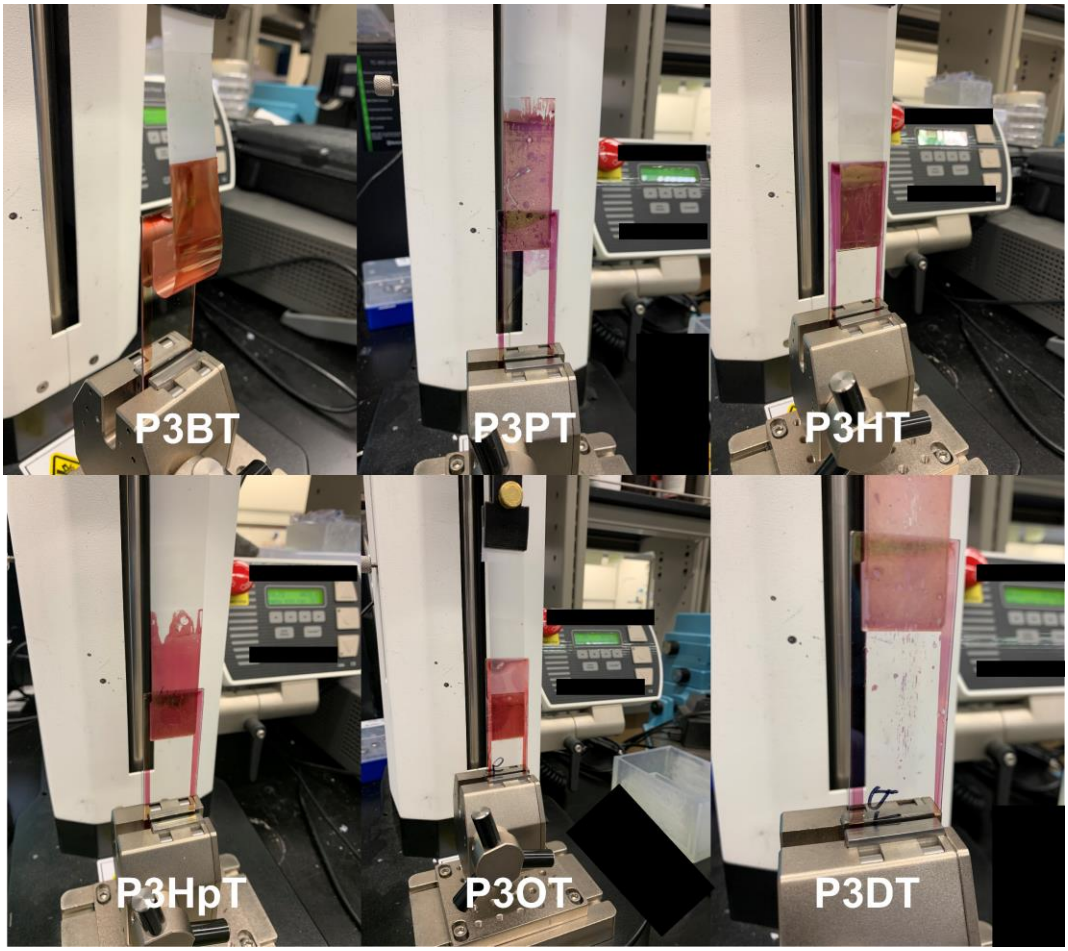

Figure D7. Photographs of representative 180° peel tests.

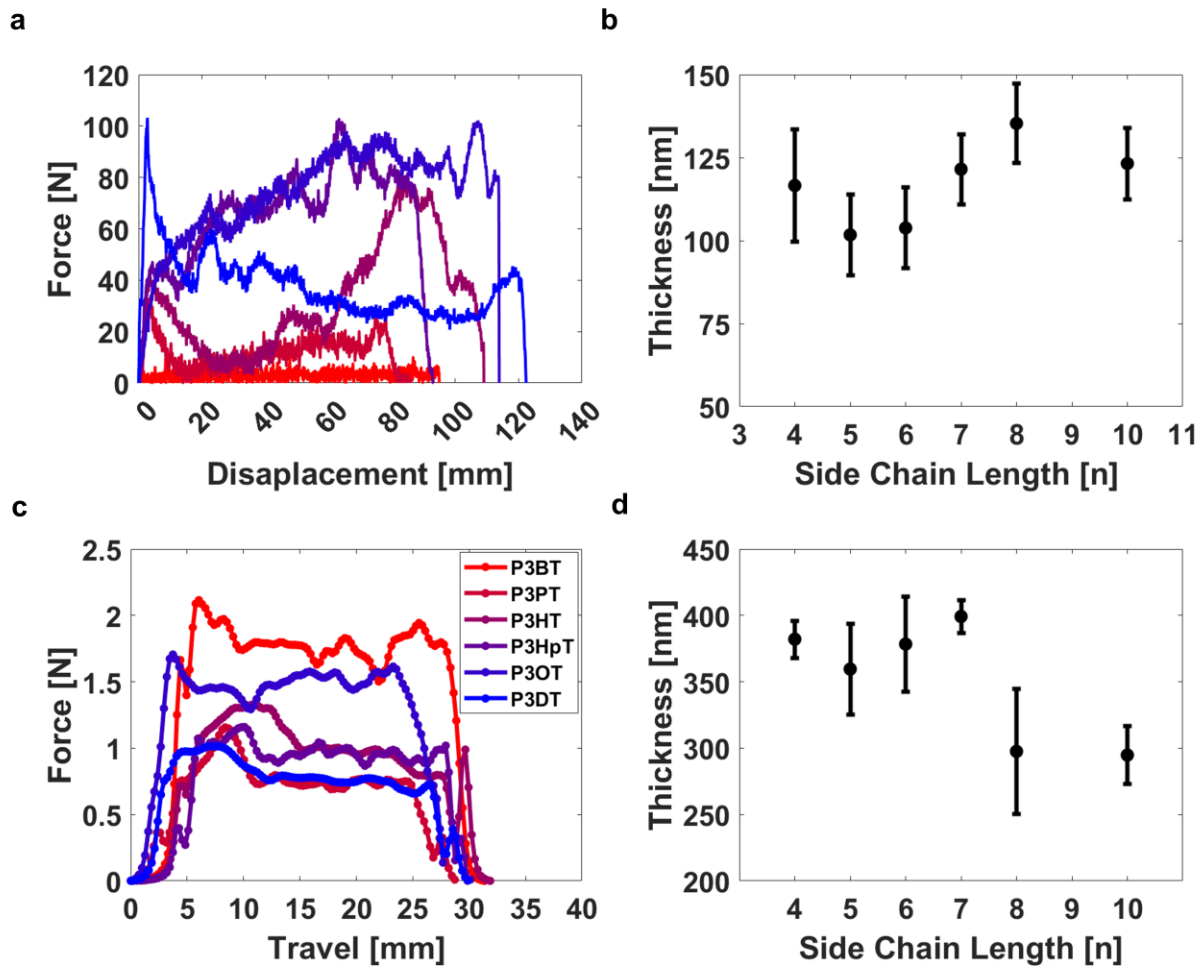

Figure D8. (**a**) Representative force-displacement curves of P3AT films subject to 180° peel tests and (**b**) the thickness of the blade coated films. (**c**) Representative force-displacement curves of P3AT films subject to 90° peel tests and (**d**) the thickness of the P3AT layer in the glass/PEDOT:PSS/P3AT stack.

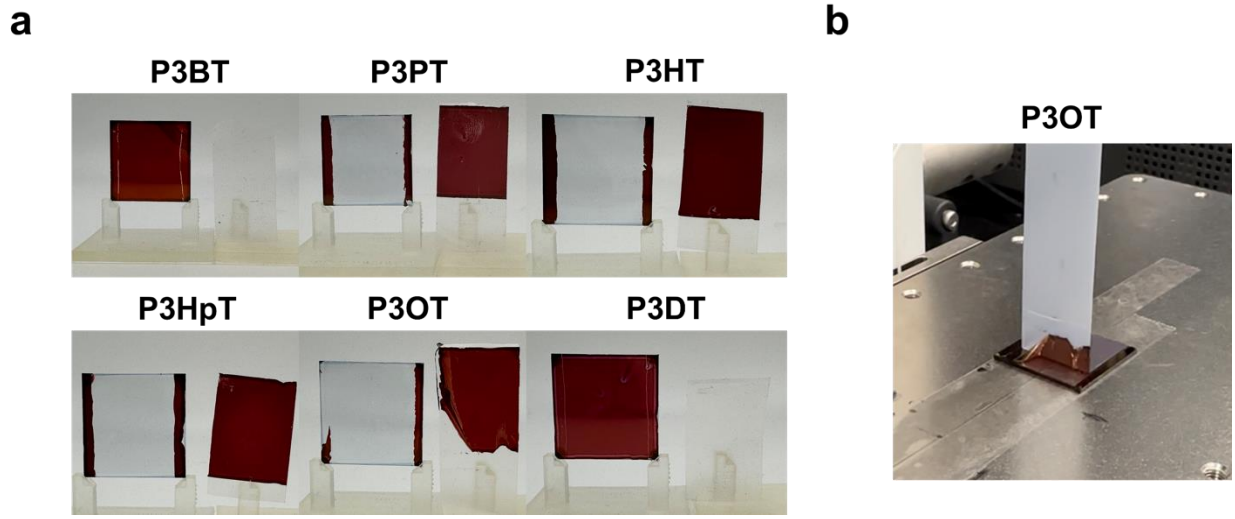

Figure D9. (**a**) Photographs of representative 90° peel tests and a (**b**) photograph of a P3OT film showing delamination at both the PEDOT:PSS/P3OT and P3OT/tape interface.

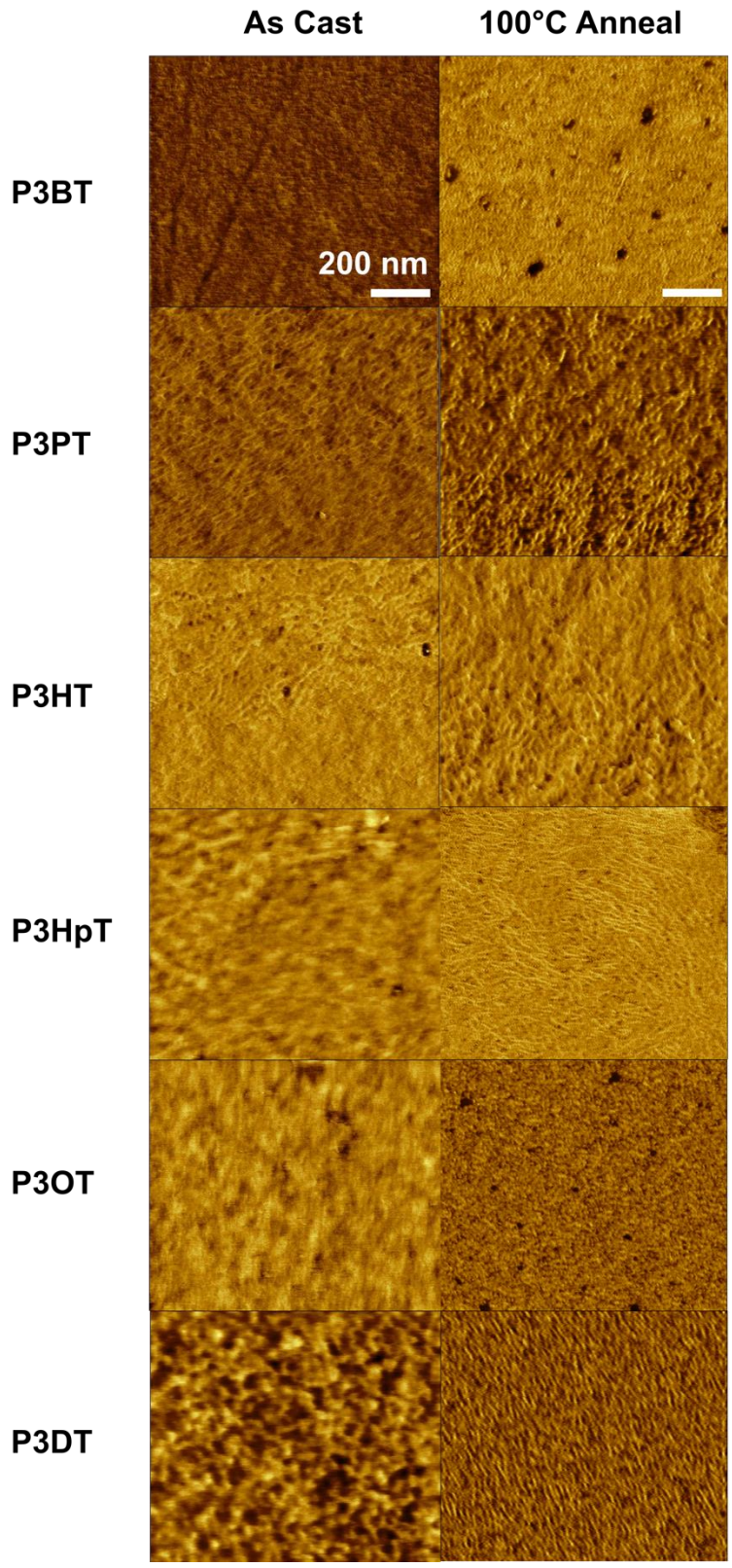

Figure D10. AFM phase plot images for as cast and annealed P3AT films.

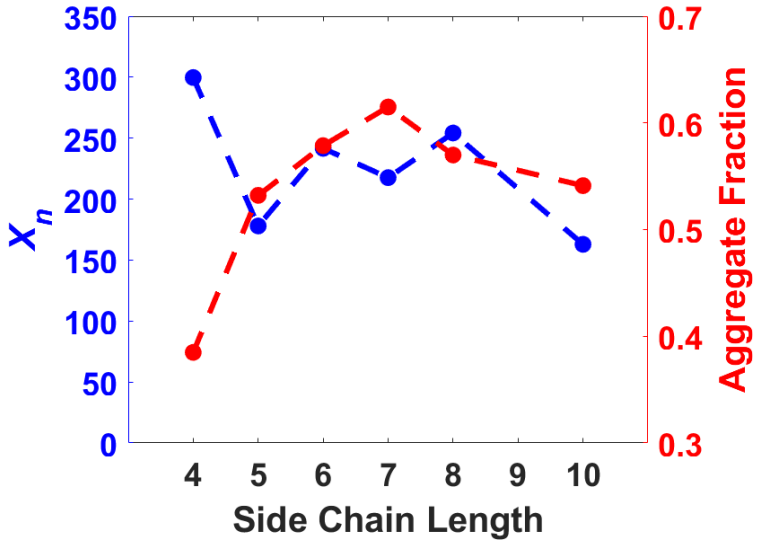

Figure D11. Comparison of degree of polymerization (X_n) relative to aggregate fraction as determined from UV-vis.

D.4 References

(1) Heffner, G. W.; Pearson, D. S. Molecular Characterization of Poly(3-Hexylthiophene). *Macromolecules* **1991**, *24*, 6295–6299.

(2) Vanlandingham, M. R.; Chang, N. K.; Drzal, P. L.; White, C. C.; Chang, S. H. Viscoelastic Characterization of Polymers Using Instrumented Indentation. I. Quasi-Static Testing. *J. Polym. Sci. Part B Polym. Phys.* **2005**, *43*, 1794–1811.

(3) White, C. C.; Vanlandingham, M. R.; Drzal, P. L.; Chang, N. K.; Chang, S. H. Viscoelastic Characterization of Polymers Using Instrumented Indentation. II. Dynamic Testing. *J. Polym. Sci. Part B Polym. Phys.* **2005**, *43*, 1812–1824.

(4) Klapperich, C.; Komvopoulos, K.; Pruitt, L. Nanomechanical Properties of Polymers Determined from Nanoindentation Experiments. *J. Tribol.* **2001**, *123*, 624–631.

(5) Mahouche-Chergui, S.; Boussaboun, Z.; Oun, A.; Kazembeyki, M.; Hoover, C. G.; Carbonnier, B.; Ouellet-Plamondon, C. M. Sustainable Preparation of Graphene-like Hybrid Nanomaterials and Their Application for Organic Dyes Removal. *Chem. Eng. Sci.* **2021**, *236*, 116482.

(6) Oliver, W. C.; Pharr, G. M. An Improved Technique for Determining Hardness and Elastic Modulus Using Load and Displacement Sensing Indentation Experiments. *J. Mater. Res.* **1992**, *7*, 1564–1583.

(7) Li, H.; Randall, N. X.; Vlassak, J. J. New Methods of Analyzing Indentation Experiments on Very Thin Films. *J. Mater. Res.* **2010**, *25*, 728–734.

(8) Chen, A. X.; Hilgar, J. D.; Samoylov, A. A.; Pazhankave, S. S.; Bunch, J. A.; Choudhary, K.; Esparza, G. L.; Lim, A.; Luo, X.; Chen, H.; Runser, R.; Mcculloch, I.; Mei, J.; Hoover, C.; Printz, A. D.; Romero, N. A.; Lipomi, D. J. Increasing the Strength, Hardness, and Survivability of Semiconducting Polymers by Crosslinking. *ACS Appl. Mater. Interfaces* **2022**.

(9) Seitz, J. T. The Estimation of Mechanical Properties of Polymers from Molecular Structure. *J. Appl. Polym. Sci.* **1993**, *49*, 1331–1351.

(10) Tahk, D.; Lee, H. H.; Khang, D.-Y. Elastic Moduli of Organic Electronic Materials by the Buckling Method. *Macromolecules* **2009**, *42*, 7079–7083.

(11) Fedors, R. F. Method for Estimating Both the Solubility Parameters and Molar Volumes of Liquids. *JPL Q Tech Rev* **1973**, *3*, 45–53.

(12) Savagatrup, S.; Makaram, A. S.; Burke, D. J.; Lipomi, D. J. Mechanical Properties of Conjugated Polymers and Polymer-Fullerene Composites as a Function of Molecular Structure. *Adv. Funct. Mater.* **2014**, *24*, 1169–1181.

(13) Choudhary, K.; Chen, A. X.; Pitch, G. M.; Runser, R.; Urbina, A.; Dunn, T. J.; Kodur, M.; Kleinschmidt, A. T.; Wang, B. G.; Bunch, J. A.; Fenning, D. P.; Ayzner, A. L.; Lipomi, D. J. Comparison of the Mechanical Properties of a Conjugated Polymer Deposited Using Spin Coating, Interfacial Spreading, Solution Shearing, and Spray Coating. *ACS Appl. Mater. Interfaces* **2021**, *13*, 51436–51446.

(14) Müller, C. On the Glass Transition of Polymer Semiconductors and Its Impact on Polymer Solar Cell Stability. *Chem. Mater.* **2015**, *27*, 2740–2754.

(15) Xie, R.; Weisen, A. R.; Lee, Y.; Aplan, M. A.; Fenton, A. M.; Masucci, A. E.; Kempe, F.; Sommer, M.; Pester, C. W.; Colby, R. H.; Gomez, E. D. Glass Transition Temperature from the Chemical Structure of Conjugated Polymers. *Nat. Commun.* **2020**, *11*, 1–8.

(16) Chen, S.-A.; Ni, J.-M. Structure/Properties of Conjugated Conductive Polymers. 1. Neutral Poly(3-Alkylthiophene)s. *Macromolecules* **1992**, *25*, 6081–6089.

(17) Rodriquez, D.; Kim, J.; Root, S. E.; Fei, Z.; Bou, P.; Heeney, M.; Kim, T.; Lipomi, D. J. Comparison of Methods for Determining the Mechanical Properties of Semiconducting Polymer Films for Stretchable Electronics. *ACS Appl. Mater. Interfaces* **2017**, *9*, 8855–8862.